Local instantaneous earth radiation budget terms measured from geostationary and polar satellites. [1]

Steven Dewitte [2]

February 10, 1998

[1]Ph. D. at the Vrije Universiteit Brussel in collaboration with the Royal Meteorological Institute of Belgium with grant in the framework of the 'Programma ter versterking van het technologisch en wetenschappelijk potentieel van de federale wetenschappelijke instellingen', grant no. WI/34/011

[2]S. Dewitte is with the Royal Meteorological Institute of Belgium, Department of Aerology, Ringlaan 3, B-1180 Brussels, Belgium. Tel.: ++32-2-3730613, fax: ++32-2-3746788, email: Steven.Dewitte@oma.be and with the Vrije Universiteit Brussel, Department of Electronics, Pleinlaan 2, B-1050 Brussels, Belgium.

Contents

Chapter 1

Introduction

Radiation budget data in the study of atmospheric physics The study of atmospheric physics is based on a combination of the (partial) *knowledge* of processes that occur within the earth's atmosphere and on its surface, and of the (partial) *measurement* of the atmospheric and surface variables.

In atmospheric models (e.g. Global Circulation Models (GCM's) and Numerical Weather Prediction (NWP) models) knowledge and measurements are combined in a type of embedded Kalman filter [Ben85], [K+95], [Ehr92]. The knowledge is present as the internal equations of a numerical model of the atmosphere. The measurements consist of various kinds of variables deduced from observations, mainly ground based and satellite based, which are *assimilated* in the internal variables of the numerical model; i.e. the internal variables are updated to correspond better to the measurements. The assimilation of the measurements brings the internal variables in correspondence with reality, if the number of available independent measurements is sufficiently high, if they are accurate enough, and if they are sufficiently correlated with the internal variables.

A large amount of measurements with uniform quality and high information content can be obtained using satellite data [R+90]. Currently mainly cloud motion winds and InfraRed (IR) soundings are used as satellite data for atmospheric models. A third possible candidate would be radiation budget terms at high space/time resolution (at least synoptic[1]) , which are of great potential interest as shown in [VM58],[VM62],[SS88].

Assimilation of radiation budget terms would greatly improve the correspondence with reality of the "cloud liquid water content" and "cloud ice water content" internal variables, because these are strongly correlated with the earth radiation budget. Moreover, assimilation of radiation budget data would obviously increase the correspondence of the model energy fluxes with the real energy fluxes in the atmosphere and partly also on the earth's surface.

The knowledge of the 3D field of energy fluxes together with the 3D field of temperature is necessary to obtain a correct quantitative description of the "thermal motors" (thermodynamical cycles converting thermal energy into mechanical energy) in the atmosphere. These motors are present in the atmosphere at all scales, ranging from large scale long term phenomena, e.g. the generation of an Hadley cell, to small scale short term phenomena, e.g. the generation of clouds and local convection.

Radiation budget data at high time/space resolution Radiation budget data at the top of the atmosphere derived from LEO (Low Earth Orbit) satellite measurements exist with

- the Earth Radiation Budget Experiment (ERBE), described by [B+89]
- the Scanning radiometer for Radiation Budget measurements (ScaRaB), described by [MKPA91]
- planned: the Cloud and the Earth's Radiant Energy System (CERES)

[1] Synoptic time/space resolution means a time resolution of approximately 3 hours and a space resolution of approximately 100 km.

However, the time resolution of these data is insufficient[2] to obtain a synoptic time sampling.

Since these LEO data were derived with the main purpose of studying the earth's radiative *climate* [WCK+95],[WBH+96], the processing technique (the maximum likelihood estimator described in [WG89] for ERBE) that is used to estimate the radiation budget components from the measured radiances, is focused exclusively on *statistically correct* results, while no attempt is made to obtain maximum accuracy on individual point measurements.

A much better time resolution can be obtained with geostationary satellites. An image is obtained every 30 minutes for the current METEOSAT (METEOrological SATellite) instrument. On board of the planned METEOSAT Second Generation (MSG) satellite, a set of spectral images will be obtained every fifteen minutes from the Spinning Enhanced Visible and InfraRed Imager (SEVIRI) instrument and a couple[3] of a Long Wave (LW) and a Short Wave (SW) image will be obtained every five minutes from the Geostationary Earth Radiation Budget (GERB) instrument.

Radiation budget terms have been estimated from geostationary satellite instruments in [SL88], [SMvdB90] (METEOSAT-RB[4] long wave term), [VF94] (METEOSAT-RB short wave term), [MH84a], [MYH91] (Geostationary Operational Environmental Satellite (GOES)-RB long wave term) and [MH84b], [D+90] (GOES-RB short wave term).

Most of these studies were done with the purpose of studying a climatological diurnal radiation cycle. Hence they were not focused on obtaining single point measurements with a maximal accuracy. They all rely on some kind of statistical subsampling of the full resolution geostationary data, either through the METEOSAT CDS (Climate Data Set) [Cam79], which gives some mean parameters for 32x32 pixel windows in the original METEOSAT data, or through the International Satellite Cloud Climatology Project (ISCCP) [R+85] subsampling, which takes one sample out of every six[5] of the original geostationary data. For the determination of the flux surface density of the reflected solar radiation, which is the radiation budget term which is the most difficult to estimate, all the mentioned studies still rely on the ERBE maximum likelihood estimator described in [WG89].

In this work these techniques will be extended and improved in order to derive radiation budget term estimates from METEOSAT data at the *highest possible time/space resolution* (time resolution, 30 minutes; spatial resolution, long wave: 5 km at nadir[6], short wave, 2.5 km at nadir) with the highest possible accuracy at individual pixel level.

As a first step to do this the instantaneous METEOSAT cloud mask and instantaneous clear sky pixel values will be estimated.

In [MH84b] clear sky grey values (counts) are estimated by a minimum reflectance or a maximum emission technique. The estimation of the cloud mask in this work will be based on a refinement of these techniques, enriched with the image processing technique of morphological filtering (see sections 7.2 and 8.6). For optimal performance of the morphological filtering new forms of image equalisation (see section 7.1) and parameter estimation (see section 8.5) are developed.

The determination of the instantaneous clear sky pixel values will be based on a completely novel image processing technique, top down Bayesian image interpolation (see sections 7.4 and 8.7).

METEOSAT measures the reflected solar radiation in a spectral narrow band. For an estimation of the energy flux of reflected solar energy an estimate of the radiance integrated over the entire solar spectrum is necessary. A radiative transfer calculation scheme [RYG96] will be applied to estimate spectrally integrated reflected solar radiances from spectrally narrow band ones.

The scene identification will be based on the instantaneous clear sky pixel values, combined with a new cloud fraction estimation technique (see section 8.11), which is a modification of the maximum likelihood estimation technique of [WG89]. The modifications are meant to remove the dependency on an assumed correlation between reflected solar radiation and emitted thermal radiation [7] and to minimise the flux surface density estimation error on individual point measurements.

[2] Most often a LEO satellite flies only two times a day over a given point on earth.

[3] The two radiation budget terms that can be estimated from earth observing satellite instruments are the long wave ($\approx$ 4 to 60 μm) and the short wave ($\approx$ 0.2 to 4 μm) term.

[4] The extension "-RB" is used to indicate radiation budget term estimates derived from geostationary imager data.

[5] or the mean of two consecutive samples out of every twelve

[6] The nadir is the point on earth just below the satellite, i.e. the intersection point of the line that connects the centre of the earth and the satellite, with the earth surface.

[7] which exists only in a statistical sense

The estimation of the flux surface density of emitted thermal radiation will be obtained by the application of the method of [SL88],[SMvdB90] to full resolution METEOSAT data.

The results of the developed stand alone method to estimate the two radiation budget terms (the flux surface density of the reflected solar radiation and the flux surface density of the emitted thermal radiation) from METEOSAT data will be compared with existing LEO (ERBE or ScaRaB) flux surface density estimates. The consistency of geostationary and LEO flux surface density estimates obtained at LEO pixel level (size $\approx$ 50 km x 50 km at nadir) will be quantified by comparison of the LEO and METEOSAT-RB estimates of the radiation budget terms over the LEO pixel footprint[8].

It will be demonstrated that stochastic regional differences between METEOSAT-RB and LEO flux surface density estimates with a Root Mean Square (RMS) value of the order of 20 W/m^2 are obtained. This is close to the theoretical lower bound on the RMS error of around 15 W/m^2 for single satellite flux surface density estimates, calculated by [DS89] using the current ERBE set of ADM's (Angular Dependency Models) [SG$^+$88].

In order to have a correct comparison of METEOSAT-RB and LEO estimates of the radiation budget terms at the top of the atmosphere, they should be compared at the best possible space and time correspondence. For an optimal space correspondence, a tool is developed to convolve the high resolution METEOSAT-RB estimates with the Point Spread Function (PSF) of the lower resolution ERBE or ScaRaB footprints (see section 8.15). For an optimal time correspondence, a new tool for motion estimation and motion interpolation for the METEOSAT data is developed (see section 8.8). For the motion estimation, the completely novel image processing technique of top down Bayesian motion interpolation is developed (see section 7.5).

On top of the *regional* difference between METEOSAT-RB and LEO flux surface density estimates of 20 W/m^2 RMS, *single footprint* differences due to radiometric noise, time and space mismatch, and statistical LEO flux surface density estimation processing exist. Without the use of the developed tools for optimal space and time correspondence (PSF convolution and motion interpolation) this difference has an RMS value larger than 100 W/m^2 over single footprints. With the use of the developed tools this RMS difference can be reduced to a value around 50 W/m^2 for a resolution around 50 km and to a value around 35 W/m^2 for a resolution of 225 km.

Once high space/time resolution radiation budget term data, checked for consistency with LEO results, are obtained, a novel image compression technique is developed which gives a compact multi resolution representation of these high resolution data (see sections 7.7 and 7.8). This compact representation will allow the cost efficient transmission of the data in near real time, which will pave the way for the long term goal of the presented work: *make radiation budget data available for operational use in atmospheric modelling.*

The structure of the current work Figure 1.1 shows the overall processing scheme developed in this work.

Part of the processing blocks in this scheme consist of radiation budget specific *satellite data processing* algorithms, part of the processing blocks in this scheme consist of more general *image processing* algorithms. Satellite processing algorithms are indicated by "SP" coloured in red, while image processing algorithms are indicated by "IP" coloured in blue. The link formed between the fields of satellite data processing and image processing is an important part of the work undertaken. Novelties introduced in this work can be classified in three categories:

- the development of novel satellite data processing algorithms
- the development of novel image processing algorithms
- the novel application of image processing algorithms in the field of satellite data processing

Before describing the structure of this thesis, it is worthwhile to mention two other general characteristics of the presented work:

- The processing is developed using currently available satellite measurements, as a preparation for the processing of future satellite data.

[8] A pixel footprint is defined as the region of the earth viewed by the pixel.

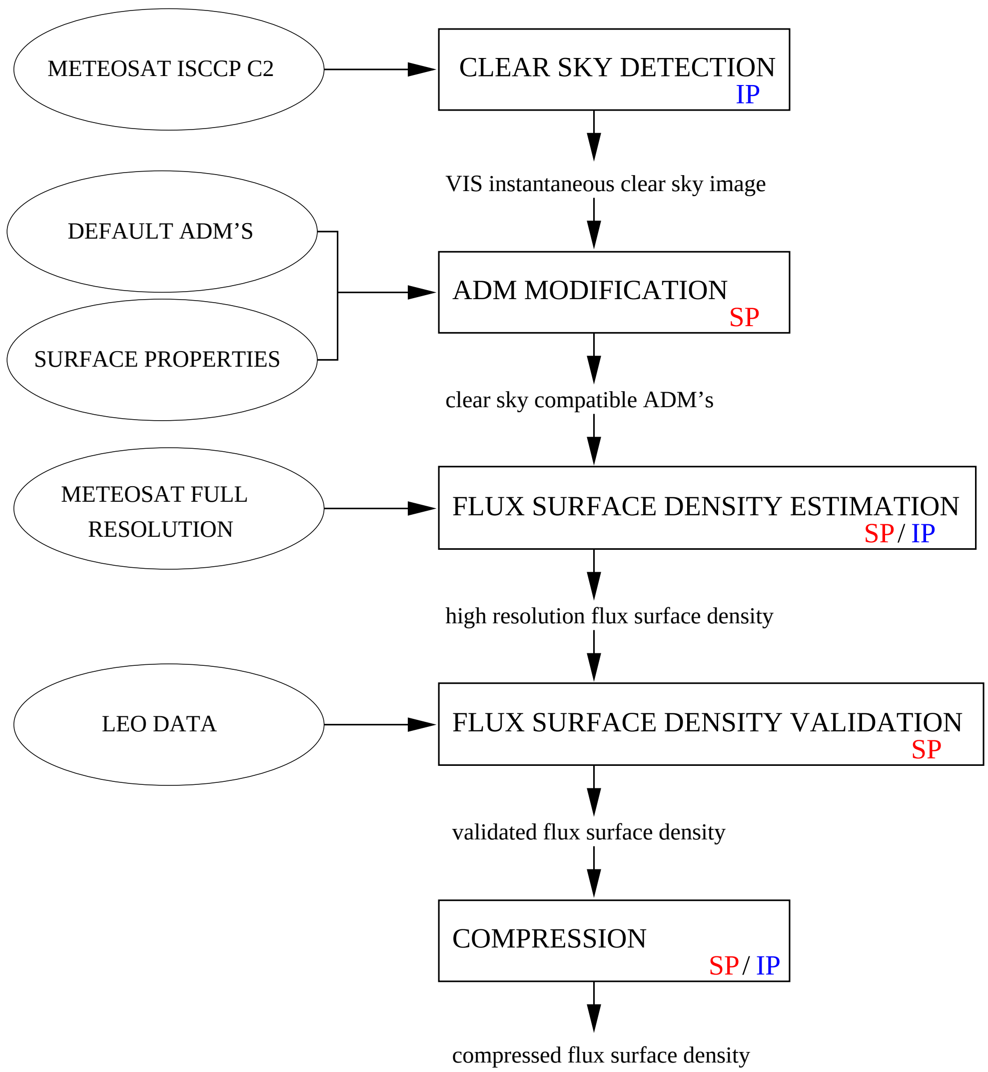

Figure 1.1: The processing scheme developed in this work for the extraction of radiation budget terms from high space/time resolution METEOSAT data and for the validation of this data with low resolution LEO data. Left (surrounded by ovals): external data used as input for the processing scheme. Right (surrounded by rectangles): major processing blocks. For every processing block an indication is given (in the bottom right corner) of the type of techniques used: image processing techniques (indicated by "IP", coloured in blue), or specific satellite data processing techniques (indicated by "SP", coloured in red), or a combination of both. For a description of the concept "ADM", see section 5.1.

- The validation of the final and the intermediate results will be done to the extent possible. Often the "validation" will be based on indirect procedures since no golden standard is available.

Chapter 2 describes the basic physics of the atmosphere and of the radiation within the atmosphere. This describes in a general way, without focus on observations, the *importance* and the *condition*[9] of the problem which is solved in this work, namely the estimation of the radiation budget terms at the top of the atmosphere at the highest possible time and space resolution.

Chapter 3 describes the general conditions for remote sensing of the earth radiation budget terms.

Chapter 4 describes the specific data, mainly satellite data, that will be used in this work. This chapter describes the *measurements* which are available to solve the basic problem.

Chapter 5 describes the simplified models of the physics described in chapter 2, that will be used to interpret the satellite data, described in chapter 4. This chapter describes the *calculations* which have to be done to solve the problem from the data that is available.

Chapter 6 gives a description of the state of the art of the techniques used in the domain of radiation budget term estimation from satellite measurements. The existing techniques have been developed in order to obtain unbiased climatological (e.g. monthly mean) estimates of the radiation budget terms. Our main contribution will be the extension/improvement of these techniques towards the estimation of local instantaneous radiation budget terms with the highest possible accuracy for use in meteorological applications.

Chapters 7 and 8 give an overview of the novel processing techniques that have been developed to achieve this goal. Chapter 7 focuses on the general image processing techniques that have been developed, chapter 8 on the remote sensing and radiation budget specific satellite data processing techniques that have been developed.

Chapters 9 and 10 give a validation of the results. Chapter 9 focuses on the validation of intermediate results, chapter 10 focuses on the final products: radiation budget term estimates.

In chapter 11 the possibility to use the work presented here in future applications is described. The main focus is on the future GERB instrument.

Chapter 12 contains the conclusions of the work.

The reader who's main interest is in the field of radiation budget term estimation, and not in the field of image processing, can skip the chapters 7 and 9 during a first reading. The reader who is exclusively interested in image processing, and not in the radiation budget application, is invited to read only those two chapters.

[9]The condition of problem describes how well the problem *can* be solved, regardless of the eventually chosen solution strategy.

Chapter 2

Radiation budget physics

In this section the importance of the atmospheric energy equation and the radiation budget at the top of the earth's atmosphere is demonstrated. By writing the primitive atmospheric equations as budget equations, it is shown that, through the radiative source term of the primitive energy budget equation, the radiation budget at the top of the earth's atmosphere is, in very good approximation, one of the two important external source terms[1] that maintain the energetics, and through the energetics the dynamics, of the earth's atmosphere. The physics of the radiation budget terms at the top of the atmosphere and their distribution over the atmosphere and the earth's surface are described.

2.1 Basic assumptions

The following assumptions will be made throughout this chapter.

- The atmosphere of the earth is considered to be composed of wet air that is in local thermodynamical equilibrium for every point of the atmosphere. As a consequence, three independent thermodynamical variables, e.g. the pressure p, the temperature T and the total water density[2] $\rho_{\mathrm{h_2o}}$ are sufficient to describe completely the thermodynamical state of the atmosphere in a given point.
- Electromagnetic energies and forces are supposed to be zero.
- Energy input from the centre of the earth to the atmosphere (geothermal heating) is supposed to be zero.
- Energy input at the top of the atmosphere is supposed to consist only of solar radiation. This means that other forms of energy input, e.g. from cosmic radiation or solar wind energy input, are supposed to be zero.

2.2 Primitive atmospheric equations

The atmosphere of the earth is a complex system, described by the combined equations of continuum mechanics, thermodynamics, radiative transfer and phenomenological equations[3]. In this section an overview is given of some of these combined equations, as found e.g. in [CR94]. These equations will be interpreted physically as budget equations, using the methodology of [VM49].

2.2.1 Coordinate system

Consider a point $\vec{P}$, fixed in the coordinate system XYZ, which is rotating together with the earth (see figure 2.1). The earth rotation vector is $\vec{\Omega}$, the local gravity acceleration is $\vec{g_0}$.

[1] The other important source term external to the earth's atmosphere is the surface radiation budget. The direct study of this term falls out of the scope of the presented work.

[2] sum of the partial densities of the three aggregation phases

[3] A phenomenological equation gives an empirical relation between two physical quantities, e.g. between a temperature gradient and a conductive heat flux.

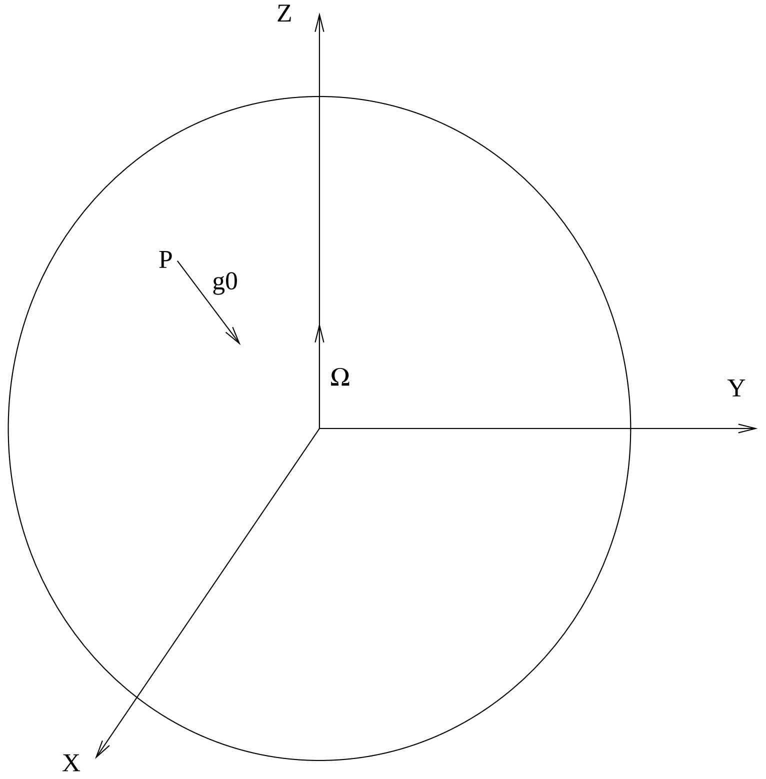

Figure 2.1: Point P in the rotating earth coordinate system XYZ.

In point $\vec{P}$ the apparent gravity acceleration $\vec{g}$ is the resultant of the local gravity acceleration minus the centripetal acceleration $\vec{\Omega}\times(\vec{\Omega}\times\vec{P})$

$$\vec{g} = \vec{g_0} - \vec{\Omega}\times(\vec{\Omega}\times\vec{P}) \tag{2.1}$$

In the point $\vec{P}$ the local coordinate system xyz is defined with z axis oriented opposite to the apparent gravity acceleration and with the yz plane containing $\vec{\Omega}$ (see figure 2.2).

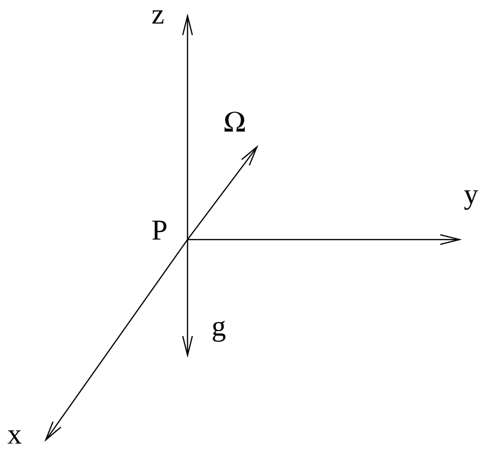

Figure 2.2: Local coordinate system xyz with origin in point P.

2.2.2 General form of a primitive budget equation

Consider a general volume V, which is fixed (does not change in time) in the coordinate system XYZ, within the atmosphere which contains a fluid with an amount F_e of a given extensive quantity.

The amount F_e can change in time due to production of the quantity F_e within the volume V or due to transport of the quantity F_e through the borders of the volume V.

Let $\sigma[F_e]$ be the amount of F_e produced per unit time and per unit volume and let $\vec{C}[F_e]$ be the vector with as i'th component (i = 1,2,3) the amount of F_e flowing per unit time and per unit surface through a surface with normal along the i'th axis (first axis = x axis, second axis = y axis, third axis = z axis).

Then the decrease in time of the quantity F_e in the volume V can be written as the loss due to transport of F_e out of the volume V minus the production of F_e in V as

$$-\frac{\delta F_e}{\delta t} = \int_\Sigma \vec{C}[F_e].\vec{n}\delta\Sigma - \int_V \sigma[F_e]\delta V \tag{2.2}$$

where Σ is the surface surrounding the volume V, and $\vec{n}$ is the outward pointing normal on the elementary surface $\delta\Sigma$.

Equation 2.2 is the general form of a budget equation written over a finite volume which does not change in time.

The left hand side of equation 2.2 can be rewritten using intensive quantities.

Let M be the amount of mass within the volume V. Let the density ρ be the amount of mass per unit volume, and let f_i be the amount per unit mass of the quantity F_e (f_i is the intensive quantity associated with the extensive quantity F_e[4]).

Then $f_i\rho$ is the amount per unit volume of the quantity F_e and F_e is the volume integral of $f_i\rho$

$$F_e = \int_V f_i\rho\delta V \tag{2.3}$$

Since the volume V does not change in time

$$-\frac{\delta F_e}{\delta t} = -\int_V \frac{\delta(f_i\rho)}{\delta t}\delta V \tag{2.4}$$

The surface integral in the right hand side of equation 2.2 can be rewritten as a volume integral using the theorem of Ostrogradsky.

$$\int_\Sigma \vec{C}[F_e].\vec{n}\delta\Sigma = \int_V \mathrm{div}(\vec{C}[F_e])\delta V \tag{2.5}$$

Using the substitutions from equation 2.4 and 2.5, equation 2.2 can be rewritten as

$$-\int_V \frac{\delta(f_i\rho)}{\delta t}\delta V = \int_V \mathrm{div}(\vec{C}[F_e])\delta V - \int_V \sigma[F_e]\delta V \tag{2.6}$$

or

$$\int_V \left(\frac{\delta(f_i\rho)}{\delta t} + \mathrm{div}(\vec{C}[F_e] - \sigma[F_e]\right)\delta V = 0 \tag{2.7}$$

Since this holds for every possible volume V, one must have

$$\frac{\delta(f_i\rho)}{\delta t} + \mathrm{div}(\vec{C}[F_e]) = \sigma[F_e] \tag{2.8}$$

Equation 2.8 is the general form of a primitive budget equation. It states that the increase of the quantity F_e per unit volume and per unit time plus the transport of F_e out of an elementary volume per unit volume and per unit time equals the amount of F_e produced within a unit volume per unit time.

In the next section the primitive atmospheric equations will be interpreted as primitive budget equations. This will allow to identify the radiative source term of the primitive energy budget equation as a source term with an important origin outside the earth's atmosphere.

[4] An extensive quantity is a quantity which is proportional to the amount of mass over which the quantity is defined. E.g. the volume of a given mass is an extensive quantity. An intensive quantity is a quantity which is independent of the amount of mass over which it is defined. E.g. the density of a given mass is an intensive quantity.

2.2.3 Primitive budget equations

Consider, contained within an elementary volume δV, a fluid parcel with speed vector $\vec{v}$. The law of mass conservation states

$$\frac{\delta \rho}{\delta t} + \mathrm{div}(\rho \vec{v}) = 0 \tag{2.9}$$

which can be interpreted as a primitive budget equation 2.8 with

- $\sigma[M] = 0$
  No mass is produced within the elementary volume.
- $\vec{C}[M] = \rho \vec{v}$
  Mass is transported by convection.

For the i'th component of the speed vector $\vec{v} = (v_1, v_2, v_3)$ of the fluid parcel, the momentum conservation equations can be written per unit volume in the xyz coordinate system as

$$\frac{\delta \rho v_i}{\delta t} + \mathrm{div}(\rho v_i \vec{v}) = \rho X_i + \sum_j \frac{\delta T_i^j}{\delta x^j} \tag{2.10}$$

where $\vec{X} = (X_1, X_2, X_3)$ is the vector of the external force (apparent gravity force plus Coriolis force) per unit mass and T_i^j is the internal force (pressure force plus viscosity force) component in the i-direction per unit surface with normal in the j-direction. Define $\vec{T_i} = (T_i^1, T_i^2, T_i^3)$, then equation 2.10 can be rewritten as a primitive budget equation for the extensive quantity $P_i = \int_V \rho v_i \delta V$ (amount of momentum in the i direction)

$$\frac{\delta \rho v_i}{\delta t} + \mathrm{div}(\rho v_i \vec{v} - \vec{T_i}) = \rho X_i \tag{2.11}$$

with

- $\sigma[P_i] = \rho X_i$
  Momentum is produced by the external forces (gravity force plus Coriolis force).
- $\vec{C}[P_i] = \rho v_i \vec{v} - \vec{T_i}$
  Momentum is transported by convection and by the internal forces (pressure force and viscosity forces).

According to the first principle of thermodynamics, one has

$$\frac{\delta \rho e}{\delta t} + \mathrm{div}(\rho e \vec{v}) + p\mathrm{div}(\vec{v}) = \rho \Delta - \mathrm{div}(\vec{q}_{rad}) - \mathrm{div}(\vec{q}_{cond}) \tag{2.12}$$

where e is the internal energy of the fluid per unit mass and p is the pressure of the fluid. Energy changes due to water phase changes are contained within changes of e. $p\mathrm{div}(\vec{v})$ is the mechanical work done by the fluid parcel when it is expanding ($\mathrm{div}(\vec{v}) > 0$)[5]. Δ is the mechanical energy dissipated by the viscosity forces per unit mass. $\vec{q}_{rad}$ is the radiative energy flux surface density vector, i.e. the vector with as i'th component the energy flux surface density (amount of energy flowing through a unit surface per unit time) due to radiation trough a surface with normal in the i'th direction (first direction = x axis, second direction = y axis, third direction = z axis). $\vec{q}_{cond}$ is the conductive energy flux surface density vector, i.e. the vector with as i'th component the energy flux surface density (amount of energy flowing through a unit surface per unit time) due to thermal conductivity trough a surface with normal in the i'th direction.

Equation 2.12 can be rewritten as a primitive budget equation for the extensive quantity $E = \int_V \rho e \delta V$ (amount of internal energy in the volume V)

[5] As an alternative to the budget equation 2.12 for the internal energy e, one can also write a budget equation for the total energy $e + |\vec{v}|^2/2 + \phi_p$, with ϕ_p the potential energy per unit mass. In the budget equation for the total energy the term $\mathrm{div}(p\vec{v}) = p\mathrm{div}(\vec{v}) + \vec{v}.\vec{\mathrm{grad}}(p)$ appears. If the budget equation for the total energy is combined with the budget equation for the mechanical energy $|\vec{v}|^2/2 + \phi_p$, which can be derived from equation 2.11, the term $\vec{v}.\vec{\mathrm{grad}}(p)$ disappears, since this term produces mechanical energy.

$$\frac{\delta \rho e}{\delta t} + \mathrm{div}(\rho e\vec{v} + \vec{q}_{cond}) = -p\mathrm{div}(\vec{v}) + \rho\Delta - \mathrm{div}(\vec{q}_{rad}) \tag{2.13}$$

with

- $\sigma[E] = -p\mathrm{div}(\vec{v}) + \rho\Delta - \mathrm{div}(\vec{q}_{rad})$
  Internal energy is produced by fluid convergence, by dissipation of kinetic energy and by radiative energy input absorption.
- $\vec{C}[E] = \rho e\vec{v} + \vec{q}_{cond}$
  Internal energy is transported by convection and by thermal conductivity.

2.2.4 Interpretation of the primitive budget equations

The primitive budget equations 2.9, 2.11, 2.13, together with the water budget equation (not given explicitly here) can be considered as 6 independent equations (mass = 1 equation, momentum = 3 equations, energy = 1 equation, water = 1 equation) for the time evolution of six independent variables (ρ = 1 variable, $\vec{v}$ = 3 variables, e = 1 variable, $\rho_{\mathrm{h_2O}}$ = 1 variable). The knowledge of these six independent variables gives a complete description of the state of the atmosphere in the point P[6].

An examination of the source terms and of the transport terms in the primitive budget equations 2.9,2.11,2.13, reveals that for all primitive budget equations, *with the exception of the primitive energy budget equation* 2.13, all source terms and transport terms are either completely *internal* to the earth's atmosphere or are determined by the *earth surface* border conditions.

For the primitive energy budget equation 2.13, all transport terms and all source terms, *with the exception of the radiative source term* $-\mathrm{div}(\vec{q}_{rad})$, are also completely *internal* to the system earth's atmosphere, or are determined by the *earth surface* border conditions.

As a conclusion the radiative source term $-\mathrm{div}(\vec{q}_{rad})$, and the external energy input directly absorbed by the surface, are the only terms through which the external energy input to the system earth-atmosphere[7] acts upon the time evolution of the six independent atmospheric variables in the point P.

In section 2.3 it will be shown how the local radiative source term $-\mathrm{div}(\vec{q}_{rad})$ depends on the radiative solar input, through the intermediate of the radiation budget terms at the top the atmosphere.

2.2.5 Border conditions for the radiative source term

The radiative source term $-\mathrm{div}(\vec{q}_{rad})$ of the primitive energy budget equation is defined in a mathematical point. It can be related to the flux of radiative energy through the surface which limits a finite volume by application of the theorem of Ostrogradsky.

$$\int_V \mathrm{div}(\vec{q}_{rad})\delta V = \int_\Sigma \vec{q}_{rad}.\vec{n}\delta\Sigma \tag{2.14}$$

Equation 2.14 states that the spatial distribution of the radiative source term $-\mathrm{div}(\vec{q}_{rad})$ is constrained by the energy flux $-\int_\Sigma \vec{q}_{rad}.\vec{n}\delta\Sigma$ flowing into the volume V.

If the radiative flux surface density vector $\vec{q}_{rad}$ is known in every point of the surface Σ limiting the finite volume V, the spatial distribution of $\vec{q}_{rad}$, and hence of $-\mathrm{div}(\vec{q}_{rad})$ is determined by the *radiative transfer equation* (given e.g. in [Kon69]) within the volume V. The values of $\vec{q}_{rad}$ in every point of the surface Σ are the necessary border conditions for the radiative transfer equation.

Equation 2.14 can be considered in particular for the volume V_{atm}, which covers the entire atmosphere of the earth.

The volume V_{atm} is limited by an ensemble of two oriented surfaces. The first oriented surface is formed by the top of the atmosphere (TOA), with normal pointing away from the earth's centre. The second oriented surface is the earth's surface, with normal pointing towards the earth's centre.

Since energy input from the centre of the earth is supposed to be zero, $\vec{q}_{rad}$ in a point of the second surface is determined by the energetic state of the earth's surface[8].

---

[6] Since local thermodynamical equilibrium is supposed, see section 2.1.
[7] which is supposed to consist uniquely of solar radiative energy input (see section 2.1)
[8] e.g. the soil wetness, the soil temperature profile, the ocean temperature, ...

The spatial distribution over the earth's atmosphere of the energy flux flowing in through the TOA surface, is determined by the radiative transfer equation, with the knowledge of $\vec{q}_{rad}$ in every point of the TOA surface and of the earth's surface as border condition.

$\vec{q}_{rad}$ at the TOA surface is the *local instantaneous radiation budget at the top of the atmosphere.* Its different terms will be described in the next section.

$\vec{q}_{rad}$ at the earth's surface is the *local instantaneous surface radiation budget.* Its direct study falls out of the scope of this work.

2.3 Top Of the Atmosphere (TOA) radiation budget terms

2.3.1 Naming conventions

In the previous section a clear distinction was made between the concept "flux", the flow of a given quantity through a given area, and the concept "flux surface density", the flux per unit area.

From here on, mainly the concept "flux surface density" will be used. For ease of naming, it will sometimes be called simply "flux" or "flux density". If the quantity for which the "flux" is mentioned is not specified, radiative energy will be supposed by default.

In what follows spectrally integrated quantities and quantities defined in limited spectral regions will be used. Spectrally integrated quantities will be indicated by "total", quantities defined in limited spectral regions will be indicated by "spectral". If nothing is specified, "total" will be supposed.

E.g. "solar flux" should be understood as "total (spectrally integrated) solar radiative energy flux surface density".

2.3.2 Definitions

The radiation from the sun is the prime energy source for the processes that occur within the earth's atmosphere and on its surface. At a given point at the top of the atmosphere of the earth, one has a total solar flux surface density (amount of solar energy falling on a surface per unit time and per unit surface) for a horizontal surface, or solar irradiance at the top of the atmosphere F_{SOL}. Part of this solar flux surface density F_{SOL} is reflected back to space as the reflected short wave flux surface density at the top of the atmosphere F_{SW}.

As a result, one has a net short wave flux surface density entering the top of the atmosphere $F_{SW,IN}$

$$F_{SW,IN} = F_{SOL} - F_{SW} \tag{2.15}$$

If this flux surface density were the only non zero one at the top of the atmosphere, the mean temperature of the earth would be rising constantly. This is not the case, because all the components of the earth and its atmosphere have a certain temperature, and therefore emit some thermal radiation which results in an emitted long wave flux surface density (flowing through a horizontal surface) at the top of the atmosphere F_{LW}. The combination of $F_{SW,IN}$ and F_{LW} gives the local instantaneous radiation budget at the top of the atmosphere RB

$$RB = F_{SW,IN} - F_{LW} \tag{2.16}$$

which can be positive (local instantaneous heating) or negative (local instantaneous cooling). The long term average of the global annual mean of RB, i.e. the average of RB over the entire TOA surface (global average), for an entire year (annual mean), has to be zero to have a climate which does not change in time. The components of the long term average of the global annual mean of RB, obtained from http://asd-www.larc.nasa.gov/erbe/ASDerbe.html, are shown in figure 2.3.

2.3.3 Behaviour of incoming solar radiation

The "solar constant" Observed from earth, the sun can be considered in good approximation as a point source. The solar constant S_{SOL} is defined as the total solar irradiance (amount of solar radiative energy per unit surface per unit time) at the mean distance earth-sun (= 1 astronomical unit) falling on a surface perpendicular to the earth-sun direction. The value of S_{SOL} is varying

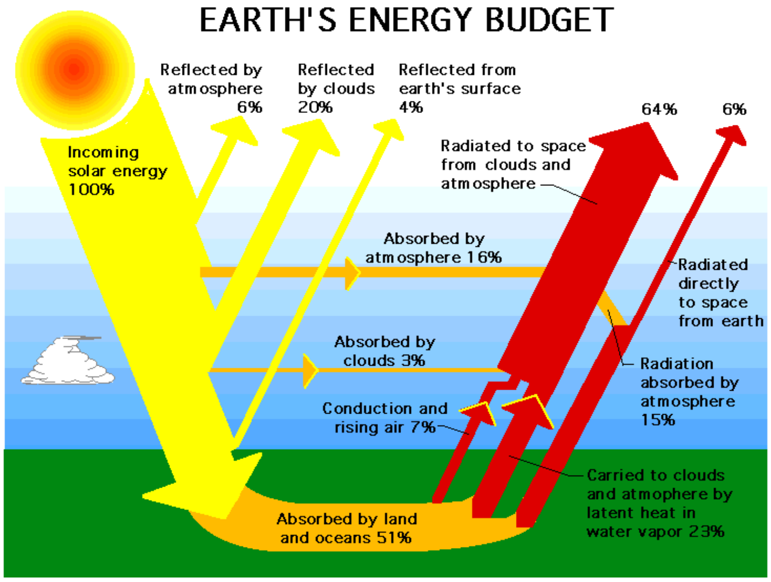

Figure 2.3: The components of the Earth's Radiation Budget (global annual mean of RB), obtained from http://asd-www.larc.nasa.gov/erbe/ASDerbe.html.

with a recurrent eleven year cycle between $1363W/m^2$ and $1369W/m^2$ (see section 4.1). In first approximation it can be considered as a constant with value $1366W/m^2$.

Observations of the total solar irradiance will be given in section 4.1 .

Solar flux surface density at the top of the atmosphere At a given point P at the top of the earth's atmosphere one has a solar flux surface density F_{SOL} (see figure 2.4)

$$F_{SOL} = \frac{S_{SOL}}{(\frac{r_{P-sun}}{1a.u.})^2} \cos(\theta_{sun}) \tag{2.17}$$

where r_{P-sun} is the distance between the sun and the considered point on earth and θ_{sun} is the solar zenith angle (angle between the direction of the sun and the vertical, depending on the position on the earth, on the date of the year and on the local time of the day).

Spectral distribution of the solar radiation at the top of the atmosphere The total solar irradiance at 1 A.U., S_{SOL}, is composed of spectral components $S_{SOL,\lambda}$

$$S_{SOL} = \int_0^\infty d\lambda S_{SOL,\lambda} \tag{2.18}$$

Solar radiation can be roughly approximated by black-body radiation with T $\approx$ 6000K (the roughly approximated solar surface temperature), hence the spectral solar radiation is concentrated in the spectral range $\approx$ [0.2 μm to 4 μm]. This spectral range is relatively short wave compared to radiation emitted by the earth (see section 2.3.6). Therefore radiation from solar origin is also called short wave radiation.

Observations of the solar spectral distribution will be given in chapter 4.

2.3.4 Radiance versus flux surface density

A radiative flux surface density is an amount of radiative energy flowing through a given surface, *with a given orientation*, per unit time. Unlike the incoming solar radiative flux surface density, which results from radiation *which flows in a fixed direction*, namely the direction from the sun to the earth, the two other components of the radiation budget at the TOA, the reflected solar flux surface density and the emitted thermal flux surface density, are composed of contributions of different components *with different directions*.

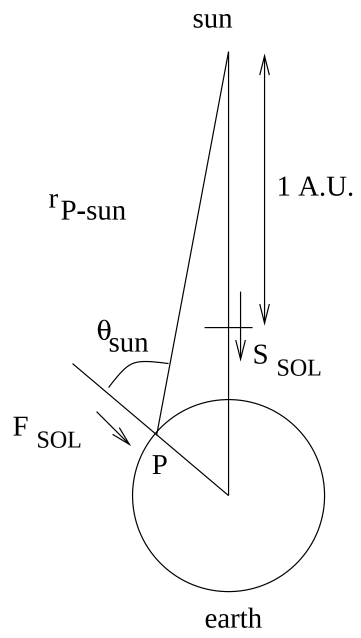

Figure 2.4: The solar flux surface density F_{SOL} (flowing through a horizontal surface) at a given point P at the top of the earth's atmosphere.

Consider an elementary surface dA, centred in a point P at the TOA, with normal along the local vertical (see figure 2.5). The flux surface density F of radiative energy flowing out of this surface is defined as the amount of radiative energy flowing out of this surface per unit time and per unit surface. In general radiative energy can flow out of the surface in any direction (θ, ϕ) of the upper hemisphere.

Consider the local xyz coordinate system with origin in P and with z axis along the local vertical (which corresponds to the normal of dA.). Consider θ and ϕ as the angular coordinates of a spherical coordinate system. The relation between the spherical coordinates (r, θ, ϕ) and the cartesian coordinates (x, y, z) is given by equation 2.19.

$$\begin{aligned} x &= r\sin(\Theta)\cos(\Phi) \\ y &= r\sin(\Theta)\sin(\Phi) \\ z &= r\cos(\Theta) \end{aligned} \tag{2.19}$$

Consider a particular direction (θ, ϕ) of the upper hemisphere, and consider an elementary solid angle $d\Omega = sin(\theta)d\phi d\theta$ centred around this direction (see figure 2.5). The radiance $L(\theta, \phi)$ flowing out of the surface in the direction (θ, ϕ), is defined as the amount of radiative energy flowing out of the surface in the direction (θ, ϕ) per unit time and per unit apparent surface. The apparent surface $cos(\theta)dA$ is the projection of the surface dA on the plane perpendicular to the direction (θ, ϕ).

The flux surface density F is the integral over the upper hemisphere of the flux contributions $L(\theta, \phi)\cos\theta$ weighted with the elementary solid angle $sin(\theta)d\phi d\theta$ of the radiances $L(\theta, \phi)$, as described by equation 2.20.

$$F = \int_0^{2\pi} d\phi \int_0^{\pi/2} sin(\theta)d\theta L(\theta, \phi)cos(\theta) \tag{2.20}$$

2.3.5 Behaviour of reflected solar radiation

Part of the solar flux surface density F_{SOL} is reflected back to space as the reflected short wave flux surface density at the top of the atmosphere F_{SW}

$$F_{SW} = \int_0^{2\pi} d\phi \int_0^{\pi/2} sin(\theta)d\theta L_{SW}(\theta, \phi)cos(\theta) \tag{2.21}$$

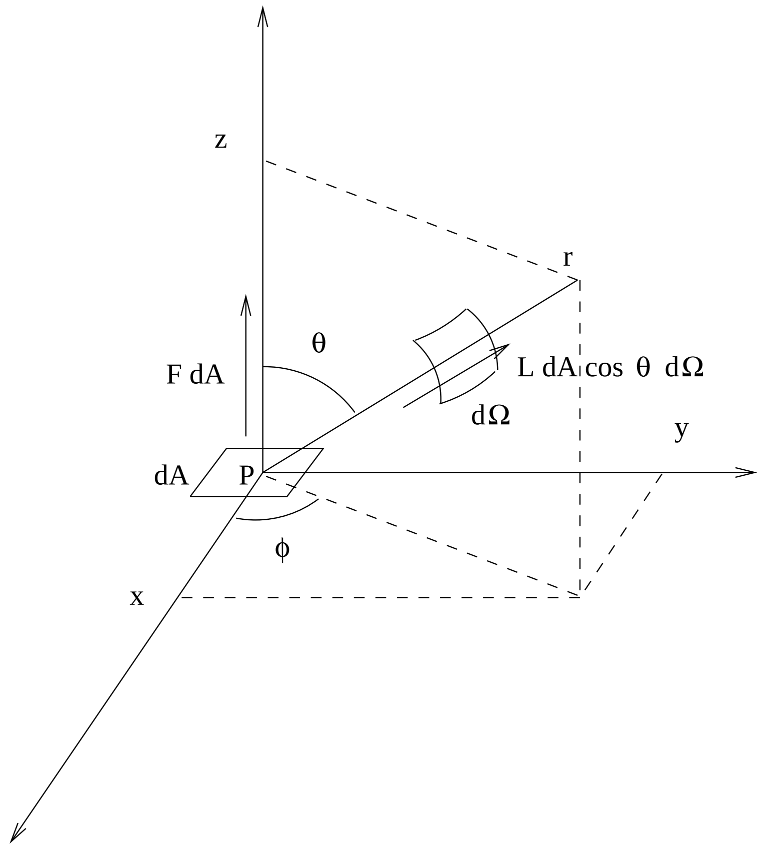

Figure 2.5: Radiative flux surface density F flowing through a horizontal surface and radiance $L(\theta,\phi)$. (r,θ,ϕ): spherical coordinates. dA: elementary surface. $d\Omega$: elementary solid angle

$$\begin{aligned} L_{SW}(\theta,\phi) &= \int_0^\infty d\lambda L_\lambda^{solar}(\theta,\phi) \\ &\approx \int_{0.2}^{4\mu m} d\lambda L_\lambda^{solar}(\theta,\phi) \end{aligned} \tag{2.22}$$

where θ and ϕ are the angular coordinates of a spherical coordinate system with z-axis corresponding to the local vertical direction (see figure 2.6). $L_{SW}(\theta,\phi)$ is the reflected short wave radiance at the top of the atmosphere. L_λ^{solar} is the spectral radiance from solar origin reflected at the top of the earth's atmosphere. It results from an interaction between the solar radiation and the earth's atmosphere and surface. This is indicated symbolically in figure 2.6.

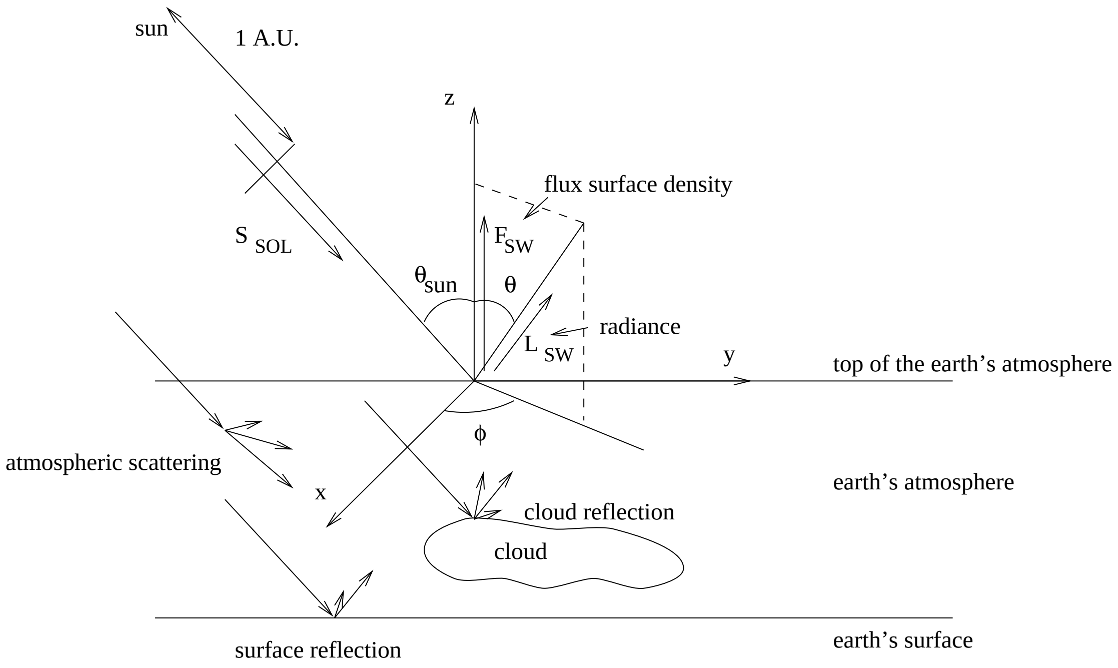

Figure 2.6: The reflected solar radiance L_{SW} in a given direction (θ,ϕ) at a given point P at the top of the earth's atmosphere. The different processes (atmospheric scattering, surface reflection, cloud reflection) that contribute to L_{SW} are indicated.

The interaction of the incoming solar radiation and the earth's atmosphere and surface, consists of

- Wavelength dependent absorption and scattering by atmospheric gases, such as water vapour, aerosols, minor constituents inclusive ozone, ... Part of the scattered radiation contributes to the reflected short wave radiation at the top of the atmosphere.

- Wavelength dependent absorption and scattering by cloud particles (water droplets, ice crystals, ...). Part of the scattered radiation contributes to the reflected short wave radiation at the top of the cloud, which itself contributes to the reflected short wave radiation at the top of the atmosphere.

- Wavelength dependent reflection by the earth's surface. Part of the reflected radiation contributes to the reflected short wave radiation at the top of the atmosphere.

2.3.6 Behaviour of thermal emission radiation

Since all the components of the earth and its atmosphere have a certain temperature, they emit thermal radiation. This radiation can roughly be approximated by black-body radiation with T $\approx$ 220 K to 320 K (the roughly approximated temperatures that occur in the earth-atmosphere system T = 220 K $\approx$ -50° C can occur for polar clear sky surfaces or for high, cold clouds. T = 320 K $\approx$ 50° C for clear sky desert surfaces at noon), hence the emitted thermal radiation is concentrated in the spectral range $\approx$ [4 μm to 60 μm]. This spectral range is relatively long wave compared to radiation from solar origin (see section 2.3.3). Therefore thermal radiation emitted by the earth is also called long wave radiation.

The emitted thermal radiation results in an emitted long wave flux surface density at the top of the atmosphere F_{LW} (see figure 2.7).

$$F_{LW} = \int_0^{2\pi} d\phi \int_0^{\pi/2} sin(\theta) d\theta L_{LW}(\theta,\phi) cos(\theta) \tag{2.23}$$

$$L_{LW}(\theta,\phi) \begin{array}{l} = \int_0^{\infty} d\lambda L_\lambda^{earth}(\theta,\phi) \\ \approx \int_{4\mu m}^{60\mu m} d\lambda L_\lambda^{earth}(\theta,\phi) \end{array} \tag{2.24}$$

where θ and ϕ are defined as in the previous section (see figure 2.7). $L_{LW}(\theta,\phi)$ is the emitted long wave radiance at the top of the atmosphere. L_λ^{earth} is the spectral radiance resulting from emission by the earth's surface or atmosphere, at the top of the earth's atmosphere. This is indicated symbolically in figure 2.7.

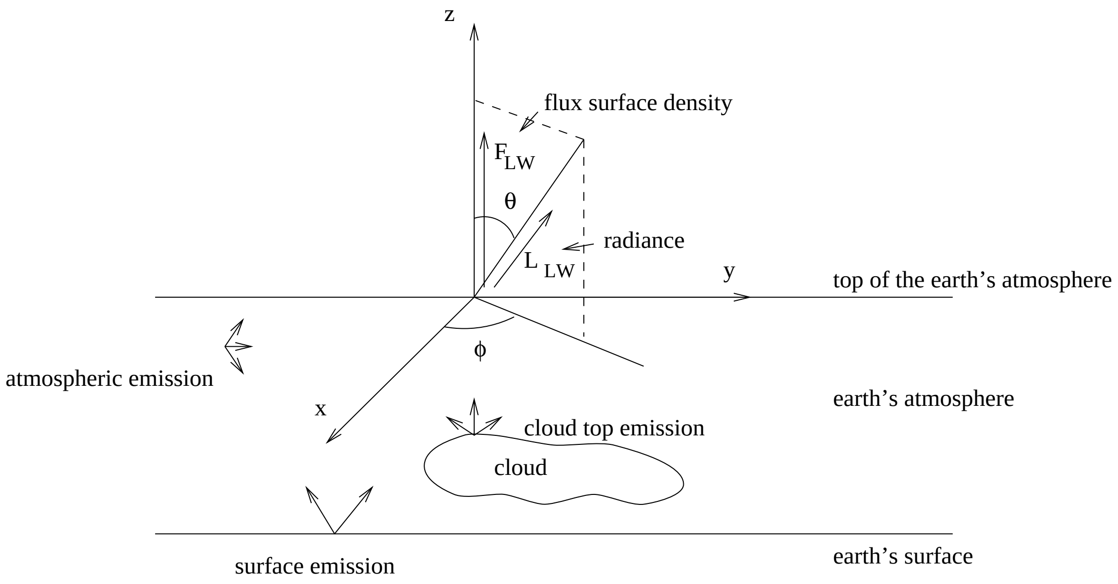

Figure 2.7: The emitted thermal radiance L_{LW} in a given direction (θ,ϕ) at a given point P at the top of the earth's atmosphere. The different processes (atmospheric emission, surface emission, cloud emission) that contribute to L_{LW} are indicated.

The emitted thermal radiance at the top of the earth's atmosphere results from the following processes

- Wavelength dependent absorption and emission (temperature dependent) by atmospheric gases. Part of the emitted radiation contributes to the emitted long wave radiation at the top of the atmosphere.
- Wavelength dependent absorption and emission (temperature dependent) by cloud particles. Part of the emitted radiation contributes to the emitted long wave radiation at the top of the cloud, which itself contributes to the emitted long wave radiation at the top of the atmosphere.
- Wavelength, temperature and emissivity dependent emission (and eventually reflection) by the earth's surface. Part of the emitted radiation contributes to the emitted long wave radiation at the top of the atmosphere.

Chapter 3

Remote sensing

In this chapter the general condition of the problem of the remote sensing of the terms of the local instantaneous radiation budget of the earth, is described. The terms of the local instantaneous radiation budget are: the solar incident flux surface density, the reflected solar flux surface density and the flux surface density of radiation emitted by the earth.

3.1 Solar observation

The observation of direct solar irradiance is well conditioned, since the sun can be considered in good approximation as a point source. The solar irradiance can therefore be measured by sun pointing radiometers from space. The measurements from space are necessary to avoid atmospheric transmission. From these measurements, the instantaneous solar irradiance S_{SOL} is determined, from which the incoming local instantaneous solar flux surface density at the top of the atmosphere F_{SOL} can be *calculated* (by application of equation 2.17) for any point on earth.

3.2 Earth observation

3.2.1 Spectral conditions

L_λ^{solar} finds its origin (through the reflection by the earth) in the radiation emitted by the sun, approximated roughly by black-body radiation with T $\approx$ 6000 K, L_λ^{earth} finds its origin in the radiation emitted by the earth, approximated roughly by black-body radiation with T $\approx$ 220 K to 320 K. Fortunately for remote sensing purposes, these temperatures are sufficiently different to have a good spectral separation between L_λ^{solar} (short wave spectral range $\approx$ [0.2 μm to 4 μm]) and L_λ^{earth} (long wave spectral range $\approx$ [4 μm to 60 μm]).

3.2.2 Satellite observation

The terms F_{SW},F_{LW} of the local instantaneous radiation budget at the top of the atmosphere RB can be estimated from earth observing satellite measurements. If one wants to estimate these outgoing terms from single satellite instrument measurements, all one has available in general are a number of filtered radiances $L_{sat,channel}$

$$L_{sat,channel} = \int_0^\infty d\lambda \Phi_{channel}(\lambda)(L_\lambda^{solar} + L_\lambda^{earth})(\theta_{sat}, \phi_{sat}) \tag{3.1}$$

where θ_{sat} and ϕ_{sat} are the angular coordinates of the radiance which reaches the satellite from the observed point on earth and where $\Phi_{channel}(\lambda)$[1] is the spectral response of the satellite instrument channel under consideration. To estimate F_{SW} or F_{LW} from filtered radiances two conversions are necessary, an angular one and a spectral one.

[1] Since normally $\Phi_{channel}(\lambda)$ is only different from zero in a finite wavelength interval, the integral 3.1 normally reduces to an integral over this finite wavelength interval.

The spectral conversion is needed to obtain an estimate of the radiation integrated spectrally over an entire spectral region (the long wave region or the short wave region) from the measured radiation in one or more limited spectral bands. The angular conversion is needed to obtain an estimate of the radiation integrated angularly over the entire upper hemisphere from the radiation measured in one single direction.

One can either start with the angular conversion, or one can start with the spectral conversion. If one starts with the angular conversion one gets as (ideal) intermediate results the so-called outgoing "filtered" flux surface densities $F_{channel}$

$$F_{channel} = \int_0^\infty d\lambda \int_0^{2\pi} d\phi \int_0^{\pi/2} sin(\theta) d\theta \Phi_{channel}(\lambda)(L_\lambda^{solar} + L_\lambda^{earth})(\theta, \phi) cos(\theta) \tag{3.2}$$

If one starts with the spectral conversion one gets as (ideal) intermediate results the so-called outgoing "unfiltered" radiances $L_{sat,type}$

$$L_{sat,type} = \int_0^\infty d\lambda L_\lambda^{type}(\theta_{sat}, \phi_{sat}) \tag{3.3}$$

where type equals earth or solar.

3.2.3 Spatial conditions

Scene homogeneity When observed from space, the earth is not a spatially homogeneous scene. The largest spatial variation exists within clouds, which can be very inhomogeneous, and between clouds and cloud free scenes. In general a larger spatial inhomogeneity exists for solar reflection images than for thermal emission images.

Point spread function Consider a spatially continuously varying scene as viewed by a satellite instrument (radiometer) with spectral characteristic $\Phi_{channel}(\lambda)$. Let δ_a, δ_c be the angles in two perpendicular directions under which the satellite views the scene. The radiance $L_{sat,channel}$ measured by the satellite will be a weighted mean of the scene radiance distribution $L_{sat,channel}(scene)$ which varies in function of the angles δ_a and δ_c.

$$L_{sat,channel} = \frac{\int PSF_{channel}(\delta_a, \delta_c) L_{sat,channel}(scene) d\delta_a d\delta_c}{\int PSF(\delta_a, \delta_c) d\delta_a d\delta_c} \tag{3.4}$$

The weighting function $PSF_{channel}(\delta_a, \delta_c)$ in equation 3.4 is called the (total) Point Spread Function (PSF) of the radiometer.

The PSF of a scanning radiometer. For a scanning radiometer in particular, an along scan angle δ_a and a cross scan angle δ_c can be considered (see figure 3.1). For a cross track scanning radiometer, the cross scan direction corresponds to the flight direction of the satellite. The static PSF or angular sensitivity $OF_{channel}(\delta_a, \delta_c)$ is defined as the PSF of the instrument when it is non scanning.

The total (dynamic) PSF of the scanning radiometer is different from the static PSF [Smi94].

If the global time impulse response of the detector (global means: sensor + electronics) is $h(t)$, and if the instrument is scanning with an angular scan speed v_{scan} in the direction of increasing δ_a, then the equivalent global angular impulse response $h_{ang}(\delta_a)$ of the detector is given by:

$$h_{ang}(\delta_a) = h(\delta_a / v_{scan}) \tag{3.5}$$

The total PSF, $PSF_{channel}(\delta_a, \delta_c)$, of the detector is obtained by convolution of the angular sensitivity $OF_{channel}(\delta_a, \delta_c)$ with the mirrored global angular impulse response $h_{ang}(-\delta_a)$:

$$PSF_{channel}(\delta_a, \delta_c) = OF_{channel}(\delta_a, \delta_c) \circledast h_{ang}(-\delta_a) \tag{3.6}$$

where $\circledast$ stands for convolution in the angular space. The mirroring, i.e. replacing δ_a with $-\delta_a$ is done because the scanning is in the direction of *increasing* δ_a, while increasing times in $h(t)$ correspond to *decreasing* δ_a.

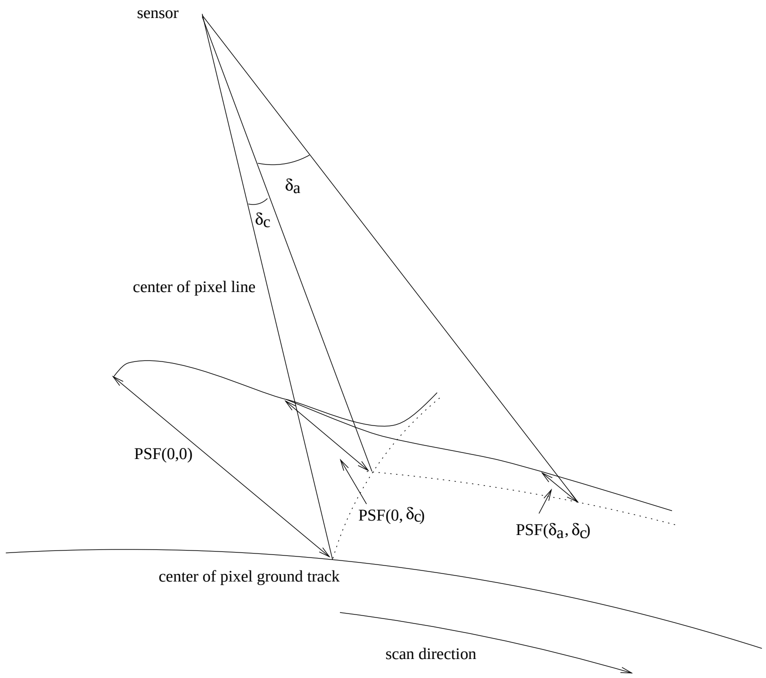

Figure 3.1: Definition of the along scan angle δ_a, the cross scan angle δ_c and part of the PSF (Point Spread Function) of a satellite sensor.

3.2.4 Temporal conditions

When followed in time, the radiation at a particular point on earth, is not the realisation of a stochastic variable with a fixed probability distribution function. Several mechanisms exist which cause systematic variation of the radiation probability distribution function with time.

Diurnal solar elevation cycle During the day the solar elevation for a particular place on earth changes. This directly affects the magnitude of the reflected solar radiation, since this radiation is in first approximation proportional to the incoming solar radiation.

Surface diurnal cycle Due to the diurnal solar elevation cycle the earth surface temperature also changes with a typical diurnal cycle, with on average maximum temperature shortly after local noon and minimum temperature during the end of the night. This directly affects the clear sky emitted thermal radiation, which is in first approximation proportional to the fourth power of the surface temperature.

Cloud motion There is a contrast in reflection and emission characteristics between clouds and clear sky surface. Therefore the motion of clouds causes time variations of the reflected solar radiation as well as of the emitted thermal radiation.

Chapter 4

Available data

In this chapter the different sources of data that will be used, are described.

4.1 Sun observation from satellites

4.1.1 Individual instrument measurements

Since 1978, space measurements of the "solar constant" are available. A number of instruments have measured the solar irradiance on a daily basis since then. The solar irradiance monitor [HKHM92] aboard the NIMBUS 7 satellite recorded measurents from 16 November 1978 until 13 December 1993. The Active Cavity Radiometer Irradiance Monitor I (ACRIM I) [Wil94] aboard the Solar Maximum Mission (SMM) satellite measured from 16 February 1980 until 14 July 1989. The solar irradiance monitor ACRIM II [Wil94] aboard the Upper Atmospheric Research Satellite (UARS) satellite started measuring on 4 October 1991. The solar irradiance monitors SOlar VAriability 1 (SOVA 1) [CDFL94] and SOVA 2 [RWF94] aboard the EUropean REtrievable CArrier (EURECA) satellite measured from 12 August 1992 until 13 May 1993. The DIfferential Absolute RADiometer (DIARAD) instrument, which is part of the Variability of solar IRradiance and Gravity Oscillations (VIRGO) [FCW+97] experiment on the SOlar and Heliospheric Observatory (SOHO) satellite started measuring on 18 January 1996. The data from these individual instruments are shown in figure 4.1.

4.1.2 Solar irradiance data homogenisation

The individual measurements shown in figure 4.1 have an absolute error with an amplitude which is larger than the typical variations of the solar constant. Therefore the compilation of individual solar irradiance measurements does not form a homogeneous time series of measurements. A single homogeneous time series has been obtained [CD97] by referencing all data series to the SARR (Space Absolute Radiometric Reference) as defined in [CFLR95]. Denote the solar constant time series as $S(t)$, and the time series obtained by a single instrument as $S_i(t)$. It is assumed that every instrument has an absolute error Δ_i which does not change on short time scales[1] and a noise term $n_i(t)$. One then has

$$S_i(t) = S(t) + \Delta_i + n_i(t) \tag{4.1}$$

If one considers different instruments built and operated independently of each other, each instrument aiming at maximal absolute accuracy, it can be supposed that the set of absolute errors Δ_i of each instrument, is a set of stochastically independent realisations of a single stochastic variable Δ. Δ is then the stochastic absolute error of a stochastic instrument, with one particular realisation Δ_i for every instrument that is actually built and operated. Δ results from common errors made by all instrument developers and operators (e.g. a particular physical phenomenon is never taken into account) and from all kinds of small deviations from absoluteness when the

[1] On very long time scales Δ_i can change due to aging effects.

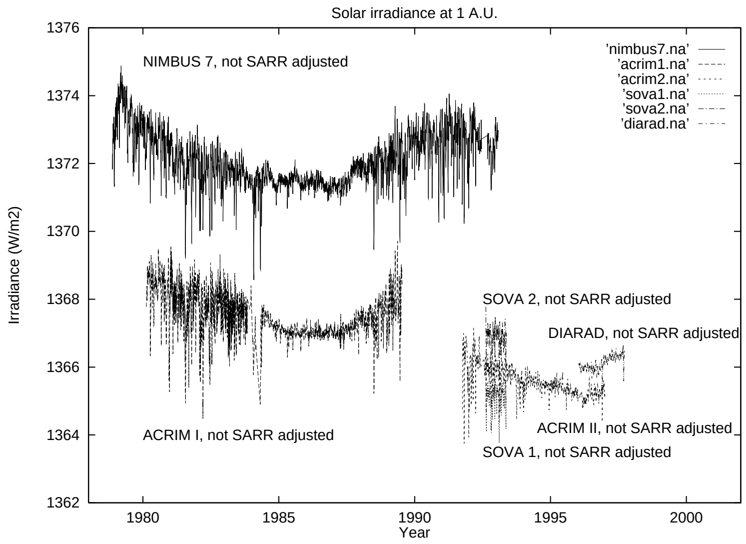

Figure 4.1: The solar constant as measured by the individual instruments aboard NIMBUS 7, ACRIM I, ACRIM II, SOVA 1, SOVA 2 and DIARAD/VIRGO.

instrument is built and operated. It is assumed to have a Gaussian distribution with mean m_Δ and standard deviation σ_Δ.

During the ATLAS 2 (Atmospheric Laboratory for Applications and Science) space shuttle flight, 8 absolute radiometers observed the sun simultaneously. The total solar observation time was approximately 40 hours, distributed over 4 days in April 1993. If for every instrument the mean "solar constant" measurement value over this 40 hour period $\overline{S_i}$ is taken, the noise contribution becomes negligible compared to the systematic error. Moreover, sun spots, which are a major cause of solar irradiance variation with time, were absent during this 40 hour time period. Consequently, the solar irradiance could be considered as a constant $S(t) \approx \overline{S}$. The mean measurements $\overline{S_i}$ that were made over the solar observation periods of ATLAS 2 by the eight considered instruments are given in table 4.1 (see [CFLR95]).

instrument	ATLAS 2 mean solar constant
SOVA1-L	1365.150 W/m^2
SOLCON-R	1366.510 W/m^2
SOVA1-R	1366.568 W/m^2
SOLCON-L	1367.323 W/m^2
ERBS	1365.650 W/m^2
SOVA2 a	1366.690 W/m^2
SOVA2 b	1366.500 W/m^2
ACRIM II	1365.757 W/m^2

Table 4.1: 40 hour mean $\overline{S_i}$ of the solar constant measurements made during four ATLAS-2 days, by eight independent absolute radiometers.

They approximately satisfy the relation

$$\overline{S_i} = \overline{S} + \Delta_i \tag{4.2}$$

From the eight available measurements listed in table 4.1, statistically optimal estimations of the mean value of the solar constant $\overline{S}$ and of the root mean square absolute error σ_Δ can be made

$$\hat{\overline{S}} = \frac{\sum_{i=1}^{8} \overline{S_i}}{8} - m_\Delta = 1366.31 \text{ W/m}^2 - m_\Delta \tag{4.3}$$

$$\widehat{\sigma_\Delta} = \sqrt{\frac{\sum_i \overline{(S_i} - \hat{\overline{S}})}{8-1}} = 0.62 \text{ W/m}^2 \tag{4.4}$$

The estimated uncertainty on $\hat{\overline{S}} + m_\Delta$ is $\widehat{\sigma_\Delta}/\sqrt(8) = 0.22$ W/m^2. Note that, since m_Δ is essentially unknown, one can not draw conclusions on the absolute accuracy with which the *true* solar irradiance value $\overline{S}$ is known. However, since radiometers of different construction are present in the set of eight radiometers used, the probability of large common errors is low.

Once the mean value $\hat{\overline{S}} + m_\Delta$ is known, the measurements of the eight radiometers can all be related to a common reference, called the Space Absolute Radiometric Reference (SARR), by application of SARR multiplicative adjustment factors a_i^{SARR} on the instrument measurements $S_i(t)$ which results in SARR adjusted measurements $S_i^{SARR}(t)$

$$S_i^{SARR}(t) = a_i^{SARR} S_i(t) \tag{4.5}$$

with

$$a_i^{SARR} = \frac{\overline{S}}{\overline{S_i}} \tag{4.6}$$

The second column of table 4.2 shows the SARR coefficients obtained by [CFLR95] for the eight radiometers from equation 4.6 together with those obtained indirectly for the ACRIM I and NIMBUS 7 radiometers.

Instrument	Former SARR adjustment coefficient	Updated SARR adjustment coefficient
SOVA1-L	1.000819	1.000819
SOLCON-R	0.999823	0.999823
SOVA1-R	0.999781	0.999781
SOLCON-L	0.999228	0.999228
ERBS	1.000453	1.000453
SOVA2 a	0.999691	0.999691
SOVA2 b	0.999830	0.999830
ACRIM II	1.000375	1.000375
ACRIM I	**0.998574**	**0.999071**
NIMBUS 7 after 1990	0.995452	0.995452
NIMBUS 7 before 1989	**0.995452**	**0.995948**
level 1 DIARAD-L	–	0.999819

Table 4.2: Instrument SARR adjustment coefficients. The SARR coefficients which been updated are printed bold. Column 2 - see section 4.1.2. Column 3 - see sections 4.1.3 and 4.1.4.

4.1.3 Preliminary SARR adjustment for DIARAD/VIRGO

The SARR adjustment coefficients from [CFLR95], listed in the second column of table 4.2, were obtained at a moment when the DIARAD/VIRGO instrument was not yet active. With the currently available data, a complementary estimate of the SARR adjustment coefficient for DIARAD/VIRGO is possible.

A preliminary estimate of the SARR adjustment coefficient for DIARAD/VIRGO a_{diarad}^{SARR} is made using the overlapping measurements of the SARR referenced ACRIM II measurements $S_{\text{acrimii}}^{SARR}(t)$ and the not yet SARR referenced DIARAD/VIRGO measurements, as follows

$$a_{\text{diarad}}^{SARR} = \sum_t \frac{\overline{S_{\text{acrimii}}^{SARR}(t)}}{\overline{S_{\text{diarad}}(t)}} = 0.999819 \tag{4.7}$$

The sum in equation 4.7 is taken over all available overlapping daily mean measurements, i.e. over approximately the whole year 1996 (see figures 4.1 and 4.2). The obtained DIARAD/VIRGO SARR coefficient $a_{\mathrm{diarad}}^{SARR}$ is preliminary, since it is obtained with the supposition that ACRIM II has not aged between the time the SARR was defined (April 1993) and the time of overlapping with DIARAD (1996). In October 1998, it is planned to have an STS-95 space shuttle flight of the reference radiometer SOLCON. For this radiometer it is known that it has remained stable since the definition of the SARR. By October 1998, level 2 VIRGO data will become available. Overlapping measurements of SOLCON and VIRGO will allow a final determination of the VIRGO SARR coefficient.

Figure 4.2 shows the SARR referenced measurements of ACRIM II and DIARAD/VIRGO from 1995 to 1997. It can be seen that both datasets agree within 0.5 W/m^2. For the irradiance dip in November 1996, caused by the occurrence of a sun spot, an excellent agreement between both data sets is obtained.

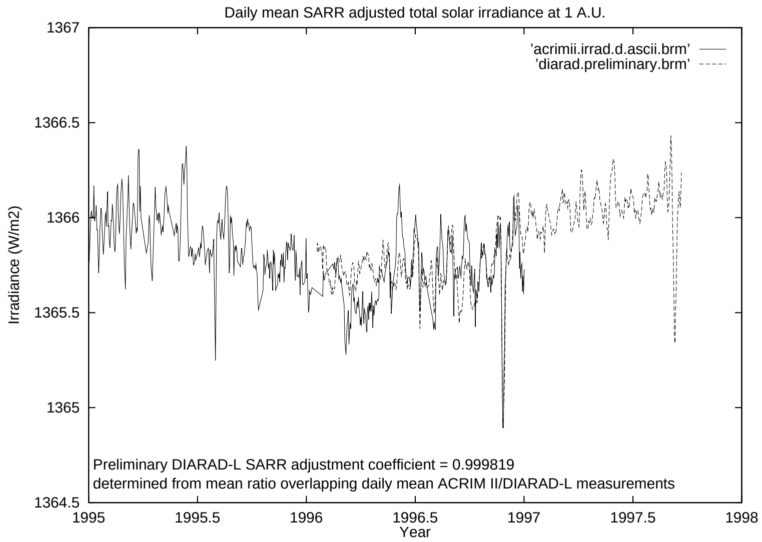

Figure 4.2: Comparison of SARR referenced ACRIM II and DIARAD/VIRGO measurements. The DIARAD/VIRGO measurements have been preliminary SARR referenced by comparison with ACRIM II measurements during 1996.

4.1.4 NIMBUS 7 instrument shift

By comparison of NIMBUS 7 and ERBE Earth Radiation Budget Satellite (ERBS) [LBC87] solar irradiance data, a shift was identified [LGWT95] of approximately 0.8 W/m^2 in the NIMBUS 7 measurements during the years 1989-1990. Since all SARR data before 1989 is SARR referenced indirectly through the NIMBUS 7 measurements, all this data might be 0.8 W/m^2 too high.

Since the identified shift occurred during a time period when only the SARR referenced NIMBUS 7 and ERBS radiometers were observing the sun, the ratios of the overlapping measurements of these two instruments are investigated in detail. Since neither NIMBUS 7 nor ERBS have aging correction, the behaviour of this ratio may be dominated by aging effects. In order to estimate the aging of ERBS, the ratios of the overlapping measurements of ERBS with the ACRIM I and ACRIM II instruments (which have aging correction) are also investigated. Figure 4.3 shows the running mean (calculated over 5 samples) of the ratios of overlapping daily mean SARR referenced measurements of ACRIM I, NIMBUS 7 and ACRIM II versus ERBS.

In this figure one can see, after an initial increase of the ratios in 1985 (which, according to the designer of the ERBS instrument [LGWT95] is due to the aging of the ERBS instrument during the first six months of its space operation) a common downward trend in the ACRIM I/ERBS and NIMBUS 7/ERBS ratios until 1990. From 1992 onwards the ratios NIMBUS 7/ERBS and ACRIM II/ERBS remain essentially constant. Apparently, the ERBS instrument seems to have become gradually more sensitive in function of time during the period 1985-1990 and seems to have become stable after 1992. Superimposed on the general trend which can be interpreted as ERBS "aging", a sudden jump of the ratio NIMBUS 7/ERBS can be seen starting approximately in 1990. This jump in ratio corresponds in time and in amplitude with the NIMBUS 7 shifts identified by [LGWT95]. Hence these shifts in the NIMBUS 7 data seem to be of permanent nature, and one should correct them.

The corrections for the NIMBUS 7 shift are chosen compatible with those suggested by [Frö97], i.e. 0.68 W/m^2 is added to the values measured before or on 1 October 1989 and 0.37 W/m^2 is added to the values measured from 2 October 1989 until 8 May 1990. Since ACRIM I was operational before 1989, and since the ACRIM I SARR coefficient was previously obtained indirectly through the NIMBUS 7 measurements, the ACRIM I SARR coefficient changes proportional to the change of the NIMBUS 7 values before 1989. One obtains for the years before 1989 (using a reference value of the solar constant of 1366.0 W/m^2 in equations 4.8 and 4.9):

$$a^{SARR}_{\text{nimbus7,new}} = a^{SARR}_{\text{nimbus7,old}} \frac{1366.68}{1366.0} = 0.995948 \tag{4.8}$$

$$a^{SARR}_{\text{acrimi,new}} = a^{SARR}_{\text{acrimi,old}} \frac{1366.68}{1366.0} = 0.999071 \tag{4.9}$$

The updated SARR adjustment coefficients are listed in the third column of table 4.2.

Figure 4.4 shows the running mean (calculated over 5 samples) of the ratios of overlapping daily mean SARR referenced measurements of ACRIM I, NIMBUS 7 and ACRIM II versus ERBS, with the use of the new SARR adjustment coefficients. While figure 4.3 was dominated by the shift in the NIMBUS 7 data, one now obtains a time series dominated by the long term ERBS trend.

4.1.5 SARR solar irradiance

With the knowledge of the updated SARR coefficients (third column of table 4.2), the measurements of section 4.1.1, can be homogenised in one single SARR referenced data series $S^{SARR}(t)$ by taking for every day the mean value of all available SARR adjusted measurements of NIMBUS 7 (with ERBS compatibility correction), ACRIM I, ACRIM II, SOVA 1, SOVA 2 and DIARAD/VIRGO.

$$S^{SARR}(t) = \frac{\sum_{i=1}^{N} a_i^{SARR} S_i(t)}{N} \tag{4.10}$$

The SARR solar irradiance time series is shown in figure 4.5.

The noise of these measurements is estimated to be around 0.01 % of the mean solar constant and the absolute value of the systematic error m_Δ is estimated to be maximally 0.1 % of the mean solar constant.

4.1.6 Spectral distribution of the solar radiation

Like the "solar constant" S_{SOL}, the spectral distribution of the solar radiation $S_{SOL,\lambda}$ can be measured most accurately from space, because one can then avoid measurement errors due to atmospheric transmission effects. This is particularly true for the UV part of the spectrum (below 400 nm), because in the UV the variability of the solar spectrum is expected to be the largest ([Lea91],[SU97]), and the UV radiation is strongly absorbed by the ozone in the atmosphere.

The solar spectrum used in this work is a combination of

- The solar spectrum $S_\lambda^{SOLSPEC}$ measured from space for the wavelength range 199 to 876 nm by the instrument SOLSPEC (described in [T+81]) during the ATLAS 1 mission (March-April 1992).
- The spectrum S_λ^{SG} of [SG74] for the wavelength range 876 to 20025 nm.

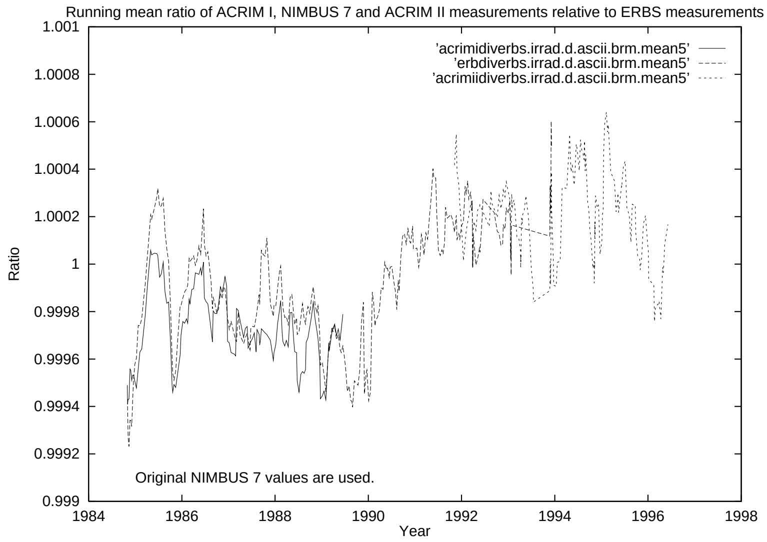

Figure 4.3: Running mean ratio of SARR referenced ACRIM I, NIMBUS 7 and ACRIM II versus ERBS measurements. No correction for a shift in NIMBUS 7 during 1989-1990 is taken into account. Means are calculated over five consecutive ratios of an overlapping daily mean ACRIM I, NIMBUS 7 or ACRIM II versus a daily mean ERBS measurement.

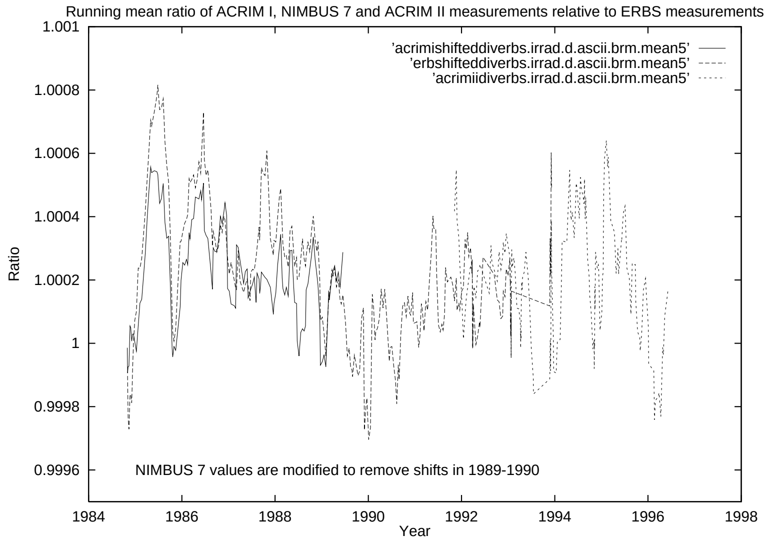

Figure 4.4: Running mean ratio of SARR referenced ACRIM I, NIMBUS 7 and ACRIM II versus ERBS measurements. Corrections for shifts in NIMBUS 7 during 1989-1990 are taken into account. Means are calculated over five consecutive ratios of an overlapping daily mean ACRIM I, NIMBUS 7 or ACRIM II versus a daily mean ERBS measurement.

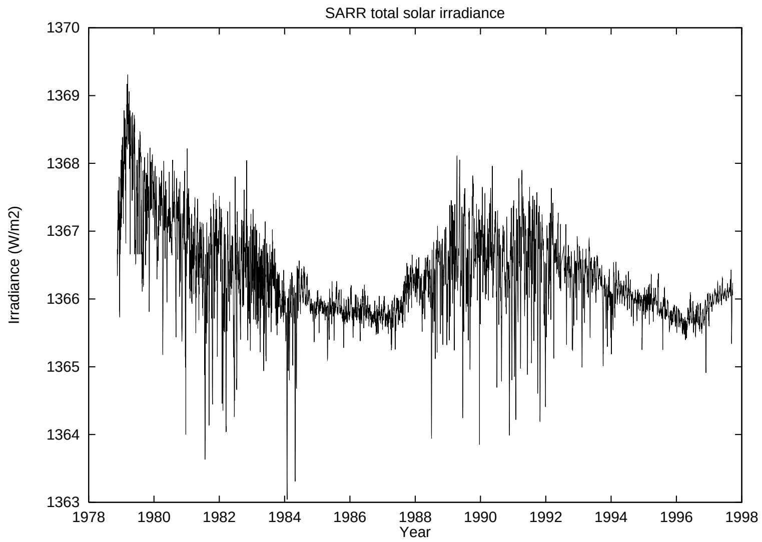

Figure 4.5: The SARR referenced solar constant as measured by the individual instruments NIMBUS 7 (with ERBS compatibility correction), ACRIM I, ACRIM II, SOVA 1, SOVA 2 and DIARAD/VIRGO.

Denote the spectrum measured by SOLSPEC as $S_\lambda^{SOLSPEC}$, denote the spectrum of [SG74] as S_λ^{SG}. A composite spectrum $S_\lambda^{composite}$ has been constructed by forcing the two spectra to coincide at their border wavelength $\lambda = 876$ nm

$$\begin{aligned} S_\lambda^{composite} &= S_\lambda^{SOLSPEC} && \text{if } \lambda \leq 876 \text{ nm} \\ &= S_\lambda^{SG} \frac{S^{SOLSPEC}_{876 \text{ nm}}}{S^{SG}_{876 \text{ nm}}} && \text{if } \lambda > 876 \text{ nm} \end{aligned} \tag{4.11}$$

The absolute value of the relative systematic error of the SOLSPEC spectrum is estimated by [CTV+96] to be maximally around 5%. A better absolute accuracy can be obtained after a scaling which makes the integrated spectral irradiance equal to the solar constant which is known quite accurately. A normalisation value of the solar constant of 1366 W/m^2 is chosen. This value lies within the range (1365.13 W/m^2 to 1366.68 W/m^2) of SARR normalised solar constant values measured by SOLCON during the ATLAS 1 mission. One obtains a normalised solar spectrum $S_{SOL,\lambda}$

$$S_{SOL,\lambda} = \frac{S_\lambda^{composite}}{\int_{199 \text{ nm}}^{20025 \text{ nm}} S_\lambda^{composite}} 1366 \text{ W/m}^2 \tag{4.12}$$

This spectrum is shown (for the range 199 to 4000 nm) in figure 4.6

4.2 Earth observation from satellites

4.2.1 Low Earth Orbit (LEO) satellites

ERBE The core of the ERBE experiment consisted of three identical scanning instruments operational on three different satellites. The first of these three instruments was operational on the satellite ERBS from November 1984 until February 1990, the second was operational on the National Oceanographic and Atmospheric Agency (NOAA) 9 satellite from January 1985 until January 1987, the third instrument was operational on the NOAA 10 satellite from October 1986 until May 1989.

The scanning instruments have three available channels:

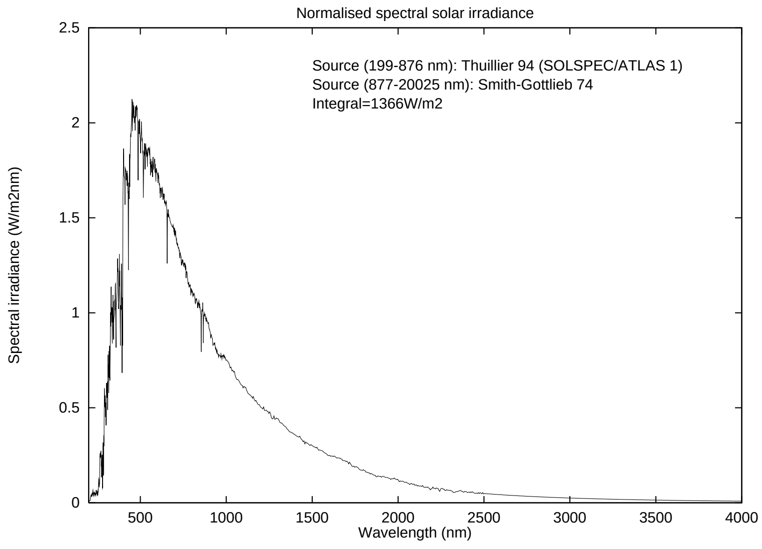

Figure 4.6: The solar spectrum normalised to an integral value of $1366W/m^2$.

- the total channel with spectral response $\Phi_{TOTAL}(\lambda)$ (spectral range $\approx$ [0.2 μm to 50 μm])
- the short wave channel with spectral response $\Phi_{SW}(\lambda)$ (spectral range $\approx$ [0.2 μm to 5 μm])
- the long wave channel with spectral response $\Phi_{LW}(\lambda)$ (spectral range $\approx$ [5 μm to 50 μm]).

From the filtered radiances measured by these channels, the ERBE secondary processing derives $F_{LW,ERBE}$ as estimate of F_{LW} and $F_{SW,ERBE}$ as estimate of F_{SW}.

The ERBE secondary processing is discussed in more detail in section 6.1.1.

Point spread function In this paragraph the total PSF ("total" means static PSF plus dynamic effects) of the scanning ERBE instrument channels is calculated using equation 3.6. For this calculation the (optical) angular sensitivity and the global impulse response ("global" means detector plus electronics) have to be known.

The angular sensitivity $OF(\delta_a, \delta_c)$ of the ERBE instrument channels has an asymmetric hexagonal shape, with the longest axis of the hexagon in the cross scan direction (see figure 4.7) with analytical expression

$$OF(\delta_a, \delta_c) = \begin{array}{ll} 1.0 & \text{if } |\delta_c| < 2.25^\circ \text{ and } |\delta_a| < \delta_r(|\delta_c|) \\ 0.0 & \text{else} \end{array} \tag{4.13}$$

The expression for the right border $\delta_r(|\delta_c|)$ is

$$\delta_r(|\delta_c|) = \begin{array}{ll} 1.5^\circ & \text{if } 0 \leq |\delta_c| < 0.75^\circ \\ 2.25^\circ - |\delta_c| & \text{if } 0.75^\circ \leq |\delta_c| < 2.25^\circ \end{array} \tag{4.14}$$

Since this angular sensitivity has values of either one or zero, the convolution with the global impulse response $h(t)$ of the detector, expressed by equation 3.6, can be rewritten in terms of the global step response $s(t)$ of the detector ("global" stands for detector plus electronics).

In analogy to the definition of the angular impulse response in equation 3.5, the angular step response $s_{ang}(\delta_a)$ can be defined as

$$s_{ang}(\delta_a) = s(\delta_a / v_{scan}) \tag{4.15}$$

For the ERBE scanners, one has a scan speed $v_{scan} = 68$ degrees/s.

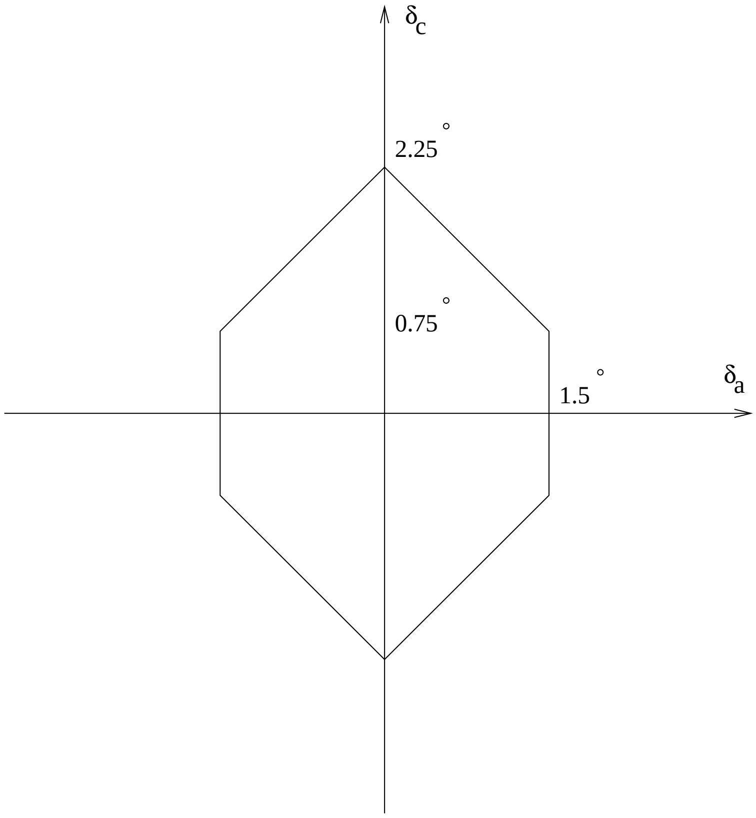

Figure 4.7: Optical field of view of ERBE scanning instruments. δ_a = along scan angle, δ_c = cross scan angle. Since the ERBE instruments are cross track scanning, the cross scan direction corresponds to the flight direction.

With the use of this scan speed, equation 3.6 can be worked out for the specific case of the scanning ERBE instruments as[2]

$$PSF_{channel}(\delta_a,\delta_c) = OF_{channel}(\delta_a,\delta_c) \circledast h_{ang}(-\delta_a) =$$

$$\begin{array}{cc} 0 & \text{if } \delta_a > \delta_r(|\delta_c|) \\ s_{ang}(-\delta_a + \delta_r(|\delta_c|) & \text{if } -\delta_r(|\delta_c|) < \delta_a \leq \delta_r(|\delta_c|) \\ s_{ang}(-\delta_a + \delta_r(|\delta_c|) - s_{ang}(-\delta_a - \delta_r(|\delta_c|) & \text{if } \delta_a \leq -\delta_r(|\delta_c|) \end{array} \tag{4.16}$$

The global transfer function $H(s) = \mathcal{L}(h(t))$ (where $\mathcal{L}$ stands for the Laplace transform) of the detector is given by equation 4.17.

$$H(s) = \frac{1}{1+s\tau_D}\frac{1}{1+s\tau_1}\frac{1+s\tau_3}{1+s\tau_2}\frac{\omega_{n1}^2}{(s+\omega_{n1})^2}\frac{\omega_{n2}^2}{(s+\zeta\omega_{n2})^2+(1-\zeta^2)\omega_{n2}^2} \tag{4.17}$$

The parameter values that occur in equation 4.17 are given by

$$\begin{array}{c} \tau_D = 1.20\text{e-}2 \text{ s} \\ \tau_1 = \left\{ \begin{array}{ll} 1.44\text{e-}5 \text{ s} & \text{for the SW channel} \\ 1.53\text{e-}5 \text{ s} & \text{for the LW channel} \\ 1.36\text{e-}5 \text{ s} & \text{for the TOTAL channel} \end{array} \right. \\ \tau_2 = 1.76\text{e-}3 \text{ s} \\ \tau_3 = \left\{ \begin{array}{ll} 1.54\text{e-}5 \text{ s} & \text{for the SW channel} \\ 1.63\text{e-}5 \text{ s} & \text{for the LW channel} \\ 1.46\text{e-}5 \text{ s} & \text{for the TOTAL channel} \end{array} \right. \\ \omega_{n1} = \frac{1}{9.56\text{e-}3 \text{ s}} \\ \omega_{n2} = \frac{1}{8.60\text{e-}3 \text{ s}} \\ \zeta = 0.628 \end{array} \tag{4.18}$$

The global step response $s(t)$ can be calculated as

$$s(t) = \mathcal{L}^{-1}(\tfrac{1}{s}H(s))$$

$$\begin{array}{l} = \mathcal{L}^{-1}(\frac{1}{s}\frac{1}{1+s\tau_D}\frac{1}{1+s\tau_1}\frac{1+s\tau_3}{1+s\tau_2}\frac{\omega_{n1}^2}{(s+\omega_{n1})^2}\frac{\omega_{n2}^2}{(s+\zeta\omega_{n2})^2+(1-\zeta^2)\omega_{n2}^2}) \\ \approx \mathcal{L}^{-1}(\frac{1}{s}\frac{1}{1+s\tau_D}\frac{\omega_{n1}^2}{(s+\omega_{n1})^2}\frac{\omega_{n2}^2}{(s+\zeta\omega_{n2})^2+(1-\zeta^2)\omega_{n2}^2}) \\ = \mathcal{L}^{-1}\left(\left(\frac{1}{s}+\frac{c}{s+a}+\frac{d}{s+b}+\frac{e}{(s+b)^2}\right)\frac{f^2+g^2}{(s+f)^2+g^2}\right) \\ = \mathcal{L}^{-1}\left(\frac{1}{s}+\frac{m}{s+a}+\frac{i}{s+b}+\frac{jb}{(s+b)^2}+\frac{k(s+f)+lg}{(s+f)^2+g^2}\right) \end{array} \tag{4.19}$$

$$\begin{array}{c} = u(t)\,(1+m\exp(-at)+i\exp(-bt)+j(bt)\exp(-bt) \\ +k\exp(-ft)\cos(gt)+l\exp(-ft)\sin(gt)) \end{array}$$

The approximate equality in the third line of equation 4.19 is obtained after neglecting the smallest time constants. The parameter values that occur in equation 4.19 are given by

[2]For a fixed δ_c, $OF(\delta_a,\delta_c)$ is a blockfunction of δ_a (see equation 4.13 and figure 4.7). This block function can be written as a difference of two step functions. Hence the convolution 3.6 of $OF(\delta_a,\delta_c)$ with the mirrored angular impulse response function $h_{ang}(-\delta_a)$, can be written as the difference of two mirrored step response response functions.

$$
\begin{aligned}
a &= \frac{1}{\tau_D} = 83.33 \text{ s}^{-1} \\
b &= \omega_{n1} = 104.6 \text{ s}^{-1} \\
\\
c &= \frac{-b^2}{(a-b)^2} = -24.18 \\
d &= \frac{-a(a-2b)}{(a-b)^2} = 23.18 \\
e &= \frac{-ab}{a-b} = 409.8 \\
\\
f &= \zeta\omega_{n2} = 73.03 \text{ s}^{-1} \\
g &= \sqrt{1-\zeta^2}\omega_{n2} = 90.49 \text{ s}^{-1} \\
\\
N_0 &= f^2 + g^2 = 1.352\text{e}4 \text{ s}^{-2} \\
N_a &= (f-a)^2 + g^2 = 8295 \text{ s}^{-2} \\
N_b &= (f-b)^2 + g^2 = 9186 \text{ s}^{-2} \\
\\
m &= c\frac{N_0}{N_a} = -39.43 \\
i &= d\frac{N_0}{N_b} + e\frac{2(b-f)N_0}{N_c^2} = 38.28 \\
j &= \left(e\frac{N_0}{N_c}\right)/b = 5.767 \\
k &= -1 - c\frac{N_0}{N_a} - d\frac{N_0}{N_b} - e\frac{2(b-f)N_0}{N_b^2} = 0.1482 \\
l &= (-2f + c\frac{(a-2f)N_0}{N_a} + d\frac{(b-2f)N_0}{N_b} + e\frac{((b-2f)N_b - 2(b-f)(f^2+g^2))N_0}{bN_b^2} \\
&\quad -kf)/g = 1.393
\end{aligned}
\tag{4.20}
$$

The global step response $s(t)$ of the ERBE detector is shown in figure 4.8.

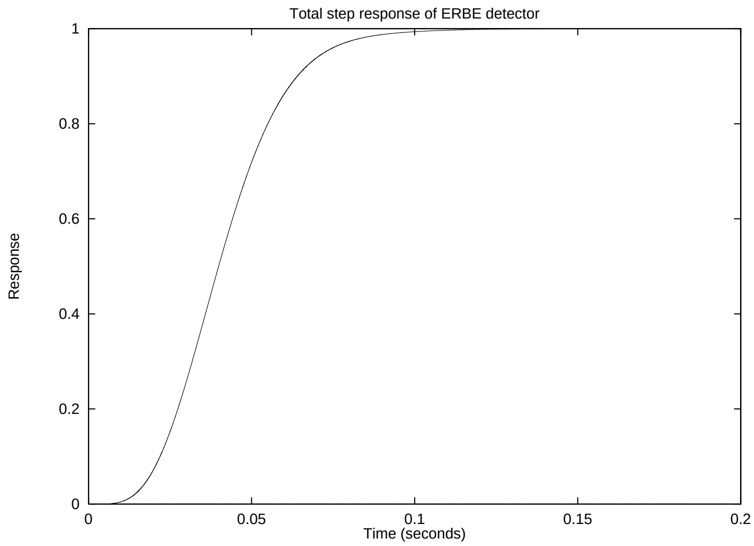

Figure 4.8: Global step response of ERBE detector.

By substitution of the expression 4.19 for the step response $s(t)$, the angular step response $s_{ang}(\delta_a)$ can be calculated from equation 4.15. By substitution of the expression of the angular step response in equation 4.16, the ERBE point spread function can be calculated. The result is shown in figure 4.9.

ScaRaB The ScaRaB instrument is designed as a follow-up of the ERBE instruments. Until now one ScaRaB instrument, ScaRaB FM (Flight Model) 1, has been operational on the satellite

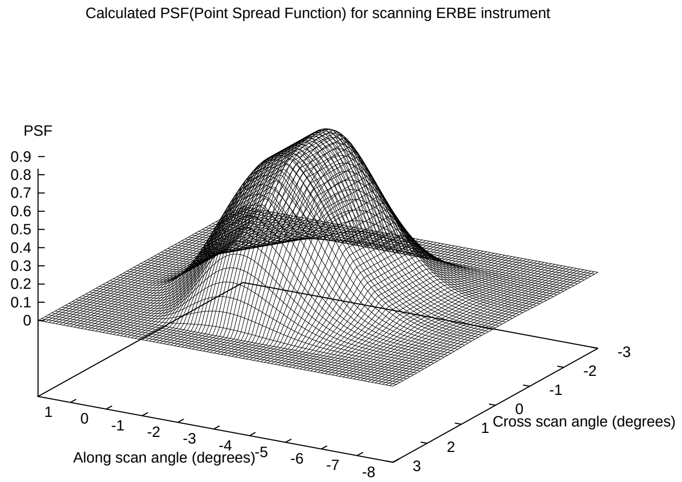

Figure 4.9: Point spread function of ERBE scanning instrument channels.

Meteor 3/7 from March 1994 until February 1995 [KVP+97]. It is planned to launch a second ScaRaB flight model, ScaRaB FM 2, on the Russian satellite RESURS in March 1998.

The scanning instrument has four available channels:

- the total channel with spectral response $\Phi_{TOTAL}(\lambda)$ (spectral range $\approx$ [0.2 μm to 50 μm])
- the short wave channel with spectral response $\Phi_{SW}(\lambda)$ (spectral range $\approx$ [0.2 μm to 4 μm])
- the infrared window channel with spectral response $\Phi_{IRW}(\lambda)$ (spectral range $\approx$ [10.5 μm to 12.5 μm])
- the visible channel with spectral response $\Phi_{VIS}(\lambda)$ (spectral range $\approx$ [0.55 μm to 0.65 μm])

From the filtered radiances measured by these channels the ScaRaB secondary processing derives $F_{LW,ScaRaB}$ as estimate of F_{LW} and $F_{SW,ScaRaB}$ as estimate of F_{SW}.

PSF of the broad band channels The angular sensitivity of the ScaRaB broad band channels (the TOTAL and the SW channel) has a square form, with the square edges tilted 45 degrees relative to the scan direction (see figure 4.10).

The detector angles α, β are defined in the edge directions. Their relation with the along track angle δ_a and the cross track angle δ_c is given by

$$\begin{bmatrix} \delta_a \\ \delta_c \end{bmatrix} = \frac{1}{\sqrt{2}} \begin{bmatrix} 1 & -1 \\ 1 & 1 \end{bmatrix} \begin{bmatrix} \alpha \\ \beta \end{bmatrix} \tag{4.21}$$

The angular sensitivity $OF_{channel}(\delta_a, \delta_c)$ can therefore be expressed in function of the angles α and β as $OF'_{channel}(\alpha, \beta)$

$$OF_{channel}(\delta_a, \delta_c) = OF'_{channel}(\alpha, \beta) \tag{4.22}$$

The angular sensitivity is a symmetrical function of α and β (see figure 4.10), so:

$$OF'_{channel}(\alpha, \beta) = f(|\alpha|)f(|\beta|) \tag{4.23}$$

Fig.4.11 shows a cross-section (for $\alpha = 0$) of the slightly idealised measured response of the TOTAL channel of the ScaRaB radiometer [SK96].

From figure 4.11, one can derive

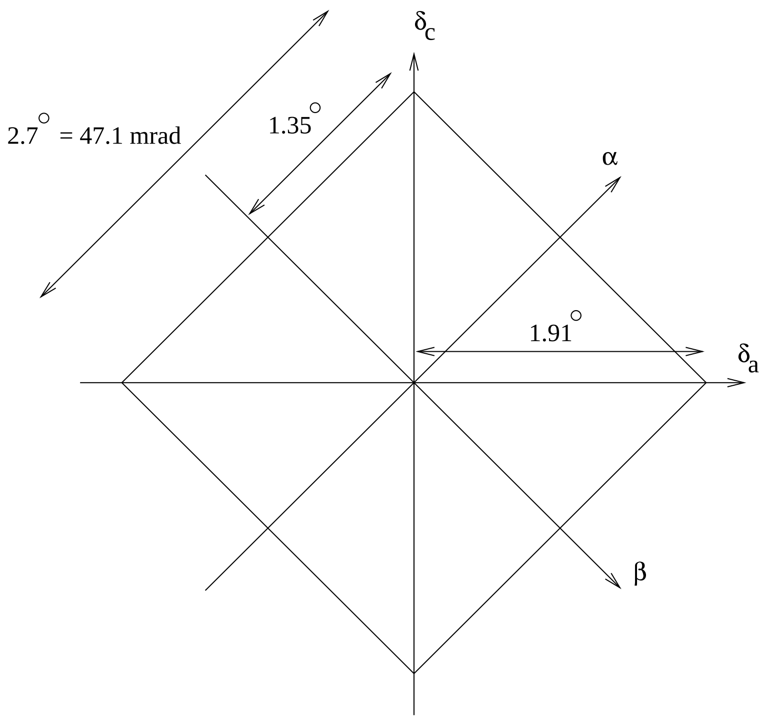

Figure 4.10: Definition of the detector angles α,β relative to the scan angles δ_a,δ_c and square form of the angular sensitivity of the ScaRaB scanning instrument broad band channels.

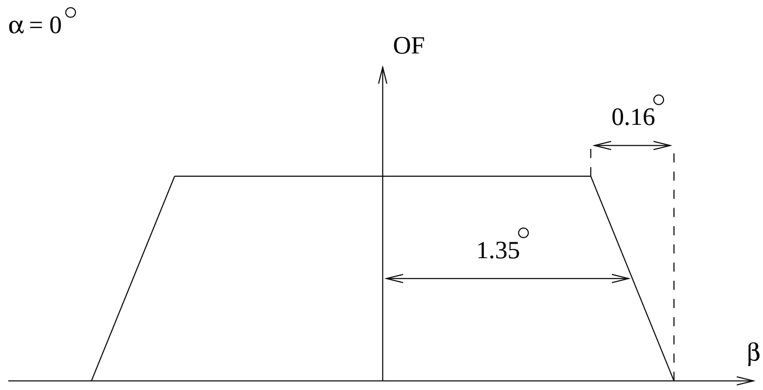

Figure 4.11: Cross section for $\alpha = 0°$ of angular sensitivity of ScaRaB scanning instrument broad band channels.

$$f(|x|) \quad \begin{array}{ll} = 1 & \text{if } |x| < 1.35° - 0.08° \\ = 0.5 * (1 - \frac{x - 1.35°}{0.08°}) & \text{if } 1.35° - 0.08° \leq |x| \leq 1.35° + 0.08° \\ = 0 & \text{if } |x| > 1.35° + 0.08° \end{array} \tag{4.24}$$

The angular sensitivity $OF'_{channel}(\alpha, \beta)$ of the ScaRaB detectors can be further simplified by approximating the trapezium-like response of Fig.4.11 as a rectangular function with half width 1.35°.

$$OF'_{ideal}(\alpha, \beta) = f_{ideal}(|\alpha|) f_{ideal}(|\beta|) \tag{4.25}$$

with

$$f_{ideal}(|x|) \quad \begin{array}{ll} = 1 & \text{if } |x| < 1.35° \\ = 0 & \text{elsewhere} \end{array} \tag{4.26}$$

The global time impulse response $h(t)$ of the ScaRaB detector can be calculated from the detector description given in [Rai96]. The pyro-electric detector behaves as a first order high pass system with a time constant of 3 s. A chopping mirror mechanism lets the input of the detector alternate between the radiance from the earth scene (sensed during 31.25 ms) and the radiance of an internal short time reference black body simulator (also sensed during 31.25 ms). The output of the pyro-eletric detector is flattened by the pre-sampling electronics, so that an ideal block function is closely approximated before sampling. See figure 4.12 for an overview of the ScaRaB detector and pre sampling electronics.

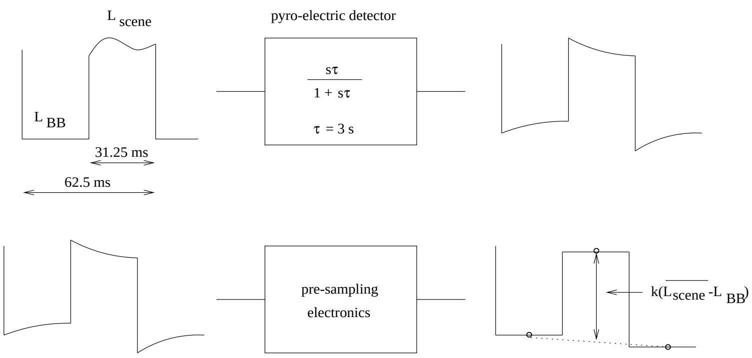

Figure 4.12: Schematic description of the ScaRaB detector plus pre-sampling electronics. At the input of the detector the radiance alternates between a short term blackbody reference radiance L_{BB} and the earth scene radiance L_{scene}. The output of the pyro-electric detector is flattened by the pre sampling electronics before sampling. The sampled points are indicated as thick black points in the output of the pre-sampling electronics.

The value which is read out, is $k(\overline{L_{\mathrm{scene}}} - L_{\mathrm{BB}})$ where $\overline{L_{\mathrm{scene}}}$ is the mean of the earth scene radiance during 31.25 ms (see figure 4.12). Therefore the global impulse response $h(t)$ of the ScaRaB detector can be approximated by a block function with width 31.25 ms.

Since the angular scan speed of the ScaRaB instrument is $v_{scan} = 40.3°/\mathrm{s}$, the global angular impulse response $h_{ang}(\delta_a) = h(\delta_a / v_{scan})$ (see equation 3.5) is approximated by a block function with width (31.25 ms)*(40.3°/s)=1.26°

$$h_{ang,ideal}(\delta_a) \quad \begin{array}{ll} = \frac{1}{1.26°} & \text{if } -0.63° < \delta_a < 0.63° \\ = 0 & \text{elsewhere} \end{array} \tag{4.27}$$

For the total (total means static PSF plus dynamic effects) broad band PSF (valid for both the TOTAL and the SW channel), one obtains

$$\begin{array}{c} PSF_{TOTAL}(\delta_a, \delta_c) = PSF_{SW}(\delta_a, \delta_c) = (f(|\alpha|) f(|\beta|)) \circledast h_{ang}(-\delta_a) \\ \approx \\ PSF_{ideal}(\delta_a, \delta_c) = OF_{ideal}(\delta_a, \delta_c) \circledast h_{ang,ideal}(-\delta_a) \end{array} \tag{4.28}$$

For a fixed δ_c, $OF_{ideal}(\delta_a, \delta_c)$ is a blockfunction of δ_a with a certain width w and $PSF_{ideal}(\delta_a, \delta_c)$ is equal to the convolution of two block functions $h_{ang,ideal}(-\delta_a)$ and $OF_{ideal}(\delta_a, \delta_c = \text{constant})$ (see figure 4.13). Depending on the value of δ_c, the width w is smaller or greater than 1.26°, and one has the top or bottom case of figure 4.13.

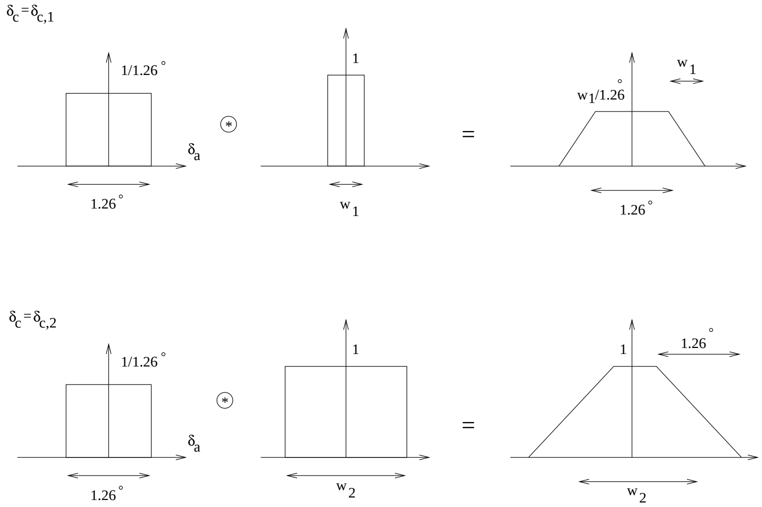

Figure 4.13: Two cases which exist in the calculation of $PSF_{ideal}(\delta_a, \delta_c)$, depending on the width w of $OF_{ideal}(\delta_a, \delta_c)$ for fixed δ_c. Top: width $w_1 < 1.26°$ for $\delta_c = \delta_{c,1}$. Bottom: width $w_2 > 1.26°$ for $\delta_c = \delta_{c,2}$.

The overall PSF can therefore be written as the product of a shape function $g_1(|\delta_a|, |\delta_c|)$ and an amplitude function $g_2(|\delta_c|)$ (see figure 4.14)

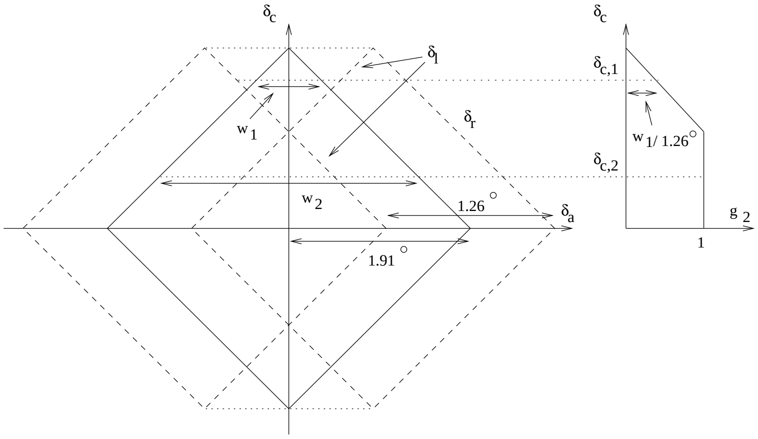

Figure 4.14: Decomposition of the idealised ScaRaB PSF $PSF_{ideal}(\delta_a, \delta_c)$ in a shape function $g_1(|\delta_a|, |\delta_c|)$ and an amplitude function $g_2(|\delta_c|)$. Left: Ground projection of the shape function $g_1(|\delta_a|, |\delta_c|)$ with indication of the left border δ_l and the right border δ_r. Right: Amplitude function $g_2(|\delta_c|)$.

$$PSF_{ideal}(|\delta_a|, |\delta_c|) = g_1(|\delta_a|, |\delta_c|)g_2(|\delta_c|) \tag{4.29}$$

The trapezoidal shape function g_1 is given by (see left part of figure 4.14)

$$g_1(|\delta_a|, |\delta_c|) \quad \begin{array}{ll} = 1 & \text{if } |\delta_a| < \delta_l \\ = \frac{\delta_r - |\delta_a|}{\delta_r - \delta_l} & \text{if } \delta_l < |\delta_a| < \delta_r \\ = 0 & \text{if } |\delta_a| > \delta_r \end{array} \tag{4.30}$$

The left border of the trapezoidal side δ_l is given by (see figure 4.14)

$$\delta_l = |1.91° - 0.63° - |\delta_c|| \tag{4.31}$$

The right border of the trapezoidal side δ_r is given by (see figure 4.14)

$$\delta_r = 1.91° + 0.63° - |\delta_c| \tag{4.32}$$

The amplitude function g_2 is given by (see right part of figure 4.14)

$$g_2(|\delta_c|) \begin{array}{ll} = 1 & \text{if } |\delta_c| < 1.91° - 0.63° \\ = \frac{1.91° - |\delta_c|}{0.63°} & \text{if } \delta_l < |\delta_c| < \delta_r \\ = 0 & \text{if } |\delta_c| > 1.91° \end{array} \tag{4.33}$$

The dynamic PSF of the ScaRaB broad band channels is shown in figure 4.15.

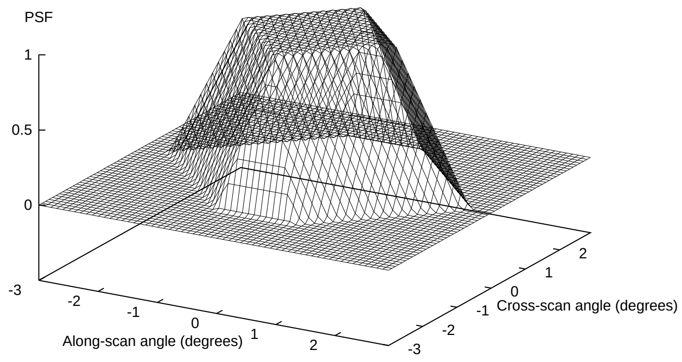

Figure 4.15: PSF of the ScaRaB scanning instrument broad band channels.

4.2.2 Geostationary satellites

The METEOSAT radiometer. METEOSAT is a series of geostationary satellites with a visible and infrared imager instrument aboard. METEOSAT 1 was operational from February 1978 until November 1979. METEOSAT 2 was operational from August 1981 until August 1988. METEOSAT 3 was operational from August 1988 until August 1991. METEOSAT 4 was operational from May 1989 until July 1991. METEOSAT 5 was operational from August 1991 until July 1997. METEOSAT 6 is operational since August 1997.

Each METEOSAT satellite is equipped with a radiometer with three channels:

- the VISible (VIS) channel with spectral response $\Phi_{VIS}(\lambda)$ (spectral range $\approx$ [0.4 μm to 1.1 μm]) and digital count (grey value)[3] C_{VIS}
- the Water Vapour (WV) channel with spectral response $\Phi_{WV}(\lambda)$ (spectral range $\approx$ [5.7 μm to 7.1 μm]) and digital count (grey value) C_{WV}
- the InfraRed (IR) window channel with spectral response $\Phi_{IR}(\lambda)$ (spectral range $\approx$[10.5 μm to 12.5 μm]) and digital count (grey value) C_{IR}

[3] The terms "count" and "grey value" are strictly equivalent in this work. The term "count" is often used when one speaks about satellite data, the term "grey value" is often used when one speaks about images.

Spectral characteristics The radiance measured by the VIS channel on METEOSAT 2 and 5 is given by

$$L_{METx,VIS} = \int_0^\infty d\lambda \Phi_{METx,VIS}(\lambda)(L_\lambda^{solar} + L_\lambda^{earth})(\theta_{MET}, \phi_{MET}) \tag{4.34}$$

The considered METEOSAT number x is 2 or 5. θ_{MET}, ϕ_{MET} are the viewing angles θ, ϕ under which the METEOSAT instrument views a given scene on earth. $\Phi_{METx,VIS}(\lambda)$ is the METEOSAT x VIS channel spectral response. The spectral responses for the METEOSAT 2 VIS channel $\Phi_{MET2,VIS}(\lambda)$ and for the METEOSAT 5 VIS channel $\Phi_{MET5,VIS}(\lambda)$, which were obtained from [RDBW92], are shown in figure 4.16.

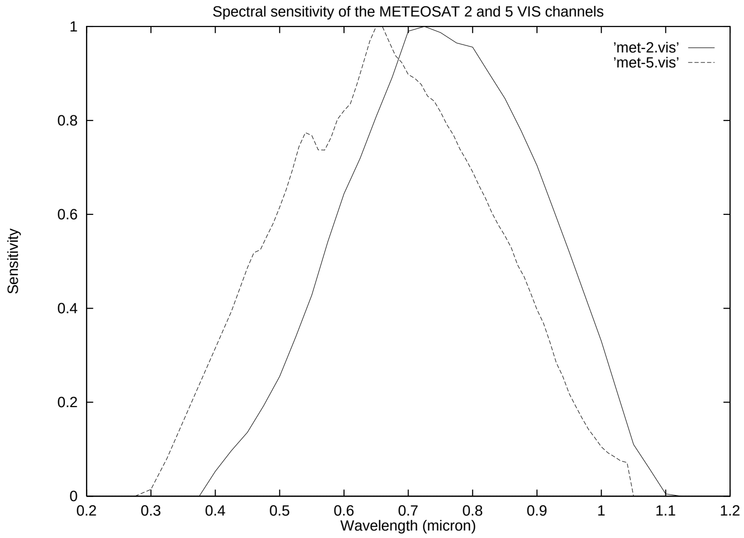

Figure 4.16: Spectral response of the VISible (VIS) channels on METEOSAT 2 and 5.

Spatial resolution The sampling distance at nadir of the IR and WV channels is 5 km in both directions (north south and east west direction). The sampling distance at nadir of the VIS channel is 2.5 km in both directions.

Time of acquisition The METEOSAT radiometer is a spinning radiometer, which scans the earth from south to north and from east to west by two different mechanisms (see figure 4.17).

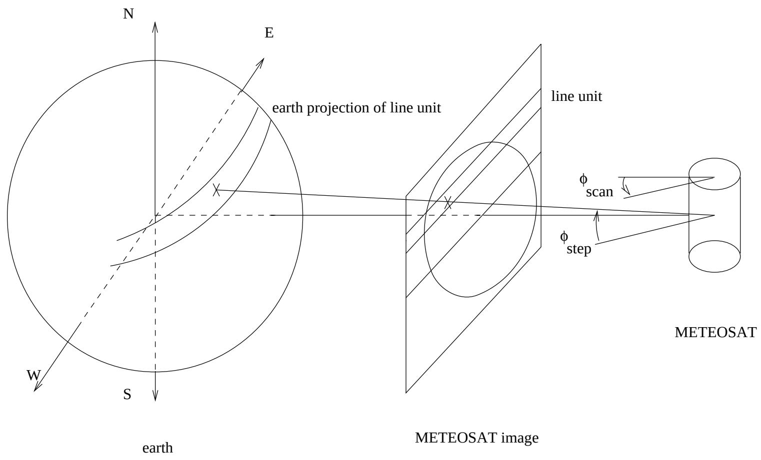

Figure 4.17: Geometry and timing of METEOSAT image acquisition.

The scanning from east to west is done automatically by the spinning of the radiometer. The rotation speed of the radiometer is 100 rotations per minute, hence the rotation period is 600 milliseconds. During those 600 milliseconds 360 degrees are scanned. Of those 360 degrees, 18 degrees are used to build up one line unit of the METEOSAT image. Hence the acquisition time duration of one line unit is (18/360)*600=30 milliseconds.

The scanning from south to north is obtained by a stepping mechanism within the METEOSAT instrument, which controls the angle ϕ_{step}. After the acquisition of each line unit, ϕ_{step} is changed by a fixed angle. The scanning starts with $\phi_{\text{step}} = -9$ degrees (bottom of the METEOSAT image) at the time of start of acquisition of a given slot $t_{\text{start}}(\text{slot})$. The total METEOSAT image slot consists of 2500 line units, scanned in 2500*600 milliseconds = 25 minutes. Hence the acquisition ends at the time of the end of the acquisition of the given slot $t_{\text{end}}(\text{slot}) = t_{\text{start}}(\text{slot}) + 25$ minutes .

In this work, the scan time of all pixels of line unit l ($0 =$ top line, $2499 =$ bottom line) of slot $slot$ is taken equal to the scan time of the middle of the line $t(l, slot)$ with a neglectable time error of maximally half the acquisition time duration of one line unit (15 milliseconds) under nominal conditions.

$$t(l, slot) = t_{\text{start}}(slot) + 300 milliseconds + (2499 - l)(600 milliseconds) \tag{4.35}$$

After the scanning from south to north in 25 minutes, 5 minutes of non imaging time are used to bring the stepping mechanism back to its south most position. 30 minutes after the start of acquisition of the previous slot, the acquisition of a new slot begins.

The start and end times of the acquisition of the 48 slots within one day are given in table 4.3. The times are given in the UTC (Coordinated Universal Time) time reference frame.

Slot	Start-end	Slot	Start-end
1	00 : 00 – 00 : 25 UTC	25	12 : 00 – 12 : 25 UTC
2	00 : 30 – 00 : 55 UTC	26	12 : 30 – 12 : 55 UTC
3	01 : 00 – 01 : 25 UTC	27	13 : 00 – 13 : 25 UTC
4	01 : 30 – 01 : 55 UTC	28	13 : 30 – 13 : 55 UTC
5	02 : 00 – 02 : 25 UTC	29	14 : 00 – 14 : 25 UTC
6	02 : 30 – 02 : 55 UTC	30	14 : 30 – 14 : 55 UTC
7	03 : 00 – 03 : 25 UTC	31	15 : 00 – 15 : 25 UTC
8	03 : 30 – 03 : 55 UTC	32	15 : 30 – 15 : 55 UTC
9	04 : 00 – 04 : 25 UTC	33	16 : 00 – 16 : 25 UTC
10	04 : 30 – 04 : 55 UTC	34	16 : 30 – 16 : 55 UTC
11	05 : 00 – 05 : 25 UTC	35	17 : 00 – 17 : 25 UTC
12	05 : 30 – 05 : 55 UTC	36	17 : 30 – 17 : 55 UTC
13	06 : 00 – 06 : 25 UTC	37	18 : 00 – 18 : 25 UTC
14	06 : 30 – 06 : 55 UTC	38	18 : 30 – 18 : 55 UTC
15	07 : 00 – 07 : 25 UTC	39	19 : 00 – 19 : 25 UTC
16	07 : 30 – 07 : 55 UTC	40	19 : 30 – 19 : 55 UTC
17	08 : 00 – 08 : 25 UTC	41	20 : 00 – 20 : 25 UTC
18	08 : 30 – 08 : 55 UTC	42	20 : 30 – 20 : 55 UTC
19	09 : 00 – 09 : 25 UTC	43	21 : 00 – 21 : 25 UTC
20	09 : 30 – 09 : 55 UTC	44	21 : 30 – 21 : 55 UTC
21	10 : 00 – 10 : 25 UTC	45	22 : 00 – 22 : 25 UTC
22	10 : 30 – 10 : 55 UTC	46	22 : 30 – 22 : 55 UTC
23	11 : 00 – 11 : 25 UTC	47	23 : 00 – 23 : 25 UTC
24	11 : 30 – 11 : 55 UTC	48	23 : 30 – 23 : 55 UTC

Table 4.3: Table of correspondence between METEOSAT slots and METEOSAT image acquisition start and end times. Acquisition starts in the south and ends in the north.

Information content The number of bits per pixel for the IR channel is 8 bits for all METEOSAT instruments. The number of bits per pixel for the VIS and WV channel is 6 bits for

METEOSAT 1,2,3 and 8 bits for METEOSAT 4,5,6.

Data availability METEOSAT data is available in full resolution and in ISCCP B2 [Pro92] format . METEOSAT images in ISCCP B2 format form a time series (4 months of consecutive images are available for this study) of METEOSAT images, subsampled in space (to a resolution of 30 km x 30 km at nadir) and in time (to a resolution of 3 hours, which means 8 images/day for the IR and WV channel, 5 images/day for the VIS channel).

4.3 Auxiliary data : surface property maps

From the CERES project, the surface properties database was obtained. This database describes with a resolution of 10 arcminutes the properties of the earth's surface. Figure 4.18 shows the map of the water fraction (fraction of a pixel covered by water, ranging between zero and hundred percent) of the earth's pixels.

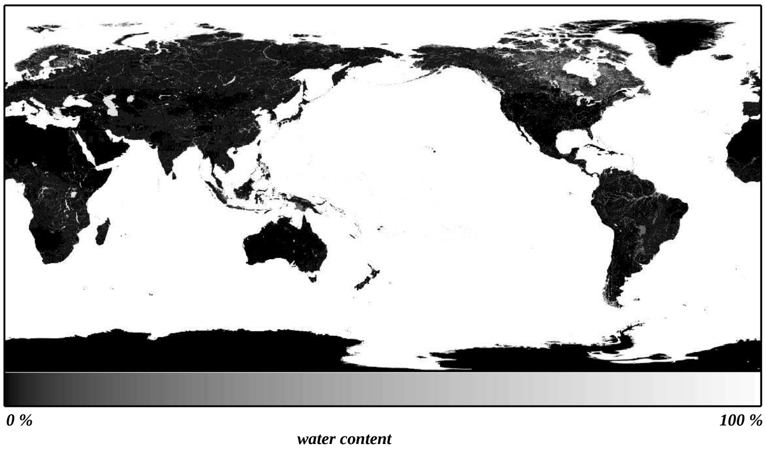

Figure 4.18: The water fraction, i.e. the fraction of a pixel covered by water, of the earth's pixels as described by the CERES surface map at 10 arcminutes resolution.

Figure 4.19 shows the map of the earth (classified in the six surface types ocean, land, mountains, snow/ice, desert and coast) of the earth's pixels.

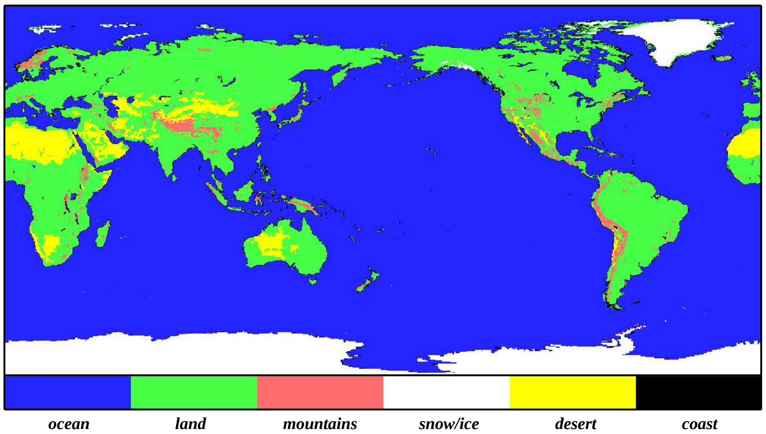

Figure 4.19: Classification of the earth in six surface types: ocean, land, mountains, snow/ice, desert and coast, at a resolution of 10 arcminutes.

Chapter 5

Models

As explained in section 3.2.2, to convert the quantities measured by earth observing satellites, namely filtered radiances, into radiation budget term estimates, namely unfiltered flux surface densities, an angular and a spectral conversion are necessary.

For these angular and spectral conversions, models are needed for the angular and spectral dependency of the reflected solar radiation. These models depend on the nature of the viewed scenes.

In this chapter the models used for the angular and for the spectral dependency of the reflected solar radiation, are presented.

5.1 Angular dependency models

The different ADM (Angular Dependency Model) sets used for the reflected solar radiation, are described.

It is generally accepted in state of the art radiation budget studies [WBH+96], that the angular dependency of the solar radiation reflected by cloudy scenes, depends on a multitude of physical parameters of the scene, among which the 3D structure of the cloud plays an important role.

Since conventional, plane-parallel, radiative transfer calculation schemes (e.g. the schemes compared in [EF91]), do not take into account the 3D structure of clouds, *calculated* estimates of ADM's of the reflected solar radiation by cloudy scenes are subject to errors. Therefore ADM's should not be calculated, but should rather be *measured*.

Different measurement based models have been developed, which give the scene dependent angular distribution of the reflected solar radiance $L_{SW}^{scene}(\theta, \phi, \theta_{sun})$ for the 12 ERBE scene types:

- clear sky ocean
- clear sky land
- clear sky snow
- clear sky desert
- clear sky land-ocean mix
- partly cloudy over ocean
- partly cloudy over land (or over desert)
- mostly cloudy over ocean
- mostly cloudy over land (or over desert)
- mostly cloudy over land-ocean mix
- overcast cloudy

Denote the angular spherical coordinates of the sun and of the satellite as $(\theta_{sun}, \phi_{sun})$ and $(\theta_{sat}, \phi_{sat})$ respectively (see figure 8.11).

θ_{sat} is the viewing zenith angle, defined as the angle between the local vertical and the local viewing direction. $\phi_{rel} = |\phi_{sat} - \phi_{sun}|$ is the relative azimuth angle, defined as the angle between the plane formed by the local vertical and the local viewing direction and the plane formed by the local vertical and the local solar direction.

For a given solar direction $(\theta_{sun}, \phi_{sun})$, there exists a one to one relationship between the couple of the viewing zenith angle θ_{sat} and the relative azimuth angle ϕ_{rel} and the couple $(\theta_{sat}, \phi_{sat})$.

The angular dependency of the radiance for every scene is characterised by an angular reflection function $r^{scene}(\theta_{sat}, \phi_{rel}, \theta_{sun})$ which gives the ratio of the reflected radiance $L_{SW}^{scene}(\theta_{sat}, \phi_{sat}, \theta_{sun})$ to the incoming solar flux surface density F_{SOL} (given by equation 2.17).

$$r^{scene}(\theta_{sat}, \phi_{rel}, \theta_{sun}) = \frac{L_{SW}^{scene}(\theta_{sat}, \phi_{sat}, \theta_{sun})}{F_{SOL}(\theta_{sun})} \tag{5.1}$$

The reflected short wave flux surface density F_{SW}^{scene} can be calculated using equation 2.21 as

$$\begin{aligned} F_{SW}^{scene}(\theta_{sun}) &= \int_0^{2\pi} d\phi \int_0^{\pi/2} sin(\theta) d\theta L_{SW}^{scene}(\theta, \phi, \theta_{sun}) cos(\theta) \\ &= 2F_{SOL}(\theta_{sun}) \int_0^{\pi} d\phi_{rel} \int_0^{\pi/2} sin(\theta) d\theta r^{scene}(\theta, \phi_{rel}, \theta_{sun}) cos(\theta) \end{aligned} \tag{5.2}$$

The albedo $a^{scene}(\theta_{sun})$ is defined as the fraction of incoming short wave radiation that is reflected by the scene

$$\begin{aligned} a^{scene}(\theta_{sun}) &= F_{SW}^{scene}(\theta_{sun}) / F_{SOL}(\theta_{sun}) \\ &= 2 \int_0^{\pi} d\phi_{rel} \int_0^{\pi/2} sin(\theta) d\theta r^{scene}(\theta, \phi_{rel}, \theta_{sun}) cos(\theta) \end{aligned} \tag{5.3}$$

In the special case of *Lambertian* reflection, the reflection function is a constant independent of angle, $r^{scene}(\theta_{sat}, \phi_{rel}, \theta_{sun}) = r^{scene}$, and in that case the albedo a^{scene} is given by

$$a^{scene} = 2 \int_0^{\pi} d\phi_{rel} \int_0^{\pi/2} d\theta r^{scene} cos(\theta) sin(\theta) = \pi r^{scene} \tag{5.4}$$

For the Lambertian reflection case, the reflected short wave flux surface density $F_{SW}^{scene}(\theta_{sun})$ can be obtained from the reflected short wave radiance $L_{SW}^{scene}(\theta, \phi, \theta_{sun})$ measured in a particular direction (θ,ϕ) by equation 5.5, i.e. by multiplying the radiance with a factor π independent of the angles $(\theta,\phi,\theta_{sun})$.

$$F_{SW}^{scene}(\theta_{sun}) = \pi L_{SW}^{scene}(\theta, \phi, \theta_{sun}) \tag{5.5}$$

In the general case of *non Lambertian* reflection, the relation between the reflected short wave flux surface density $F_{SW}^{scene}(\theta_{sun})$ and the reflected short wave radiance $L_{SW}^{scene}(\theta, \phi, \theta_{sun})$ *will* be angular dependent. The deviation from the Lambertian case is described by the bidirectional reflection function $R^{scene}(\theta_{sat}, \phi_{rel}, \theta_{sun})$, which is defined by the relation

$$F_{SW}^{scene}(\theta_{sun}) = \frac{\pi L_{SW}^{scene}(\theta_{sat}, \phi_{rel}, \theta_{sun})}{R^{scene}(\theta_{sat}, \phi_{rel}, \theta_{sun})} \tag{5.6}$$

Substitution of the definition of the albedo $a^{scene}(\theta_{sun})$ (equation 5.3) and of the reflection function $r^{scene}(\theta_{sat}, \phi_{rel}, \theta_{sun})$ (equation 5.1) into the defining equation for the bidirectional reflection function $R^{scene}(\theta_{sat}, \phi_{rel}, \theta_{sun})$ (equation 5.6) yields the relationship 5.7 between the three quantities $a^{scene}(\theta_{sun})$, $r^{scene}(\theta_{sat}, \phi_{rel}, \theta_{sun})$ and $R^{scene}(\theta_{sat}, \phi_{rel}, \theta_{sun})$.

$$r^{scene}(\theta_{sat}, \phi_{rel}, \theta_{sun}) = \frac{a^{scene}(\theta_{sun}) R^{scene}(\theta_{sat}, \phi_{rel}, \theta_{sun})}{\pi} \tag{5.7}$$

From equations 5.3 and 5.7, it becomes clear that the knowledge of the reflection function $r^{scene}(\theta_{sat}, \phi_{rel}, \theta_{sun})$ is equivalent with the knowledge of both the albedo $a^{scene}(\theta_{sun})$ and the bidirectional reflection function $R^{scene}(\theta_{sat}, \phi_{rel}, \theta_{sun})$.

In the following sections different existing ADM's, that give the reflected short wave radiances $L_{SW}^{scene}(\theta, \phi, \theta_{sun})$ for given scene types, are described shortly.

5.1.1 ERBE production models

The ADM's [SG+88] that have been used to produce the ERBE flux surface densities, have been obtained by sorting NIMBUS 7 short wave radiances for predefined scenes in predefined angular interval combinations, denoted as "angular bins".

The predefined scenes were recognised using long wave radiances.

Since NIMBUS 7 was a sun synchronous satellite with equator crossing time around local noon, NIMBUS 7 radiances for low solar zenith angle bins were not always available. When possible, missing values for particular angular bins have been obtained using the Helmholtz reciprocity principle $F_{SOL}(\theta_{sun})r^{scene}(\theta_{sat},\phi_{rel},\theta_{sun}) = F_{SOL}(\theta_{sat})r^{scene}(\theta_{sun},\phi_{rel},\theta_{sat})$. The remaining empty bins have been filled using interpolation from surrounding bin values.

The ERBE production models give the albedo $a^{scene}(\theta_{sun})$ and the bidirectional reflection function $R^{scene}(\theta_{sat},\phi_{rel},\theta_{sun})$ in tabular form.

5.1.2 Analytical models

Analytical functions have been fitted to the ERBE production models, yielding angular models with smoother angular variation [MSSS94].

The analytical models give the reflection function $r^{scene}(\theta_{sat},\phi_{rel},\theta_{sun})$ as an analytical function for every scene type. The albedo $a^{scene}(\theta_{sun})$ is obtained through integration of the reflection function
$r^{scene}(\theta_{sat},\phi_{rel},\theta_{sun})$ (equation 5.3). The albedo $a^{scene}(\theta_{sun})$ is given either as an analytical function (if analytical integration of $r^{scene}(\theta_{sat},\phi_{rel},\theta_{sun})$ is possible) or through numerical integration. The bidirectional reflection function $R^{scene}(\theta_{sat},\phi_{rel},\theta_{sun})$ is obtained from equation 5.7.

5.1.3 Models obtained by the Radiance Pair Method (RPM)

From analysis of processed ERBE results [GOH97], it has been demonstrated that the angular behaviour of the models from section 5.1.1 is wrong for low viewing zenith and solar zenith angles. New ADM's have been derived from the NIMBUS 7 data set using the novel Radiance Pair Method (RPM) [GOH96]. These new ADM's seem to have a correct behaviour for low viewing zenith and solar zenith angles [GOH97].

The RPM models give the albedo $a^{scene}(\theta_{sun})$ and the bidirectional reflection function $R^{scene}(\theta_{sat},\phi_{rel},\theta_{sun})$ in tabular form.

5.1.4 Specific clear sky desert models

In addition to the previous three ADM sets, which are defined for all 12 ERBE scene types, two more ADM's will be used. Those two models are derived for clear sky desert only. The first model was derived from METEOSAT data in [CK95]. The second model was derived from ScaRaB data in [Cap96].

The bidirectional reflection function $R^{scene}(\theta_{sat},\phi_{rel},\theta_{sun})$ and the so-called directional albedo $a^{scene}(\theta_{sun})/a^{scene}(0)$ are given in tabular form.

5.2 Spectral dependency models

Since METEOSAT measured the reflected solar radiation with a spectral narrow VIS channel, while the desired radiation budget term F_{SW} is an energy flux surface density integrated over the entire solar spectrum, it is essential to model how the reflected solar radiation in spectral regions not covered by the METEOSAT VIS channel, are related to the METEOSAT measurements.

In this section the spectral dependency model used for the reflected solar radiation measured by the METEOSAT VIS channel, will be described.

The spectral distribution of the reflected solar radiation depends on the spectral transmission, absorption, scattering and reflection characteristics of the components (inclusive cloud components) of the earth's atmosphere and the earth's surface. All these parameters are described quite well in conventional, plane-parallel, radiative transfer calculation schemes.

The publicly available radiative transfer calculation scheme of [RYG96] has been chosen to model the scene types which are the most relevant ones, in the METEOSAT field of view, with different spectral behaviour (indicated by their expected visible colour):

- clear sky ocean (blue)
- clear sky land (green)
- clear sky desert (yellow)
- overcast cloudy (grey)

The surface reflectance characteristics of the clear sky scenes have been chosen so that the modelled broad band albedos for a solar zenith angle $\theta_{sun} = 45°$ are close to the ones measured for the RPM model (see section 5.1.3) for the respective ERBE scene types "clear sky ocean", "clear sky land" and "clear sky desert".

Table 5.2 list the surface reflectance and aerosol model parameters used for the different scene types.

scene	surface reflectance	aerosol model
clear sky ocean	100 % of the sea water reflectance	oceanic, visibility=23 km
clear sky land	50 % of the vegetated land reflectance	rural, visibility=23 km
clear sky desert	150 % of the sand reflectance	none
overcast cloudy	0	none

Table 5.1: Parameters used in the radiative transfer model [RYG96], for the modelling of the coloured spectral scenes "clear sky ocean", "clear sky land", "clear sky desert" and "overcast cloudy".

The overcast cloudy scene is modelled as a water cloud at altitude 1 km, with an effective cloud droplet radius of 8 μm. A cloud optical depth of 20 has been chosen, so that the modelled broad band albedo for a solar zenith angle $\theta_{sun} = 45°$ is close to the one measured for the RPM model (see section 5.1.3) ERBE scene type "overcast cloudy". The model calculations are done for the "mean" solar zenith angle $\theta_{sun} = 45°$ and for the "minimal" solar zenith angle $\theta_{sun} = 45°$. From these calculations under different solar illumination conditions, it will become clear that the spectral dependency of the reflected solar radiation is, in a reasonable first approximation, decoupled from the angular dependency of the reflected solar radiation.

The US 62 standard atmosphere is used for all models. All model parameters which are not explicitly mentioned have the [RYG96] default values.

The spectral components of the modelled reflected short wave flux surface density F_{SW}^{scene} are defined as $F_{SW,\lambda}^{scene}$.

$$F_{SW}^{scene} = \int_0^\infty d\lambda F_{SW,\lambda}^{scene} \tag{5.8}$$

Figure 5.1 shows the modelled $F_{SW,\lambda}^{scene}$ for the three clear sky scenes for the case $\theta_{sun} = 45°$.

Figure 5.2 shows $F_{SW,\lambda}^{scene}$ for the overcast cloudy scene for the case $\theta_{sun} = 45°$.

The filtered flux $F_{METx,VIS}^{scene}$ for a particular modelled scene for a particular METEOSAT x (2 and 5 are considered) VIS channel is defined by equation 5.9.

$$F_{METx,VIS}^{scene} = \int_0^\infty d\lambda \Phi_{METx,VIS}(\lambda) F_{SW,\lambda}^{scene} \tag{5.9}$$

The spectral components of the incoming solar flux surface density F_{SOL} are defined as $F_{SOL,\lambda}$.

$$F_{SOL} = \int_0^\infty d\lambda F_{SOL,\lambda} \tag{5.10}$$

The filtered solar flux surface density $F_{METx,VIS}^{SOL}$ for a particular METEOSAT x (2 and 5 are considered) VIS channel is defined by equation 5.11.

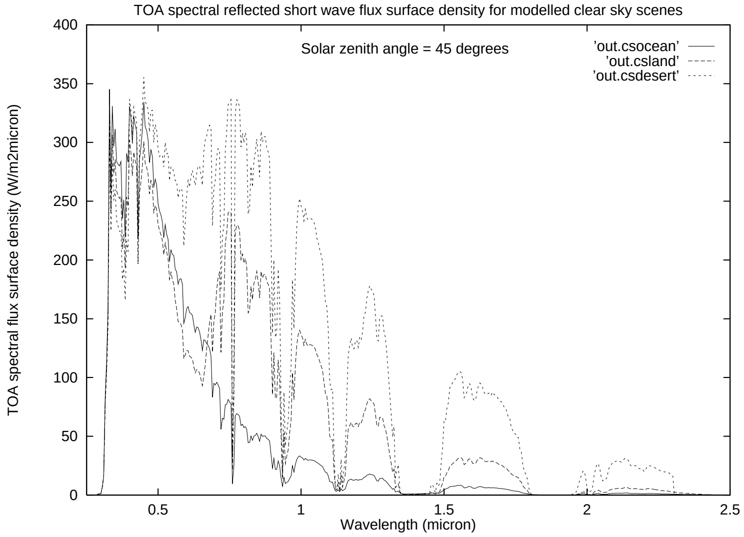

Figure 5.1: Modelled spectral reflected solar flux densities at the top of the atmosphere for clear sky ocean, clear sky land and clear sky desert. $\theta_{sun} = 45°$.

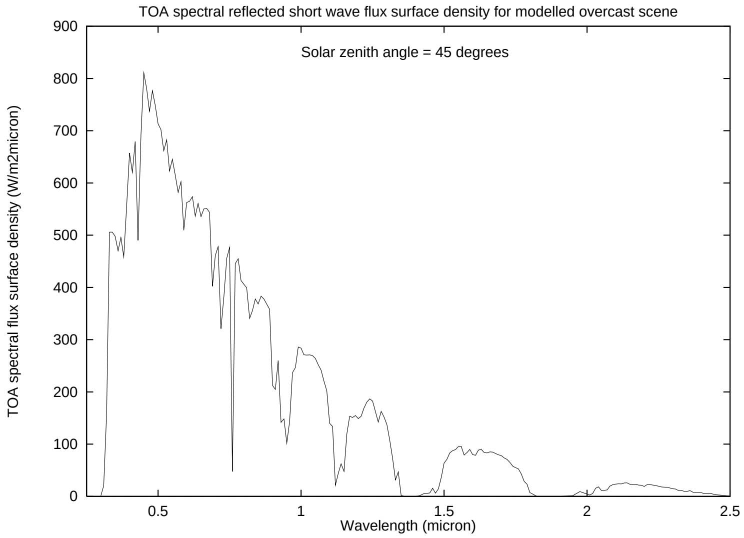

Figure 5.2: Modelled spectral reflected solar flux density at the top of the atmosphere for overcast cloudy scene. $\theta_{sun} = 45°$.

$$F^{SOL}_{METx,VIS} = \int_0^\infty d\lambda \Phi_{METx,VIS}(\lambda) F_{SOL,\lambda} \tag{5.11}$$

The model narrow band albedo a^{scene}_{METx} for a particular modelled scene for a particular METEOSAT x (2 and 5 are considered) VIS channel is defined by equation 5.12.

$$a^{scene}_{METx} = \frac{F^{scene}_{METx,VIS}}{F^{SOL}_{METx,VIS}} \tag{5.12}$$

Table 5.2 shows the model broad band and narrow band albedos for the four modelled scenes, for $\theta_{sun} = 45°$. The rough correspondence between the (broad band) albedo, a^{scene}_{RPM}, "measured" by the RPM method (see section 5.1.3) and the (broad band) albedo, a^{scene}_{BB}, modelled by the radiative transfer calculations, should give some faith in the realism of the model calculations. The differences between the broad band albedo, a^{scene}_{BB}, and the narrow band albedos, a^{scene}_{MET2} and a^{scene}_{MET5}, obtained by the radiative transfer calculations, are due to the "coloured" behaviour of the modelled scenes.

scene	a^{scene}_{RPM}	a^{scene}_{BB}	a^{scene}_{MET2}	a^{scene}_{MET5}
clear sky ocean	0.096	0.111	0.103	0.133
clear sky land	0.169	0.158	0.174	0.166
clear sky desert	0.253	0.260	0.287	0.260
overcast cloudy	0.521	0.539	0.598	0.616

Table 5.2: Model scene broad band albedos, for $\theta_{sun} = 45°$. a_{RPM}: RPM albedo. a_{BB}: modelled broad band albedo. And model scene narrow band albedos, for $\theta_{sun} = 45°$. a_{MET2}: modelled METEOSAT 2 narrow band albedo. a_{MET5}: modelled METEOSAT 5 narrow band albedo.

$\theta_{sun} = 45°$ has been chosen as a solar zenith angle representative for "mean" solar illumination conditions. The spectral distribution of the reflected solar flux surface density (integral over full hemisphere of radiance contributions, see equation 2.20) has been chosen as representative of the spectral distribution of the radiance in a "mean" direction.

In order to quantify how well the *spectral* and the *angular* dependency of the radiation are decoupled, the calculation of model albedos has been repeated for $\theta_{sun} = 0°$. Table 5.3 shows the results.

scene	a^{scene}_{RPM}	a^{scene}_{BB}	a^{scene}_{MET2}	a^{scene}_{MET5}
clear sky ocean	0.074	0.077	0.068	0.093
clear sky land	0.166	0.138	0.156	0.140
clear sky desert	0.251	0.252	0.284	0.251
overcast cloudy	0.420	0.495	0.550	0.566

Table 5.3: Model scene broad band albedos, for $\theta_{sun} = 0°$. a_{RPM}: RPM albedo. a_{BB}: modelled broad band albedo. And model scene narrow band albedos, for $\theta_{sun} = 0°$. a_{MET2}: modelled METEOSAT 2 narrow band albedo. a_{MET5}: modelled METEOSAT 5 narrow band albedo.

The spectral dependency of the radiance for every scene is characterised by a spectral conversion function f^{scene}_{METx} which gives the ratio of the reflected flux surface density F^{scene}_{SW} to the narrow band (METEOSAT 2 or 5 VIS in this work) filtered flux surface density $F^{scene}_{METx,VIS}$.

$$f^{scene}_{METx} = \frac{F^{scene}_{SW}}{F^{scene}_{METx,VIS}} \tag{5.13}$$

In the special case of *white* reflection, the spectral albedo $F^{scene}_{SW,\lambda}/F_{SOL,\lambda} = f^{white}_{METx}$ is by definition a constant independent of wavelength and the spectral conversion factor f^{white}_{METx} is given by equation 5.14

$$f^{white}_{METx} = \frac{F^{white}_{SW}}{F^{white}_{METx,VIS}} = \frac{F^{SOL}}{F^{SOL}_{METx,VIS}} = \frac{S^{SOL}}{S^{SOL}_{METx,VIS}} \tag{5.14}$$

$S^{SOL}_{METx,VIS}$ is the so called "METEOSAT instrument solar constant" given by equation 5.15.

$$S^{SOL}_{METx,VIS} = \int_0^\infty d\lambda \Phi_{METx,VIS}(\lambda) S_{SOL,\lambda} \tag{5.15}$$

Table 5.4 list the white spectral conversion factors f^{white}_{METx}, calculated with the solar spectrum $S_{SOL,\lambda}$ described in section 4.1.6.

f^{white}_{MET2}	f^{white}_{MET5}
2.71	2.36

Table 5.4: White spectral conversion factors for METEOSAT VIS channels.

For a realistic (coloured) scene, the scene dependent spectral conversion factor f^{scene}_{METx} can be written as the product of the scene independent white conversion factor f^{white}_{METx} and a scene dependent spectral correction factor fc^{scene}_{METx}.

$$f^{scene}_{METx} = f^{white}_{METx} fc^{scene}_{METx} \tag{5.16}$$

The spectral correction factor fc^{scene}_{METx} can be calculated as

$$fc^{scene}_{METx} = f^{scene}_{METx} / f^{white}_{METx} = \frac{F^{scene}_{SW}}{F^{scene}_{METx,VIS}} \frac{F^{SOL}_{METx,VIS}}{F^{SOL}} = \frac{F^{scene}_{SW}}{F^{SOL}} \frac{F^{SOL}_{METx,VIS}}{F^{scene}_{METx,VIS}} = a^{scene}_{BB} / a^{scene}_{METx} \tag{5.17}$$

For the transition from the first to the second line in equation 5.17, the definitions 5.13 and 5.14 of the spectral conversion factors f^{scene}_{METx} and f^{white}_{METx} have been used. For the transition from the third to the fourth line the definitions 5.3 and 5.12 for the albedos a^{scene}_{BB} and a^{scene}_{METx} have been used.

Table 5.5 lists the spectral correction factors calculated with equation 5.17 from the albedos listed in tables 5.2 and 5.3.

	$\theta_{sun} = 45°$		$\theta_{sun} = 0°$	
scene	fc^{scene}_{MET2}	fc^{scene}_{MET5}	fc^{scene}_{MET2}	fc^{scene}_{MET5}
clear sky ocean	1.16	0.842	1.20	0.839
clear sky land	0.911	0.955	0.884	0.984
clear sky desert	0.906	0.999	0.889	1.00
overcast cloudy	0.902	0.875	0.901	0.876

Table 5.5: Spectral correction factors calculated by usage of the radiative transfer calculation scheme of [RYG96].

It can be seen that

- For all scene types and both instruments, the spectral correction factor for $\theta_{sun} = 0°$ does not differ more than 4 % (0.04) from the spectral correction factor for $\theta_{sun} = 45°$. For "overcast cloudy", the brightest scene (highest albedo in table 5.2), the difference is even as low as 0.1 % (0.001) for both instruments.
- For METEOSAT 2, by coincidence, for all scenes, except "clear sky ocean", the spectral conversion factors are within 2 % (0.02) of each other for a given θ_{sun}. For METEOSAT 5, there is much more difference in the spectral correction factor among scenes, e.g. the "clear sky desert" spectral conversion factor differs as much as 13.4 % (0.134) from the "overcast cloudy" spectral conversion factor.
- For METEOSAT 2 and METEOSAT 5 the spectral correction factors for "overcast cloudy" are close to each other. This can be understood from [CJ92]. In [CJ92], spectral surface solar radiation measurements for homogeneous clear sky and cloudy skies have been investigated. It has been found that clouds can be modelled in good approximation as gray absorbers in

the spectral range 0.3 to 1.0 μm, i.e. they do not modify the spectral distribution of the incoming global solar radiation in the spectral range 0.3-1.0 μm, which corresponds more or less with the METEOSAT VIS channel spectral range. Consequently, the METEOSAT 2 and 5 narrow band albedos for overcast cloudy scenes should be in good approximation the same. From equation 5.17, their overcast cloudy spectral correction factors, fc^{ov}_{METx}, should therefore also be nearly the same.

Chapter 6

State of the art

In this chapter a short overview, which is not meant to be complete, is given of the state of the art in radiation budget and geostationary image processing. A short appreciation of the existing methods is given, and it is indicated how these methods are improved and applied in this work.

6.1 Radiation budget processing

6.1.1 ERBE and ScaRaB radiation budget processing

The most elaborate radiation budget results so far are those obtained by ERBE [B+89] and ScaRaB [KVP+97]. Processed ERBE and ScaRaB files contain the following information for every individual scanner pixel:

- The acquisition time of the pixel.
- The geolocation, i.e. the latitude and longitude of the centre of the pixel.
- The viewing angles, i.e. the values θ_{sun},θ_{sat},ϕ_{rel} (see section 5.1) with which the pixel is viewed.
- The calibrated radiances measured by the instrument channels. These radiances are called "filtered radiances" in the ERBE or ScaRaB terminology because they are filtered with the spectral responses of the instrument channels.
- The estimated short wave and long wave radiance (estimated for ideally flat spectral characteristics) of the pixel. These radiances are called "unfiltered radiances" in the ERBE or ScaRaB terminology. In the ERBE or ScaRaB terminology, unfiltering means estimating unfiltered (spectrally corrected) radiances from filtered (spectrally not corrected) radiances.
- The scene identification, i.e. the number of the ERBE scene (one of the twelve possibilities clear sky ocean,...,overcast described in section 5.1) that was assigned to the pixel.
- The estimated short wave and long wave flux surface density of the pixel.

In the ERBE and ScaRaB projects, radiation budget results have been derived from LEO satellites with the purpose to obtain *statistically* correct results only. Radiation budget terms (the reflected short wave flux surface density and the emitted long wave flux surface density) are estimated from the measured radiances, by a radiance based *scene identification*, followed by a scene dependent radiance to flux surface density conversion.

The used scene identification is the Maximum Likelihood Estimation (MLE) method of [WG89], which is illustrated in the top part of figure 6.1.

For a pixel of a given a priori surface type ("ocean", "land", "desert" or "mixed land-ocean (coast)", see figure 4.19), four cloud cover classes ("clear sky", indicated by the superscript "cs", "partly cloudy", indicated by the superscript "pc", "mostly cloudy", indicated by the superscript "mc" and "overcast", indicated by the superscript "ov") are considered. One calculates

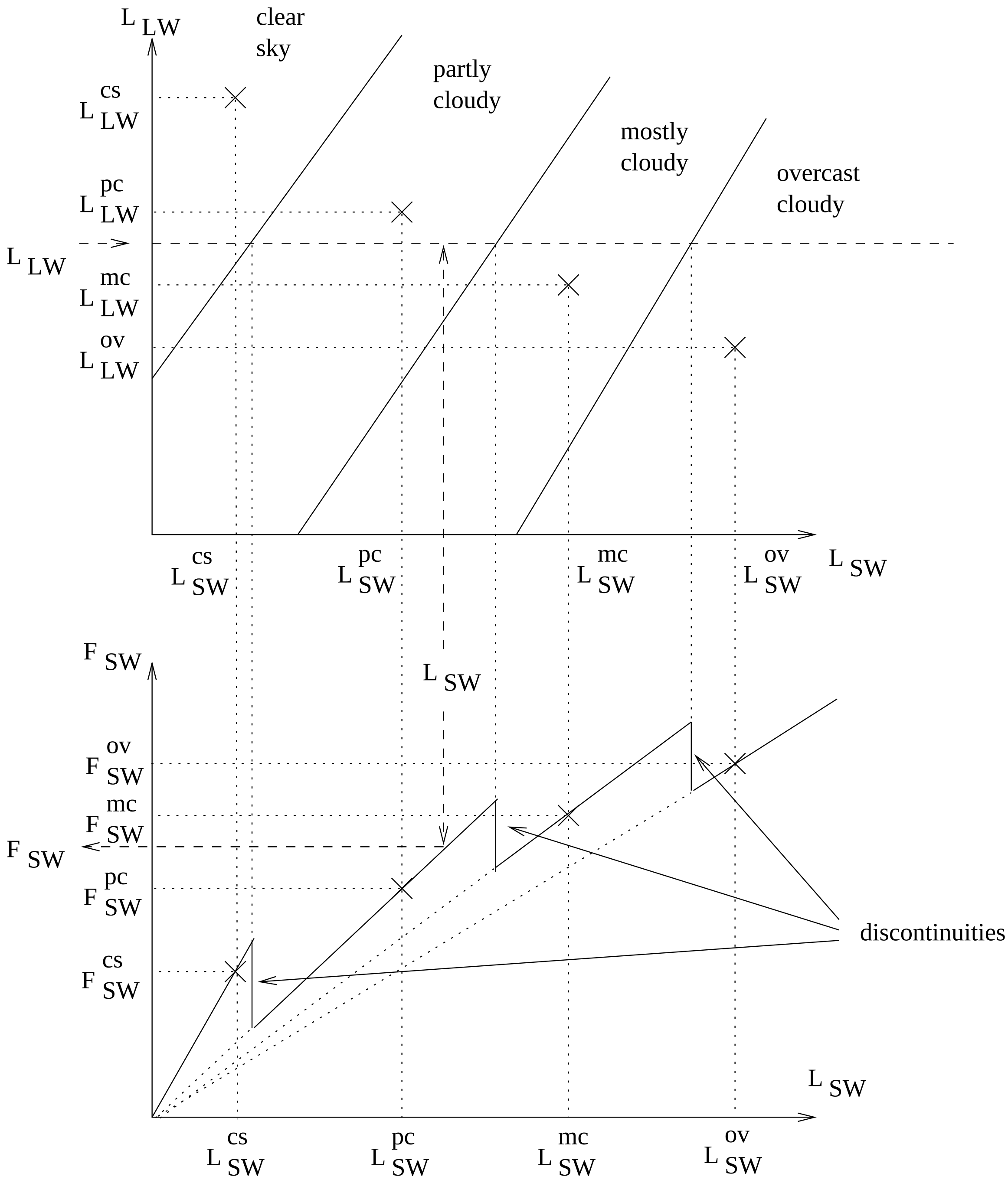

Figure 6.1: MLE scene identification method (top) and related short wave radiance to flux surface density conversion (bottom).

- for the "clear sky" class, the model short wave radiance L_{SW}^{cs} and the model long wave radiance L_{LW}^{cs}.
- for the "partly cloudy" class, the model short wave radiance L_{SW}^{pc} and the model long wave radiance L_{LW}^{pc}.
- for the "mostly cloudy" class, the model short wave radiance L_{SW}^{mc} and the model long wave radiance L_{LW}^{mc}.
- for the "overcast" class, the model short wave radiance L_{SW}^{ov} and the model long wave radiance L_{LW}^{ov}.

In general, with higher cloud coverage L_{LW} becomes lower (the scene becomes colder) and L_{SW} becomes higher (the scene becomes brighter), so there exists a *statistical* relation between L_{LW} and L_{SW}.

The four calculated couples $(L_{SW}^{cs}, L_{LW}^{cs})$, $(L_{SW}^{pc}, L_{LW}^{pc})$, $(L_{SW}^{mc}, L_{LW}^{mc})$ and $(L_{SW}^{ov}, L_{LW}^{ov})$ are located in the plane of all possible couples (L_{SW}, L_{LW}) (see top part of figure 6.1). In between these couples separation lines (with statistical optimal location, see [WG89]) are drawn, which divide the plane in four zones, corresponding to the four cloud cover classes.

A LEO footprint with the radiance couple (L_{SW}, L_{LW}) is labelled with the scene type which corresponds to the zone to which the couple (L_{SW}, L_{LW}) belongs (see top part of figure 6.1).

Based on the scene type assigned to the footprint, radiance to flux surface density conversion curves are selected. For the reflected short wave radiance L_{SW} to flux surface density F_{SW} conversion (see bottom part of figure 6.1) the radiance to flux surface density conversion curve for a given scene type is a line passing through the origin in the (L_{SW}, F_{SW}) plane. For a given value of the emitted long wave radiance L_{LW} (dashed line in top part of figure 6.1) this results in a piecewise linear conversion curve of L_{SW} to F_{SW} (bottom part of figure 6.1).

The main points in which these results will be improved in this work are:

- Full resolution METEOSAT images will be used instead of bands of low resolution LEO pixels. This will strongly improve the time and space sampling of the radiation budget terms.
- For the scene identification, independent cloud detection will be done in the VIS and IR channel images. In the ERBE and ScaRaB projects, correlation between short wave and long wave cloudiness is assumed. This is only true in a statistical sense.
- A continuous scene identification will be done in this work instead of a discrete one (resulting in the discontinuities between the linear pieces of the radiance to flux surface density conversion curve of figure 6.1). This will avoid the introduction of artificial spatial and temporal discontinuities in the high resolution radiation budget term estimates.

Since these improved results, will be derived from METEOSAT images, it is worthwhile to describe the existing processing techniques for geostationary (e.g. METEOSAT) images. This will be done in the next section for the processing techniques which are not radiation budget specific.

6.2 Geostationary image processing

Geostationary imagers, such as the European METEOSAT or the American Geostationary Operational Environmental Satellite (GOES), are operationally used to provide meteorological data. Some of the existing processing of the geostationary imager data can, even when this processing has not been explicitly designed with this purpose, be useful for radiation budget studies.

In this section, a non exhaustive overview of existing, not radiation budget specific, geostationary data processing is given.

6.2.1 METEOSAT image rectification

The nominal state of the METEOSAT satellite is given by

- The METEOSAT satellite position is fixed at geostationary height (35.8e3 km) above the point on earth with latitude 0 degrees and longitude 0 degrees.
- The METEOSAT rotation axis orientation is fixed in time and is parallel with the earth rotation axis.
- The METEOSAT rotation speed is fixed in time at 600 rpm.

If METEOSAT were constantly in this nominal state, the METEOSAT instrument Line Of Sight (LOS) for a given METEOSAT pixel, would cross the earth surface in a fixed point. As a result the geolocation of a given METEOSAT pixel would be constant in time.

In reality, the METEOSAT state varies slightly around the nominal one, and the geolocation of the METEOSAT image pixels is not entirely constant in time.

By the so-called rectification processing [BCL+95], from the real image, also called the "raw" image, obtained by the METEOSAT instrument, the ideal image, also called the "rectified" image, that would have been obtained by the METEOSAT instrument if the satellite would have been in the nominal state, is *calculated*.

In this work only rectified METEOSAT images will be used. They have the advantage that for a given pixel of the image, a fixed place on earth is seen.

6.2.2 Cloud mask determination

Various methods have been worked out to identify the presence of clouds in geostationary images, e.g. in [SD87], [MH84a], [R+85]. These methods exploit the different time space characteristics of cloudy pixels compared to clear sky pixels. All of these methods have been applied to spatially and temporally subsampled geostationary images, with emphasis on a *statistically* correct clear sky detection.

These methods will be improved in chapter 8 in a two-fold way:

- In stead of determining only a statistically correct *cloud mask*, i.e. a binary value indicating the presence of clouds, the best possible estimate of the instantaneous clear sky count (grey value) will be obtained for every pixel.
- Results will not only be obtained for spatially and temporally subsampled images, but also for full resolution images. The obtained full resolution clear sky values will be spatially and temporally coherent, i.e. there will be no spatial or temporal discontinuities introduced by the processing used to obtain the clear sky images.

6.2.3 MIEC-MPEF METEOSAT operational processing

The operational processing of METEOSAT images was done by the European Space Operation Centre (ESOC) in the past and is done by the EUropean METeorological SATellite exploitation organisation (EUMETSAT) in the present. Meteorological information was extracted by the ESOC Meteorological Information Extraction Chain (MIEC) in the past and is extracted by the EUMETSAT Meteorological Product Extraction Facility (MPEF) in the present.

This extraction of meteorological information is based on the division of full resolution METEOSAT images in non overlapping segments of 32x32 pixels. Various processings are applied to these segments.

The processings which are relevant to this work, are summarised in the next paragraphs.

Unsupervised classification From a multi spectral[1] image analysis [Tom81], which is a form of unsupervised image classification, a number of clusters is extracted for every segment. A cluster is the set of segment pixels which have been assigned to the same class by the unsupervised classification algorithm.

Height assignment Using radiative transfer calculations [Sch86] and auxiliary ECMWF meteorological data, every segment cluster is characterised physically. A cloud detection is done, and for each cloud segment, the height of the cloud is determined.

[1] i.e. using the different METEOSAT spectral channels

Cloud motion wind extraction Using an image matching technique [S+93] to match a segment with the previous or next image, cloud motion winds are derived from the detected segment motion.

This analysis will be improved in chapter 7 in a two-fold way:

- The correlation matching technique will be replaced by the distance matching technique, for which a theoretical motivation exists, and which gives better experimental results.
- The block matching technique will be refined to an iterative matching technique, which results in *pixel wise* motion estimations.

This improved technique will be applied for the time interpolation of the METEOSAT images.

6.3 METEOSAT radiation budget processing

In this section an overview is given of the most relevant existing radiation budget specific METEOSAT data processing techniques.

6.3.1 Long wave processing

In [SL88], [SMvdB90] a method has been worked out to obtain estimates of the long wave radiation budget term from the METEOSAT long wave channels (IR channel and WV channel) data. The method is based on the approximation of radiative transfer calculation results by numerically fitted analytical expressions. This method has been applied in combination with the unsupervised classification of section 6.2.3, in order to obtain long wave radiation budget term estimates for every cluster.

This method will be applied in chapter 8 to full resolution METEOSAT images.

6.3.2 Short wave processing

In [VF94] a method has been worked out to obtain estimates of the short wave radiation budget term from METEOSAT VIS images. The method firstly obtains an estimate of the short wave broad band radiance from the VIS radiance, and then the ERBE short wave flux surface density estimation method is applied [WG89]. The method used to obtain broad band estimates from METEOSAT VIS narrow band radiances is based on an empirical fit between collocated METEOSAT and ERBE measurements.

In this work, similar results will be obtained, but this time for full resolution images and using a more elaborate scene identification algorithm, which does not rely on a statistical relation between VIS and IR cloudiness. The novel flux surface density estimation method, based on the new scene identification, produces spatially and temporally coherent results, i.e. no spatial or temporal discontinuities are introduced by the flux surface density estimation processing.

Moreover, since instantaneous clear sky count (grey value) estimation is integrated in the new scene identification and short wave flux surface density estimation method, it becomes possible to use measured instantaneous surface states[2] for an optimal scene dependent short wave flux surface density estimation.

The new method does not rely on collocated METEOSAT and ERBE measurements for the estimation of the short wave broad band radiance. Instead a spectral conversion method based on radiative transfer calculations is used. Since the new flux surface density estimates are obtained completely independent of the LEO (ERBE or ScaRaB) flux surface density estimates, the METEOSAT based estimates can be validated by the LEO based estimates (or vice versa).

[2] which can change in time, e.g. due to seasonal evolution of non permanent deserts

Chapter 7

General image processing techniques

In this chapter the general image processing algorithms that have been developed for the processing related to radiation budget data, are described. In the general processing scheme given in figure 1.1, these image processing algorithms are used in the blocks "Clear sky detection", "Flux surface density estimation" and "Compression". The more detailed processing schemes of these three blocks are given in the figures 7.1, 7.2 and 7.3 respectively.

The description of the actual use of these algorithms in the radiation budget context will be given in chapter 8. For every algorithm described in this chapter, an algorithm description card is given, which includes references to the use of the algorithm in the chapter 8.

7.1 Image equalisation

Image equalisation is a technique which typically transforms an input image with low contrast into an output image with high contrast.

The low contrast image is typically characterised by grey values (counts) which are close to each other, i.e. the image is typically characterised by a narrow grey value histogram. Image (histogram) equalisation achieves contrast enhancement for this kind of images by mapping the grey values of the input image so that for the output image with mapped grey values, a grey value histogram which is close to uniform is obtained. Since for the output image the pixel grey values are more separated than for the input image, the output image has higher contrast than the input image.

The image equalisation technique is used in section 8.6 to improve the contrast of METEOSAT VIS and IR images, in order to have a better detectability of clouds in these images. Compare e.g. the non equalised IR image of figure 8.13 with its equalised version, shown in figure 8.21. It can e.g. be seen that the large stratocumulus cloud field over the Gulf of Guinea has a strongly improved contrast relative to the clear sky ocean in figure 8.21 (the equalised IR image) compared to figure 8.13 (the non equalised IR image).

The main novelty of the image equalisation technique developed in this work is that it does not only apply to individual images, but also to *time series* of images. This will be applied in section 8.6 for the cloud detection from time series of images.

In this section a mathematical description of the developed image equalisation technique is given.

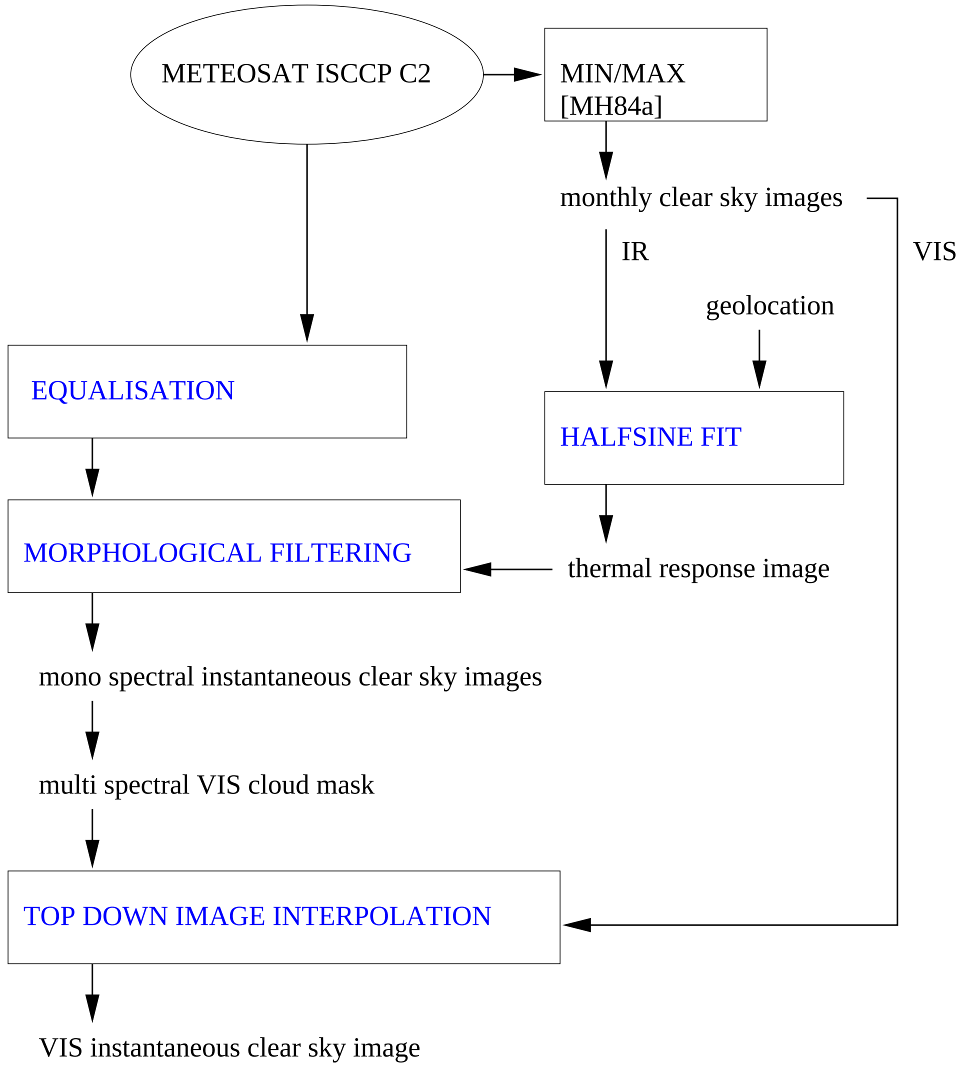

Figure 7.1: The processing scheme developed for the clear sky detection in METEOSAT data. METEOSAT data in ISCCP C2 format is used as external input data. The processing algorithms are indicated by rectangles. For every algorithm an indication is given whether the algorithm is an image processing technique originally developed in this work (indicated by a descriptive text coloured in blue), or whether it is an algorithm of external origin (indicated by a descriptive text coloured in black and by a reference in square brackets).

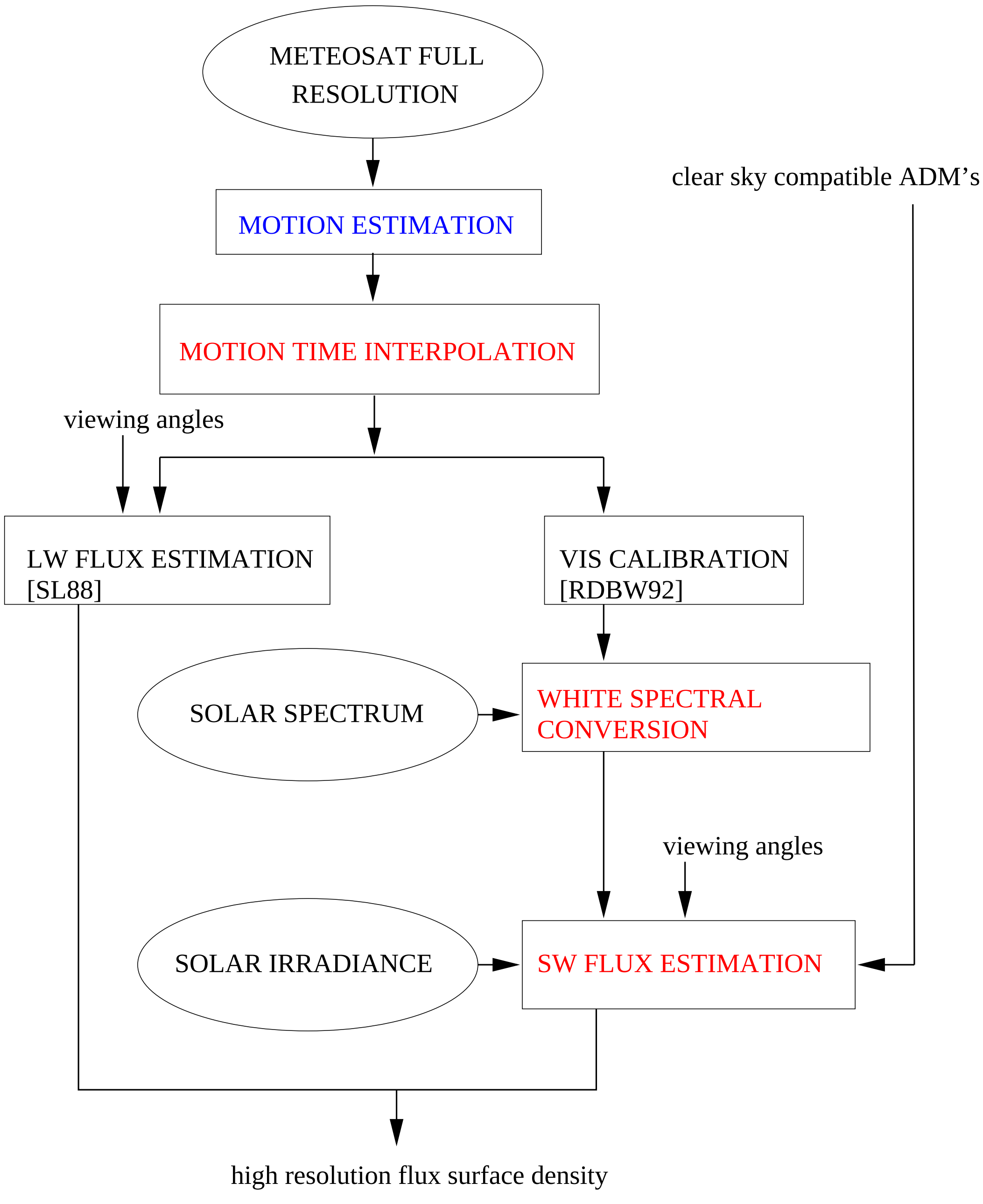

Figure 7.2: The processing scheme developed in this work for the estimation of high resolution fluxes derived from METEOSAT data. METEOSAT full resolution data is used as external input data. Processing algorithms are indicated by rectangles. For every algorithm an indication is given whether the algorithm is an image processing technique originally developed in this work (indicated by a descriptive text coloured in blue), or a specific satellite data processing algorithm originally developed in this work (indicated by a descriptive text coloured in red), or whether it is an algorithm of external origin (indicated by a descriptive text coloured in black and by a reference in square brackets).

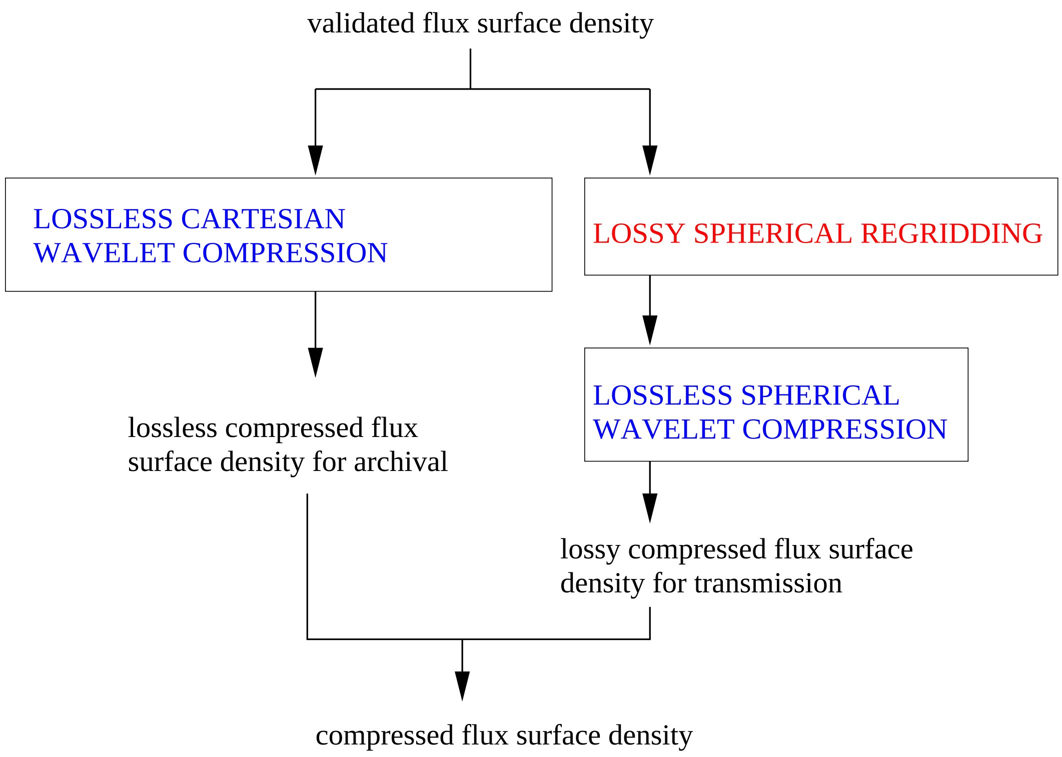

Figure 7.3: The processing scheme developed in this work for the compression of high resolution flux surface densities derived from METEOSAT data. Processing algorithms are indicated by rectangles. For every algorithm an indication is given whether the algorithm is an image processing technique originally developed in this work (indicated by a descriptive text coloured in blue), or whether it is a specific satellite data processing algorithm originally developed in this work (indicated by a descriptive text coloured in red).

7.1.1 Algorithm description card

name algorithm	image equalisation
technical novelty	equalisation for a time series of images
novel application	METEOSAT cloud mask determination (section 8.6)
references	*none*

Table 7.1: Algorithm card for image equalisation algorithm

7.1.2 Problem definition

Consider a two dimensional grey level image $I(i,j)$ $i = 1,\ldots,n$; $j = 1,\ldots,m$ or a time series of two dimensional grey level images $I_t(i,j)$ $i = 1,\ldots,n$; $j = 1,\ldots,m$; $t = t_1,\ldots,t_k$. The number of appearances of a given grey value g is given by the histogram count $H(g)$. The histogram is given by equation 7.1 in the case of a single 2D image, and by equation 7.2 in the case of a time series of images.

$$H_I(g) = \#\{(i,j)|I(i,j) = g\} \tag{7.1}$$

$$H_{I_t}(g) = \#\{(i,j,t)|I_t(i,j) = g\} \tag{7.2}$$

The problem of image equalisation consists of finding a grey level mapping function $T^{eq}(g)$ which transforms the old grey values g in new grey values $g' = T^{eq}(g)$ so that the new image or the new time series of images has a histogram which is close to uniform, i.e. with histogram values which are close to constant. The problem is formulated mathematically by equation 7.3 for the equalisation of an individual image and by equation 7.4 for the equalisation of a time series of images.

$$\begin{array}{c} I^{eq}(i,j) = T^{eq}(I(i,j)) \\ H_{I'}(g') \approx constant \end{array} \tag{7.3}$$

$$\begin{array}{c} I_t^{eq}(i,j) = T^{eq}(I_t(i,j)) \\ H_{I_t'}(g') \approx constant \end{array} \tag{7.4}$$

7.1.3 Solution

One can note that an almost constant histogram $H_I(g)$ corresponds to an almost linear cumulative histogram $C_I(g)$. The cumulative histogram is defined as

$$C(g) = \sum_{h \leq g} H(h) \tag{7.5}$$

In order to have a linear behaviour of the cumulative histogram $C_{I^{eq}}(g')$ after mapping $g' = T^{eq}(g)$, the difference $T^{eq}(g) - T^{eq}(g-1)$ between two mapped consecutive values g-1,g should become proportional to the difference between the corresponding cumulative histogram values $C_I(g) - C_I(g-1) = H(g) = C_{I^{eq}}(T^{eq}(g)) - C_{I^{eq}}(T^{eq}(g-1))$. This means (see figure 7.4) that the ideal mapping function $T^{eq}(g)$ is given by a linearly rescaled version of the original cumulative histogram $C_I(g)$.

If the minimum occurring grey value is g_{min} and the maximum occurring grey value is g_{max}

$$\begin{array}{ll} H(g) = 0 & \text{if } g < g_{min} \\ H(g_{min}) \neq 0 & \\ H(g_{max}) \neq 0 & \\ H(g) = 0 & \text{if } g > g_{max} \end{array} \tag{7.6}$$

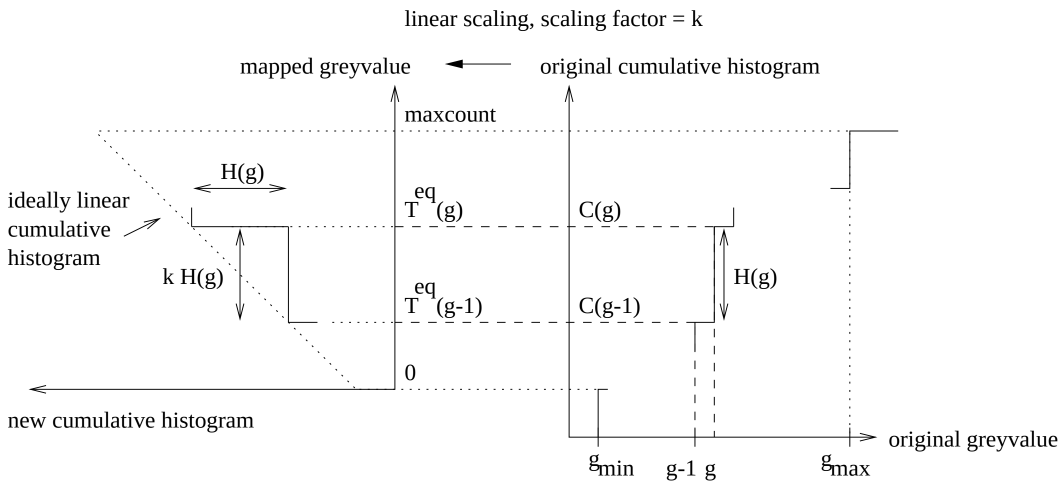

Figure 7.4: The equalisation function $T^{eq}(g)$ obtained by a linear rescaling of the original cumulative histogram. Right: Original cumulative histogram in function of the original grey values. Left: New cumulative histogram in function of the mapped grey values. The grey value g is mapped to $T^{eq}(g)$, the grey value $g-1$ is mapped to $T^{eq}(g-1)$.

and if the equalised image should have values between 0 and $maxcount$ the integer transfer function $T^{eq}(g)$ which gives an approximate[1] linear behaviour for $C_{I^{eq}}(g')$ is

$$
\begin{array}{ll}
T^{eq}(g) = 0 & \text{if } g < g_{min} \\
T^{eq}(g) = [\frac{maxcount}{C_I(g_{max}) - C_I(g_{min})} C_I(g)] & \text{if } g_{min} < g < g_{max} \\
T^{eq}(g) = maxcount & \text{if } g > g_{max}
\end{array}
\tag{7.7}
$$

where [...] stands for "integer part".

7.1.4 Application

The equalisation technique which has been described here is applied in section 8.6 for the equalisation of time series of VIS images (see equation 8.34) and time series of IR images (see equation 8.38), in order to improve the detectability of clouds in these images (see also box "Equalisation" in figure 7.1).

7.2 Morphological filtering

Morphological filtering of a grey value time series is a technique to determine the *time varying* extremum (minimum or maximum) of the time series. The amount of time variation of the obtained extremum series depends on the choice of the *morphological kernel*, which is a function of time which describes the maximum "normal" temporal variation of the grey values that is allowed, i.e. the temporal variation which is not detected as extremum variation, in the time series.

Morphological filtering is used in section 8.6 as a refinement to the classical VIS minimum and IR maximum technique (described in section 8.4) for the determination of clear sky images. The introduction of morphological filtering for clear sky image determination, allows a good separation between cloud contaminated pixels, characterised by fast grey value temporal variation (steep temporal gradient), and clear sky pixels, characterised by slow grey value temporal variation (small temporal gradient).

The main technical novelty of the morphological filtering used in this work, is the choice of a specific morphological kernel, which allows the determination of a time varying extremum with one single morphological filter operation[2], and the parametrisation of this kernel with a slope parameter

[1] The linear behaviour is only approximate due to the integer quantification.

[2] Whereas general morphological kernels require more than one morphological filter operation to achieve the same result.

sl, which controls the extremum time variation detected by the morphological filter. The value of this slope parameter will be tuned in section 8.6 for optimal cloud detection performance in function of the properties of the underlying surface. E.g. for a desert pixel, less sensitive extermum detection is used than for a non desert pixel, since it is noticed that for desert pixels the temporal variation of the clear sky grey values is higher than for non desert pixels.

In this section a mathematical description of the used morphological filtering technique, is given.

7.2.1 Algorithm description card

name algorithm	morphological filtering
technical novelty	specific choice of the kernel
novel application	METEOSAT cloud mask determination (section 8.6)
references	[Mar89]

Table 7.2: Algorithm card for morphological filtering algorithm

7.2.2 Definition

Given a discrete time series of values $f(t)$ $t = 1, \ldots, k$, the morphological filtering of the minimum type with the morphological kernel $K(t)$ $t = -\infty, \ldots, \infty$ is defined as

$$(f \ominus K)(t) = \min_{l} \quad (f(t-l) + K(l)) \tag{7.8}$$

The morphological filtering of the maximum type of $f(t)$ $t = 1, \ldots, k$ with the morphological kernel $K(t)$ $t = -\infty, \ldots, \infty$ is defined as

$$(f \oplus K)(t) = \max_{l} \quad (f(t-l) + K(l)) \tag{7.9}$$

7.2.3 Specific kernel choice

For morphological filtering of the minimum type the upward V shaped kernel $V_{sl}(t)$

$$V_{sl}(t) = sl|t| \quad sl \geq 0 \tag{7.10}$$

is chosen (see figure 7.5). The shape of this kernel depends on the parameter sl, which controls the slope of the V sides.

For morphological filtering of the maximum type the downward V shaped kernel $V_{-sl}(t)$

$$V_{-sl}(t) = -sl|t| \quad sl \geq 0 \tag{7.11}$$

is chosen (see figure 7.6). The shape of this kernel depends again on the parameter sl, which controls the slope of the downward V sides.

7.2.4 Properties

As illustrated in figure 7.5, the morphologically filtered time series $(f \ominus V_{sl})(t)$ gives a time varying minimum of the time series $f(t)$. The higher the slope parameter sl is chosen, the closer the time varying minimum $(f \ominus V_{sl})(t)$ follows $f(t)$ in time. In the case of the lowest allowed slope parameter $sl = 0$, the time varying minimum is constant in time and equals the minimum of the time series $f(t)$.

As illustrated in figure 7.6, the morphologically filtered time series $(f \oplus V_{-sl})(t)$ gives a time varying maximum of the time series $f(t)$. The higher the slope parameter sl is chosen, the closer the time varying maximum $(f \oplus V_{sl})(t)$ follows $f(t)$ in time. In the case of the lowest allowed slope parameter $sl = 0$, the time varying maximum is constant in time and equals the maximum of the time series $f(t)$.

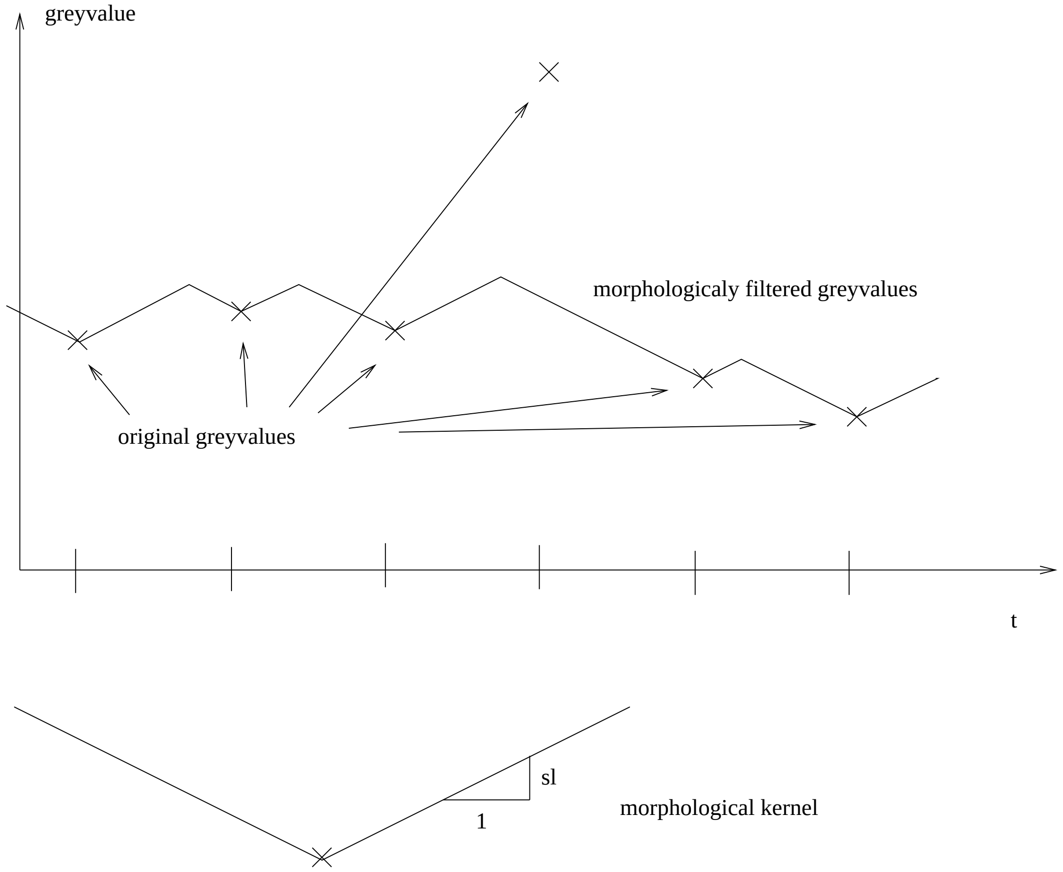

Figure 7.5: Morphological filtering of the minimum type with an upward V shaped morphological kernel, applied to a series of grey values. The morphologically filtered time series is a time varying minimum of the original grey value series. The time variability of the obtained minimum is controlled by the slope parameter sl.

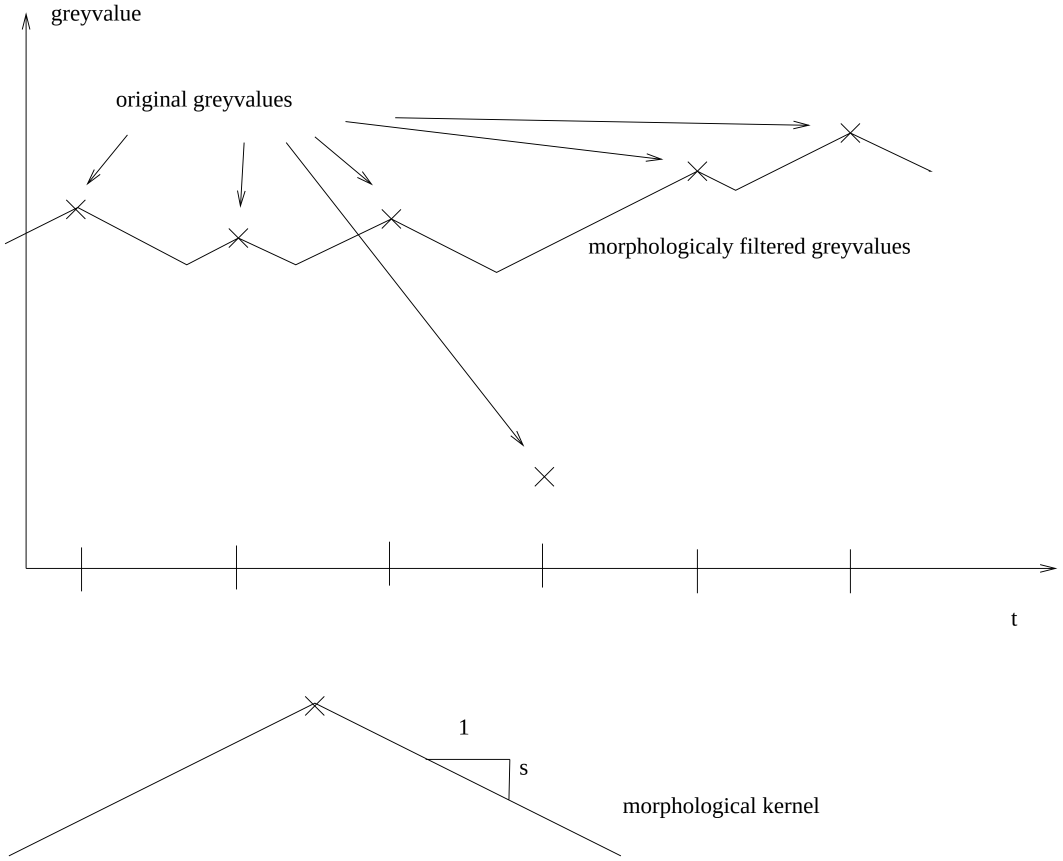

Figure 7.6: Morphological filtering of the maximum type with an downward V shaped morphological kernel, applied to a series of grey values. The morphologically filtered time series is a time varying maximum of the original grey value series. The time variability of the obtained maximum is controlled by the slope parameter sl.

7.2.5 Application

The morphological filtering which has been described here, will be applied in section 8.6 for the determination of clear sky images from equalised VIS and IR images (See equation 8.35 for the VIS case and equation 8.39 for the IR case; see also the box "Morphological filtering" in figure 7.1, the IR and VIS clear sky images obtained by the morphological filtering are called "mono spectral instantaneous clear sky images" in figure 7.1.).

7.3 Top down Bayesian analysis framework

Top down Bayesian image analysis is a general image analysis framework, originally developed in this work. This framework has the advantage that is extends the application of relatively complex image processing tasks (e.g. image segment matching for motion estimation) which normally require information over relatively large image *segments* (windows). Thanks to the top down Bayesian image analysis framework the use of these algorithms is extended to image segments with arbitrarily low size (with a 1 x 1 segment, a pixel, as smallest possible segment).

At low segment sizes the complex algorithms can not be applied directly, since the contextual information, which is only present for large segment sizes, is missing. In top down Bayesian image analysis, this missing contextual information is provided by the so-called *regularisation* mechanism, which limits the possible analysis results for small size segments, from the knowledge of the analysis results for larger size segments. Thus the top down Bayesian image analysis framework allows the derivation of complex image analysis results at very high resolution (down to a single pixel).

In this work the top down Bayesian image analysis framework is used for

- The derivation of very high resolution motion estimation, used for METEOSAT image time interpolation in section 8.8.
- High resolution (pixel wise) non smoothing interpolation, used in section 8.7 to derive spatially coherent clear sky images from the clear sky detection based on the morphological filtering in section 8.6.

A mathematical description is given of

- the general top down Bayesian image analysis framework, in section 7.3.2.
- the application of this framework for non smoothing image interpolation, in section 7.4.
- the application of this framework for motion estimation, in section 7.5.

7.3.1 Introduction

Many of the classical image processing algorithms, especially in the field of pattern recognition, are bottom up algorithms, i.e. they start with working on a large amount of local data (pixels, features, micro segments, ...) and end with combining the information gained from these data in the later stages to obtain a smaller amount of global information (classes, segments,...). This way of working is not very efficient, neither in computing time, nor in human development effort. The inefficiency in computing time comes from the use of a large amount of local data to obtain a smaller set of final results. The inefficiency in development effort lies in the specificity of the algorithm to a certain problem which is a consequence of starting the information extraction at the local level.

As an alternative to the problem specific bottom up algorithms, this work presents a generic top down algorithm (section 7.3.2), i.e. a general purpose image analysis algorithm which starts with analysing a small amount of global data and refines the analysis results up to the large amount of available local information. The top down mechanism used, is inspired by the Laplacian pyramid and by pel-recursive motion estimation techniques: an analysis is done on non-overlapping square segments of which the dimensions are recursively divided by two. The recursion starts with analysing one segment, which is the entire image (top of the pyramid) and ends with an analysis of every pixel as a separate segment (bottom of the pyramid).

As refinement mechanism the theorem of Bayes is used. The analysis result of a child segment, which is part of an already analysed parent segment, is determined as the most probable result, calculated according to the theorem of Bayes. The parent analysis is used to compute the prior probabilities, the local analysis within the child segment is used to compute the a posteriori probabilities. In this way refinement by local analysis is combined with regularisation by larger scale analysis.

This leads to an "empty" generic image analysis tool, which can be "filled" with a specific analysis type to obtain a specific image analysis algorithm. Two different image analysis algorithms, used in the remainder of the work presented here, are obtained with very little effort by choosing different specific analysis schemes: non smoothing image interpolation (section 7.4) and motion estimation (section 7.5). These different algorithms will be used in chapter 8 for the processing of satellite images: non smoothing interpolation for instantaneous cloud mask determination (section 8.7), motion estimation for METEOSAT time interpolation (section 8.8).

7.3.2 Top down Bayesian analysis as a general image analysis tool

In this section a mathematical definition of top down Bayesian image analysis is given.

Consider a multiband input image $\vec{I}$ with height n, width m and p bands (see left part of figure figure 7.7), as described by equation 7.12.

$$\vec{I}(i,j) = \begin{bmatrix} i_1(i,j) \\ \vdots \\ i_k(i,j) \\ \vdots \\ i_p(i,j) \end{bmatrix} \qquad \begin{matrix} i = 1,\ldots,n \\ j = 1,\ldots,m \end{matrix} \tag{7.12}$$

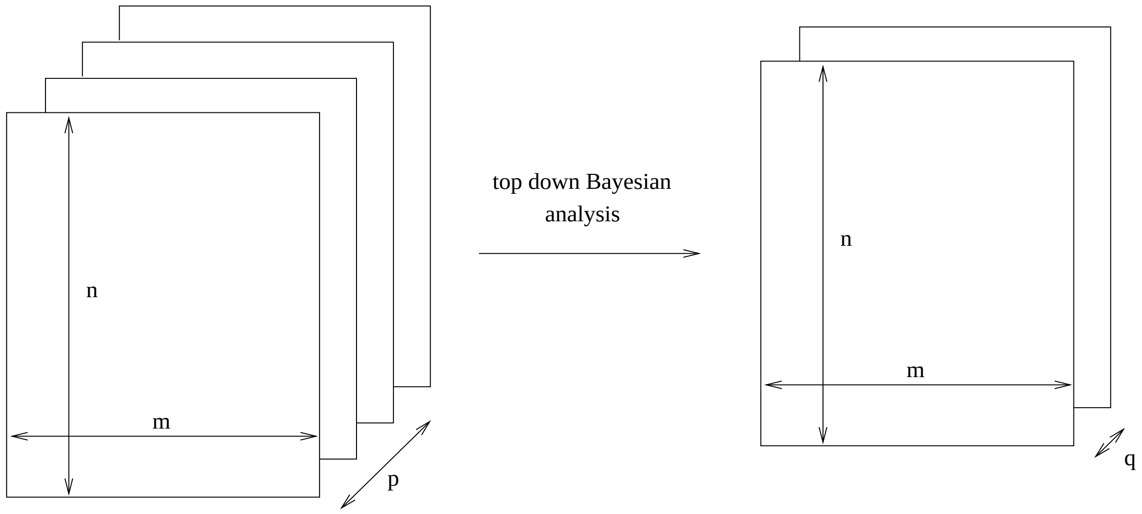

Figure 7.7: General input/output configuration of a top down Bayesian analysis. Left: Multiband input image with width n, height m and p bands. Right: Multi band output image with width n, height m and q bands.

A *segment* $S_s(i_c, j_c)$ with linear size s and top left corner (i_c,j_c) is defined as (see left part of figure 7.8)

$$S_s(i_c, j_c) = \{\vec{I}(i,j) | i_c \leq i < i_c + s, j_c \leq j < j_c + s\} \tag{7.13}$$

A *grid* $G_s(i_g, j_g, N_g, M_g)$ with segment size s, top left corner (i_g,j_g), height N_g and width M_g is defined as (see middle part of figure 7.8)

$$G_s(i_g, j_g, N_g, M_g) = \{S_s(i_g + (k_i - 1)s, j_g + (k_j - 1)s) | 1 \leq k_i \leq N_g, 1 \leq k_j \leq M_g\} \tag{7.14}$$

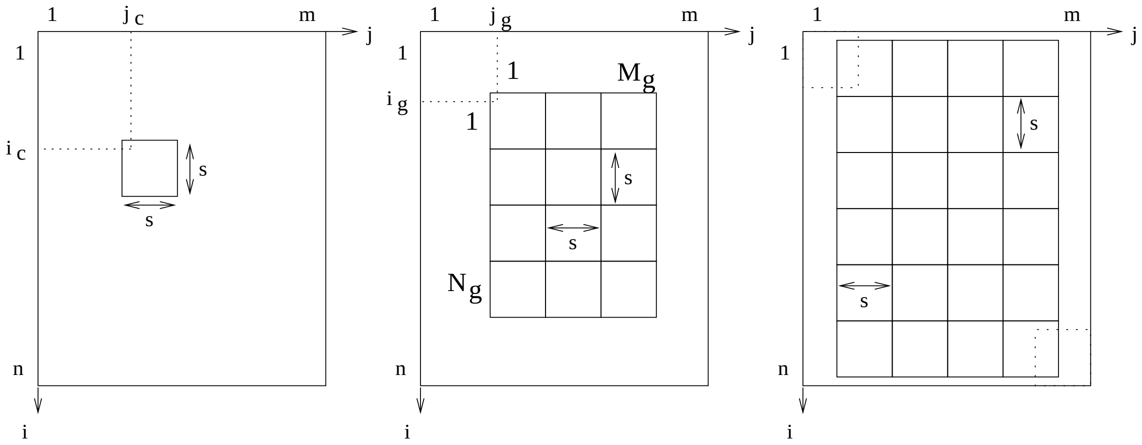

Figure 7.8: Definition of segment and grids in a rectangular image with width m and height n. Left: segment $S_s(i_c, j_c)$ with linear size s and top left corner (i_c, j_c). Middle: grid $G_s(i_g, j_g, N_g, M_g)$ with segment size s, top left corner (i_g, j_g), height N_g and width M_g. Right: centred grid G_s^c with segment size s.

The bottom right point of $G_s(i_g, j_g, N_g, M_g)$ is $(i_g + N_g s - 1, j_g + M_g s - 1)$

The *centred grid* G_s^c with segment size s is defined as the grid with maximal size that fits in the image and that is maximally centred (see right part of figure 7.8).

$$\begin{array}{c} G_s^c = G_s(i_g, j_g, N_g, M_g) \\ with \\ (1,1) \leq (i_g, j_g) < (s, s) \\ (n - s + 1, m - s + 1) < (i_g + N_g s - 1, j_g + M_g s - 1) \leq (n, m) \\ (0,0) \leq (i_g - 1, j_g - 1) - ((n, m) - (i_g + N_g s - 1, j_g + M_g s - 1)) \leq (1,1) \end{array} \quad (7.15)$$

The first inequality of equation 7.15 means that the top and left borders between the centred grid G_s^c and the image $\vec{I}$ (see right part of figure 7.8) are smaller than s. The second inequality means that the bottom and right borders are smaller than s. The third inequality means that the grid is maximally centred in the image.

A top down Bayesian analysis (see figure 7.7) produces an output image $\vec{O}$ with height n, width m and q bands (see right part of figure 7.7), as described by equation 7.16

$$\vec{O}(i,j) = \begin{bmatrix} o_1(i,j) \\ \vdots \\ o_q(i,j) \end{bmatrix} \qquad \begin{array}{l} i = 1, \ldots, n \\ j = 1, \ldots, m \end{array} \quad (7.16)$$

The input image $\vec{O}$ is obtained by analysing the input image $\vec{I}$ iteratively on centred grids (see figure 7.9) $G_{s_{ri}}^c$, given by equation 7.17.

$$G_{s_{ri}}^c = G_{s_{ri}}(i_{g,ri}, j_{g,ri}, N_{g,ri}, M_{g,ri}) \quad (7.17)$$

The segment sizes s_{ri} of $G_{s_{ri}}^c$ are iteratively halved, as described by equation 7.18.

$$s_{ri} = 2^{RI-ri} \quad ri = 0, 1, \ldots, RI \quad (7.18)$$

ri is the iteration counter, $s_{RI} = 2^{RI}$ is the start segment size, the end segment size is 1, the number of iterations is RI+1.

For every iteration an intermediate output image $\vec{O}_{ri}$ with height $N_{g,ri}$, width $M_{g,ri}$ and q bands is generated (see figure 7.9), as described by equation 7.19.

$$\vec{O}_{ri}(i,j) = \begin{bmatrix} o_1(i,j) \\ \vdots \\ o_q(i,j) \end{bmatrix} \qquad \begin{array}{l} i = 1, \ldots, N_{g,ri} \\ j = 1, \ldots, M_{g,ri} \end{array} \quad (7.19)$$

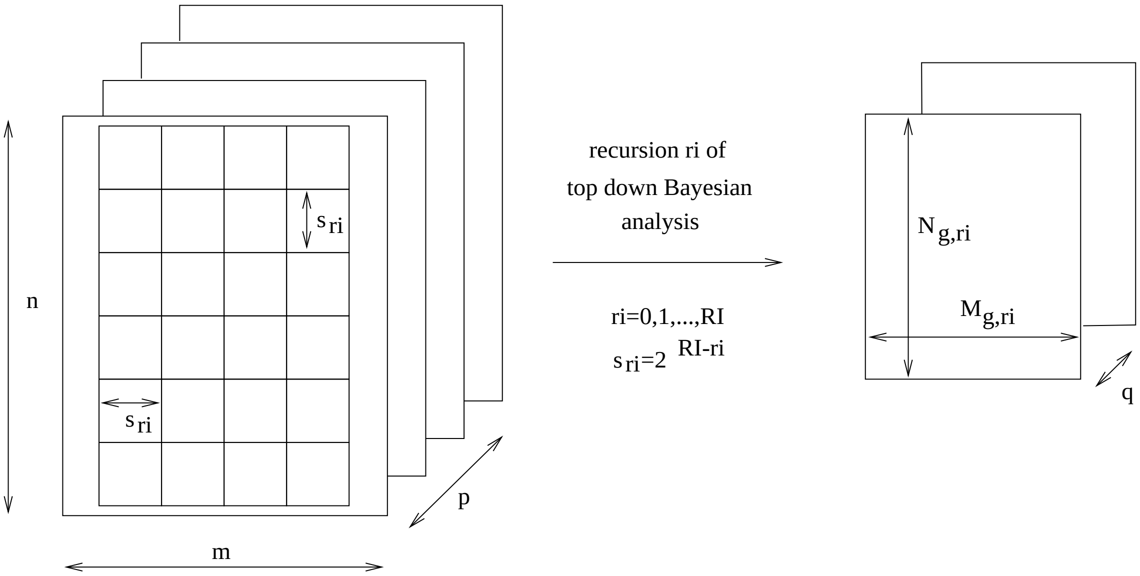

Figure 7.9: ri'th recursion in top down Bayesian analysis. The ri'th recursion analyses the multi-band input image on a centred square grid with segment size $s_{ri} = 2^{RI-ri}$. The recursion starts at $ri = 0$ and ends with $ri = RI$ (when segments become pixels).

The vector $\vec{O_{ri}}(i_{ri}, j_{ri})$ contains the analysis for the segment $S_{s_{ri}}(i_c(i), j_c(j))$, given by equation 7.20.

$$S_{s_{ri}}(i_c(i), j_c(j)) = S_{s_{ri}}(i_{g,ri} + (i-1)s_{ri}, j_{g,ri} + (j-1)s_{ri}) \tag{7.20}$$

The iteration starts (ri=0) by taking the maximum likelihood estimation for $\vec{O}_0(i,j)$, as described by equation 7.21, i.e. for the analysis of the segment, one takes the parameter vector which corresponds to the most probable realization of the segment.

$$\vec{O}_0(i,j) = \underset{\vec{O}_0}{argmax} \quad P(S_{s_0}(i_c(i), j_c(j))||\vec{O}_0) \qquad \begin{array}{l} i = 1, \ldots, N_{g,0} \\ j = 1, \ldots, M_{g,0} \end{array} \tag{7.21}$$

For every consecutive ($ri > 0$) iteration, this analysis is refined by taking the Bayesian estimation for $\vec{O}_{ri}(i,j)$, as described by equation 7.22, i.e. the most probable parameter vector for the segment $S_{s_{ri}}(i_c(i), j_c(j))$ is taken as analysis result vector for the segment.

$$\begin{aligned} \vec{O}_{ri}(i,j) &= \underset{\vec{O}_{ri}}{argmax} \quad P(\vec{O}_{ri}||S_{s_{ri}}(i_c(i), j_c(j))) \\ &= \underset{\vec{O}_{ri}}{argmax} \quad P(S_{s_{ri}}(i_c(i), j_c(j))||\vec{O}_{ri})P(\vec{O_{ri}}) \end{aligned} \qquad \begin{array}{l} i = 1, \ldots, N_{g,ri} \\ j = 1, \ldots, M_{g,ri} \end{array} \tag{7.22}$$

The Bayesian estimations $\vec{O}_{ri}(i,j)$, obtained by maximising the product of the a posteriori probability $P(S_{s_{ri}}(i_c(i), j_c(j))||\vec{O}_{ri})$ and the prior probability $P(\vec{O}_{ri})$ are a refinement of the previously obtained $\vec{O}_{ri-1}(i,j)$. Let $\vec{O}_{ri,p}(i,j)$ be the linear interpolated version of $\vec{O}_{ri-1}(i,j)$, described by equation 7.23, then the prior probability $P(\vec{O_{ri}}(i,j))$ is taken according to equation 7.24.

$$\begin{array}{cc} \vec{O}_{ri-1}(i,j) & \begin{array}{l} i = 1, \ldots, N_{g,ri-1} \\ j = 1, \ldots, M_{g,ri-1} \end{array} \\ \Downarrow & interpolation \\ \vec{O}_{ri,p}(i,j) & \begin{array}{l} i = 1, \ldots, N_{g,ri} \\ j = 1, \ldots, M_{g,ri} \end{array} \end{array} \tag{7.23}$$

$$P(\vec{O_{ri}}(i,j)) = P(\vec{O_{ri}}(i,j)||\vec{O}_{ri,p}(i,j)) \qquad \begin{array}{l} i = 1, \ldots, N_{g,ri} \\ j = 1, \ldots, M_{g,ri} \end{array} \tag{7.24}$$

The expression 7.24 of the prior probability can be substituted in equation 7.22, yielding the general recursion formula 7.25.

$$\vec{O}_{ri}(i,j) = \underset{\vec{O}_{ri}}{argmax} \quad P(S_{s_{ri}}(i_c(i), j_c(j)) \| \vec{O}_{ri}) P(\vec{O}_{ri}(i,j) \| \vec{O}_{ri,p}(i,j)) \qquad \begin{array}{l} i = 1, \ldots, N_{g,ri} \\ j = 1, \ldots, M_{g,ri} \end{array} \tag{7.25}$$

At the last iteration ($ri = RI$) the segment size becomes one (s_{RI}=1), every individual pixel becomes a segment ($N_{g,RI} = n; M_{g,RI} = m$) and the intermediate output becomes the final output.

$$\vec{O}(i,j) = \vec{O}_{RI}(i,j) \qquad \begin{array}{l} i = 1, \ldots, n \\ j = 1, \ldots, m \end{array} \tag{7.26}$$

This concludes the definition of the general top down Bayesian image analysis. A specific image analysis is obtained by describing explicitly the content of the input and output band images, and by making explicit assumptions about the distributions $P(S_{s_{ri}} \| \vec{O}_{ri})$ and $P(\vec{O}_{ri} \| \vec{O}_{ri,p})$. This will be done in the next sections for the specific cases of interpolation and motion estimation.

7.4 Non smoothing image interpolation

Image interpolation is a technique were from known parts of an image, unknown parts of the image are tentatively reconstructed.

In commonly used, parametric, interpolation techniques, the parameters of a given analytical function of the image coordinates (e.g. a polynomial) are determined (fitted) so that the analytic function gives a close approximation of the known parts of the image. The fitted analytic function can then be used as an approximation for the unknown parts of the image too.

Normally, in order to have a numerically stable fit, the number of fitted parameters is considerably lower than the number of approximated (known) image pixels. As a result, not all of the spatial variation of the known image pixels can be reproduced by the fitted function, in other words the fitting introduces some *smoothing* of the known pixel values.

In this work, thanks to the application of the top down Bayesian image analysis framework, introduced in the previous section, a novel image interpolation method is developed. This novel method has the advantage of being non parametric and non smoothing. Moreover, completely independent interpolation of different image classes, e.g. ocean parts and land parts, is integrated in the interpolation. The known pixels can be distributed in an arbitrary way over the image, i.e. random sampling is allowed.

The novel non smoothing image interpolation technique is applied in section 8.7 in order to obtain spatially coherent clear sky images.

In this section a mathematical description of the non smoothing image interpolation technique is given.

7.4.1 Algorithm description card

name algorithm	non smoothing interpolation
technical novelty	non parametric non smoothing *and* numerically stable random sampling classified interpolation
novel application	METEOSAT instantaneous clear sky count determination (section 8.7)
references	[DCC96]

Table 7.3: Algorithm card for non smoothing interpolation algorithm

7.4.2 Problem definition

For the case of non smoothing interpolation consider a grey level input image $I(i,j)$. The pixels are classified in q classes.

$$\text{class of pixel}(i,j) = C(i,j) \in \{1,\ldots,q\} \tag{7.27}$$

There are known and unknown pixel values indicated by a mask image $M(i,j)$

$$\begin{array}{ll} M(i,j) = 0 \Leftrightarrow I(i,j) \text{ unknown} & i = 1,\ldots,n \\ M(i,j) = 1 \Leftrightarrow I(i,j) \text{ known} & j = 1,\ldots,m \end{array} \tag{7.28}$$

As output one wants the interpolated pixel values $o_c(i,j)$ for all classes c and for all pixels (i,j), as given by equation 7.29, with the restriction 7.30 that for a known pixel, the interpolated value for the class of the pixel must be exactly (non smoothing) equal to the known pixel value.

$$\vec{O}(i,j) = \begin{bmatrix} o_1(i,j) \\ \vdots \\ o_c(i,j) \\ \vdots \\ o_q(i,j) \end{bmatrix} \quad \begin{array}{c} o_c(i,j)\text{=interpolated value for class } C \\ \text{for pixel } (i,j) \end{array} \tag{7.29}$$

$$o_c(i,j) = I(i,j) \quad \text{if } M(i,j)\text{=1} \tag{7.30}$$

7.4.3 Solution

Non smoothing interpolation can be obtained by a top down analysis (see figure 7.10) where the intermediate output $\vec{O_{ri}}(i,j)$, described by equation 7.31, contains the estimated mean grey values per class and per segment $S_{s_{ri}}(i_c(i), j_c(j))$.

$$\vec{O_{ri}}(i,j) = \begin{bmatrix} o_1(i,j) \\ \vdots \\ o_c(i,j) \\ \vdots \\ o_q(i,j) \end{bmatrix} \quad \begin{array}{l} i = 1,\ldots,N_{g,ri} \\ j = 1,\ldots,M_{g,ri} \end{array} \tag{7.31}$$

Let S_c contain the known pixels of class c of segment S

$$S_c = \{\vec{I}(i,j) | M(i,j) = 1, C(i,j) = c, \vec{I}(i,j) \in S\} \tag{7.32}$$

It is supposed that the realization of the segment pixel values for the different classes are statistically independent, as described by equation 7.33, and that the different pixel values of one class are statistically independent realizations of the same Gaussian distribution 7.34, in which $\sigma^2_{c,k}$ is the variance observed from the k known pixel values in S_c.

$$P(S\|O) = \prod_{c \in \{1,\ldots,q\}} P(S_c\|o_c) \tag{7.33}$$

$$P(S_c\|o_c) = \prod_{I(i,j) \in S_c} \frac{1}{\sqrt{2\pi\sigma^2_{c,k}}} \exp\left(-\frac{(I(i,j)-o_c)^2}{2\sigma^2_{c,k}}\right) \tag{7.34}$$

For the start of the iteration, the equation 7.21 becomes equation 7.35, in which k is the number of pixel values in S_c.

$$\begin{aligned} o_c &= \underset{o_c}{argmin} \sum_{I(i,j) \in S_c} (I(i,j) - o_c)^2 \\ &= \frac{1}{k} \sum_{I(i,j) \in S_c} I(i,j) \quad \equiv o_{c,m} \end{aligned} \qquad c = 1,\ldots,q \tag{7.35}$$

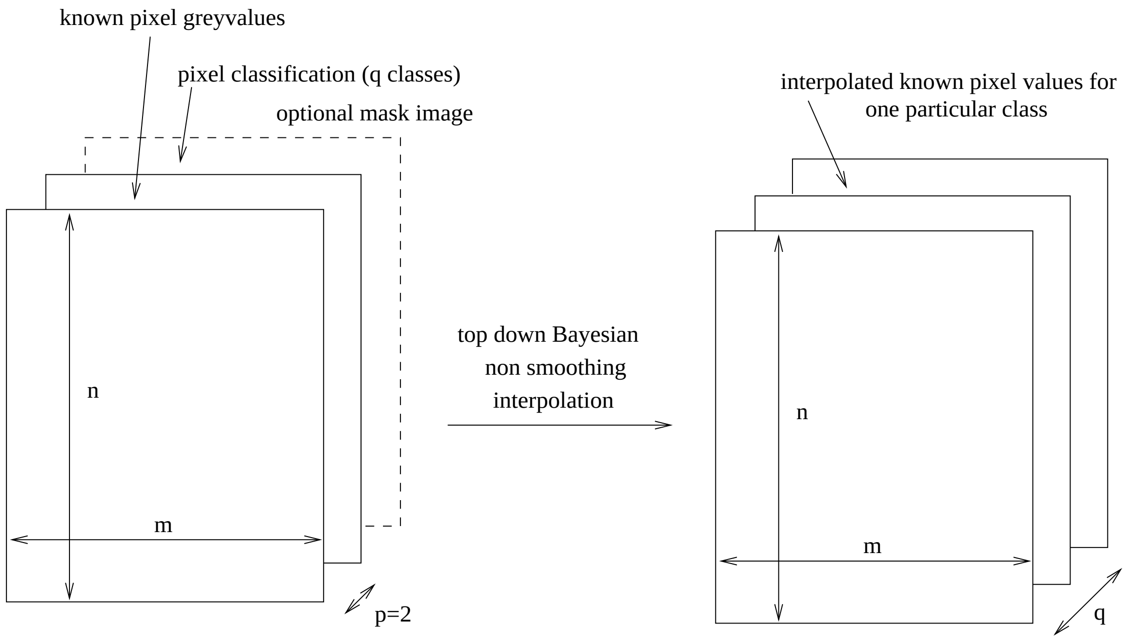

Figure 7.10: Non smoothing interpolation obtained by a top down Bayesian analysis. Left: Two or three band input image, consisting of grey level input image, class image and optionally a mask image. Right: q band output image. q is the number of classes.

The optimal estimation for o_c is the observed mean value $o_{c,m}$ of the known pixels of the class c over the segment.

For the prior probability equation 7.24, one also assumes stochastic independence between classes, described by equation 7.36 (in which $o_{c,p}$ is defined as in equation 7.23) and Gaussian distributions 7.37.

$$P(O\|O_p) = \prod_{c \in \{1,\ldots,q\}} P(o_c\|o_{c,p}) \tag{7.36}$$

$$P(o_c\|o_{c,p}) = \frac{1}{\sqrt{2\pi\sigma_{c,p}^2}} \exp\left(\frac{-(o_c - o_{c,p})^2}{2\sigma_{c,p}^2}\right) \tag{7.37}$$

$\sigma_{c,p}$ is estimated as the difference between the prior estimation for the mean $o_{c,p}$ and the measured mean $o_{c,m}$

$$\sigma_{c,p} = |o_{c,p} - o_{c,m}| \tag{7.38}$$

The specific expressions for the a posteriori probability (equation 7.34) and for the prior probability (equation 7.37) for the specific case of non smoothing interpolation can be substituted in the general recursion formula 7.25, yielding the specific recursion formula for non smoothing interpolation. The substitution for the c'th component of equation 7.25 becomes equation 7.39 (to simplify the notations the recursion index ri and the output pixel index (i,j) are omitted).

$$o_c = \underset{o_c}{argmax} \quad P(S\|o_c)P(o_c\|o_{c,p})$$
$$= \underset{o_c}{argmax} \left(\left(\prod_{I(i,j) \in S_c} \exp\left(-(I(i,j) - o_c)^2/(2\sigma_{c,k}^2)\right)\right) \exp\left(-(o_c - o_{c,p})^2/(2\sigma_{c,p}^2)\right)\right) \tag{7.39}$$

Equation 7.39 can be worked out as

$$o_c = \frac{o_{c,m} + \lambda o_{c,p}}{1+\lambda} \text{ with } \lambda = \left(k\sigma_{c,k}^2/\sigma_{c,p}^2\right) \tag{7.40}$$

$\sigma_{c,k}$ is the maximum likelihood estimation of the standard deviation of the known pixels for class c

$$\sigma_{c,k} = \sqrt{(1/k) \sum_{I(i,j) \in S_c} (I(i,j) - o_{c,m})^2} \quad c = 1, \ldots, q \tag{7.41}$$

One gets in particular

$$k = 1 \quad \Rightarrow \quad \sigma_{c,k} = 0, \lambda = 0, o_c = o_{c,m} \tag{7.42}$$

which ensures that equation 7.30 is valid.

7.4.4 Application

The non smoothing interpolation which has been described here, will be applied in section 8.7 (see equation 8.43 and 8.44) for the determination of spatially coherent clear sky images from the cloud mask after morphological filtering (See also the box "Top down image interpolation" in figure 7.1. The cloud mask which defines the known part of the clear sky image (see equation 8.43) is called "multi spectral VIS cloud mask" in figure 7.1. The final resulting spatially coherent clear sky image is called "VIS instantaneous clear sky image" in figure 7.1.).

7.5 Motion estimation

Motion interpolation is a technique which, from two or more consecutive images of a given set of objects, estimates the motion vector of moving objects.

For the particular case of METEOSAT images, the considered moving "objects" are moving cloud fields. Classically, low resolution motion fields, i.e. motion fields applicable for image segments, are derived by the ESOC/MIEC or EUMETSAT/MPEF cloud motion wind extraction.

In this work, by application of the previously introduced top down Bayesian image analysis framework, a novel motion estimation technique is developed, which yields very high resolution motion vectors (applicable to individual pixels).[3]

The novel motion estimation technique will be applied in section 8.8 for the time interpolation of METEOSAT images, which is necessary to obtain radiation budget term estimates with maximal time resolution.

In this section a mathematical description of the novel motion estimation technique is given.

7.5.1 Algorithm description card

name algorithm	motion estimation
technical novelty	pixel wise motion estimation spatially coherent *and* scene-adapted motion field
novel application	time interpolation (section 8.8)
references	[DCC96]

Table 7.4: Algorithm card for motion estimation algorithm

7.5.2 Problem definition

In the case of motion estimation, one has given a two band input image $\vec{I}$, described by equation by equation 7.43, containing image values $i_1(i,j)$ at time t_1 and image values $i_2(i,j)$ at time t_2.

$$\vec{I}(i,j) = \begin{bmatrix} i_1(i,j) \\ i_2(i,j) \end{bmatrix} \quad \begin{matrix} i = 1, \ldots, n \\ j = 1, \ldots, m \end{matrix} \tag{7.43}$$

[3] In EUMETSAT/MPEF context cloud motion winds derived from segments of 32x32 pixels are called "low resolution", cloud motion winds derived from segments of 16x16 pixels are called "high resolution".

For a given time t between t_1 and t_2, described by equation 7.44[4], one wants to obtain the two band output image $\vec{O}$, described by equation 7.45, where $o_1(i,j)$ is the first component (top to bottom, i direction) of the displacement and $o_2(i,j)$ is the second component (left to right, j direction) of the displacement from i_1 to i_2 measured at time t and at location (i,j).

$$t = (1-f) * t_1 + f * t2 \quad 0 \leq f < 1 \tag{7.44}$$

$$\vec{O}(i,j) = \begin{bmatrix} o_1(i,j) \\ o_2(i,j) \end{bmatrix} \quad \begin{array}{c} i = 1, \ldots, n \\ j = 1, \ldots, m \end{array} \tag{7.45}$$

7.5.3 Solution

The problem of motion estimation can be solved by a top down Bayesian analysis (see figure 7.11) where the intermediate output image $\vec{O}_{ri}$, described by equation 7.46, contains the estimated mean motion components for segment $S_{s_{ri}}(i_c(i), j_c(j))$ at time t.

$$\vec{O_{ri}}(i,j) = \begin{bmatrix} o_1(i,j) \\ o_2(i,j) \end{bmatrix} \quad \begin{array}{c} i = 1, \ldots, N_{g,ri} \\ j = 1, \ldots, M_{g,ri} \end{array} \tag{7.46}$$

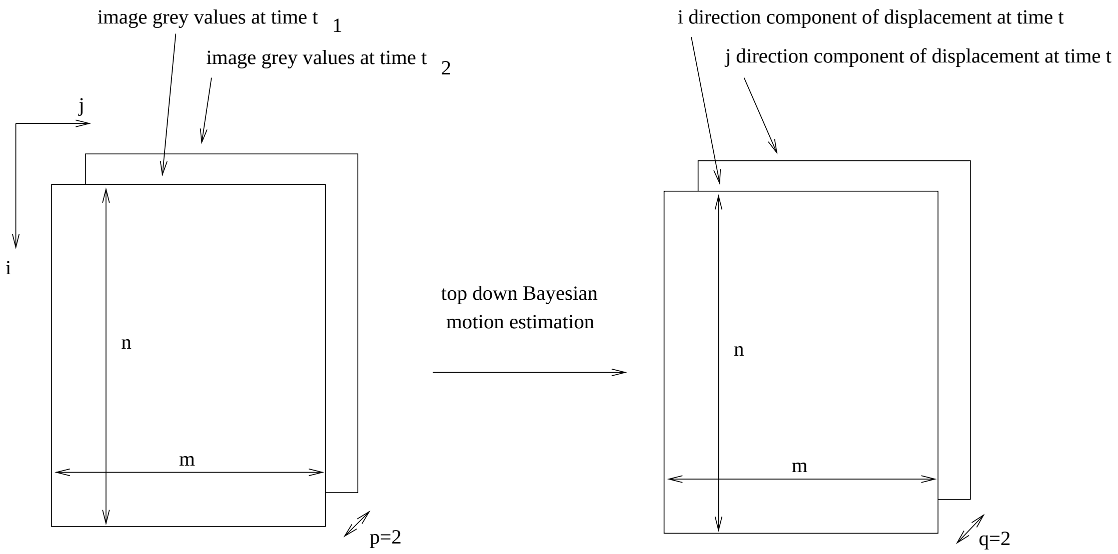

Figure 7.11: Motion estimation obtained by a top down Bayesian analysis. Left: Two band input image, consisting of grey value input images at times t_1 and t_2. Right: Two band output image, containing the i and j direction components of the displacement at time t between grey value input images at t_1 and t_2.

It is supposed that for every segment $S_{s_{ri}}$ at time t the image deformation from t_1 to t_2 can be modelled as a rigid motion with addition of white Gaussian noise as described by equations 7.47 and 7.48.

$$i_1(i - fo_1, j - fo_2) = i_2(i + (1-f)o_1, j + (1-f)o_2) + n(i,j) \tag{7.47}$$

$$n(i,j) \sim N(0, \sigma_n^2) \tag{7.48}$$

It is supposed that $n(i,j)$ and $n(i',j')$ are statistically independent if $(i,j) \neq ((i',j')$ so that equation 7.49 is valid, where P_n is the Gaussian noise distribution.

[4]where * denotes multiplication

$$
\begin{aligned}
&P(S\|(o_1,o_2)) = \\
&\prod_{(i,j)\in S} P_n(i_1(i-fo_1,j-fo_2)-i_2(i+(1-f)o_1,j+(1-f)o_2)) \\
&= \prod_{(i,j)\in S} \left(1/\sqrt{2\pi\sigma_n^2}\right)\exp\left(-(i_1(i-fo_1,j-fo_2)-i_2(i+(1-f)o_1,j+(1-f)o_2))^2/(2\sigma_n^2)\right)
\end{aligned}
\tag{7.49}
$$

For the start of the iteration, equation 7.21 becomes equation 7.50 with $D_S(o_1, o_2)$ given by equation 7.51.

$$
(o_1,o_2) = \underset{(o_1,o_2)}{argmin} \quad D_S(o_1,o_2) \tag{7.50}
$$

$$
\begin{aligned}
&D_S(o_1,o_2) = \\
&\sum_{(i,j)\in S} (i_1(i-fo_1,j-fo_2)-i_2(i+(1-f)o_1,j+(1-f)o_2))^2
\end{aligned}
\tag{7.51}
$$

$D_S(o_1, o_2)$ is the Euclidean distance between i_1 and i_2 for segment S at time t. This theoretical deduction of Euclidean distance matching agrees well with the experimental finding that among various matching techniques, the Euclidean distance matching has the best performances [DVAC95], as will be demonstrated in section 9.2.

For the prior probability equation 7.24, the Gaussian distribution 7.52 is assumed where $(o_{1,p}, o_{2,p})$ is the a priori estimation for (o_1, o_2).

$$
P((o_1,o_2)\|(o_{1,p},o_{2,p}) = \left(\frac{1}{\sqrt{2\pi\sigma_p^2}}\right)^2 exp\frac{-((o_1-o_{1,p})^2+(o_2-o_{2,p})^2)}{2\sigma_p^2} \tag{7.52}
$$

Equation 7.22 becomes equation 7.53 with the function to be minimised $F(o_1, o_2)$ given by equation 7.54 and with the regularisation parameter λ given by equation 7.55.

$$
(o_1,o_2) = \underset{(o_1,o_2)}{argmin} \quad F(o_1,o_2) \tag{7.53}
$$

$$
F(o_1,o_2) = D_S(o_1,o_2) + \lambda((o_1-o_{1,p})^2+(o_2-o_{2,p})^2) \tag{7.54}
$$

$$
\lambda = \frac{\sigma_n^2}{\sigma_p^2} \tag{7.55}
$$

One takes equation 7.56 with k equal to the number of pixels in a segment.

$$
\sigma_n^2 = \frac{D_S(o_{1,p},o_{2,p})}{k} \tag{7.56}
$$

This means the allowed typical image deformation due to Gaussian noise $(k\sigma_n^2)$ is equal to the Euclidean distance for the prior estimation.

The allowed deviation from the prior estimation is controlled by the parameter σ_p. This parameter is chosen such that the absolute maximum deviation from the prior estimation is half the segment size s_{ri} in both i and j direction. For this absolute maximum deviation, one has

$$
\begin{aligned}
F(o_1,o_2) &= D_S(o_1,o_2) + \lambda((o_1-o_{1,p})^2+(o_2-o_{2,p})^2) \\
&\le \lambda((o_1-o_{1,p})^2+(o_2-o_{2,p})^2) = \lambda 2(s_{ri}/2)^2
\end{aligned}
\tag{7.57}
$$

This deviation can be made the maximum allowed, by imposing the condition

$$
\lambda 2(s_{ri}/2)^2 \le F(o_{1,p},o_{2,p}) = D_S(o_{1,p},o_{2,p}) \tag{7.58}
$$

The highest λ is chosen for which condition 7.58 is always satisfied, yielding equations 7.59 and 7.60, and, after substitution of equations 7.55 and 7.56, equation 7.61.

$$\lambda 2(s_{ri}/2)^2 = D_S(o_{1,p}, o_{2,p}) \tag{7.59}$$

$$\lambda = \frac{D_S(o_{1,p}, o_{2,p})}{2(s_{ri}/2)^2} \tag{7.60}$$

$$\sigma_p^2 = \frac{2(s_{ri}/2)^2}{k} \tag{7.61}$$

7.5.4 Application

The motion estimation technique which has been described here, will be applied in section 8.8 for METEOSAT time interpolation (See equation 8.47; see also the blocks "Motion estimation" and "Motion time interpolation" of figure 7.2.).

7.6 Wavelet compression

Wavelet compression is a technique used for the compact representation of images.

Classically lossy wavelet compression algorithms for cartesian images are available (e.g. from [ABMD92]). Lossy compression algorithms are characterised by a non perfect reconstruction (decompression) of the original image from its compact representation (compressed version).

In this work, two extensions to classical, lossy wavelet compression algorithms for cartesian images are developed:

- A *lossless* wavelet transform for cartesian images, which allows the construction of a lossless wavelet compression algorithm, is developed.
- A lossless wavelet transform for data *sampled on a spherical surface*, which allows the construction of a lossless wavelet compression algorithm for spherically sampled data, is developed.

These novel techniques will be applied in sections 8.16 and 8.17 for the lossless archival and the lossy distribution of METEOSAT derived radiation budget terms. Moreover, the potential interest for assimilation purposes of spherical sampling of radiation budget data (or remote sensing data on a sphere in general) and of the associated lossless spherical wavelet transform, will be discussed.

In the sections 7.7 and 7.8, a mathematical description of the novel developed lossless wavelet transforms will be given.

7.7 Lossless wavelet compression of cartesian images

7.7.1 Algorithm description card

name algorithm	lossless cartesian compression
technical novelty	lossless multi resolution transform compression
novel application	lossless archival of radiation budget results (section 8.8)
references	[DC97], [ABMD92], [Swe94], [Mal89]

Table 7.5: Algorithm card for cartesian lossless compression algorithm

7.7.2 Introduction

Signal compression can be obtained by wavelet transformation of integer input data followed by quantification and coding. As the quantification is usually lossy, the whole compression/decompression scheme is lossy too. A critical wavelet coefficient quantification, i.e. the coarsest quantification which allows perfect reconstruction, is defined. This is demonstrated for the Haar transform and for arbitrarily smooth wavelet transforms derived from it. The new integer wavelet transform allows implementation of multiresolution subband compression schemes in which the decompressed data are gradually refined, retaining the option of perfect reconstruction.

First the lossless transform based on Haar wavelets is defined, then this lossless transform is extended to wavelets with the l lowest order moments equal to zero. The corresponding perfect reconstruction filter banks (PRFB's) are l-th order regular PRFB's. High order regularity ensures good compression results and avoids blocking effects during progressive decompression [ABMD92].

7.7.3 Definitions

In this section the general 1D Perfect Reconstruction Filter Bank (PRFB) is defined. The notations of [ABMD92] are used. The general 1D PRFB is given in figure 7.12.

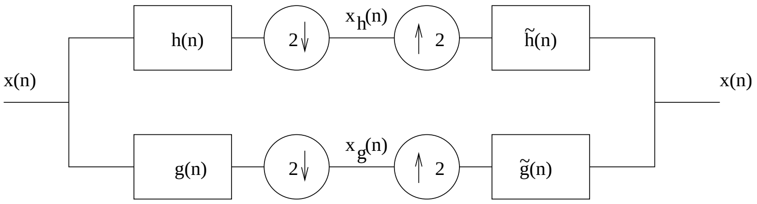

Figure 7.12: General 1D PRFB. Left: The forward (analysis) part of the PRFB which transforms the input $x(n)$ into the low-pass coefficients $x_h(n)$ and the high-pass coefficients $x_g(n)$. Right: The inverse (synthesis) part of the PRFB which reconstructs $x(n)$ from $x_h(n)$ and $x_g(n)$.

The perfect reconstruction conditions assure that the input $x(n)$ of the PRFB is perfectly reconstructed at the output of the PRFB. They are given in their most general form (this will be proven in the next paragraph) by equations 7.62 to 7.65.

$$\sum_n h(-n)\tilde{h}(n+2k) = \delta_{k,0} \tag{7.62}$$

$$\sum_n h(-n)\tilde{g}(n+2k) = 0 \tag{7.63}$$

$$\sum_n g(-n)\tilde{h}(n+2k) = 0 \tag{7.64}$$

$$\sum_n g(-n)\tilde{g}(n+2k) = \delta_{k,0} \tag{7.65}$$

To allow easy filter design, one can impose the extra conditions 7.66 and 7.67

$$\tilde{g}(n) = (-1)^n h(n-1) \tag{7.66}$$

$$g(n) = (-1)^n \tilde{h}(n+1) \tag{7.67}$$

With the use of the extra condition 7.66, the perfect reconstruction condition 7.63 becomes automatically satisfied.

$$\begin{aligned}
&\textstyle\sum_n h(-n)\tilde{g}(n+2k) = \\
&\textstyle\sum_n h(-n)(-1)^{n+2k} h(n+2k-1) \\
&\stackrel{n'=n+k}{=} \textstyle\sum_{n'=-\infty}^{\infty} h(-n'+k)(-1)^{n'+k} h(n'+k-1) \\
&= \textstyle\sum_{n'=-\infty}^{0} \cdots + \sum_{n'=1}^{\infty} \cdots \\
&\stackrel{n''=-n'+1}{=} \textstyle\sum_{n'=-\infty}^{0} \cdots + \sum_{n''=-\infty}^{0} h(n''+k-1)(-1)^{1-n''+k} h(-n''+k) \\
&= \textstyle\sum_{n'=-\infty}^{0} \cdots - \sum_{n''=-\infty}^{0} \cdots \\
&= 0
\end{aligned} \tag{7.68}$$

Analogously, with the use of the extra condition 7.67, the perfect reconstruction condition 7.64 becomes automatically satisfied.

$$\begin{array}{c} \sum_n g(-n)\tilde{h}(n+2k) = \\ \sum_n (-1)^{-n}\tilde{h}(-n+1)\tilde{h}(n+2k) \\ = \dots \\ = 0 \end{array} \tag{7.69}$$

With the use of both extra conditions 7.66 and 7.67, the perfect reconstruction condition 7.65 becomes identical to the perfect reconstruction condition 7.62, since the left hand parts of these perfect reconstruction conditions become identical.

$$\begin{array}{c} \sum_n g(-n)\tilde{g}(n+2k) = \\ \sum_n (-1)^{-n}\tilde{h}(-n+1)(-1)^{n+2k}h(n+2k-1) \\ \stackrel{n'=-(n+2k-1)}{=} \sum_n' \tilde{h}(n'+2k)h(-n') \end{array} \tag{7.70}$$

A PRFB is useful for compression if the representation $x_h(n)$,$x_g(n)$ is potentially more compact than the representation $x(n)$. For "natural", i.e. mostly smoothly varying, signals $x(n)$ this can be assured by making $h(n)$ and $g(n)$ low pass and high pass filters with passbands which cover complementary halves of the spectrum. As minimal requirement for good compression performance, the conditions 7.71 to 7.74 are imposed.

$$\sum_n h(n) = \sqrt{2} \tag{7.71}$$

$$\sum_n \tilde{h}(n) = \sqrt{2} \tag{7.72}$$

$$\sum_n (-1)^n h(n) = 0 \tag{7.73}$$

$$\sum_n (-1)^n \tilde{h}(n) = 0 \tag{7.74}$$

Conditions 7.71 to 7.74 are necessary to make $h(n)$, $\tilde{h}(n)$ regular low pass filters and $g(n)$, $\tilde{g}(n)$ the associated high pass filters [ABMD92].

Even better compression performance can be obtained by imposing l-th order regularity on the high pass filter $g(n)$, as imposed by equation 7.75

$$\sum_{l'} n^{l'} g(n) = 0 \quad l' = 0, \dots, l \tag{7.75}$$

l-th order regularity of the high pass filter $g(n)$ assures that the high pass coefficients are exactly zero when polynomials with degree lower or equal to l are used as input $x(n)$ of the PRFB.

Note that equation 7.74, combined with equation 7.67, imposes 0'th order regularity on $g(n)$.

7.7.4 The PRFB as a linear transformation.

In this paragraph it is proven that equations 7.62 to 7.65 are the most general perfect reconstructions for the PRFB of figure 7.12.

The decomposition of $x(n)$ into the series $x_h(n)$ and $x_g(n)$ (see left part of figure 7.12) can be seen as the linear transformation 7.76.

$$Y_{tr} = AX_{tr} \tag{7.76}$$

with

$$Y_{tr} = \begin{bmatrix} \vdots \\ x_h(n) \\ x_g(n) \\ x_h(n+1) \\ x_g(n+1) \\ \vdots \end{bmatrix} \tag{7.77}$$

$$A = \begin{bmatrix} \ddots & & & & & & \\ \dots & h(0) & h(-1) & \dots & & & \\ \dots & g(0) & g(-1) & \dots & & & \\ & & \dots & h(0) & h(-1) & \dots & \\ & & \dots & g(0) & g(-1) & \dots & \\ & & & & & & \ddots \end{bmatrix} \tag{7.78}$$

$$X_{tr} = \begin{bmatrix} \vdots \\ x(2n) \\ x(2n+1) \\ x(2(n+1)) \\ x(2(n+1)+1) \\ \vdots \end{bmatrix} \tag{7.79}$$

The reconstruction of $x(n)$ from the series $x_h(n)$ and $x_g(n)$ (see right part of figure 7.12) can be seen as the linear transformation 7.80.

$$X_{tr} = BY_{tr} \tag{7.80}$$

with

$$B = \begin{bmatrix} \ddots & & & & & & \\ \dots & \tilde{h}(0) & \tilde{g}(0) & \dots & & & \\ \dots & \tilde{h}(1) & \tilde{g}(1) & \dots & & & \\ & & \dots & \tilde{h}(0) & \tilde{g}(0) & \dots & \\ & & \dots & \tilde{h}(1) & \tilde{g}(1) & \dots & \\ & & & & & & \ddots \end{bmatrix} \tag{7.81}$$

The perfect reconstruction becomes, from equations 7.76 and 7.80

$$AB = I_1 \tag{7.82}$$

with I_1 the unity matrix. After usage of the expressions 7.78 and 7.81, equation 7.82 becomes perfectly equivalent to the expressions 7.62 to 7.65.

7.7.5 Critical lossless quantification for the Haar PRFB.

One of the simplest 0-th order regular PRFB's is the Haar PRFB, with low pass filter coefficients $h(0) = h(-1) = 2^{-1/2}$, high-pass coefficients $g(0) = -g(-1) = 2^{-1/2}$ and all other $h(n), g(n) = 0$. After scaling of the Haar filter coefficients, one obtains (see figure 7.13):

$$\begin{bmatrix} m(n) \\ d(n) \end{bmatrix} = \begin{bmatrix} 1/2 & 1/2 \\ 1 & -1 \end{bmatrix} \begin{bmatrix} x(2n) \\ x(2n+1) \end{bmatrix} \tag{7.83}$$

The linear transformation of the stream $x(n)$ into the two streams $m(n)$ and $d(n)$ is decoupled into a set of independent 2x2 transformations 7.83. This 2x2 transformation is presented graphically in figure 7.15.

Coarse quantification generally introduces errors in a PRFB. Critical quantification is defined as the coarsest lossless quantification.

As $x(n)$ is a stream of integers, the possible values before the quantification step in figure 7.13 are given by the lattice $(x(2n), x(2n+1)) \in Z^2$, indicated by the circles in figure 7.15. The quantification step shown in figure 7.13 truncates $m(n)$ and $d(n)$ to their integer parts.

$$\begin{aligned} m_q(n) &= [m(n)] \\ d_q(n) &= [d(n)] = d(n) \end{aligned} \tag{7.84}$$

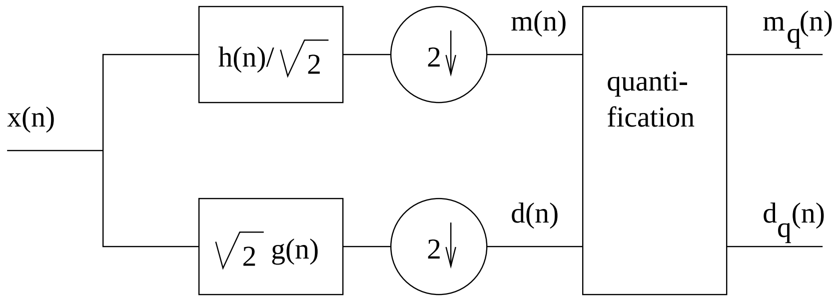

Figure 7.13: Forward integer Haar transform.

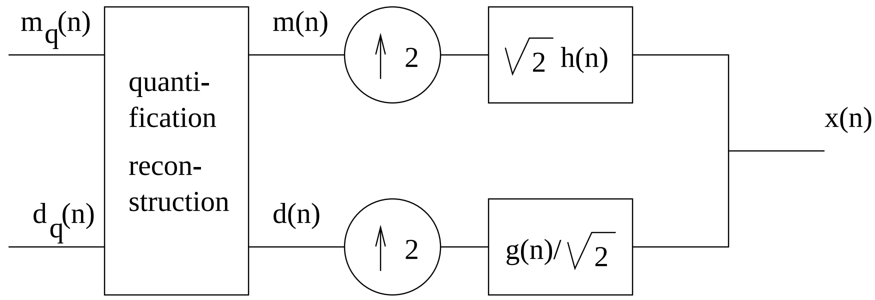

Figure 7.14: Inverse integer Haar transform.

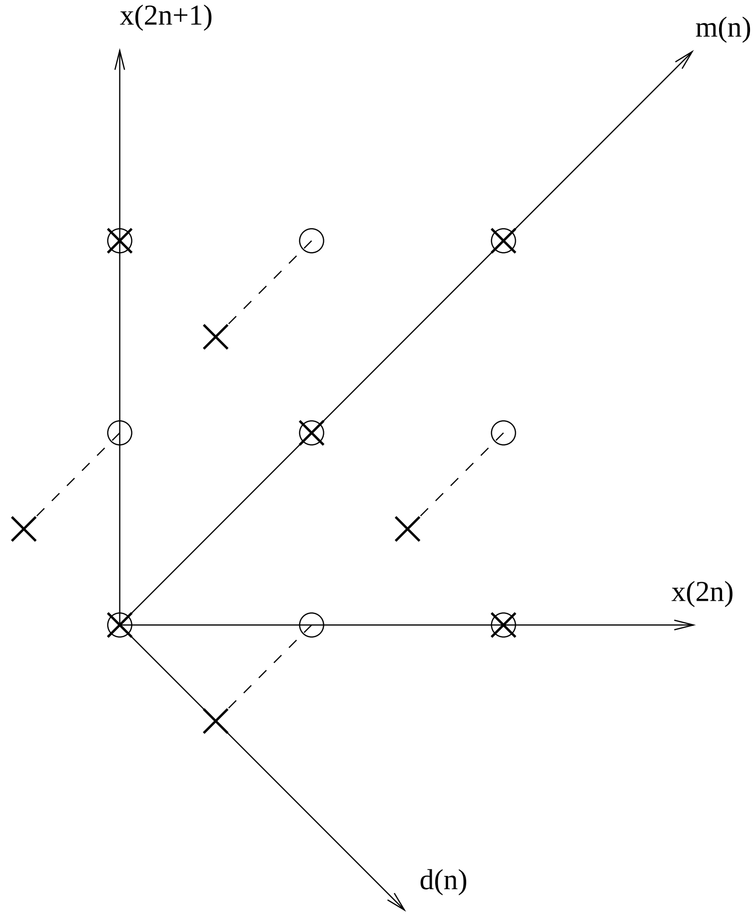

Figure 7.15: Transformation of $(x(2n), x(2n+1))$ to $(m_q(n), d_q(n))$.

This means that one is moving from the lattice $(x(2n), x(2n+1)) \in Z^2$ towards the lattice $(m_q(n), d_q(n)) \in Z^2$, indicated by the crosses in figure 7.15. As there is a one to one correspondence between the original values $(m(n), d(n))$ (circles in figure 7.15) and the quantified values $(m_q(n), d_q(n))$ (crosses in figure 7.15), the quantification is critical. The "quantification reconstruction" step, shown in figure 7.14, is given by

$$\begin{array}{ll} m(n) & \begin{array}{ll} = m_q(n) & \text{if } d_q(n) \text{ is even} \\ = m_q(n) + 0.5 & \text{if } d_q(n) \text{ is odd} \end{array} \\ d(n) = d_q(n) & \end{array} \tag{7.85}$$

7.7.6 Critical lossless quantification for l-th order regular PRFB's.

The lifting scheme [Swe94] can be used to transform the critically quantified Haar PRFB (which has only zero order regularity) to PRFB's with higher order regularity, and hence better compression performance. By applying it once, the couple $(m_q(n), d_q(n))$ can be transformed into $(m_q(n), d_q^*(n))$ as shown in figure 7.16.

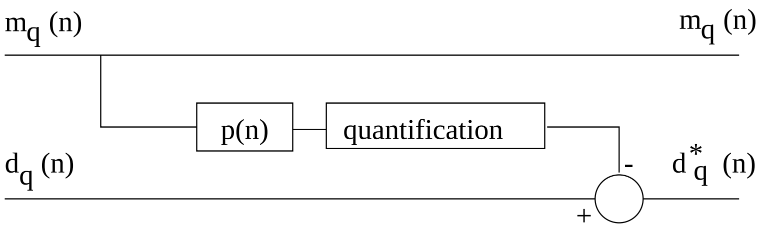

Figure 7.16: Single forward lifting operation.

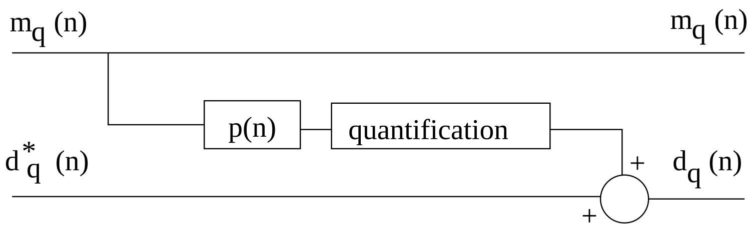

Figure 7.17: Single inverse lifting operation.

The application of the lifting scheme can be seen as a prediction of the high-pass coefficient $d_q(n)$ from the values $m_q(n)$, by the predictor $p(n)$. The difference between the integer $d_q(n)$ and its quantified prediction yields a new integer high-pass output $d_q^*(n)$, which has a smaller dynamic range than $d_q(n)$ if the prediction is good. A particular predictor $p(n)$ with $p(-1) = -2b$, $p(0) = 0$, $p(1) = 2b$ is chosen, yielding:

$$d_q^*(n) = d_q(n) - [-2b\ m_q(n+1) + 2b\ m_q(n-1)] \tag{7.86}$$

Consider the unquantified version of $d_q^*(n)$:

$$d^*(n) = d(n) - (-2b\ m(n+1) + 2b\ m(n-1)) \tag{7.87}$$

It can be seen from figure 7.18 that $x_h(n) = \sqrt{2}m(n)$ and $x_g(n) = (\sqrt{2})^{-1}d^*(n)$ are the outputs of the forward part of a PRFB with $h(n)$ unchanged compared to the Haar case and $g(n)$ modified to $g(n) + b\ h(n-2) - b\ h(n+2)$. The modified $g(n)$ is shown in figure 7.19.

The value of the predictor parameter b which yields first order regularity of $g(n)$ is chosen, i.e. the high-pass output samples should become zero for constant and linearly varying input sequences. This can be imposed by the first order regularity condition $\sum_n ng(n) = 0$ (derived from equation 7.75 combined with equation 7.67, with l'=1), yielding $b = 1/8$. With this value of b, $d(n)$ is perfectly predicted by $p(n)$ (see figure 7.16) in the case of linearly varying $x(n)$.

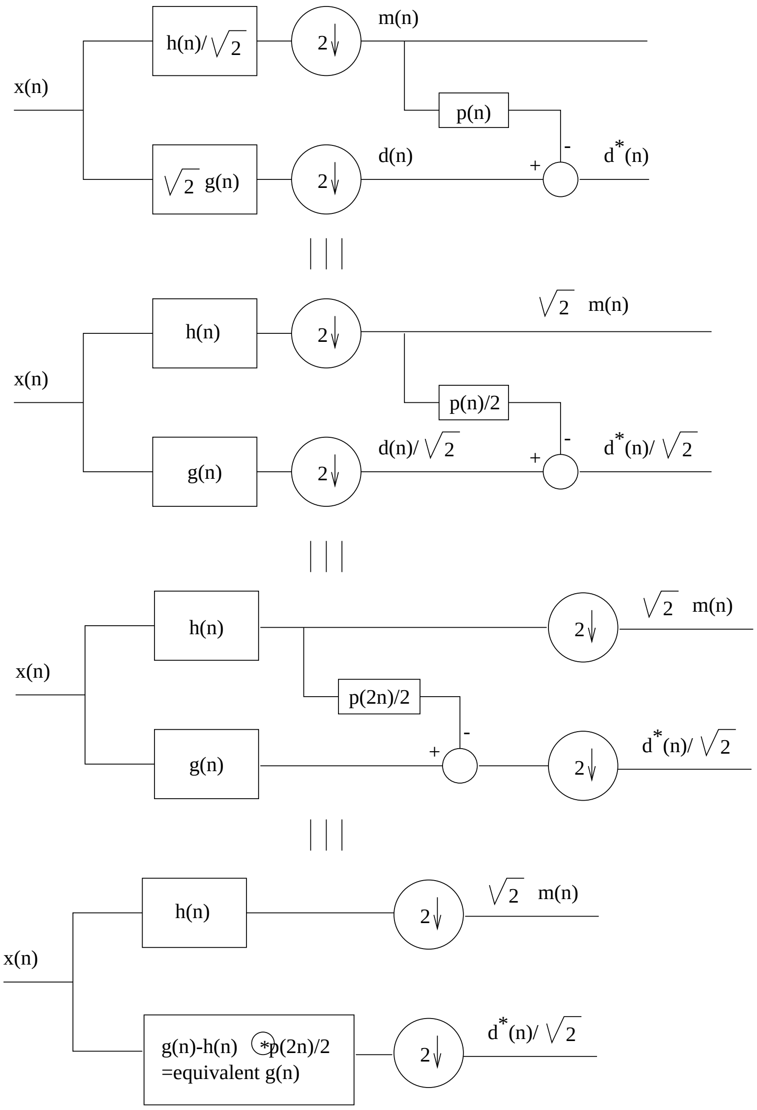

Figure 7.18: Equivalence of the forward part of the Haar PRFB plus the forward lifting to the forward part of a new PRFB with modified $g(n)$.

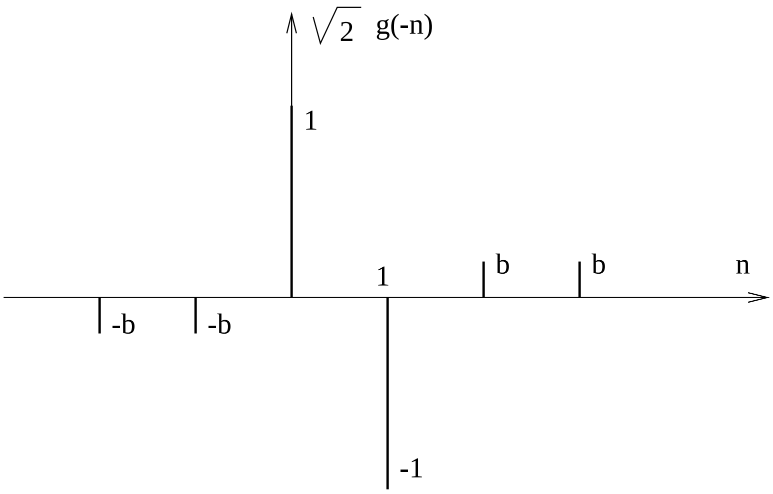

Figure 7.19: Equivalent $g(n)$ obtained after lifting.

7.7.7 Lossless image compression

A lossless integer wavelet transform is obtained by applying the method of [Mal89] to construct 2D transforms from the previously derived 1D PRFB's. Figure 7.20 demonstrates how a two dimensional PRFB is constructed from the application of a one dimensional PRFB in the row direction and in the column direction of the original image.

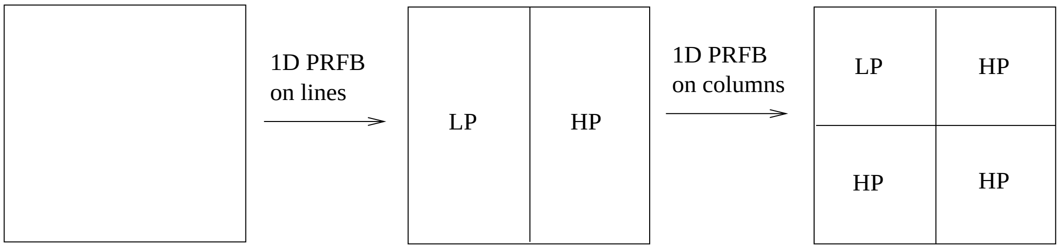

Figure 7.20: Construction of two dimensional PRFB from one dimensional PRFB. "LP" indicates a low pass subimage, "HP" indicates a high pass subimage.

Figure 7.21 demonstrates how a two dimensional wavelet transform is obtained by recursive application of this two dimensional PRFB on the low pass image.

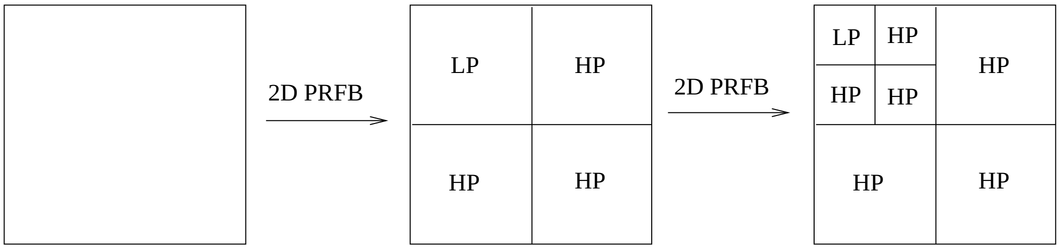

Figure 7.21: Construction of two dimensional wavelet transform by recursive application of a two dimensional PRFB on the low pass image. "LP" indicates a low pass subimage, "HP" indicates a high pass subimage.

Lossless image compression can be obtained by applying an entropy coding to the obtained wavelet coefficients. In the simplest case scalar coding can be used, like direct Huffman coding or arithmetic coding of the wavelet coefficients. The lower bound of the number of bits with which a pixel can be coded using scalar coding is given by the weighted mean pixel entropy H_{mean} in bit per pixel, given by

$$H_{mean} = \frac{\sum_{subimages} N_{subimage} H_{subimage}}{\sum_{subimages} N_{subimage}} \tag{7.88}$$

where $N_{subimage}$ is the number of points in a subimage and $H_{subimage}$ is the subimage entropy in bit per pixel, given by

$$H_{subimage} = \sum_{values} P(value) ln_2(1/P(value)) \tag{7.89}$$

where $value$ is an arbitrary value a subimage wavelet coefficient can have and $P(value)$ is the observed probability of occurrence of the value within the subimage.

7.7.8 Application

The lossless compression algorithm described here, will be applied in section 8.16 for the lossless archival of METEOSAT derived radiation budget term estimates (See also box "Lossless cartesian wavelet compression" in figure 7.3).

7.8 Spherical wavelet compression

In this section, the wavelet construction approach from section 7.7 is extended from cartesian wavelets towards spherical wavelets [SS95]. This presupposes sampling on a spherical surface of the data that is to be compressed.

The spherical wavelet compression will be applied in section 8.17 for the lossy distribution of radiation budget data.

In this section a mathematical description is given of spherical grids with maximally uniform resolution, and of a lossless spherical wavelet transform over these grids.

7.8.1 Algorithm description card

name algorithm	spherical compression
technical novelty	uniform spatial resolution *and* metrological quality preservation
novel application	lossy distribution of radiation budget results (section 8.17)
references	[SS95]

Table 7.6: Algorithm card for spherical compression algorithm

7.8.2 Ideal spherical grid

Radiation budget data can be collected by different instruments, with different time and space sampling characteristics. For easy usage, all data should be mapped to a common grid, which should ideally fulfil the following conditions

- The grid should be independent of individual satellite viewing conditions.
- A priori all areas on the globe are equally important, so an equal area grid should be used.
- Visualisation of the data should be easy to obtain.
- Large amounts of data are possible, so compression of the data should be easy to achieve.
- Different users can use different spatial resolutions and spatial coverage.

To meet the visualisation demand and the compression demand, a regular grid structure is favoured. To meet the multi resolution and multi coverage demand, it should be possible to define a spherical wavelet over the selected spherical grid. This favours again the use of a regular grid structure.

As a conclusion, the ideal spherical grid should be close to perfectly regular *and* close to perfectly equal area.

7.8.3 Recursive pseudo-regular polyhedra

Ideal spherical grids can be obtained by taking the corner points of regular polyhedra as grid points. Only five regular polyhedra exist [Hum86]:

- The tetrahedron, with four faces and four corner points.
- The cube, with six faces and eight corner points.
- The octahedron (the dual[5] of the cube), with eight faces and six corner points.
- The dodecahedron, with twelve faces and twenty corner points.

[5] Two regular polyhedra are each others dual if the corner points of the one are the midpoints of the faces of the other.

- The icosahedron (the dual of the dodecahedron), with twenty faces and twelve corner points.

Figure 7.22 shows the five regular polyhedra. This illustration has been obtained from http://gauss.technician.ac.il/ rl/unipoly/background.html .

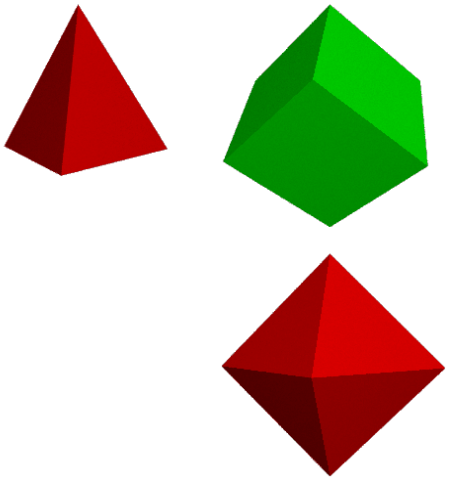

Figure 7.22: The five regular polyhedra. Top left: Tetrahedron. Top middle: Cube. Top right: Dodecahedron. Bottom middle: Octahedron. Bottom right: Icosahedron.

The perfectly regular and perfectly equal area grid with the maximum number of grid points that can be obtained, is obtained using the icosahedron mid points (corresponding to the dodecahedron corner points), leading to 20 grid points.

Grids with higher number of grid points, but which still are close to perfectly regular and close to perfectly equal area, can be obtained by a subdivision of the faces of the regular polyhedra. The resulting grid points are the corner points of so-called pseudo-regular polyhedra. The subdivision of the faces can be done in two steps:

- The faces, which are regular polygons, are subdivided in a plane by twodimensional regular lattices.
- The new points obtained in the plane of the face are projected onto the sphere containing the corner points of the original polyhedron.

This is illustrated in figure 7.23 starting from the faces of the icosahedron, which are plane regular triangles with edge length l. They can be subdivided by hexagonal lattices into a number n^2 of smaller regular triangles with edge length l/n.

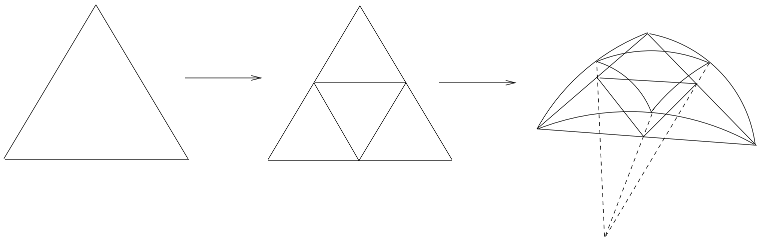

Figure 7.23: The subdivision of the icosahedron faces. Left: Original icosahedron face. Middle: Face subdivided in plane. Right: Projection of new points obtained in the plane on to the sphere, yielding four spherical triangles.

In order to define a spherical wavelet transform, one needs a series of spherical grids at different resolutions, where the high resolution grids contain the low resolution grids in a recursive way. This can be obtained by taking a series of pseudo-regular polyhedra provided by recursive subdivisions of the polyhedra faces.

This is illustrated in figure 7.24 starting from the face of an icosahedron, which is a plane regular triangle with edge length l. The regular triangle can be subdivided into 4 smaller regular triangles with edge length $l/2$. If this subdivision is repeated recursively for every newly obtained regular triangle, 4^2 triangles are obtained with edge length $l/2^2$. If the recursive subdivision is carried out k times, 4^k triangles are obtained with edge length $l/2^k$.

For the remainder of this work, only this kind of recursive pseudo-regular polyhedra will be considered.

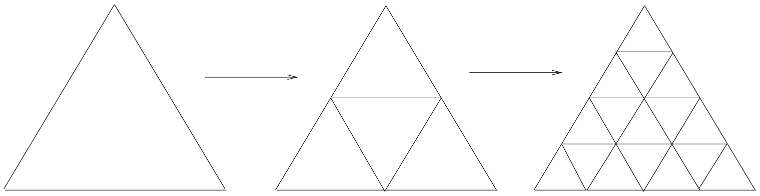

Figure 7.24: Recursive subdivision of an icosahedron face. Left: Original (spherical) triangular face. Middle: Face subdivided in 4 smaller spherical triangles. Right: Face recursively subdivided in 16 spherical triangles.

7.8.4 Spherical Haar PRFB

Consider 4 adjacent spherical triangles as shown in figure 7.25. A value ct is associated with the central triangle, a value tt is associated with the top triangle, a value lt is associated with the left triangle and a value rt is associated with the right triangle.

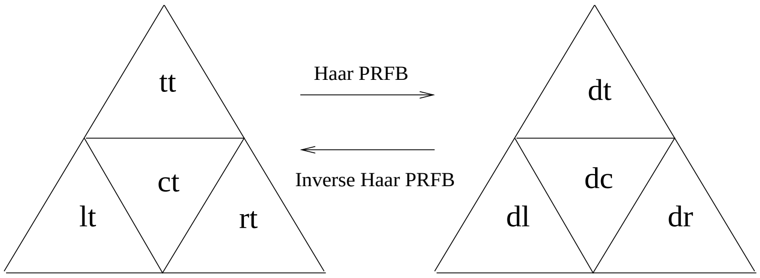

Figure 7.25: Four adjacent spherical triangles for the definition of the spherical Haar PRFB.

The forward part of the spherical Haar PRFB can be defined by

$$\begin{bmatrix} dc \\ dt \\ dl \\ dr \end{bmatrix} = \begin{bmatrix} 1 & 1 & 1 & 1 \\ 1 & 1 & -1 & -1 \\ 1 & -1 & 1 & -1 \\ 1 & -1 & -1 & 1 \end{bmatrix} \begin{bmatrix} ct \\ tt \\ lt \\ rt \end{bmatrix} \tag{7.90}$$

dc is the low-pass coefficient, dt,dl,dr are the high-pass coefficients, which give the gradients in the centre top, centre left and centre right directions respectively. From those four coefficients, the original ones can be reconstructed by inverting the relation 7.90. So the inverse part of the spherical Haar PRFB is given by

$$\begin{bmatrix} ct \\ tt \\ lt \\ rt \end{bmatrix} = \frac{1}{4} \begin{bmatrix} 1 & 1 & 1 & 1 \\ 1 & 1 & -1 & -1 \\ 1 & -1 & 1 & -1 \\ 1 & -1 & -1 & 1 \end{bmatrix} \begin{bmatrix} dc \\ dt \\ dl \\ dr \end{bmatrix} \tag{7.91}$$

7.8.5 Critical lossless quantification for the spherical Haar PRFB.

If the values ct,tt,lt,rt at the input of the spherical Haar PRFB are integer, the transformed values dc,dt,dl,dr are integer too. However, since the orthogonal transformation matrix in equation

7.90 has determinant 2^4 (each of the 4 orthogonal rows has length 2), only one out of every 2^4 combinations of integer values (dc,dt,dl,dr) can be obtained from transformation 7.90 starting from integer values (ct, tt, lt, rt).

Scaled versions (dc_s, dt_s, dl_s, dr_s) of the integer transformed coefficients (dc,dt,dl,dr) can be introduced

$$\begin{aligned} dc_s &= dc/4 \\ dt_s &= dt/2 \\ dl_s &= dl/2 \\ dr_s &= dr \end{aligned} \tag{7.92}$$

with the following properties

- The total scaling factor is $1/4 * 1/2 * 1/2 = 1/2^4$, hence the scaled coefficients are obtained from the coefficients (ct, tt, lt, rt) by a transformation with determinant 1.
- dc_s is the mean of (ct, tt, lt, rt)

Equation 7.92 is the analogon for the spherical Haar PRFB, of equation 7.83 for the one dimensional cartesian Haar PRFB.

A critical lossless quantification of the Haar filtered coefficients dc,dt,dl,dr can be introduced, analogously to the one of equation 7.84 for the one dimensional cartesian Haar PRFB. A critical lossless quantification is given by

$$\begin{aligned} dc_q &= [dc_s] \\ dt_q &= [dt_s] \\ dl_q &= [dl_s] \\ dr_q &= [dr_s] \end{aligned} \tag{7.93}$$

For the quantification reconstruction, the reconstruction of the last 2 bits of dc and of the last bits of dt and of dl is needed

$$\begin{aligned} dc &= 4dc_q + last2bits(dc) \\ dt &= 2dt_q + lastbit(dt) \\ dl &= 2dl_q + lastbit(dl) \\ dr &= dr_q \end{aligned} \tag{7.94}$$

where $lastbit(d)$ stands for the value of the last bit of the value d

$$lastbit(d) = d \bmod 2 \tag{7.95}$$

and $last2bits(d)$ stands for the value of the combined last 2 bits of the value d

$$last2bits(d) = d \bmod 4 \tag{7.96}$$

Since the difference between dr and dt,dl is an even number

$$dr = dt - 2(tt - rt) = dl - 2(lt - rt) \tag{7.97}$$

and the last bit of an even number is zero

$$lastbit(-2(tt - rt)) = lastbit(-2(lt - rt)) = 0 \tag{7.98}$$

the last bit of dt,dl is equal to the known last bit of $dr = dr_q$

$$lastbit(dt) = lastbit(dl) = lastbit(dr) = lastbit(dr_q) \tag{7.99}$$

Since the difference between dc and $-(dt + dl + dr)$ is a multiple of 4

$$-(dt + dl + dr) = -3ct + tt + lt + rt = -4ct + dc \tag{7.100}$$

and the last 2 bits of a multiple of 4 are zero

$$last2bits(-4ct) = 0 \tag{7.101}$$

the last 2 bits of dc are equal to the known last 2 bits of $-(dt+dl+dr) = -(2dt_q+lastbit(dr_q)+2dl_q+lastbit(dr_q)+dr_q)$

$$\begin{aligned} last2bits(dc) &= last2bits(-(dt+dl+dr)) \\ &= last2bits(-(2dt_q+2dl_q+dr_q+2lastbit(dr_q))) \end{aligned} \tag{7.102}$$

Summarising, from the quantified values dc_q,dt_q,dl_q,dr_q the unquantified integer values dc,dt,dl,dr can be reconstructed by

$$\begin{aligned} dc &= 4dc_q + last2bits(-(2dt_q+2dl_q+dr_q+2lastbit(dr_q))) \\ dt &= 2dt_q + lastbit(dr_q) \\ dl &= 2dl_q + lastbit(dr_q) \\ dr &= dr_q \end{aligned} \tag{7.103}$$

7.8.6 Critical lossless quantification for spherical l-th order regular PRFB's.

As for the one dimensional cartesian case, the lifting scheme [Swe94] can be used to transform the (eventually critically quantified) spherical Haar PRFB (which has only zero order regularity) to PRFB's with higher order regularity, and hence better compression performance. Consider the situation of figure 7.26 with Haar coefficients dc,dt,dl,dr for the central (spherical) triangle, and lowpass coefficients Haar coefficients dc_r,dc_l,dc_t for the three neighbouring (spherical) triangles.

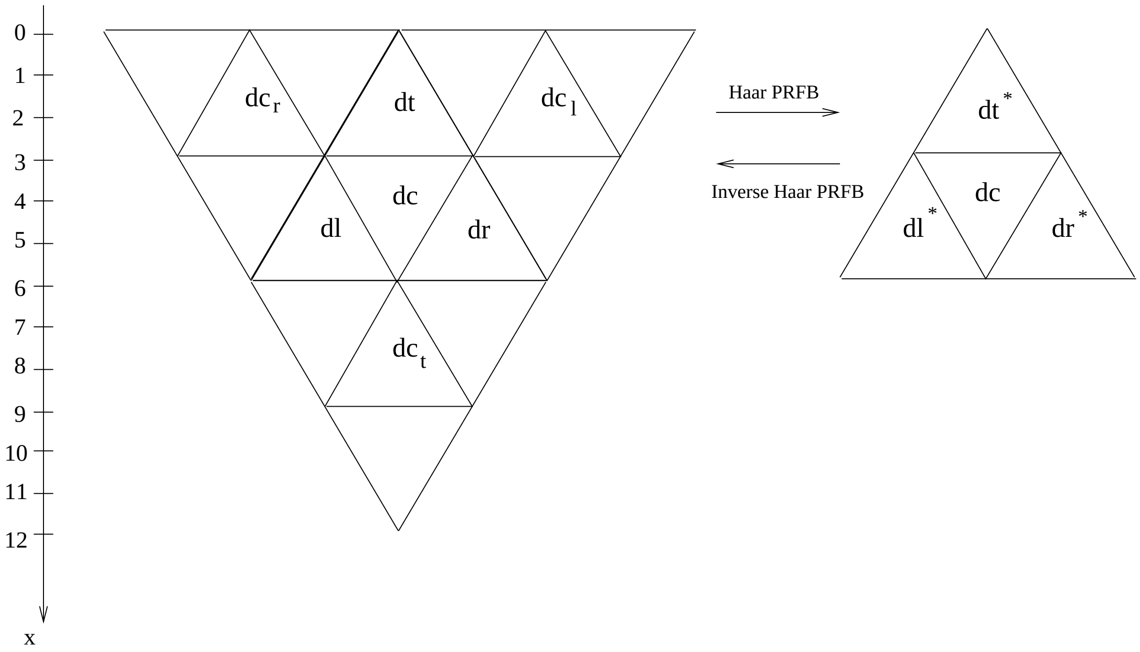

Figure 7.26: Haar transformed central spherical triangle and three neighbouring spherical triangle lowpass values for definition of lifting scheme application. Centre: Haar transformed spherical triangle with lowpass value dc indicated in the centre and highpass (gradient) values dt,dl,dr indicated in the gradient directions. Left: lowpass value dc_r for the nearest neighbour spherical triangle in dr direction. Right: lowpass value dc_l for the nearest neighbour spherical triangle in dl direction. Right: lowpass value dc_t for the nearest neighbour spherical triangle in dt direction.

The lifting scheme can be applied, to replace the values of the highpass coefficients dt,dl,dr, by new values dt^*,dl^*,dr^* which are the difference between the old values and predictions of the old values based on the neighbouring lowpass coefficients dc_r,dc_l,dc_t.

$$\begin{aligned} dt^* &= dt - b((dc_r+dc_l)/2 - dc_t) \\ dl^* &= dl - b((dc_t+dc_r)/2 - dc_l) \\ dr^* &= dr - b((dc_l+dc_t)/2 - dc_r) \end{aligned} \tag{7.104}$$

The parameter b is chosen so that the prediction is perfect (i.e. the new highpass values are zero) in the case of a linear variation at the input of the PRFB. In the case where the input values equal x (see figure 7.26), one has

$$\begin{aligned} dc &= 2+4+5+5 = 16 \\ dc_r &= dc_l = 1+1+2+4 = 8 \\ dc_t &= 7+7+8+10 = 32 \\ dt &= 2+4-5-5 = -4 \\ dt^* &= -4+24b = 0 \end{aligned} \tag{7.105}$$

yielding $b = 1/6$.

7.8.7 Lossless data compression

A lossless spherical wavelet transform is obtained by recursively applying the previously defined lossless spherical PRFB's. In the first recursion step the PRFB is applied to the original data, defined over a pseudo icosahedral spherical grid. In the following recursion steps, the PRFB is applied to the low-pass coefficients obtained obtained in the previous recursion step. Lossless compression of integer data defined on a pseudo icosahedral grid is obtained by scalar coding of the obtained integer wavelet coefficients, e.g. using Huffman coding or arithmetic coding. A lower bound of the number of bits with which a pixel can be coded using scalar coding is given by the weighted mean pixel entropy H_{mean} in bit per pixel, defined as in section 7.7.7 (by equations 7.88 and 7.89).

7.8.8 Application

The pseudo icosahedral spherical grids, and the associated lossless spherical wavelet transform, that have been described here, will be applied in section 8.17 for the lossy compression of METEOSAT derived radiation budget term data (See also box "Lossless spherical wavelet compression" in figure 7.3.). The "lossy compression" consists of a lossy spherical sampling of the original METEOSAT derived data followed by a lossless compression of the spherically sampled data. If one is only interested in the data in it's (uniform resolution) spherical form, as can be anticipated for the use[6] in atmospheric models, the compression can be considered lossless.

[6] for comparison or for assimilation

Chapter 8

Satellite image processing and results

In this chapter the *specific* satellite data processing algorithms that have been developed for the processing of radiation budget data are described. In the general processing scheme given in figure 1.1, these image processing algorithms are used in the blocks “ADM modification”, “Flux surface density estimation”, “Flux surface density validation” and “Compression”. The more detailed processing schemes of these three blocks are given in the figures 8.1, 7.2, 8.2 and 7.3 respectively.

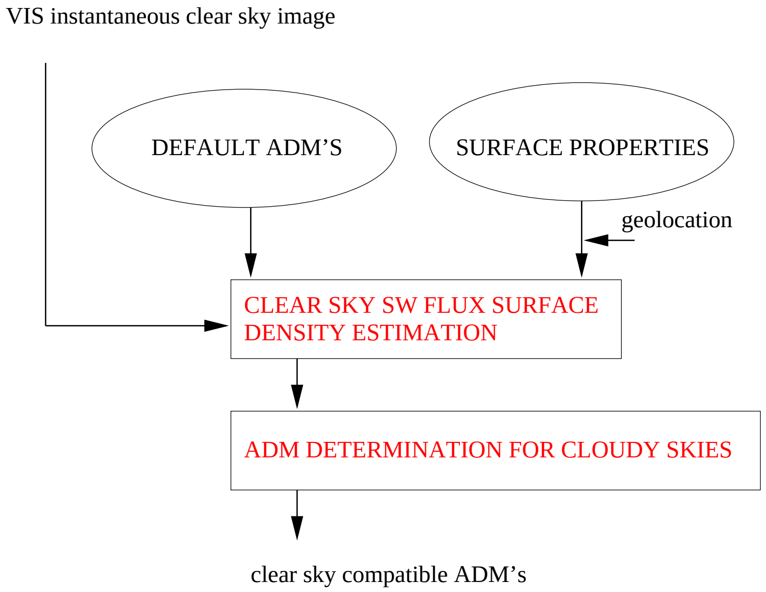

Figure 8.1: The processing scheme developed in this work for the modification of ADM's, in order to make them compatible with the previously derived VIS instantaneous clear sky images. The default ADM's are used as external input data. The processing algorithms are indicated by rectangles. For every algorithm an indication is given that the algorithm is a specific satellite data processing algorithm originally developed in this work (indicated by a descriptive text coloured in red).

For every algorithm described in this chapter, a processing description card is given, which includes references to the used image processing algorithms from chapter 7.

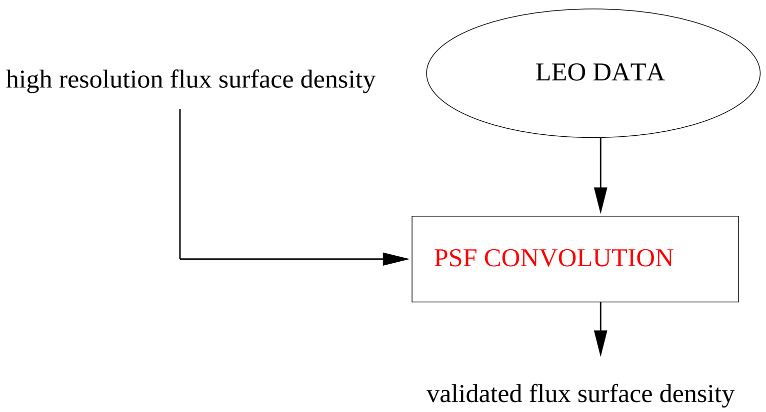

Figure 8.2: The processing scheme developed in this work for the validation of the high resolution flux surface density derived from METEOSAT data. LEO data is used as external input data. The processing algorithm is indicated by a rectangle. An indication is given that the algorithm is a specific satellite data processing technique originally developed in this work (indicated by a descriptive text coloured in red).

8.1 METEOSAT Geolocation

METEOSAT geolocation means the calculation of the geographical coordinates of an arbitrary METEOSAT pixel.

This operation is necessary for

- The calculation of the surface properties of a METEOSAT pixel from the surface properties database, described in section 4.3. METEOSAT pixel surface properties are used in section 8.7 for clear sky image interpolation and in section 8.11 for scene dependent radiance to flux surface density conversion.
- The calculation of the METEOSAT viewing angles (in section 8.2), needed for the radiance to flux surface density conversion in section 8.11.

In this section, the calculation of the geolocation coordinates of a METEOSAT pixel, and the application of this calculation to obtain surface properties for METEOSAT pixels, are described.

8.1.1 Processing description card

name processing	geolocation
technical novelty	none
novel algorithms	none
references	[RB86], [DB94], [Iqb83, pages 1-28]

Table 8.1: Processing card for geolocation

8.1.2 Cartesian and spherical coordinates.

Consider the coordinate system (O;XYZ), as defined in section 2 (see figure 2.1). This is a cartesian coordinate system with origin in the centre of the earth, that is rotating together with the earth.

In this reference system a point (X, Y, Z) can be expressed in spherical coordinates (R, Θ, Φ) by the defining relations 8.1.

$$\begin{aligned} X &= R\sin(\Theta)\cos(\Phi) \\ Y &= R\sin(\Theta)\sin(\Phi) \\ Z &= R\cos(\Theta) \end{aligned} \tag{8.1}$$

From the cartesian coordinates of a given point P, the spherical coordinates can be calculated by the inversion of equation 8.1, given by equation 8.2.

$$\begin{aligned} R &= \sqrt{X^2 + Y^2 + Z^2} \\ \Theta &= \cos^{-1}(\tfrac{Z}{R}) \\ \Phi &= \tan^{-1}(Y, X) \end{aligned} \tag{8.2}$$

$\tan^{-1}(Y, X)$ is defined as the angle whose tangent is equal to Y/X, whose cosine has the same sign as X and whose sine has the same sign has Y[1].

8.1.3 Earth scaled space.

In the (O;XYZ) coordinate system, the earth surface can be idealised to be an ellipsoid with equatorial radius $R_E = 6357$ km and polar radius $R_P = 6378$ km.

The idealised earth surface can be made an exact sphere by scaling the Z axis with a factor $R_E/R_P = 1.003$. The space obtained after this scaling is defined as the earth scaled space. The cartesian coordinates in this space are defined as (X', Y', Z') and the spherical coordinates are defined as (R', Θ', Φ').

[1] This definition is identical to the definition of the C function atan2(Y, X)

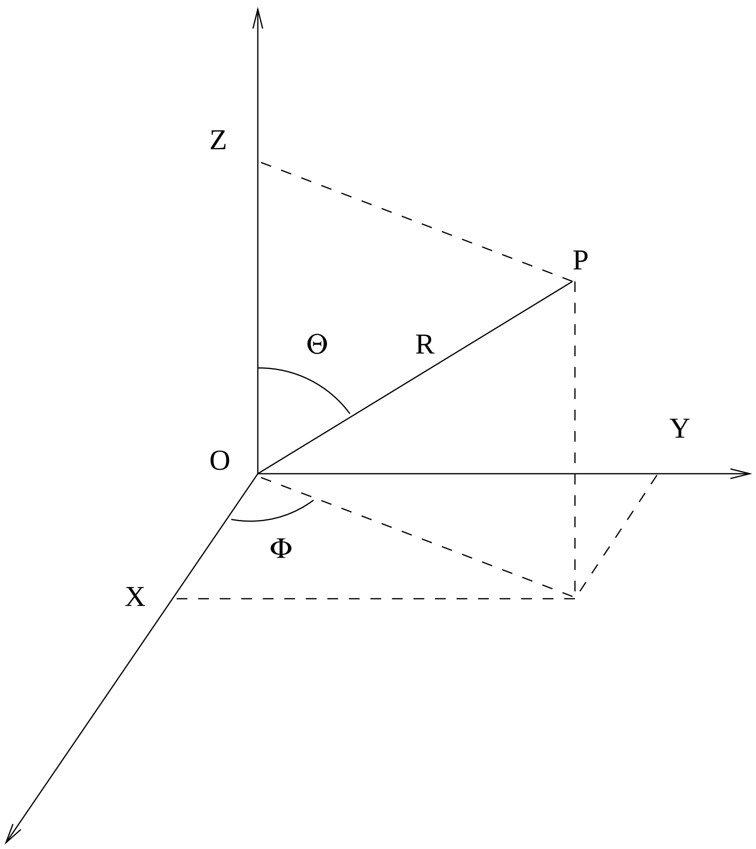

Figure 8.3: Cartesian coordinates (X, Y, Z) and spherical coordinates (R, Θ, Φ) of a point P.

The relationship between the cartesian coordinates (X, Y, Z) of a point P in the physical space and the cartesian coordinates (X', Y', Z') of the same point P in the earth scaled space is given by equation 8.3

$$\begin{aligned} X' &= X \\ Y' &= Y \\ Z' &= \tfrac{R_E}{R_P} Z \end{aligned} \tag{8.3}$$

The relation between the cartesian coordinates $(O; X', Y', Z')$ and the spherical coordinates $(O; R', \Theta', \Phi')$ in the earth scaled space have exactly the same form (equations 8.1 and 8.2) as the relations between the cartesian coordinates $(O; X, Y, Z)$ and spherical coordinates $(O; R, \Theta, \Phi)$ in the physical space.

In the earth scaled space the equation of the idealised earth surface is given by $R' = R_E$.

8.1.4 METEOSAT viewing geometry

METEOSAT is a geostationary satellite with idealised fixed position[2] relative to the earth. The spherical coordinates of this fixed position are $(O; R, \Theta, \Phi) = (O; R_{geostat}, 90°, 0°)$. $R_{geostat} = 35.8e3km$ is the geostationary satellite radius.

Denote the METEOSAT satellite position vector as $\vec{S}$.

The pixel with coordinate (i, j) of the rectified METEOSAT image, is obtained by observing the earth from the position $\vec{S}$ in the direction with spherical coordinate angles $\Theta = \Theta_i$, $\Phi = \Phi_j$.

Figure 8.4 shows how Θ_i depends on the image row coordinate i.

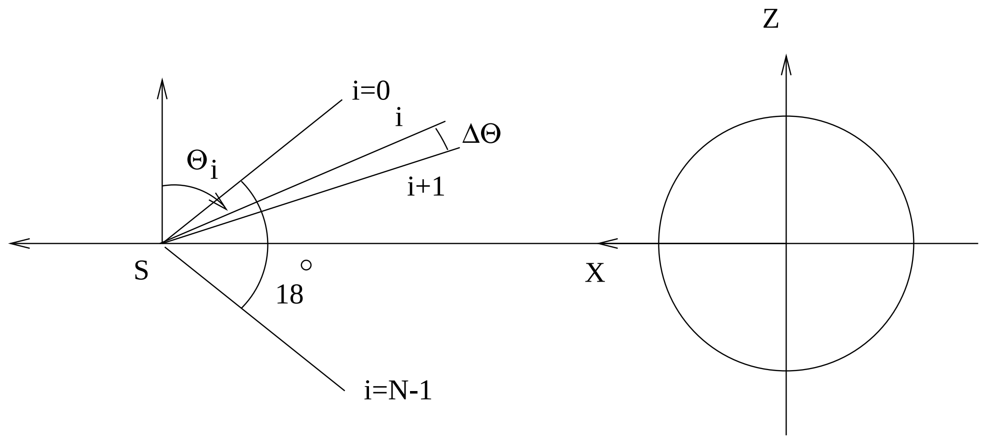

Figure 8.4: Relationship between rectified METEOSAT row i and viewing angle Θ_i.

The height of the image is N, with $N = 2500$ for the IR and WV image and $N = 5000$ for the VIS image. i varies from 0 (top most = north most row of the image) to N-1 (bottom most = south most row of the image).

The angular interval covered by the full height of the image is 18°. The angular interval $\Delta\Theta$ between two image rows is constant. Consequently, $\Delta\Theta = \frac{18°}{N-1}$.

In the centre of the image ($i = \frac{N-1}{2}$), one has $\Theta = 90°$.

Summarising, Θ_i is given in function of i by equation 8.4.

$$\Theta_i = 90° + \left(i - \frac{N-1}{2}\right) \frac{18°}{N-1} \tag{8.4}$$

Figure 8.5 shows how Φ_j depends on the image column coordinate j.

The width of the image is equal to the height N. j varies from 0 (left most = west most column of the image) to N-1 (right most = east most column of the image).

[2]The METEOSAT rectification process calculates the image as observed from this idealised position, see section 6.2.1.

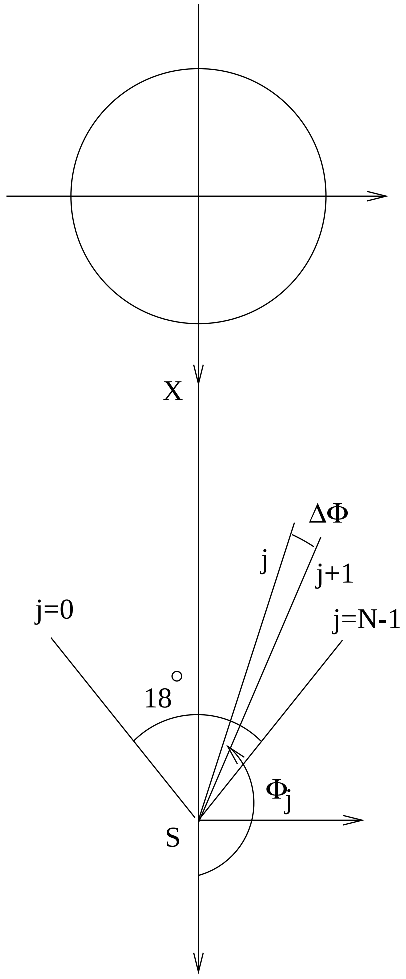

Figure 8.5: Relationship between rectified METEOSAT column j and viewing angle Φ_j.

The angular interval covered by the full width of the image is 18°. The angular interval $\Delta\Phi$ between two image columns is constant. Consequently, $\Delta\Phi = \frac{18°}{N-1}$.

In the centre of the image ($j = \frac{N-1}{2}$), one has $\Phi = 180°$.

Summarising, Φ_j is given in function of j by equation 8.5.

$$\Phi_j = 180° - \left(j - \frac{N-1}{2}\right)\frac{18°}{N-1} \tag{8.5}$$

The line, with direction (Θ_i, Φ_j), along which a given pixel (i, j) views the earth, is called the Line Of Sight (LOS) of that pixel.

8.1.5 Line Of Sight (LOS) geolocation

Geolocation of a rectified METEOSAT image consists of finding, for those pixels that view the earth, the location of the point on earth viewed by the pixel. This can be done by calculating the intersection point of the LOS and the earth ellipsoid. From the two possible intersection points, the one which is the closest to the satellite, has to be selected.

Consider the plane formed by the earth origin $\vec{O}$, the intersection point to be found, $\vec{P}$, and the satellite position, $\vec{S}$. Consider this plane in the earth scaled space (see figure 8.6).

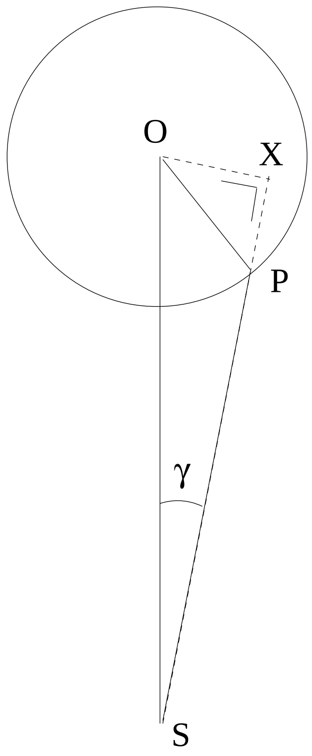

Figure 8.6: Intersection of the earth surface and the METEOSAT pixel LOS in the plane formed by the points $\vec{O}$, $\vec{P}$ and $\vec{S}$ in the earth scaled space. $\vec{O}$: origin of the earth. $\vec{P}$: intersection point earth-LOS. $\vec{S}$: satellite position. $\vec{X}$: auxiliary point.

In this plane, the problem of finding the intersection of the LOS and the earth sphere simplifies to finding the intersection of a line and a circle. $|OP| = R_E$ and $|OS| = R_{geostat}$ are known. γ, the angle between the lines SO and SP, can be calculated from the METEOSAT viewing angles. The geometrical problem to be solved consists in finding the length $|SP|$ so that P lies on the earth circle.

Consider the auxiliary point $\vec{X}$, which is defined so that X lays on the line SP and so that the line OX is perpendicular to the line PX (see figure 8.6).

From figure 8.6, it can be seen that

$$\begin{aligned} |SP| &= |SX| - |PX| \\ |SX| &= |SO|\cos(\gamma) \\ |PX| &= \sqrt{|PO|^2 - |XO|^2} \\ |XO| &= |SO|\sin(\gamma) \end{aligned} \tag{8.6}$$

and hence

$$\begin{aligned} |SP| &= |SO|\cos(\gamma) - \sqrt{|PO|^2 - |SO|^2\sin^2(\gamma)} \\ &= R_{geostat}\cos(\gamma) - \sqrt{R_E^2 - R_{geostat}^2\sin^2(\gamma)} \end{aligned} \tag{8.7}$$

The complete geolocation of a rectified METEOSAT image pixel (i, j) is obtained by the execution of the following steps

- The cartesian coordinates of $\vec{S}$ are calculated as $(O; X, Y, Z) = (O; R_{geostat}, 0, 0)$.
- The spherical coordinates of the unit pixel viewing direction[3] $\vec{1}_{SP}$ are calculated as $(S; 1, \Theta_i, \Phi_j)$, with Θ_i given by equation 8.4 and Φ_j given by equation 8.5.
- The cartesian components $(O; X_{ref}, Y_{ref}, Z_{ref})$ of the unit pixel viewing direction $\vec{1}_{SP}$ translated to the origin O, are calculated from the spherical coordinates by application of equation 8.1.
- The cartesian coordinates $(O; X'_{ref}, Y'_{ref}, Z'_{ref})$ in the earth scaled space of the unit pixel viewing direction $\vec{1}_{SP}$ are calculated by application of equation 8.3.
- The radius in the earth scaled space R'_{ref} of the unit pixel viewing direction $\vec{1}_{SP}$ is calculated by application of the first line of equation 8.1.
- The cartesian coordinates of the unit pixel viewing direction in the earth scaled space[4] $\vec{1'}_{SP}$ are calculated as $(O; X'_{ref}/R'_{ref}, Y'_{ref}/R'_{ref}, Z'_{ref}/R'_{ref})$.
- The angle γ between the line SO and SP in the earth scaled space is calculated as[5] $\gamma = \cos^{-1}(\vec{1'}_{SO}.\vec{1'}_{SP})$.
- The radius R'_{SP} of $\vec{SP}$ in the earth scaled space is calculated from equation 8.7.
- The cartesian coordinates $(S; X_{SP}, Y_{SP}, Z_{SP})$ of $\vec{SP}$ in the physical space are calculated as $(\frac{R'_{SP}}{R'_{ref}}X_{ref}, \frac{R'_{SP}}{R'_{ref}}Y_{ref}, \frac{R'_{SP}}{R'_{ref}}Z_{ref})$.
- The cartesian coordinates of $\vec{P}$ are calculated as $\vec{S} + \vec{SP}$.

8.1.6 METEOSAT format sampling of geolocated databases

The surface property maps described in section 4.3 are given in function of latitude and longitude.

For every METEOSAT pixel, surface properties are obtained in the following way:

- The cartesian coordinates of the pixel position in the physical space are transformed into the cartesian coordinates in the earth scaled space by application of equation 8.3.
- The spherical coordinates in the earth scaled space are obtained from the cartesian coordinates in the earth scaled space by application of equation 8.1.
- The pixel latitude is obtained as $90° - \Theta'$.
- The pixel longitude is obtained as Φ'.
- The surface property values are linearly interpolated from the surface properties latitudes and longitudes towards the pixel latitude and longitude.

[3] The notation $\vec{1}_Y$ is used for the unit vector in the physical space with the same direction as a given vector $\vec{Y}$.

[4] The notation $\vec{1'}_Y$ is used for the unit vector in the earth scaled space with the same direction as a given vector $\vec{Y}$.

[5] Where . denotes the scalar product.

8.1.7 Application

The METEOSAT geolocation described here will be applied:

- in section 8.2 for the METEOSAT viewing angle calculation.
- in section 8.5 for the calculation of the local time for a given METEOSAT pixel.
- in section 8.7 for clear sky image interpolation with an auxiliary ocean/land classification image (see equation 8.44).
- in section 8.11 for the construction of surface property dependent ADM's (See also line "geolocation" under oval "Surface properties" in figure 8.1.).

8.2 METEOSAT viewing angles

METEOSAT viewing angle calculation means the calculation of the solar zenith angle, θ_{sun}, the satellite (viewing) zenith angle, θ_{sat}, and the relative azimuth angle, ϕ_{rel}. These angles have been introduced in section 5.1 and are necessary for the radiance to flux surface density conversion in section 8.11.

In this section, a mathematical description of the METEOSAT viewing angle calculation is given.

8.2.1 Processing description card

name processing	viewing angles
technical novelty	none
novel algorithms	none
references	[Gre87, pages 21-22],[Iqb83, pages 1-28]

Table 8.2: Processing card for viewing angle calculation

8.2.2 Local geometrical vertical

The local geometrical vertical in a given point P of the earth ellipsoid is defined as the axis which is perpendicular to the earth ellipsoid in the point P and which points away from the earth centre O.

Figure 8.7 shows how the local geometrical vertical can be constructed as the axis perpendicular to the tangent vector $\vec{T}$. $\vec{T}$ is defined as a vector which lies in the plane formed by P and the Z axis, which is tangent to the earth ellipsoid in P and which points towards the Z axis. The top of figure 8.7 shows the construction of $\vec{T}$ in the earth scaled space, and the bottom of figure 8.7 shows the construction of the local geometrical vertical $\vec{1}_{perp}$, perpendicular to $\vec{T}$, in the physical space.

In the earth scaled space the cartesian components (X_t', Y_t', Z_t') of $\vec{T}$ can be calculated by equation 8.8.

$$\vec{T} = \left(\vec{P} \times (0,0,1)\right) \times \vec{P} = (X_t', Y_t', Z_t') \tag{8.8}$$

The cartesian components (X_t, Y_t, Z_t) of $\vec{T}$ in the physical space are obtained by application of equation 8.3.

In the physical space the coordinates of the local geometrical vertical $\vec{1}_{perp}$ can be calculated with equation 8.9.

$$\vec{1}_{perp} = \vec{1}_{\vec{T} \times \left(\vec{P} \times (0,0,1)\right)} \tag{8.9}$$

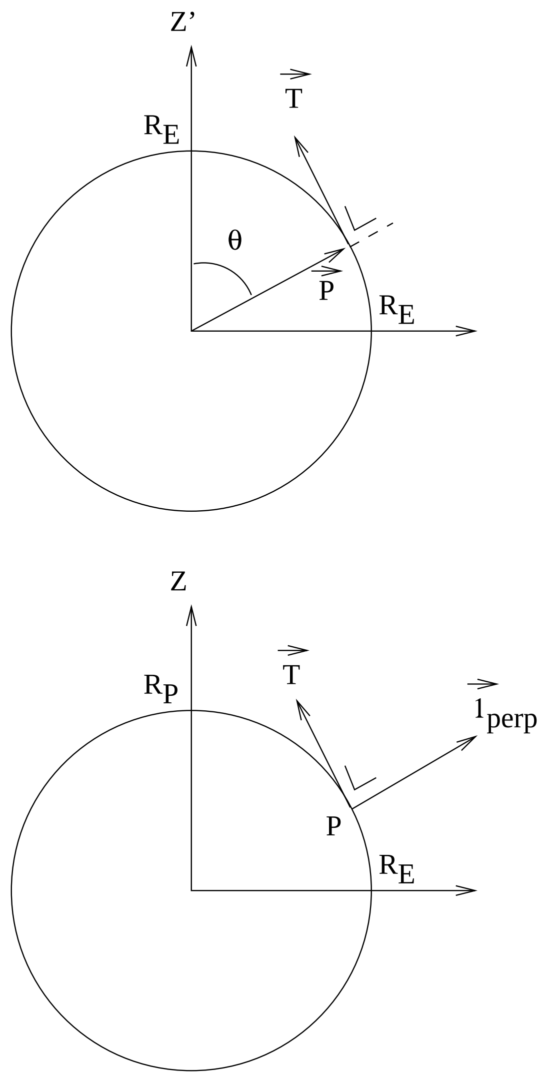

Figure 8.7: The tangent direction $\vec{T}$ in the earth scaled space (top) and in the physical space (bottom), and the orthogonal relationship with the geometrical vertical $\vec{1}_{perp}$ in the physical space.

8.2.3 Earth sun direction

The earth rotates around its own axis with a period of 24 hours. Seen from the earth, in the coordinate system (O;XYZ) that rotates together with the earth, this results in an apparent rotation of the sun around the earth. Since the sun goes up in the east, this apparent rotation goes from east to west. This results in an apparent motion of the sun around the earth with a time varying angle $\Phi_{sun}(t)$, given by equation 8.10 (see figure 8.8).

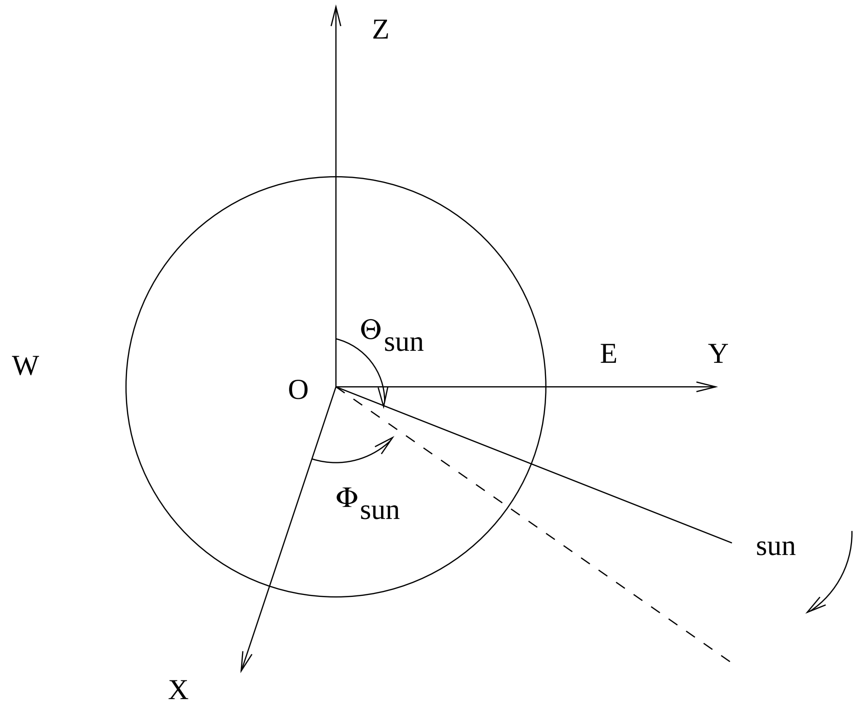

Figure 8.8: The apparent motion of the sun around the earth due to the earth's rotation, seen from the earth fixed coordinate system.

$$\Phi_{sun}(t) = -\frac{t + \Delta t^{corr} - 12:00 \text{ UTC}}{24 \text{ hours}} \tag{8.10}$$

t is expressed in UTC (Coordinated Universal Time). $t+\Delta t^{corr}$ is the True Solar Time (TST) at the Greenwich meridian. The factor Δt^{corr}, also called "the equation of time" in [Iqb83], accounts for time varying non uniformities of the rotation of the earth around the sun and of the earth around its own rotation axis. Δt^{corr} is given by equation 8.11, after [Iqb83].

$$\begin{aligned}\Delta t^{corr} = {} & (0.000075 + 0.001868 \cos\Gamma - 0.032077 \sin\Gamma \\ & -0.014615 \cos 2\Gamma - 0.04089 \sin 2\Gamma)(229.18 \text{ minutes})\end{aligned} \tag{8.11}$$

with the so-called day angle Γ given by equation 8.12

$$\Gamma = 2\pi(\text{day of year} - 1)/365 \tag{8.12}$$

Figure 8.9 shows Δt^{corr} in function of the day of the year.

The earth translates around the sun with a period of 365.25 days in a slightly elliptical orbit in a plane called the ecliptic plane, which is tilted with an inclination $inc = 23°.44$ relative to the earth equatorial plane. Seen from the earth, the sun seems to translate around the earth in the ecliptic plane.

The sun crosses the equatorial plane of the earth at two times of the year, called the equinox times, once in spring (approximately at 21 March) and once in autumn (approximately at 21 September). The spring equinox crossing point, also called Vernal Equinox (VE) point, is used as a reference point for the definition of the so called equatorial coordinate system, which is an

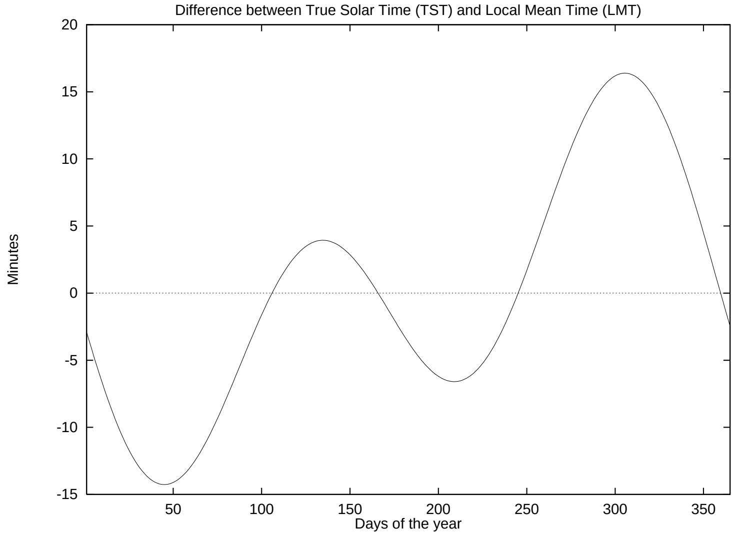

Figure 8.9: The equation of time = the difference between the True Solar Time (TST) and the Local Mean Time (LMT), Δt^{corr}, in function of the day of the year.

inertial (i.e. not rotating together with the earth rotation) coordinate system which translates together with the earth around the sun.

The equatorial coordinate system is defined as the (O;$X_{eq}Y_{eq}Z_{eq}$) system with

- Origin in the earth's centre.
- The Z_{eq} corresponding to the Z axis (the earth rotation axis).
- The positive X_{eq} containing the vernal equinox point.
- The Y_{eq} axis completing the right axis set.

Figure 8.10 shows the equatorial coordinate system, together with the vernal equinox point VE and the apparent orbit of the sun around the earth.

For the calculation of Θ_{sun} in function of time, the apparent orbit of the sun around the earth can be well approximated by a circle. The equatorial components (X_{eq}, Y_{eq}, Z_{eq}) of the unit vector $\vec{1}_{sun}$ pointing from the earth to the sun are therefore in good approximation given by equation 8.13 (see figure 8.10).

$$\begin{aligned} X_{eq} &= \cos(\delta) \\ Y_{eq} &= \sin(\delta)\cos(inc) \\ Z_{eq} &= \sin(\delta)\sin(inc) \end{aligned} \tag{8.13}$$

with δ the angle of $\vec{1}_{sun}$ with the positive X_{eq} direction (see figure 8.10). With the knowledge of t_{VE}, the time at which the sun passes the vernal equinox, δ can be calculated in function of the time t with equation 8.14.

$$\delta = \frac{t - t_{VE}}{365.25 \text{ days}} \tag{8.14}$$

Table 8.2.3 lists the values of t_{VE} for the year 1986 and 1994, obtained from [RB86, page A1] and [DB94, page A1] respectively[6].

Since $Z_{eq} = \cos(\Theta_{sun})$, Θ_{sun} can be calculated using the last line of equation 8.13, as in equation 8.15.

$$\Theta_{sun} = \cos^{-1}(\sin(\delta)\sin(inc)) \tag{8.15}$$

The cartesian coordinates of $\vec{1}_{sun}$ can be calculated from its spherical coordinates $(O; 1, \Theta_{sun}, \Phi_{sun})$ by application of equation 8.1.

[6] The reference time frame UT (Universal Time) mentioned in [RB86, page A1] and [DB94, page A1] has been replaced by the UTC reference time frame since those two never differ more than 0.7 seconds.

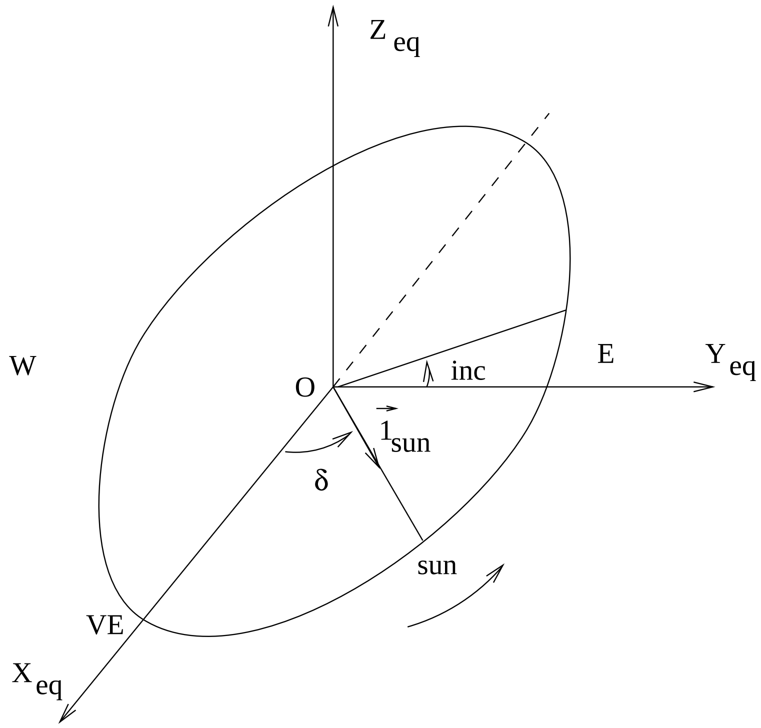

Figure 8.10: The apparent motion of the sun around the earth due to the earth's orbit around the sun, seen from the equatorial coordinate system.

t_{VE}	
20/03/1986	$22h03'$ UTC
20/03/1994	$20h28'$ UTC

Table 8.3: The time of the vernal equinox, t_{VE}, for the years 1986 and 1994.

8.2.4 Viewing angle calculation

Figure 8.11 shows the viewing zenith angle, θ_{sat}, the relative azimuth angle, ϕ_{rel}, and the solar zenith angle, θ_{sun}, in a given point P, in function of the local geometrical vertical $\vec{1}_{perp}$, the local satellite direction $\vec{1}_{PS}$ and the solar direction $\vec{1}_{sun}$.

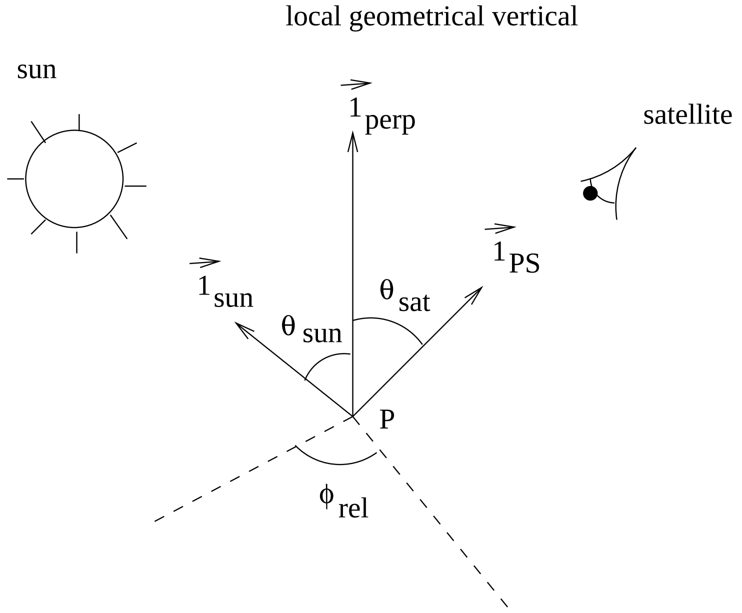

Figure 8.11: Dependency of the local viewing angles $(\theta_{sat}, \phi_{rel}, \theta_{sun})$ in a point P on the local geometrical vertical $\vec{1}_{perp}$, the local satellite direction $\vec{1}_{PS}$ and the solar direction $\vec{1}_{sun}$.

Once the cartesian components of $\vec{1}_{perp}$, $\vec{1}_{sun}$ and $\vec{1}_{PS}$ are known, the viewing zenith angle θ_{sat}, the relative azimuth angle ϕ_{rel} and the solar zenith angle θ_{sun} can be calculated with equations 8.16, 8.17 and 8.18 respectively.

$$\theta_{sat} = \cos^{-1}(\vec{1}_{perp}.\vec{1}_{PS}) \tag{8.16}$$

$$\phi_{rel} = \cos^{-1}(\vec{1}_{\vec{1}_{perp}\times\vec{1}_{sun}}.\vec{1}_{\vec{1}_{perp}\times\vec{1}_{PS}}) \tag{8.17}$$

$$\theta_{sun} = \cos^{-1}(\vec{1}_{perp}.\vec{1}_{sun}) \tag{8.18}$$

8.2.5 Application

The calculation of the METEOSAT viewing angles, that has been described here, will be applied in section 8.11 for the conversion of METEOSAT pixel reflected solar radiances to reflected solar flux surface densities.

8.3 Earth sun distance calculation

For the geometrical calculations in the sections 8.1 and 8.2, the orbit of the earth around the sun could be considered in good approximation as circular. However, for the calculation of the solar radiation falling on the earth, which is a direct function of the earth sun distance (see e.g. equation 2.17), the sun earth distance variation, due to the ellipticity of the orbit of the earth around the sun, has to be taken into account.

In this section, a mathematical description of the calculation of the earth sun distance is given.

8.3.1 Processing description card

name processing	earth sun distance calculation
technical novelty	none
novel algorithms	none
references	[RB86], [DB94], [Iqb83, pages 1-28]

Table 8.4: Processing card for earth sun distance calculation

8.3.2 Description

The earth translates around the sun in the ecliptic plane in a slightly elliptical orbit with eccentricity $ecc = 0.16714$. Consequently the earth sun distance changes approximately $2ecc \approx 3\%$[7] between the time the earth is closest to the sun, called the apohelium time, and the time the earth is farthest from the sun, called the perihelium time. Since the solar irradiance falling on the earth depends inverse quadratically on the sun earth distance (see equation 2.17), the distance change of approximately 3 % between the apohelium and the perihelium time, results in a irradiance change of approximately 6 %[8], which can not be neglected.

The apohelium falls approximately on the 4th of January of each year, the perihelium falls approximately on the 4th of July of each year. Table 8.5 lists the values of the apohelium time t_{ap} for the years 1986 and 1994, obtained from [RB86, page A1] and [DB94, page A1] respectively[9].

t_{ap}	
02/01/1986	$5h$ UTC
02/01/1994	$6h$ UTC

Table 8.5: The time of the apohelium, t_{ap}, for the years 1986 and 1994.

The earth sun distance, $r_{earth-sun}$, is given in sufficiently good approximation (see [RB86, page 24] and [DB94, page 24]) by equation 8.19.

$$r_{earth-sun} = \frac{1 \text{ A.U.}}{1 + ecc * \cos \delta_{ap}} \tag{8.19}$$

with

$$\delta_{ap} = \frac{t - t_{ap}}{365.25 \text{ days}} \tag{8.20}$$

For a given point P at the top of the earth atmosphere, the distance between P and the sun, r_{P-sun}, needed in the evaluation of equation 2.17, can be well approximated by the distance between the centre of the earth and the sun, $r_{earth-sun}$, since the earth radius is approximately 20000 times smaller than the earth sun distance.

[7] This change is relative to the mean earth sun distance.

[8] This change is relative to the mean solar irradiance falling on the earth.

[9] The reference time frame UT has again been replaced by the UTC time frame, since those two never differ more than 0.7 seconds.

8.3.3 Application

The calculation of the earth sun distance is used for the calculation of F_{SOL} (by means of equation 2.17), which is used in section 8.11 for solar reflected radiance to flux surface density conversion and in section 8.12 for the calculation of the net absorbed solar flux surface density, $F_{SW,IN}$ (by means of equation 2.15).

8.4 Monthly METEOSAT clear sky images

Monthly clear sky image determination is a simple, robust way to obtain images without cloud contamination (clear sky images) from a time series obtained for a fixed time of the day during the different days of a given month.

Combined with the cloud detection for individual daily images, obtained in section 8.6, the monthly clear sky images will be used to obtain instantaneous VIS clear sky images (see figure 7.1) in section 8.7.

The determination of monthly clear sky image grey values, and additional images of the uncertainties of these values, is described in this section.

8.4.1 Processing description card

name processing	clear sky determination
technical novelty	additional image of uncertainty factor
novel algorithms	none
references	[MH84a], [SD87], [DNCC95]

Table 8.6: Processing card for monthly clear sky determination

8.4.2 Description

Following [MH84a], [SD87], monthly METEOSAT clear sky images are obtained for every moment of the day through combination of the pixel grey values over one month. It is assumed that, for every pixel (location on earth) and for every moment of the day, at least one clear sky day occurs during the month[10].

For the IR images, it is assumed that clouds[11] are colder than the earth's surface, and thus that cloud IR grey values are lower than clear sky IR grey values. Therefore, for each pixel and for every slot of the day, the maximum over all grey values of the month is taken as clear sky value $C_{IR}^{cs}(pixel, slot, month)$.

$$C_{IR}^{cs}(pixel, slot, month) = \max_{day \in month} C_{IR}(pixel, slot, day) \tag{8.21}$$

The day for which the maximum is encountered, is denoted $day_{max}(pixel, slot, month)$

$$C_{IR}(pixel, slot, day_{max}) = C_{IR}^{cs}(pixel, slot, month) \tag{8.22}$$

The uncertainty of the maximum $u_{IR}^{cs}(pixel, slot, month)$ is defined as the difference of the maximum $C_{IR}^{cs}(pixel, slot, month)$ and the maximum of the remaining grey values

[10] If this assumption is not fulfilled, as can be the case for cloud fields that are very consistent in time, some cloud contamination will exist in the derived clear sky images. See e.g. the remaining cloud traces indicated in figure 8.14.

[11] The same holds for snow or ice cover, when this cover is not permanent over one month. For this reason, non permanent snow or ice cover will be treated as cloud throughout this study. Permanent snow or ice cover will be treated as clear-sky surface.

$$u^{cs}_{IR}(pixel, slot, month)$$
$$= C^{cs}_{IR}(pixel, slot, month) - \max_{\substack{day \in month \\ day \neq day_{max}}} C_{IR}(pixel, slot, day) \tag{8.23}$$

With this definition, the uncertainty is zero when the maximum occurs two times.

For the VIS images, it is assumed that clouds are more reflective than the earth's surface, and thus that cloud VIS grey values are higher than clear sky VIS grey values. Therefore, for each pixel and for every slot of the day, the minimum over all the grey values of the month is taken as clear sky value $C^{cs}_{VIS}(pixel, slot, month)$.

$$C^{cs}_{VIS}(pixel, slot, month) = \min_{day \in month} C_{VIS}(pixel, slot, day) \tag{8.24}$$

The day for which the minimum is encountered, is denoted $day_{min}(pixel, slot, month)$

$$C_{VIS}(pixel, slot, day_{min}) = C^{cs}_{VIS}(pixel, slot, month) \tag{8.25}$$

The uncertainty of the minimum $u^{cs}_{VIS}(pixel, slot, month)$ is defined as the difference of the minimum $C^{cs}_{VIS}(pixel, slot, month)$ and the minimum of the remaining grey values

$$u^{cs}_{VIS}(pixel, slot, month)$$
$$= C^{cs}_{VIS}(pixel, slot, month) - \min_{\substack{day \in month \\ day \neq day_{min}}} C_{VIS}(pixel, slot, day) \tag{8.26}$$

With this definition, the uncertainty is zero when the minimum occurs two times.

METEOSAT data in ISCCP B2 [Pro92] format yields one image every 3 hours, i.e. 8 IR images per day and 5 VIS images per day. The above clear sky determination applied to METEOSAT data in ISCCP B2 format yields 8 IR clear sky images and 5 VIS clear sky images per month.

Figures 8.14 and 8.15 show the VIS and IR clear-sky image of time slot 18 for November 1986. As a reference, the VIS and IR images of slot 18 for 8/11/86 are given in figures 8.12 and 8.13.

It can be seen that in the clear sky images, no more cloud traces are visible, except a few over the Gulf of Guinea in the VIS clear sky image (figure 8.14).

8.4.3 Shortcomings

The monthly clear sky determination yields clear sky images in a very simple and robust way, but it has the main disadvantage that it assumes that the clear sky values do not change over one month. In reality the clear sky values do vary during one month, due to changes in solar elevation and changes in surface state, especially in desert regions, and therefore grey values different from the monthly clear sky image grey values are not necessarily cloud contaminated. As a consequence the clear sky values can not be used for cloud detection, especially not in desert regions. In section 8.6, a strict separation between clear sky and cloud contaminated pixels will be made.

8.4.4 Application

The IR monthly clear sky images will be used, together with the derived images of uncertainty factors, in the next section for the estimation of IR diurnal cycle parameters. The VIS monthly clear sky image will be used in section 8.7 for the determination of an instantaneous VIS clear sky image (Referring to figure 7.1, see also box "Min/Max" (= monthly clear sky determination), the arrows to the boxes "Halfsine fit" (= IR diurnal cycle parameter estimation, explained in section 8.5) and "Top down image interpolation", explained in section 8.7.).

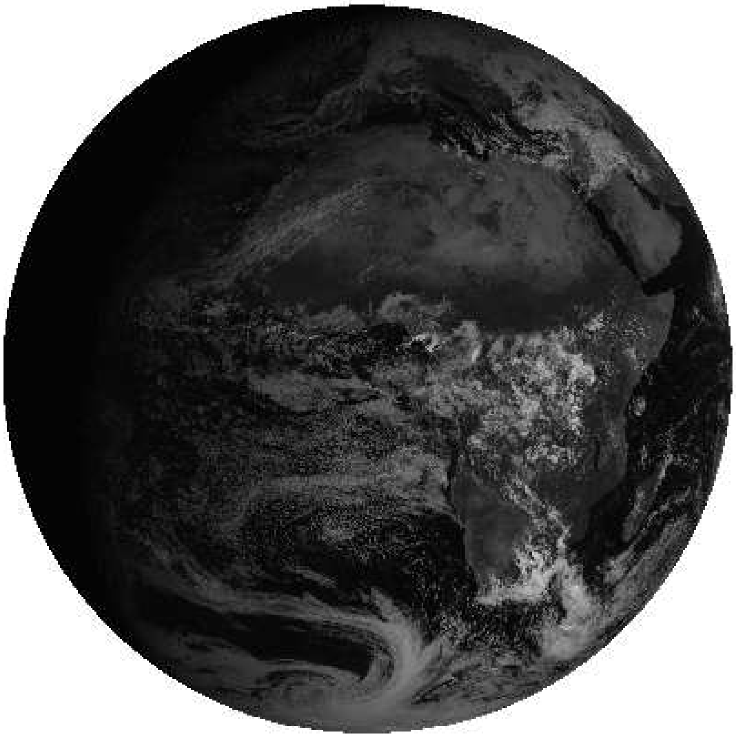

Figure 8.12: VIS image, 08/11/86, slot 18.

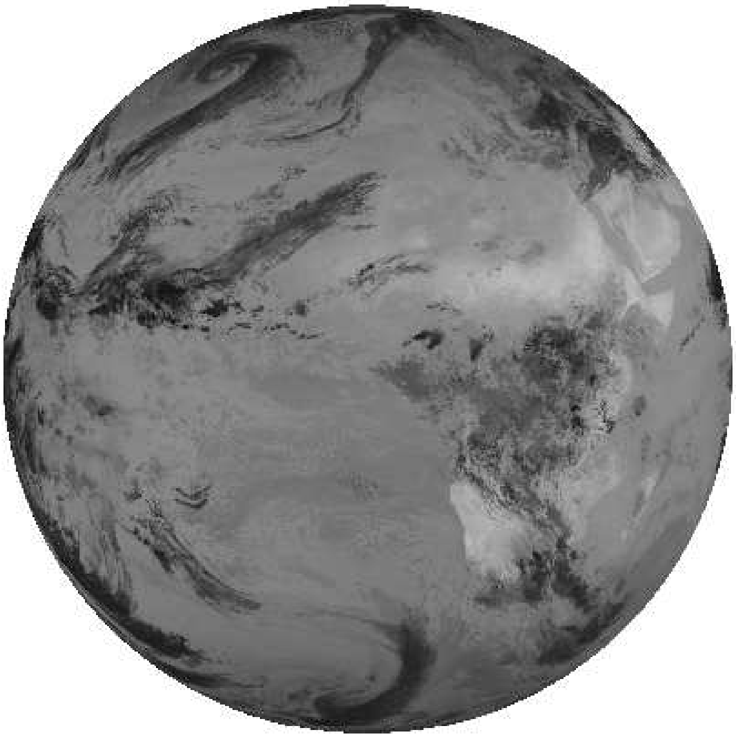

Figure 8.13: IR image, 08/11/86, slot 18.

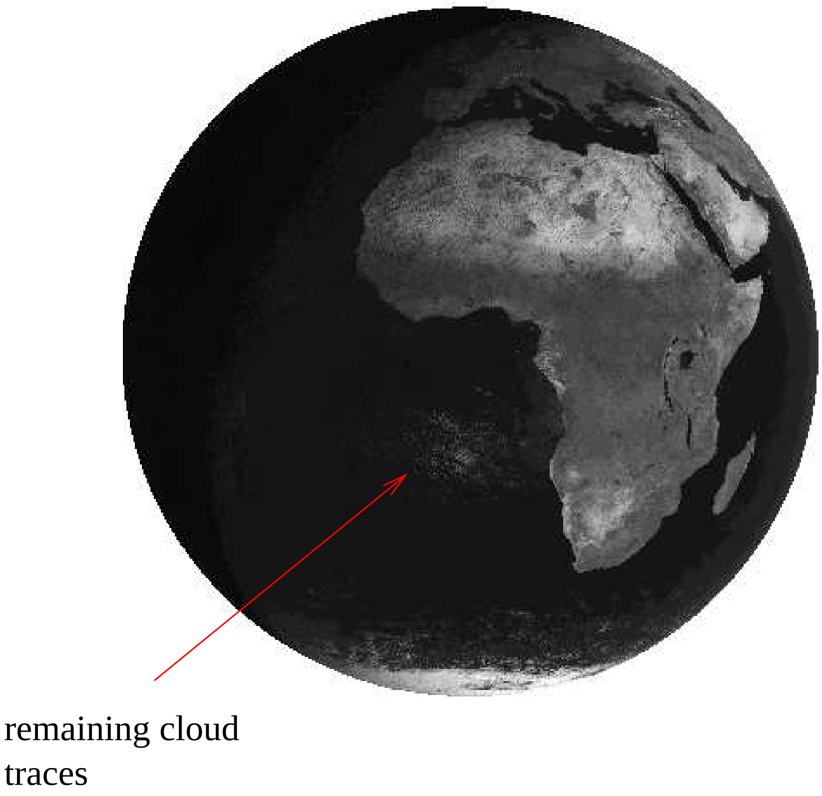

Figure 8.14: Monthly clear sky VIS image, 11/86, slot 18. Some remaining cloud traces over the Gulf of Guinea are indicated.

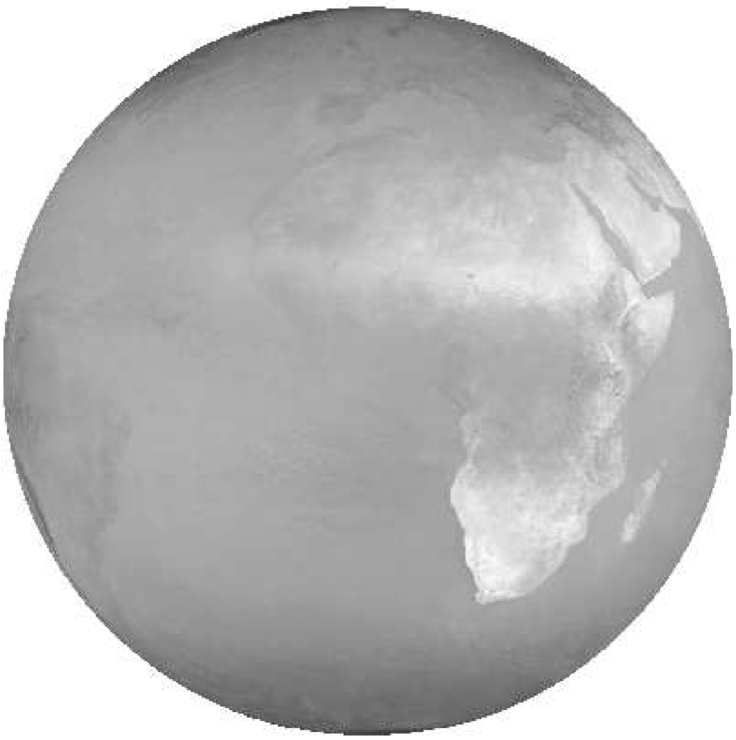

Figure 8.15: Monthly clear sky IR image, 11/86, slot 18.

8.5 METEOSAT IR surface diurnal cycle

From the IR monthly clear sky images derived in the previous section for 8 different times of the day, one can get a good idea of the diurnal cycle of the IR radiance (and hence implicitly of the temperature) for the different regions viewed by METEOSAT. This can serve as a basis for the recognition, through a parameter estimation method, of regions with high diurnal cycle variation amplitude (desert regions). This is interesting since regions with diurnal cycle variation amplitude, i.e. with high *thermal response* (typically desert regions, which have a high diurnal temperature change amplitude), are in general only covered by cloud systems which have very low persistence in time, while regions with low thermal response (typically oceans, which have almost no diurnal temperature change) can be covered by cloud systems which are very persistent in time (e.g. the stratocumulus field over the Gulf of Guinea, well visible in figure 8.12, which is very persistent in time, as can be seen from the remaining cloud traces in figure 8.14). Hence the separation of clear sky and cloud contaminated pixels based on the time variation of the pixel radiances, can be optimised if the thermal response of the clear sky pixel is known. This will be applied in section 8.6.

In this section the procedure to obtain a thermal response image from monthly IR clear sky images, is described.

8.5.1 Processing description card

name processing	diurnal cycle fit
technical novelty	fitting functions
novel algorithms	none
references	[MH84a], [DNCC95]

Table 8.7: Processing card for diurnal cycle fit

8.5.2 Description

In this section, the IR clear sky images obtained in the previous section are further combined, yielding a thermal response image, describing the diurnal variation of the clear sky radiance as seen by the IR channel of the METEOSAT satellite.

It is assumed that the diurnal variation of the clear sky radiance as seen by the METEOSAT IR channel can be modelled as a linear variation between the sunset value and the sunrise value, superimposed with a half sine variation during day (maximum at noon, zero at sunset and sunrise). The fit used in [MH84a] to model the clear-sky temperature variation is shown in figure 8.16, the model used in this section is depicted in figure 8.18.

For every pixel (location on earth) and for every METEOSAT slot the pixel acquisition time (for the day in the middle of the month) is calculated. From this pixel acquisition time and from the pixel geolocation, the local time for the pixel is calculated. The variation of the monthly clear sky radiance of the pixel in function of the local time is approximated with regression expression 8.27, with the clear sky sunrise pixel value, $C_{IR}^{cs,sr}$, the clear sky sunset value, $C_{IR}^{cs,ss}$, and the clear sky half sine amplitude, $C_{IR}^{cs,hs}$, as regression parameters.

$$C_{IR}^{cs,fit}(t) = C_{IR}^{cs,sr} f_{sr}(t) + C_{IR}^{cs,ss} f_{ss}(t) + C_{IR}^{cs,hs} f_{hs}(t) \tag{8.27}$$

If t is the relative local time (0.5=local noon; 0,1=local midnight; t_{sr}=sunrise time, t_{ss}=sunset time), the regression functions are given by equation 8.28 (see also figure 8.17).

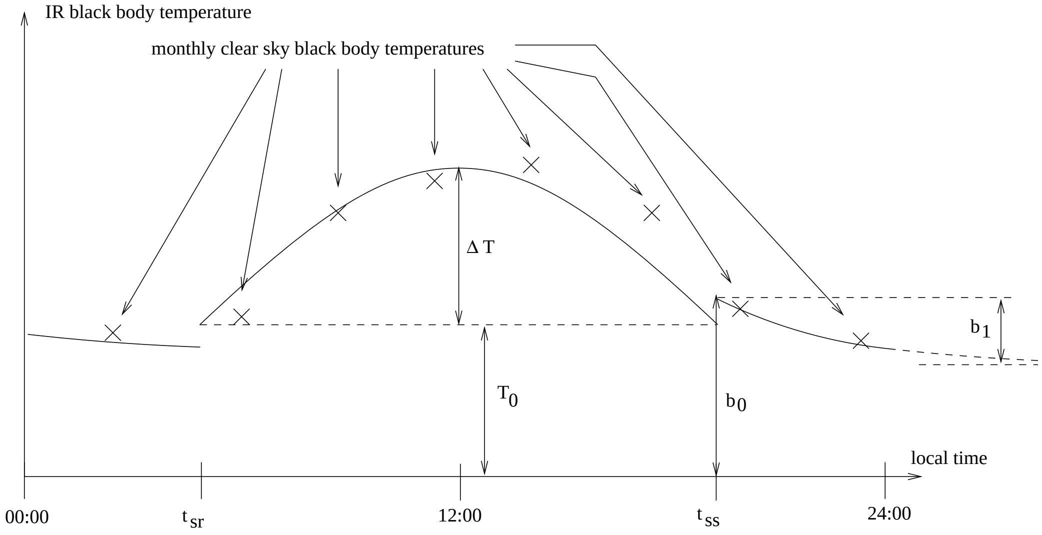

Figure 8.16: Diurnal cycle fit (case k=1) as carried out by [MH84a]. t_{sr} = sunrise time. t_{ss} = sunset time. Fitted parameters: T_0, ΔT, b_0, b_1.

$$
\begin{aligned}
f_{sr}(t) &= \begin{array}{ll} \frac{(1-t_{ss})+t}{t_{sr}+(1-t_{ss})} & \text{if } 0 \le t < t_{sr} \\ \frac{t_{ss}-t}{t_{ss}-t_{sr}} & \text{if } t_{sr} \le t < t_{ss} \\ \frac{t-t_{ss}}{1+t_{sr}-t_{ss}} & \text{if } t_{ss} \le t \le 1 \end{array} \\
f_{ss}(t) &= 1-(1-f_{sr}) \\
f_{hs}(t) &= \begin{array}{ll} 0 & \text{if } 0 \le t < t_{sr} \\ \cos\left(\frac{|t-0.5|}{t_{ss}-0.5}\frac{\pi}{2}\right) & \text{if } t_{sr} \le t < t_{ss} \\ 0 & \text{if } t_{ss} \le t \le 1 \end{array}
\end{aligned}
\tag{8.28}
$$

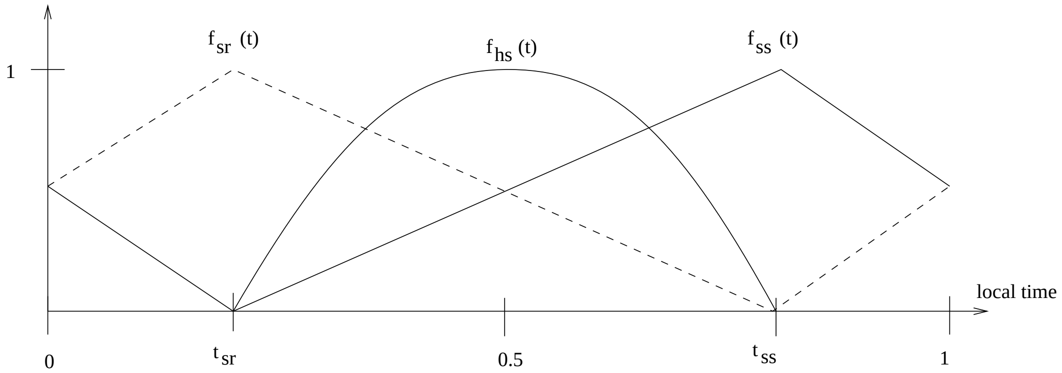

Figure 8.17: Regression functions, $f_{sr}(t)$, $f_{ss}(t)$ and $f_{hs}(t)$, used in regression 8.27. t_{sr} = sunrise time. t_{ss} = sunset time.

The 3 regression parameters $C_{IR}^{cs,sr}(pixel, month)$, $C_{IR}^{cs,ss}(pixel, month)$ and $C_{IR}^{cs,hs}(pixel, month)$ are determined from the quantities $C_{IR}^{cs}(pixel, slot, month)$ measured for the eight ISCCP slots by solving the weighted least squares equations

$$H^T W H X_{ls} = H^T W Y_{ls} \tag{8.29}$$

with

$$H = \begin{bmatrix} \vdots & \vdots & \vdots \\ f_{sr}(t_i) & f_{ss}(t_i) & f_{hs}(t_i) \\ \vdots & \vdots & \vdots \end{bmatrix} \tag{8.30}$$

$$W = \begin{bmatrix} \ddots & & 0 \\ & 1/(1+u_{IR}^{cs}(t_i))^2 & \\ 0 & & \ddots \end{bmatrix} \tag{8.31}$$

$$X_{ls} = \begin{bmatrix} C_{IR}^{cs,sr} \\ C_{IR}^{cs,ss} \\ C_{IR}^{cs,hs} \end{bmatrix} \tag{8.32}$$

$$Y_{ls} = \begin{bmatrix} \vdots \\ C_{IR}^{cs}(t_i) \\ \vdots \end{bmatrix} \tag{8.33}$$

The weighted least squares fit is demonstrated graphically in figure 8.18.

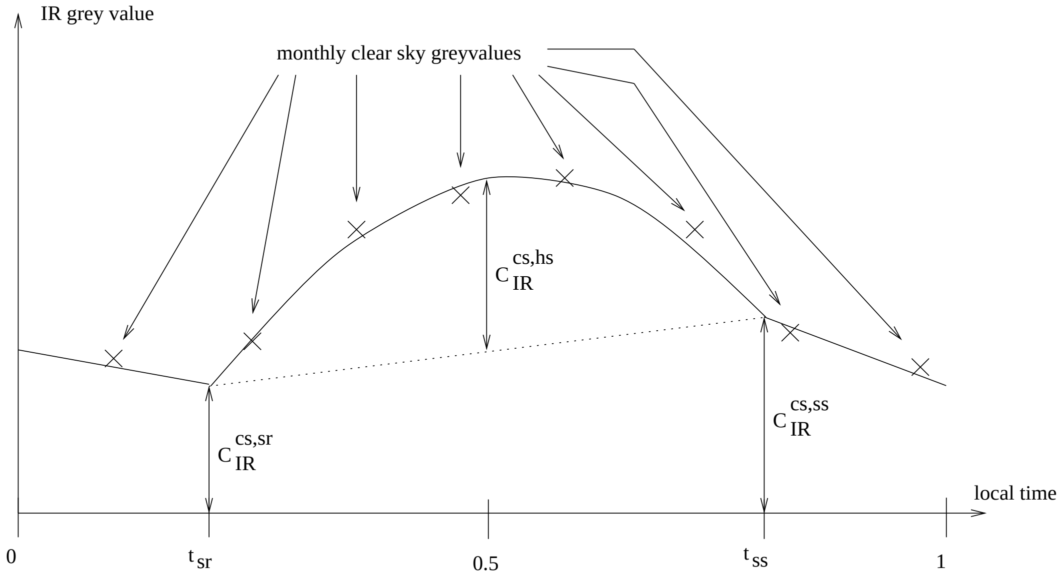

Figure 8.18: Half sine fit for clear sky IR images. Local time is given relatively (0.5=local noon; 0,1=local midnight, $t_{sunrise}$=sunrise time, t_{sunset}=sunset time). The three regression parameters are the sunrise value $C_{IR}^{cs,sr}$, the sunset value $C_{IR}^{cs,ss}$ and the half sine amplitude $C_{IR}^{cs,hs}$.

It is assumed that the sunrise and sunset values depend mainly on seasonal influences and that the half sine amplitude depends mainly on surface properties. The half sine amplitude is a measurement of the thermal response of the surface and can thus be considered as a kind of measurement of desertuousness. The thermal response image for November 1986 is shown in figure 8.19.

8.5.3 Application

The thermal response images that have been obtained in this section, will be used in the next section for tuning the parameters of the morphological filtering technique (see section 7.2) for optimal cloud detection (see also box “Half sine fit” = diurnal cycle estimation in figure 7.1).

Figure 8.19: Thermal response image, 11/86.

8.6 METEOSAT cloud mask

A METEOSAT cloud mask is a binary image, indicating the presence of clouds in the METEOSAT image to which it is associated.

In this work, the METEOSAT VIS cloud mask, i.e. the cloud mask associated to a given METEOSAT VIS image, is applied in section 8.7 for the determination of METEOSAT VIS clear sky images, which are themselves used for an optimal scene identification in section 8.11.

In this work, separate VIS and IR METEOSAT cloud masks are determined. The IR cloud masks are used as intermediate results which improve the quality of the VIS cloud masks.

In this section, the procedure to obtain a multi spectral (i.e. obtained from combined IR and VIS information) VIS (i.e. applicable to a VIS image) cloud mask, is described.

8.6.1 Processing description card

name processing	cloud mask determination
technical novelty	separate cloud mask for IR and VIS images
novel algorithms	image equalisation (section 7.1) morphological filtering (section 7.2)
references	[DNCC95],[DCC96]

Table 8.8: Processing card for cloud mask determination

8.6.2 Description

In this section, VIS cloud mask images, i.e. binary images indicating the presence of clouds in the VIS images, are obtained. In an intermediate stage, IR cloud mask images are also obtained. It is assumed, supported by experimental evidence, that no pixels can be cloudy in the VIS image if they are clear sky in the IR image. Hence the IR cloud mask image is used as auxiliary data in the determination of the VIS clear sky image.

Figure 8.20 describes the different steps in the determination of the (multi spectral) VIS cloud mask. These different steps are described below.

Mono spectral VIS cloud mask In this paragraph, a mono spectral[12] VIS cloud mask (see left most branch of figure 8.20) is determined.

In order to obtain a maximum contrast between clouds and clear sky values, image equalisation (see section 7.1) is applied to the time series of VIS images obtained for consecutive days of a given month, for a given fixed slot (time of the day).

$$\begin{aligned}
&I_t(i,j) = C_{VIS}(pixel = (i,j), slot, day = t, month) \\
&I_t^{eq}(i,j) = T^{eq}(I_t(i,j)) \\
&C_{VIS}^{eq}(pixel = (i,j), slot, day = t, month) = I_t^{eq}(i,j)
\end{aligned} \tag{8.34}$$

Next, a daily clear sky image is obtained using morphological minimum filtering (see section 7.2) as a refinement of the minimum method used in section 8.4.

$$\begin{aligned}
&C_{VIS}^{eq,cs}(pixel, slot, day = t, month) \\
&= C_{VIS}^{eq}(pixel, slot, day = t, month) \ominus V_{sl}(t)
\end{aligned} \tag{8.35}$$

Experimentally it was found that for zones with high thermal diurnal variation (deserts) in general there is low cloud persistence (few cloudy days, and therefore good detectability of clouds through morphological filtering) and high monthly clear sky variation (resulting in possible false detection of clear-sky variation as cloudiness). Therefore the slope parameter sl used in the morphological filtering 8.35 is made dependent on the diurnal cycle amplitude (thermal response), $C_{IR}^{cs,hs}$, found in section 8.5. An experimentally obtained value for the slope parameter

[12] i.e. using only VIS image information to derive a VIS cloud mask

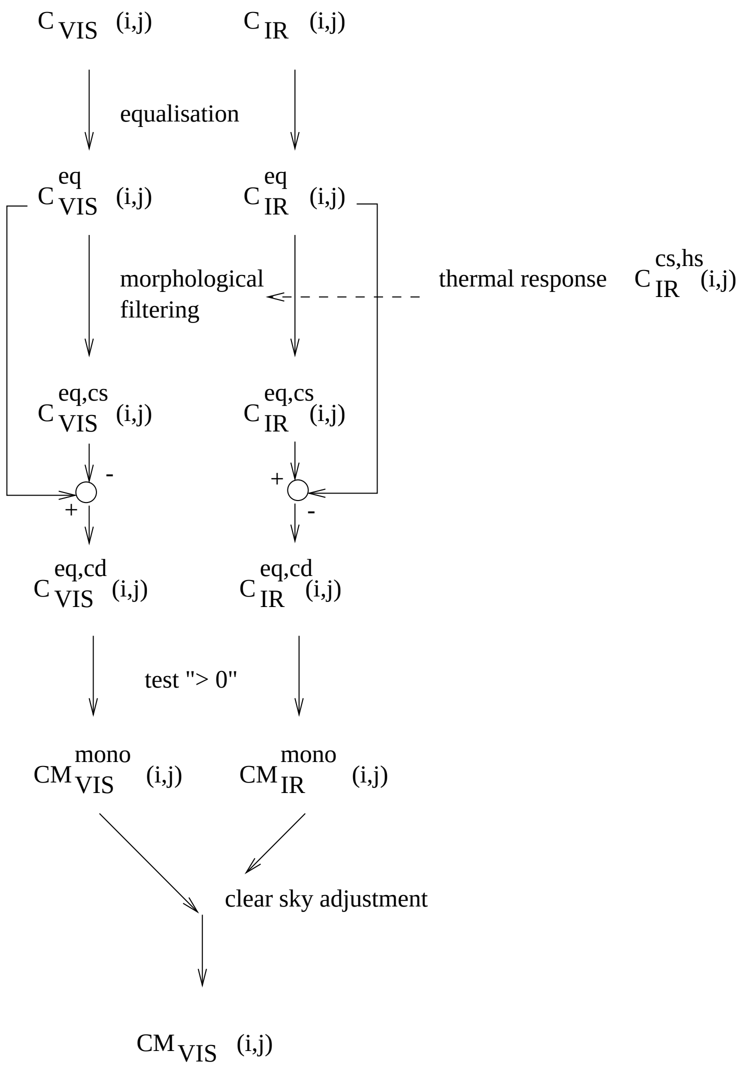

Figure 8.20: Overview of the different steps carried out, and intermediate results used, to obtain a multi spectral VIS cloud mask $CM_{VIS}(i,j)$ from METEOSAT VIS image counts (grey values), $C_{VIS}(i,j)$, and METEOSAT IR image counts (grey values), $C_{IR}(i,j)$.

$sl = (8 \text{ counts} + 0.8 C_{IR}^{cs,hs})$/day was chosen to obtain a good follow-up of the time variation of the VIS clear sky values.

Next a cloud difference image $C_{VIS}^{eq,cd}(pixel, slot, day, month)$ is obtained as the difference between the equalised VIS image and its corresponding clear sky image.

$$\begin{aligned} & C_{VIS}^{eq,cd}(pixel, slot, day, month) \\ = & C_{VIS}^{eq}(pixel, slot, day, month) - C_{VIS}^{eq,cs}(pixel, slot, day, month) \end{aligned} \tag{8.36}$$

Finally the mono spectral VIS cloud mask $CM_{VIS}^{mono}(pixel, slot, day, month)$ is obtained by identifying clear sky with zero cloud difference.

$$\begin{aligned} CM_{VIS}^{mono}(pixel, slot, day, month) = 0 \quad & \text{if } C_{VIS}^{eq,cd}(pixel, slot, day, month) = 0 \\ CM_{VIS}^{mono}(pixel, slot, day, month) = 1 \quad & \text{if } C_{VIS}^{eq,cd}(pixel, slot, day, month) > 0 \end{aligned} \tag{8.37}$$

The different steps in the determination of $CM_{VIS}^{mono}(i,j)$ are summarised as the left most branch of figure 8.20.

Mono spectral IR cloud mask In this paragraph, a mono spectral[13] IR cloud mask (see right most branch of figure 8.20) is determined. The way of obtaining this mask is analogous as the one followed for the mono spectral VIS cloud mask.

As in the VIS case, image equalisation (see section 7.1) is applied to the time series of IR images obtained for consecutive days of a given month, for a given fixed slot (time of the day).

$$\begin{aligned} & I_t(i,j) = C_{IR}(pixel = (i,j), slot, day = t, month) \\ & I_t^{eq}(i,j) = T^{eq}(I_t(i,j)) \\ & C_{IR}^{eq}(pixel = (i,j), slot, day = t, month) = I_t^{eq}(i,j) \end{aligned} \tag{8.38}$$

Figure 8.21 shows the equalised IR image for 08/11/86, slot 18 (8:30-8:55 UTC). When this image is compared with its non equalised version (figure 8.13), it can be seen that e.g. the detectability of the large stratocumulus cloud field over the Gulf of Guinea has been improved thanks to the image equalisation.

Next, a daily clear sky image is obtained using morphological maximum filtering (see section 7.2) as a refinement of the maximum method in section 8.4.

$$\begin{aligned} & C_{IR}^{eq,cs}(pixel, slot, day = t, month) \\ = & C_{IR}^{eq}(pixel, slot, day = t, month) \oplus V_{-sl}(t) \end{aligned} \tag{8.39}$$

A value $sl = (3 \text{ count} + 0.5 C_{IR}^{cs,hs})$/day was chosen experimentally to obtain a good follow-up of the time variation of the IR clear sky values.

Next, a cloud difference image $C_{IR}^{eq,cd}(pixel, slot, day, month)$ is obtained as the difference between the equalised VIS image and its corresponding clear sky image.

$$\begin{aligned} & C_{IR}^{eq,cd}(pixel, slot, day, month) \\ = & C_{IR}^{eq,cs}(pixel, slot, day, month) - C_{IR}^{eq}(pixel, slot, day, month) \end{aligned} \tag{8.40}$$

Finally, the mono spectral IR cloud mask $CM_{IR}^{mono}(pixel, slot, day, month)$ is obtained by identifying clear sky with zero cloud difference.

$$\begin{aligned} CM_{IR}^{mono}(pixel, slot, day, month) = 0 \quad & \text{if } C_{IR}^{eq,cd}(pixel, slot, day, month) = 0 \\ CM_{IR}^{mono}(pixel, slot, day, month) = 1 \quad & \text{if } C_{IR}^{eq,cd}(pixel, slot, day, month) > 0 \end{aligned} \tag{8.41}$$

The different steps in the determination of $CM_{IR}^{mono}(i,j)$ are summarised as the right most branch of figure 8.20.

[13] i.e. using only IR image information to derive an IR cloud mask

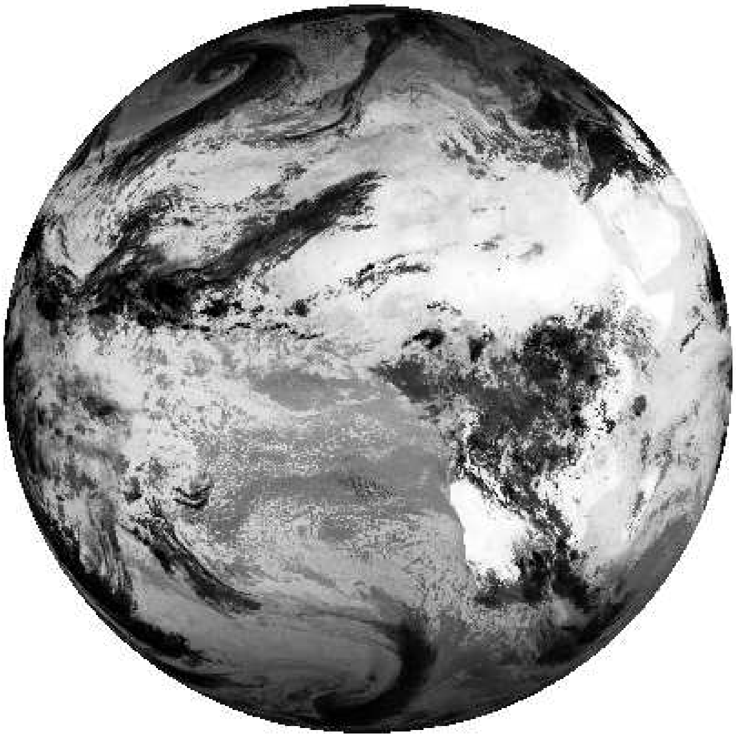

Figure 8.21: Equalised IR image, 08/11/86, slot 18.

Multi spectral VIS cloud mask In this paragraph, a multi spectral VIS cloud mask (see bottom part of figure 8.20) is determined by combining the mono spectral VIS and IR cloud masks. Since it is found experimentally that no VIS cloudy values occur for IR clear sky values, the multi spectral VIS cloud mask $CM_{VIS}(pixel, slot, day, month)$ is obtained from the mono spectral VIS cloud mask $CM_{VIS}^{mono}(pixel, slot, day, month)$ where IR clear sky cases (identified by $CM_{IR}^{mono}(pixel, slot, day, month) = 0$) are adjusted to clear sky.

$$\begin{array}{c} CM_{VIS}(pixel, slot, day, month) = CM_{VIS}^{mono}(pixel, slot, day, month) \\ \text{if } CM_{IR}^{mono}(pixel, slot, day, month) = 1 \\ \\ CM_{VIS}(pixel, slot, day, month) = 0 \\ \text{if } CM_{IR}^{mono}(pixel, slot, day, month) = 0 \end{array} \tag{8.42}$$

This operation in indicated in the bottom part of figure 8.20.

8.6.3 Application

The multi spectral VIS cloud mask derived here, is used in section 8.7 to estimate an instantaneous VIS clear sky count (grey value), which will be used in section 8.11 for scene identification (See also lines "mono spectral instantaneous clear sky images" and "multi spectral VIS cloud mask" in figure 7.1.).

8.7 METEOSAT instantaneous clear sky count

The instantaneous clear sky count for a given METEOSAT pixel, is the count (grey value) the pixel has when the pixel is not cloud contaminated. The term "instantaneous" is used to make a distinction with the monthly clear sky counts (grey values) derived in section 8.4.

Since the clear sky count for a given pixel can change during one month, the instantaneous count of a clear sky pixel does not necessarily correspond to the monthly clear sky count of the pixel.

Instantaneous clear sky counts are obtained by spatial interpolation (application of the technique of section 7.4) of the differences of the instantaneous counts of detected clear sky pixels (application of the results obtained in section 8.6) with the monthly clear sky counts of these pixels (obtained in section 8.4).

This results in a clear sky image with the following properties :

- For detected clear sky pixels, the clear sky image count is exactly the METEOSAT image count.
- The image is spatially coherent, i.e. no artificial spatial discontinuities exist in the images. In particular, clear sky/cloud borders in the METEOSAT image from which the clear sky image is derived, are not visible as discontinuities in the derived clear sky image.

The obtained clear sky images will be used in the radiance to flux surface density conversion of section 8.11 for

- an application of clear sky and cloudy ADM's which does not introduce spatial discontinuities in the estimated flux surface densities
- the recognition of time varying clear sky surface states (due to e.g. seasonal evolution of non permanent desert areas)

In this section, it is described how an instantaneous METEOSAT VIS clear sky image is obtained.

8.7.1 Processing description card

name processing	instantaneous clear sky count determination
technical novelty	non smoothing in cloud free zones values for cloud covered zones are spatially coherent with values for cloud free zones
novel algorithms	non smoothing interpolation (section 7.4)
references	[DCC96]

Table 8.9: Processing card for instantaneous clear sky count determination

8.7.2 Description

From the VIS monthly clear sky image $C^{cs}_{VIS}(pixel, slot, month)$ obtained in section 8.4 and from the multi spectral VIS cloud mask $CM_{VIS}(pixel, slot, day, month)$ obtained in section 8.6, a difference between the instantaneous clear sky count and the monthly clear sky count $C^{cs,diff}_{VIS}(pixel, slot, day, month)$ can be calculated for the detected instantaneous clear sky pixels.

$$\begin{array}{c} C^{cs,diff}_{VIS}(pixel, slot, day, month) = C_{VIS}(pixel, slot, day, month) - C^{cs}_{VIS}(pixel, slot, month) \\ \text{if } CM_{VIS}(pixel, slot, day, month){=}1 \\ \\ \text{not calculated elsewhere} \end{array} \tag{8.43}$$

This difference can be interpolated using a non smoothing interpolation, described in section 7.4, with the cloud mask as mask image, and the land/ocean values from the database described in section 4.3 as class image.

$$\begin{array}{l} M(i,j) = CM_{VIS}(pixel, slot, day, month) \\ C(i,j) = 1 \quad \text{if ocean} \\ C(i,j) = 0 \quad \text{if land} \\ I(i,j) = C^{cs,diff}_{VIS}(pixel, slot, day, month) \\ C^{cs,diff-ip}_{VIS}(pixel, slot, day, month) = I(i,j) \end{array} \tag{8.44}$$

This results in an interpolated clear sky difference image, with counts $C_{VIS}^{cs,diff-ip}$, which is defined for clear sky as well as for cloudy pixels, and which is spatially coherent. This allows the calculation of instantaneous clear sky pixel values $C_{VIS}^{cs}(pixel, slot, day, month)$

$$\begin{aligned} & C_{VIS}^{cs}(pixel, slot, day, month) \\ = & C_{VIS}^{cs}(pixel, slot, month) + max(C_{VIS}^{cs,diff-ip}(pixel, slot, day, month), 0) \end{aligned} \tag{8.45}$$

which are spatially coherent and which are exactly equal to the pixel values $C_{VIS}(pixel, slot, day, month)$ for detected instantaneous clear sky pixels ($CM_{VIS}(pixel, slot, day, month) = 1$).

8.7.3 Application

The instantaneous VIS clear sky image, that has been derived here (see also box "Top down image interpolation" in figure 7.1), will be applied in section 8.11 (see also figure 8.1) for the determination of clear sky compatible, spatially coherent ADM's for individual METEOSAT pixels.

8.8 METEOSAT time interpolation

METEOSAT time interpolation can be used in order to obtain METEOSAT derived radiation budget term estimates at maximal time resolution.

Time interpolation based on motion estimation yields in principle better results than simple linear time interpolation. However, with classical segment based motion estimation, block artifacts can occur in the time interpolated results.

In this work, thanks to the use of the novel motion estimation technique of section 7.5, block artifacts in the motion interpolated results are avoided.

In this section, METEOSAT image time interpolation, with and without the use of motion interpolation, is described.

8.8.1 Processing description card

name processing	time interpolation
technical novelty	no block artifacts
novel algorithms	motion estimation (section 7.5)
references	[DCC96]

Table 8.10: Processing card for time interpolation

8.8.2 Description

If two slots of METEOSAT images are given for a given channel and for a given day

$$\begin{aligned} i_1(i,j) &= C_{channel}(pixel, slot_1, day, month) \\ i_2(i,j) &= C_{channel}(pixel, slot_2, day, month) \end{aligned} \tag{8.46}$$

a motion estimation can be carried out as explained in section 7.5 which yields the motion vector $(o_1(i,j), o_2(i,j))$ applicable at slot $s = (1-f) * slot_1 + f * slot_2$.

The time interpolated image $i_{(1-f)*1+f*2}(i,j)$ for slot s is given by

$$i_{(1-f)*1+f*2}(i,j) = \begin{array}{c} (1-f) * i_1(i - f * o_1(i,j), j - f * o_2(i,j)) \\ +f * i_2(i + (1-f) * o_1(i,j), j + (1-f) * o_2(i,j)) \end{array} \tag{8.47}$$

Alternatively, if no motion estimation is available, a simple linear time interpolation can be obtained as

$$i_{(1-f)*1+f*2}(i,j) = (1-f) * i_1(i,j) + f * i_2(i,j) \tag{8.48}$$

8.8.3 Application

METEOSAT time interpolation is used for time resolution enhancement of METEOSAT data prior to radiation budget estimation (see box "Motion time interpolation" in figure 7.2).

8.9 METEOSAT radiation budget term estimation

The ultimate goal of all the processing steps explained so far in chapters 7 and 8 (with the exception of the compression techniques at the end of chapter 7) is to obtain radiation budget term (reflected solar flux surface density, F_{SW}, and emitted thermal flux surface density, F_{LW}) estimates from METEOSAT data

- at the highest possible space/time resolution
- without introducing artificial spatial or temporal discontinuities in the radiation budget term estimates
- with a stand alone method, i.e. with an estimation method independent of any other radiation budget term estimate data set, so that validation with e.g. an independent LEO radiation budget term data set remains possible

For the long wave (thermal emission) radiation budget term, these requirements can be met by application of the existing estimation method of [SL88], [SMvdB90] to full resolution METEOSAT IR and WV data. This will be done in section 8.10.

For the short wave radiation budget term, scene identification is an integral part of the radiation budget term estimation, because the dependency of the reflected solar flux surface density (the short wave radiation budget term) on the VIS radiance measured by METEOSAT, is strongly scene dependent.

Cloud/clear sky separation is an important part of the scene identification required for an optimal short wave radiation budget term estimation from METEOSAT data. Therefore, in order to obtain high resolution, spatially coherent (i.e. without artificial spatial discontinuities) short wave radiation budget term estimates, the high resolution, spatially coherent clear sky determination obtained so far (section 8.7) is integrated in the reflected solar flux surface density estimation in section 8.11.

Before describing the reflected solar flux surface density estimation in section 8.11, the emitted thermal flux surface density estimation is described in section 8.10.

8.10 Long wave flux surface density estimation

8.10.1 Processing description card

name processing	long wave flux surface density estimation
technical novelty	applied to high resolution images
novel algorithms	none
references	[SL88], [SMvdB90]

Table 8.11: Processing card for long wave flux surface density estimation

8.10.2 Description

For the estimation of F_{LW} from METEOSAT data, the method of [SL88], [SMvdB90] is used and applied to full resolution IR and WV data. For completeness, the different steps are described here briefly.

1. The digital counts C_{IR},C_{WV} are converted to calibrated filtered radiances L_{IR},L_{WV} using the linear calibration relations

$$L_{IR} = k_{IR}(C_{IR} - C_{IR,0}) \tag{8.49}$$

$$L_{WV} = k_{WV}(C_{WV} - C_{WV,0}) \tag{8.50}$$

   where the calibration coefficients k_{IR}, $C_{IR,0}$, k_{WV} and $C_{WV,0}$ are given in the ESOC/MIEC or EUMETSAT/MPEF METEOSAT radiometer calibration reports.

2. From the filtered radiances, L_{IR} and L_{WV}, the filtered flux surface densities, F_{IR} and F_{WV}, are estimated as

$$F_{IR} = a(\theta_{sat})L_{IR}(\theta_{sat}) + b(\theta_{sat}) \tag{8.51}$$

$$F_{WV} = c(\theta_{sat})L_{WV}(\theta_{sat}) + d(\theta_{sat}) \tag{8.52}$$

$$a(\theta_{sat}) = k_1 + k_2(sec(\theta_{sat}) - 1) + k_3(sec(\theta_{sat}) - 1)^2 \tag{8.53}$$

$$b(\theta_{sat}) = k_4 + k_5(sec(\theta_{sat}) - 1) + k_6(sec(\theta_{sat}) - 1)^2 \tag{8.54}$$

$$c(\theta_{sat}) = l_1 + l_2(sec(\theta_{sat}) - 1) + l_3(sec(\theta_{sat}) - 1)^2 \tag{8.55}$$

$$d(\theta_{sat}) = l_4 + l_5(sec(\theta_{sat}) - 1) + l_6(sec(\theta_{sat}) - 1)^2 \tag{8.56}$$

   where the coefficients k_i, l_i, $i = 1, \ldots, 6$ are obtained as best fit coefficients from radiative transfer simulations [SL88], [SMvdB90].

3. From the filtered flux surface densities F_{IR},F_{WV} the (unfiltered) emitted long wave flux surface density F_{LW} is estimated as

$$F_{LW} = \xi_0 + \sum_{i=1}^{3} \xi_i (F_{IR})^i + \sum_{i=1}^{3} \zeta_i (F_{WV})^i \tag{8.57}$$

   where the coefficients ξ_i, $i = 0, \ldots, 3$ ζ_i, $i = 1, \ldots, 3$ are also obtained as best fit coefficients from radiative transfer simulations [SL88], [SMvdB90].

Figure 8.22 shows the result of this procedure applied to the METEOSAT IR and WV data of 08/11/1986(dd/mm/yyyy) time slot 18 (08:30 UTC-08:55 UTC).

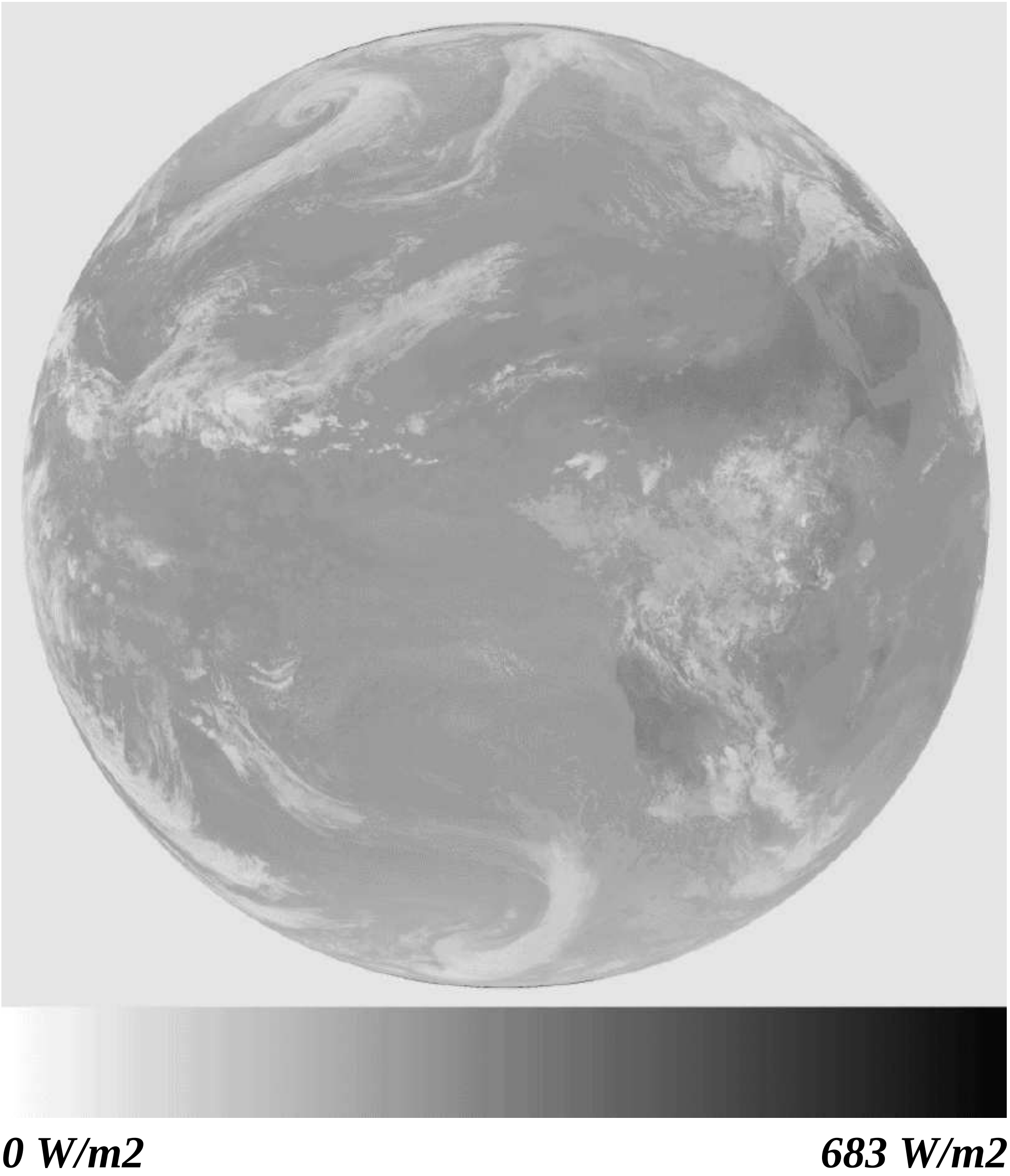

Figure 8.22: Long wave flux surface density estimated from METEOSAT IR and WV data, for 08/11/1986 time slot 18 (08:30 UTC-08:55 UTC).

8.11 Reflected short wave flux surface density

8.11.1 Processing description card

name processing	short wave flux surface density estimation
technical novelty	scene dependent spectral conversion included in radiance to flux surface density conversion, instantaneous clear sky count estimation included in radiance to flux surface density conversion, continuous broad band scene identification applied to high resolution images
novel algorithms	novel scene identification
references	[RDBW92], [DMSCC]

Table 8.12: Processing card for short wave flux surface density estimation

8.11.2 Description

In this section, short wave flux surface density estimates are derived from full resolution METEOSAT VIS images. This involves calibration, scene identification, scene dependent spectral conversion, and scene dependent radiance to flux surface density conversion.

8.11.3 Calibration of the METEOSAT 2 visible channel

The digital counts C_{VIS} are converted to calibrated filtered radiances L_{VIS} using the linear calibration relation

$$L_{VIS} = k_{VIS}(C_{VIS} - C_{VIS,0}) \tag{8.58}$$

where $C_{VIS,0}$ (lowest count during night) = 2 and where k_{VIS} is the calibration factor. The default value of k_{VIS} is based on the factors

$$k_{VIS,ISCCP}(date) = k_{VIS}^{nominal} k_{VIS,ISCCP}^{nominal \rightarrow absolute}(date) \tag{8.59}$$

reported in [RDBW92]. $k_{VIS,ISCCP}(date)$ is the calibration factor k_{VIS} given by ISCCP for a given date. It consists of the nominal calibration factor $k_{VIS}^{nominal}$ multiplied by a correction factor $k_{VIS,ISCCP}^{nominal \rightarrow absolute}(date)$. The correction factors $k_{VIS,ISCCP}^{nominal \rightarrow absolute}(date)$ are measured every three months by comparison of METEOSAT 2 visible channel measurements and NOAA 9 AVHHR channel 1 (spectral range $\approx$ [0.55 μm to 0.7 μm]) measurements with coinciding viewing geometry and time of acquisition. The factors $k_{VIS,ISCCP}^{nominal \rightarrow absolute}(date)$ from 04/1985 to 04/1987, calculated from [RDBW92] are given in table 8.13.

month/year	$k_{VIS,ISCCP}^{nominal \rightarrow absolute}$	month/year	$k_{VIS,ISCCP}^{nominal \rightarrow absolute}$
04/1985	1.1886	07/1986	1.1897
07/1985	1.1842	10/1986	1.2397
10/1985	1.1702	01/1987	1.1728
01/1986	1.1275	04/1987	1.1946
04/1986	1.1731		

Table 8.13: Factors $k_{VIS,ISCCP}^{nominal \rightarrow absolute}(date)$ from 04/1985 to 04/1987 with time step of three months.

It can be noticed that the factors $k_{VIS,ISCCP}^{nominal \rightarrow absolute}(date)$ are almost constant over this two-year period, with a downward exception for 01/1986, and an upward exception for 10/1986.

It is assumed that this downward and upward exception are calibration measurement anomalies. This leads to the assumption that k_{VIS} is a constant in time (i.e. the METEOSAT 2 visible channel doesn't seem to degrade in time). As best estimate, the mean of the ISCCP measurements over the two year period is taken.

$$k_{VIS} = \frac{\sum_{date=04/85}^{04/87} k_{VIS,ISCCP}(date)}{9} = k_{VIS}^{nominal} 1.18 = 0.685 W/m^2 sr \tag{8.60}$$

According to [RDBW92], the ISCCP calibration factors have an absolute accuracy of 10 %.

8.11.4 Calibration of the METEOSAT 5 visible channel

For METEOSAT 5, the ISCCP calibration factor for March 1994 is used, obtained from ftp://isccp.giss.nasa.gov/pub/calibration/met-5.coefs. This corresponds to $k_{VIS} = 0.581 W/m^2 sr$. $C_{VIS,0} = 4$ is the lowest count during night.

8.11.5 Spectral conversion

By default, L_{VIS} can be converted to the "white" broad band radiance estimation $L_{SW,METx}^{white}$, given by equation 8.61, with the white spectral conversion factor f_{METx}^{white} as defined in section 5.2 and listed in table 5.4 for the METEOSAT 2 and METEOSAT 5 VIS channels.

$$L_{SW,METx}^{white} = f_{METx}^{white} L_{VIS} \tag{8.61}$$

If it is known from which scene type L_{VIS} is originating, a more accurate estimate of the broadband radiance L_{SW} can be obtained using equation 8.62.

$$L_{SW} = fc_{METx}^{scene} L_{SW,METx}^{white} \tag{8.62}$$

The scene dependent spectral correction factor, fc_{METx}^{scene}, is defined in section 5.

For the four scenes "clear sky ocean", "clear sky land","clear sky desert" and "overcast cloudy", the spectral corrections factors, fc_{METx}^{scene}, listed in table 5.5 for $\theta_{sun} = 45°$ are used. Mixed cloudy scenes are modelled as a mixture of those four basic scenes. The spectral correction of the mixed cloudy scenes is integrated in the scene identification and radiance to flux surface density conversion, which is discussed in section 8.11.6.

8.11.6 Reflected solar flux surface density estimation

To estimate the reflected short wave flux surface density, F_{SW}, from the measured METEOSAT VIS radiance, L_{VIS}, for a given METEOSAT pixel, the following two operations are in principle necessary:

- Scene identification based on the measured L_{VIS} and eventual auxiliary information (e.g. surface properties, clear sky count).
- For the identified scene, the proper scene dependent spectral correction factor, fc_{METx}^{scene}, and scene dependent bidirectional reflection function, $R^{scene}(\theta_{sat}, \phi_{rel}, \theta_{sun})$, have to be selected, so that F_{SW} can be estimated as (combination of equations 8.61, 8.62 and 5.6)

$$F_{SW} = \frac{\pi f_{METx}^{white} fc_{METx}^{scene} L_{VIS}}{R^{scene}(\theta_{sat}, \phi_{rel}, \theta_{sun})} \tag{8.63}$$

However, in order to obtain a scene identification based on L_{VIS}, it is necessary to calculate *in advance* the model scene VIS radiances L_{VIS}^{scene} for candidate model scene types. The scene identification results from a comparison of the measured L_{VIS} with the the candidate model VIS radiances L_{VIS}^{scene}.

Therefore the following steps are required for the estimation of F_{SW} from L_{VIS}:

1. For a number of candidate model scene types, the couples $(L_{VIS}^{scene}, F_{SW}^{scene})$ are calculated by equations 8.64 and 8.65, where $a^{scene}(\theta_{sun})$ is the model scene albedo, defined by equation 5.3.

$$F_{SW}^{scene} = F_{SOL} * a^{scene}(\theta_{sun}) \tag{8.64}$$

$$L_{VIS}^{scene} = \frac{R^{scene}(\theta_{sat}, \phi_{rel}, \theta_{sun}) F_{SW}^{scene}}{\pi f_{METx}^{white} fc_{METx}^{scene}} \tag{8.65}$$

Equation 8.65 is the inverse of equation 8.63.

2. The measured radiance L_{VIS} is compared with the model radiances L_{VIS}^{scene}, and is written as a weighted sum of the best matching model radiances.

3. F_{SW} is estimated as a corresponding weighted sum of the model F_{SW}^{scene} values.

This method is referred to as the "fractional model method". The first step is referred to as the "model calculation step". The second step is referred to as the "decomposition step". The third step is referred to as the "recomposition step".

The complete method used for the estimation of F_{SW} from L_{VIS}, the instantaneous VIS clear sky count $C_{VIS}^{cs}(pixel, slot, day, month)$ and the water fraction wf of a METEOSAT pixel, is as follows:

1. From the instantaneous clear sky count, a METEOSAT VIS radiance, L_{VIS}^{cs}, is obtained. From L_{VIS}^{cs}, the clear sky reflected short wave flux surface density F_{SW}^{cs} is estimated with the fractional model method. The considered candidate model scenes are "clear sky desert" and "clear sky non desert". The "clear sky non desert" is obtained by merging (see equations 8.66 and 8.67) the "clear sky ocean" and "clear sky land" model scene types according to the water fraction wf (see figure 8.23).

2. From L_{VIS}, F_{SW} is estimated by a second fractional model method. The considered candidate model scenes are "clear sky", "partly cloudy", "mostly cloudy" and "overcast". In the calculation step, L_{VIS}^{scene} and F_{SW}^{scene} are calculated compatible (see equations 8.79 and 8.81) with L_{VIS}^{cs} and F_{SW}^{cs}.

The first fractional model method is referred to as the "clear sky fractional model method". The second fractional model method is referred to as the "cloudy sky fractional model method".

The mathematical details of the clear sky and the cloudy sky fractional model methods are explicited in the following sections.

Clear sky reflected solar flux surface density estimation (Clear sky fractional model method) In a first step[14], an image of the water fraction of the earth in METEOSAT projection is constructed (figure 8.23). This image is obtained from the water fraction surface map (fig. 4.18) described in section 4.3. The map in latitude-longitude format (figure 4.18) is remapped to METEOSAT format using linear interpolation (described in section 8.1). The resulting water fraction wf of the earth in METEOSAT projection format is shown in figure 8.23.

In a second step, for every METEOSAT pixel the viewing angles, θ_{sat}, ϕ_{rel} and θ_{sun} (defined in section 5.1), are evaluated (this is described in section 8.2.4) and the albedos, $a^{scene}(\theta_{sun})$, and bidirectional reflection functions, $R_{scene}(\theta_{sat}, \phi_{rel}, \theta_{sun})$ (defined in section 5.1), are evaluated for the clear sky ADM's for the model scene types "clear sky ocean", "clear sky land", "clear sky desert" of one of the ADM sets described in section 5.1. From the water fraction wf (a value between 0 and 1, giving the fraction of the considered pixel covered by water), the albedos $a^{scene}(\theta_{sun})$, and the bidirectional reflection functions $R_{scene}(\theta_{sat}, \phi_{rel}, \theta_{sun})$, albedos and bidirectional reflection functions for every pixel are constructed for the clear sky class "clear sky non desert" (indicated by the superscript "cs,nd"), as follows

$$a^{cs,nd}(\theta_{sun}) = wf * a^{cs,ocean}(\theta_{sun}) + (1 - wf) * a^{cs,land}(\theta_{sun}) \tag{8.66}$$

[14] Start of the model calculation step of the clear sky fractional model method.

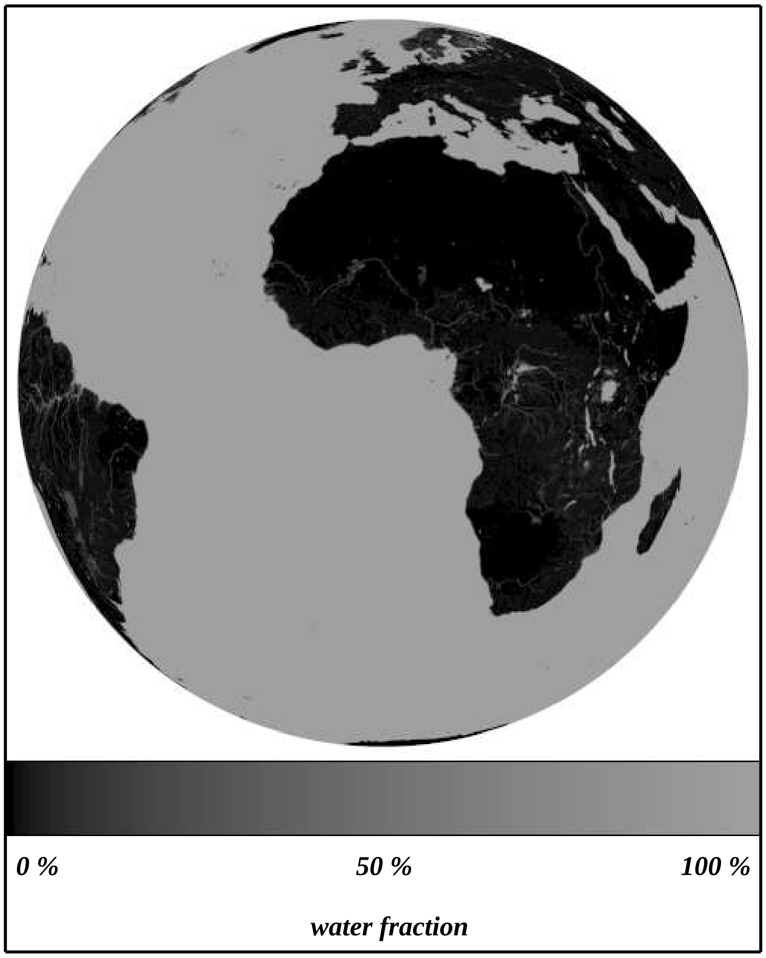

Figure 8.23: Water fraction (fraction of a pixel covered by water) of the earth in METEOSAT projection format.

$$
\begin{aligned}
R^{cs,nd}(\theta_{sat},\phi_{rel},\theta_{sun}) &= wf*(a^{cs,ocean}(\theta_{sun})/a^{cs,nd}(\theta_{sun}))*R^{cs,ocean}(\theta_{sat},\phi_{rel},\theta_{sun}) \\
&+(1-wf)*(a^{cs,land}(\theta_{sun})/a^{cs,nd}(\theta_{sun}))*R^{cs,land}(\theta_{sat},\phi_{rel},\theta_{sun})
\end{aligned} \tag{8.67}
$$

Next, the model METEOSAT VIS radiance for "non desert clear sky", L_{VIS}^{cs-nd}, and the model METEOSAT VIS radiance for "clear sky desert", $L_{VIS}^{cs,desert}$, are calculated as follows[15]

$$
\begin{aligned}
L_{VIS}^{cs,nd} &= wf*a^{cs,ocean}(\theta_{sun})*F_{SOL}*R^{cs,ocean}(\theta_{sat},\phi_{rel},\theta_{sun})/(\pi f_{METx}^{white} fc_{METx}^{cs,ocean}) \\
&+(1-wf)*a^{cs,land}(\theta_{sun})*F_{SOL}*R^{cs,land}(\theta_{sat},\phi_{rel},\theta_{sun})/(\pi f_{METx}^{white} fc_{METx}^{cs,land})
\end{aligned} \tag{8.68}
$$

$$
L_{VIS}^{cs,desert} = \frac{a^{cs,desert}(\theta_{sun})R^{cs,desert}(\theta_{sat},\phi_{rel},\theta_{sun})}{\pi f_{METx}^{white} fc_{METx}^{cs,desert}} F_{SOL} \tag{8.69}
$$

On the other hand, a estimate of the VIS radiance for a clear sky scene, L_{VIS}^{cs}, can be calculated from the *measured* instantaneous VIS clear sky count, C_{VIS}^{cs}, obtained in section 8.7, by application of the calibration equation 8.58.

$$
L_{VIS}^{cs} = k_{VIS}(C_{VIS}^{cs} - C_{VIS,0}) \tag{8.70}
$$

A desert fraction, *df* (value between 0 and 1, describing the fraction of a pixel covered by desert), can be derived from a comparison of the measured clear sky radiance, L_{VIS}^{cs}, with the model VIS radiances for non desert and desert clear sky pixels, $L_{VIS}^{cs,nd}$ and $L_{VIS}^{cs,desert}$,[16] as follows[17]

$$
\begin{array}{ll}
df = 0 & \text{if } L_{VIS}^{cs} \leq L_{VIS}^{cs,nd} \\
df = \frac{L_{VIS}^{cs}-L_{VIS}^{cs,nd}}{L_{VIS}^{cs,desert}-L_{VIS}^{cs,nd}} & \text{if } L_{VIS}^{cs,nd} < L_{VIS}^{cs} < L_{VIS}^{cs,desert} \\
df = 1 & \text{if } L_{VIS}^{cs} \geq L_{VIS}^{cs,desert}
\end{array} \tag{8.71}
$$

Finally,[18] the clear sky albedo, $a^{cs}(\theta_{sun})$, for the considered METEOSAT pixel can be estimated, as follows

$$
\begin{array}{ll}
a^{cs}(\theta_{sun}) = a^{cs,nd}(\theta_{sun}) * \frac{L_{VIS}^{cs}}{L_{VIS}^{cs,nd}} & \text{if } df = 0 \\
a^{cs}(\theta_{sun}) = (1-df)*a^{cs,nd}(\theta_{sun}) + df*a^{cs,desert}(\theta_{sun}) & \text{if } L_{VIS}^{cs,nd} < L_{VIS}^{cs} < L_{VIS}^{cs,desert} \\
a^{cs}(\theta_{sun}) = a^{cs,desert}(\theta_{sun}) * \frac{L_{VIS}^{cs}}{L_{VIS}^{cs,desert}} & \text{if } df = 1
\end{array} \tag{8.72}
$$

The clear sky reflected solar flux surface density, F_{SW}^{cs}, can be estimated as

$$
F_{SW}^{cs} = F_{SOL} * a^{cs}(\theta_{sun}) \tag{8.73}
$$

Figure 8.24 gives a graphical illustration of the determination of the desert fraction, *df*, and the clear sky albedo, a^{cs}, from the measured clear sky radiance, L_{VIS}^{cs}. Note that the L_{VIS}^{cs} to a^{cs} conversion curve is a *continuous* curve. This avoids the introduction of artificial discontinuities in the estimated clear sky reflected solar flux surface density.

Cloudy sky ADM modification [19]

The albedo and bidirectional reflection function for overcast skies (indicated by the superscript "ov"), $a^{ov}(\theta_{sun})$ and $R^{ov}(\theta_{sat},\phi_{rel},\theta_{sun})$, can be directly evaluated from one of the ADM sets described in section 5.1.

[15] This completes the model calculation step of the clear sky fractional model method.

[16] It is supposed that $L_{VIS}^{cs,nd} < L_{VIS}^{cs,desert}$.

[17] Decomposition step of the clear sky fractional model method.

[18] Recomposition step of the clear sky fractional model method.

[19] Model calculation step of the cloudy sky fractional model method.

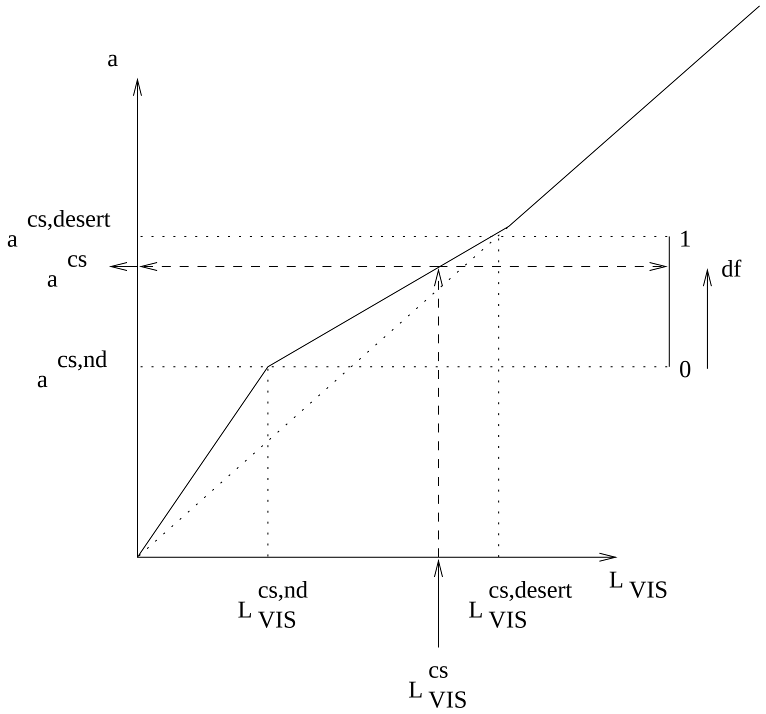

Figure 8.24: Determination of the desert fraction *df* and the clear sky albedo a^{cs} from the measured clear sky radiance L_{VIS}^{cs}.

The model METEOSAT VIS radiance for overcast skies, L_{VIS}^{ov}, can be evaluated by equation 8.74

$$L_{VIS}^{ov} = \frac{a^{ov}(\theta_{sun})R^{ov}(\theta_{sat},\phi_{rel},\theta_{sun})}{\pi f_{METx}^{white} fc_{METx}^{ov}} F_{SOL} \tag{8.74}$$

The spectral correction factor for overcast skies, $fc_{METx}^{cs,ov}$, from section 5.2 (case $\theta_{sun} = 45°$), is used.

For the mixed clear sky/cloudy scenes ("partly cloudy" and "mostly cloudy"), the albedos for non desert scenes ("non desert partly cloudy", indicated by the superscript "pc,nd", and "non desert mostly cloudy", indicated by the superscript "mc,nd"), $a^{pc,nd}(\theta_{sun})$ and $a^{mc,nd}(\theta_{sun})$, can be evaluated as[20]

$$a^{pc,nd}(\theta_{sun}) = wf * a^{pc,ocean}(\theta_{sun}) + (1-wf) * a^{pc,land}(\theta_{sun}) \tag{8.75}$$

$$a^{mc,nd}(\theta_{sun}) = wf * a^{mc,ocean}(\theta_{sun}) + (1-wf) * a^{mc,land}(\theta_{sun}) \tag{8.76}$$

The bidirectional reflection functions for the mixed clear sky/cloudy scenes, $R^{pc}(\theta_{sat},\phi_{rel},\theta_{sun})$ and $R^{mc}(\theta_{sat},\phi_{rel},\theta_{sun})$, can be evaluated as

$$\begin{aligned} R^{pc}(\theta_{sat},\phi_{rel},\theta_{sun}) &= wf * (a^{pc,ocean}(\theta_{sun})/a^{pc,nd}(\theta_{sun})) * R^{pc,ocean}(\theta_{sat},\phi_{rel},\theta_{sun}) \\ &+(1-wf) * (a^{pc,land}(\theta_{sun})/a^{pc,nd}(\theta_{sun})) * R^{pc,land}(\theta_{sat},\phi_{rel},\theta_{sun}) \end{aligned} \tag{8.77}$$

$$\begin{aligned} R^{mc}(\theta_{sat},\phi_{rel},\theta_{sun}) &= wf * (a^{mc,ocean}(\theta_{sun})/a^{mc,nd}(\theta_{sun})) * R^{mc,ocean}(\theta_{sat},\phi_{rel},\theta_{sun}) \\ &+(1-wf) * (a^{mc,land}(\theta_{sun})/a^{mc,nd}(\theta_{sun})) * R^{mc,land}(\theta_{sat},\phi_{rel},\theta_{sun}) \end{aligned} \tag{8.78}$$

[20] It is supposed the the "land-desert" ADM's described in section 5.1, are dominated by "land" scenes.

Finally, the clear sky compatible albedos for the mixed clear sky/cloudy scenes, $a^{pc}(\theta_{sun})$ and $a^{mc}(\theta_{sun})$, can be evaluated by equation 8.79, where the "partly cloudy" cloud fraction, cf^{pc}, and the "mostly cloudy" cloud fraction, cf^{mc}, are used as intermediate variables.

$$\begin{aligned} cf^{pc} &= \left(a^{pc,nd}(\theta_{sun}) - a^{cs}(\theta_{sun})\right) / \left(a^{ov}(\theta_{sun}) - a^{cs,nd}(\theta_{sun})\right) \\ a^{pc}(\theta_{sun}) &= (1 - cf^{pc}) * a^{cs}(\theta_{sun}) + cf^{pc} * a^{ov}(\theta_{sun}) \\ cf^{mc} &= \left(a^{mc,nd}(\theta_{sun}) - a^{cs}(\theta_{sun})\right) / \left(a^{ov}(\theta_{sun}) - a^{cs,nd}(\theta_{sun})\right) \\ a^{mc}(\theta_{sun}) &= (1 - cf^{mc}) * a^{cs}(\theta_{sun}) + cf^{mc} * a^{ov}(\theta_{sun}) \end{aligned} \tag{8.79}$$

The reflected solar flux surface densities for the mixed clear sky/cloudy scenes, F_{SW}^{pc} and F_{SW}^{mc}, can be estimated from the model albedos, $a^{pc}(\theta_{sun})$ and $a^{mc}(\theta_{sun})$, as

$$\begin{aligned} F_{SW}^{pc} &= F_{SOL} * a^{pc}(\theta_{sun}) \\ F_{SW}^{mc} &= F_{SOL} * a^{mc}(\theta_{sun}) \end{aligned} \tag{8.80}$$

Figure 8.25 gives a graphical illustration of the determination of the intermediate cloud fractions, cf^{pc} and cf^{mc}, and the clear sky compatible mixed cloudy albedos, a^{pc} and a^{mc}, from the model albedos, $a^{cs,nd}$, $a^{pc,nd}$, $a^{mc,nd}$ and a^{ov}, and the measured clear sky albedo, a^{cs}.

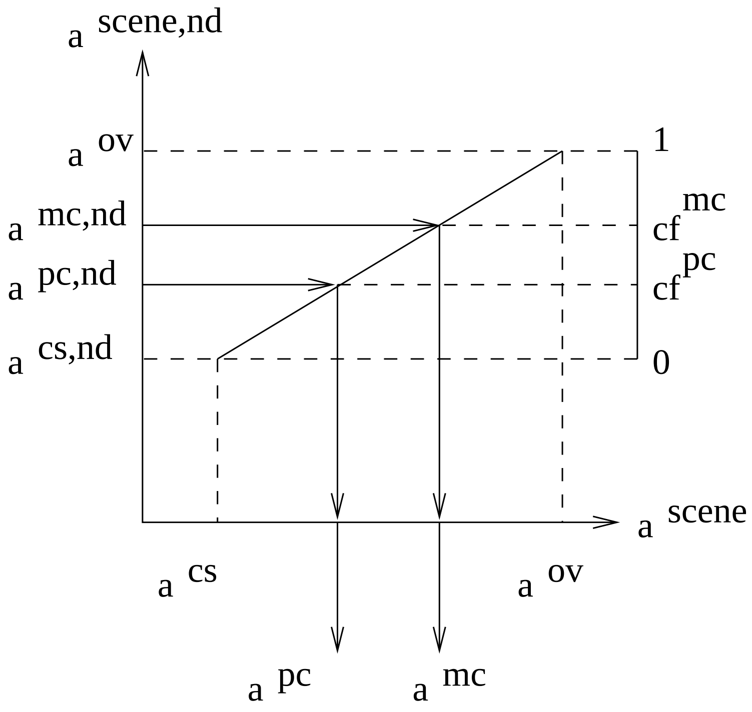

Figure 8.25: Determination of the intermediate cloud fractions cf^{pc}, cf^{mc} and the clear sky compatible mixed cloudy albedos a^{pc}, a^{mc} from the model albedos $a^{cs,nd}$, $a^{pc,nd}$, $a^{mc,nd}$, a^{ov} and the measured clear sky albedo a^{cs}.

The METEOSAT VIS radiances for the mixed clear sky/cloudy scenes, L_{VIS}^{pc} and L_{VIS}^{mc}, are obtained by equation 8.81, where the "partly cloudy" radiance cloud fraction cf'^{pc} and the "mostly cloudy" radiance cloud fraction cf'^{mc} are used as intermediate variables.

$$\begin{aligned}
cf'^{pc} &= (a^{pc}(\theta_{sun})R^{pc}(\theta_{sat},\phi_{rel},\theta_{sun}) - a^{cs}(\theta_{sun})R^{cs}(\theta_{sat},\phi_{rel},\theta_{sun})) \\
&\quad / (a^{ov}(\theta_{sun})R^{ov}(\theta_{sat},\phi_{rel},\theta_{sun}) - a^{cs}(\theta_{sun})R^{cs}(\theta_{sat},\phi_{rel},\theta_{sun})) \\
L^{pc}_{VIS} &= (1 - cf'^{pc}) * L^{cs}_{VIS} + cf'^{pc} * L^{ov}_{VIS} \\
cf'^{mc} &= (a^{mc}(\theta_{sun})R^{mc}(\theta_{sat},\phi_{rel},\theta_{sun}) - a^{cs}(\theta_{sun})R^{cs}(\theta_{sat},\phi_{rel},\theta_{sun}) \\
&\quad / (a^{ov}(\theta_{sun})R^{ov}(\theta_{sat},\phi_{rel},\theta_{sun}) - a^{cs}(\theta_{sun})R^{cs}(\theta_{sat},\phi_{rel},\theta_{sun})) \\
L^{mc}_{VIS} &= (1 - cf'^{mc}) * L^{cs}_{VIS} + cf'^{mc} * L^{ov}_{VIS}
\end{aligned} \tag{8.81}$$

Figure 8.26 gives a graphical illustration of the determination of the intermediate radiance cloud fractions, cf'^{pc} and cf'^{mc}, and the mixed cloudy radiances, L^{pc}_{VIS} and L^{mc}_{VIS}, from the albedos a^{cs}, a^{pc}, a^{mc} and a^{ov}, the bidirectional reflection functions R^{cs}, R^{pc}, R^{mc} and R^{ov}, and the radiances L^{cs}_{VIS} and L^{ov}_{VIS}.

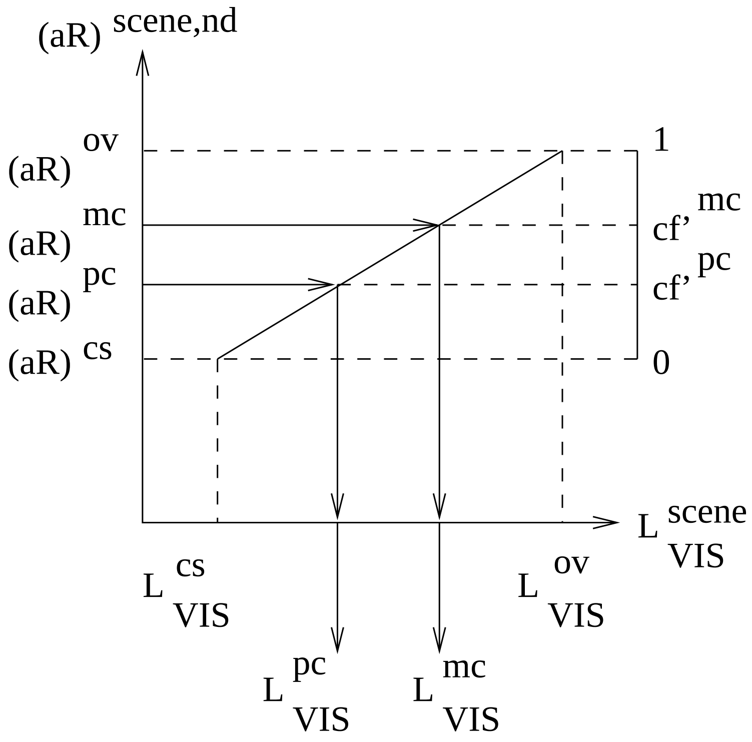

Figure 8.26: Determination of the intermediate radiance cloud fractions cf'^{pc}, cf'^{mc} and the METEOSAT VIS radiances L^{pc}_{VIS}, L^{mc}_{VIS} from the albedos a^{cs}, a^{pc}, a^{mc}, a^{ov}, the bidirectional reflection functions R^{cs}, R^{pc}, R^{mc}, R^{ov} and the VIS radiances L^{cs}_{VIS}, L^{ov}_{VIS}. The notation $(aR)^{scene}$ is used for $a^{scene} * R^{scene}$.

All sky reflected solar flux surface density estimation

Scene separation [21]

It is necessary to do a scene identification/separation in order to use the correct bidirectional reflection function and the correct spectral conversion factor to estimate F_{SW} from L_{VIS}.

L_{VIS} is decomposed as (see figure 8.27)

$$L_{VIS} = (1 - fs) * L^{scene-lower}_{VIS} + fs * L^{scene-upper}_{VIS} \tag{8.82}$$

where $L^{scene-lower}_{VIS}$ and $L^{scene-upper}_{VIS}$ are the METEOSAT VIS radiances for the discrete cloud cover ("clear sky", "partly cloudy", "mostly cloudy", "overcast") scenes with value just lower and

[21] Decomposition step of the cloudy sky fractional model method.

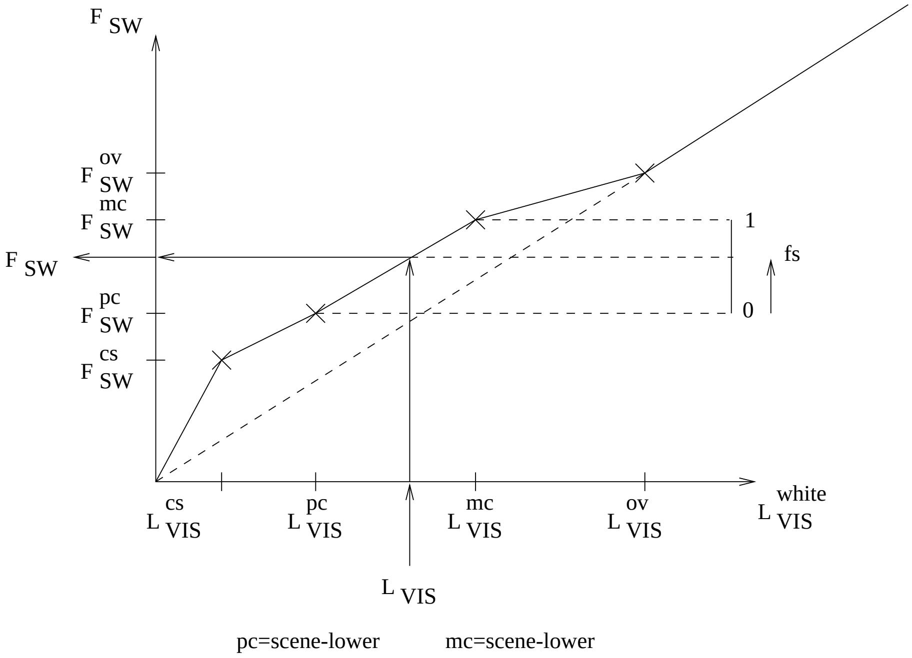

Figure 8.27: METEOSAT VIS radiance to broad band short wave flux surface density conversion.

just higher than the measured METEOSAT pixel VIS radiance L_{VIS}. fs is a scene fraction with $0 \leq fs \leq 1$.

Scene composition [22]
The flux surface density F_{SW} is composed from the discrete cloud cover fluxes using

$$F_{SW} = (1 - fs) * F_{SW}^{scene-lower} + fs * F_{SW}^{scene-upper} \tag{8.83}$$

where fs, "scene-lower" and "scene-upper" are the same as obtained in the radiance decomposition of equation 8.82. Figure 8.27 illustrates the process of conversion of the METEOSAT VIS radiance L_{VIS} to the reflected solar flux surface density F_{SW}.

8.12 Net short wave TOA flux surface density

8.12.1 Processing description card

name processing	net short wave flux surface density estimation
technical novelty	none
novel algorithms	none
references	none

Table 8.14: Processing card for net short wave flux surface density estimation

8.12.2 Description

For every METEOSAT pixel, F_{SOL} is calculated from equation 2.17. $F_{SW,IN}$ is calculated by equation 2.15 from F_{SOL} and F_{SW}, obtained in section 8.11. Figure 8.28 shows the result for 08/11/1986 time slot 18.

[22] Recomposition step of the cloudy sky fractional model method.

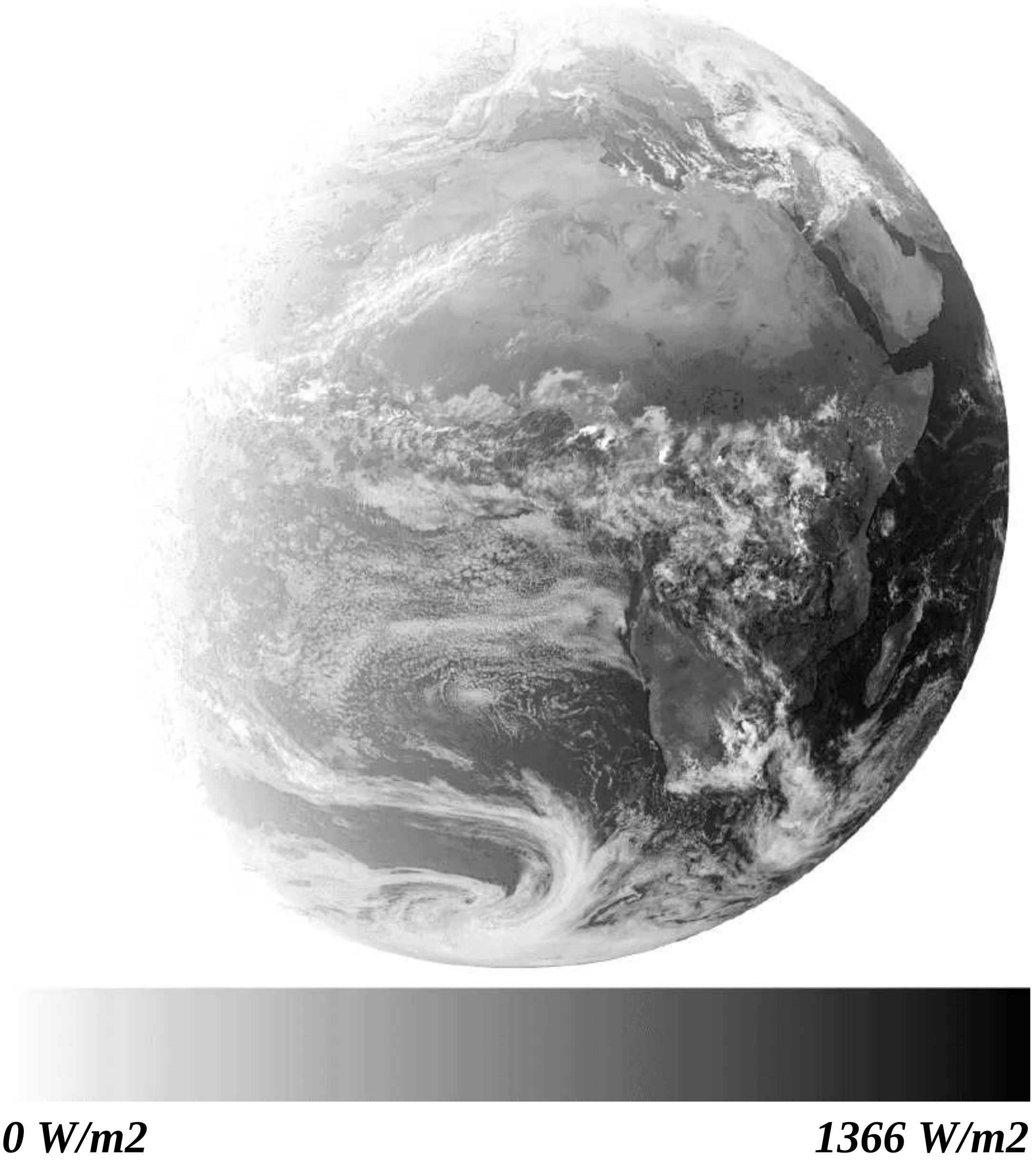

Figure 8.28: Net short wave flux surface density estimated from METEOSAT VIS data, for 08/11/1986 time slot 18 (nominally 08:30 UTC-08:55 UTC).

8.13 Radiation budget at the top of the atmosphere

8.13.1 Processing description card

name processing	TOA radiation budget
technical novelty	none
novel algorithms	none
references	none

Table 8.15: Processing card for the estimation of the TOA radiation budget

8.13.2 Description

For every METEOSAT pixel, RB is calculated by equation 2.16 from $F_{SW,IN}$ and F_{LW}, obtained in sections 8.10 and 8.12 respectively. Figure 8.29 shows the result for 08/11/1986 time slot 18.

8.14 Naming convention

The METEOSAT derived estimates of the TOA radiation budget or its components (e.g. figures 8.22, 8.28, 8.29) will be denoted as "METEOSAT-RB" products from now on.

8.15 Convolution of high resolution METEOSAT-RB estimates with a low resolution LEO point spread function

To obtain METEOSAT-RB flux surface density estimates at LEO (ERBE or ScaRaB) pixel level $F_{LEO(METEOSAT-RB)}$ from the full resolution METEOSAT-RB flux surface density estimates $F_{METEOSAT-RB}$ (F_{LW} or F_{SW} obtained in the previous section), a convolution is done with the LEO scanner point spread function $PSF_{channel}(\delta_a, \delta_c)$ (the channel is LW or SW, in correspondence with $F_{METEOSAT-RB}$) calculated in section 4.2.1

$$F_{LEO(METEOSAT-RB)} = \frac{\int PSF_{channel}(\delta_a, \delta_c) F_{METEOSAT-RB} d\delta_a d\delta_c}{\int PSF_{channel}(\delta_a, \delta_c) d\delta_a d\delta_c} \tag{8.84}$$

where δ_a is the LEO cross scan angle and δ_c is the LEO along scan angle.

8.16 Lossless archival of METEOSAT-RB products

Since the METEOSAT-RB products obtained in this work have a high spatial and temporal resolution, a large amount of storage capacity is required to archive these products. With the use of the novel lossless wavelet compression technique for cartesian images described in section 7.7, the required storage capacity can be reduced, without loss of data quality.

In this section, it is described how lossless compression can be applied to the METEOSAT-RB products.

8.16.1 Processing description card

name processing	lossless archival of radiation budget results
technical novelty	high lossless compression ratio
novel algorithms	lossless cartesian compression (section 7.7)
references	[DC97]

Table 8.16: Processing card for METEOSAT-RB archival

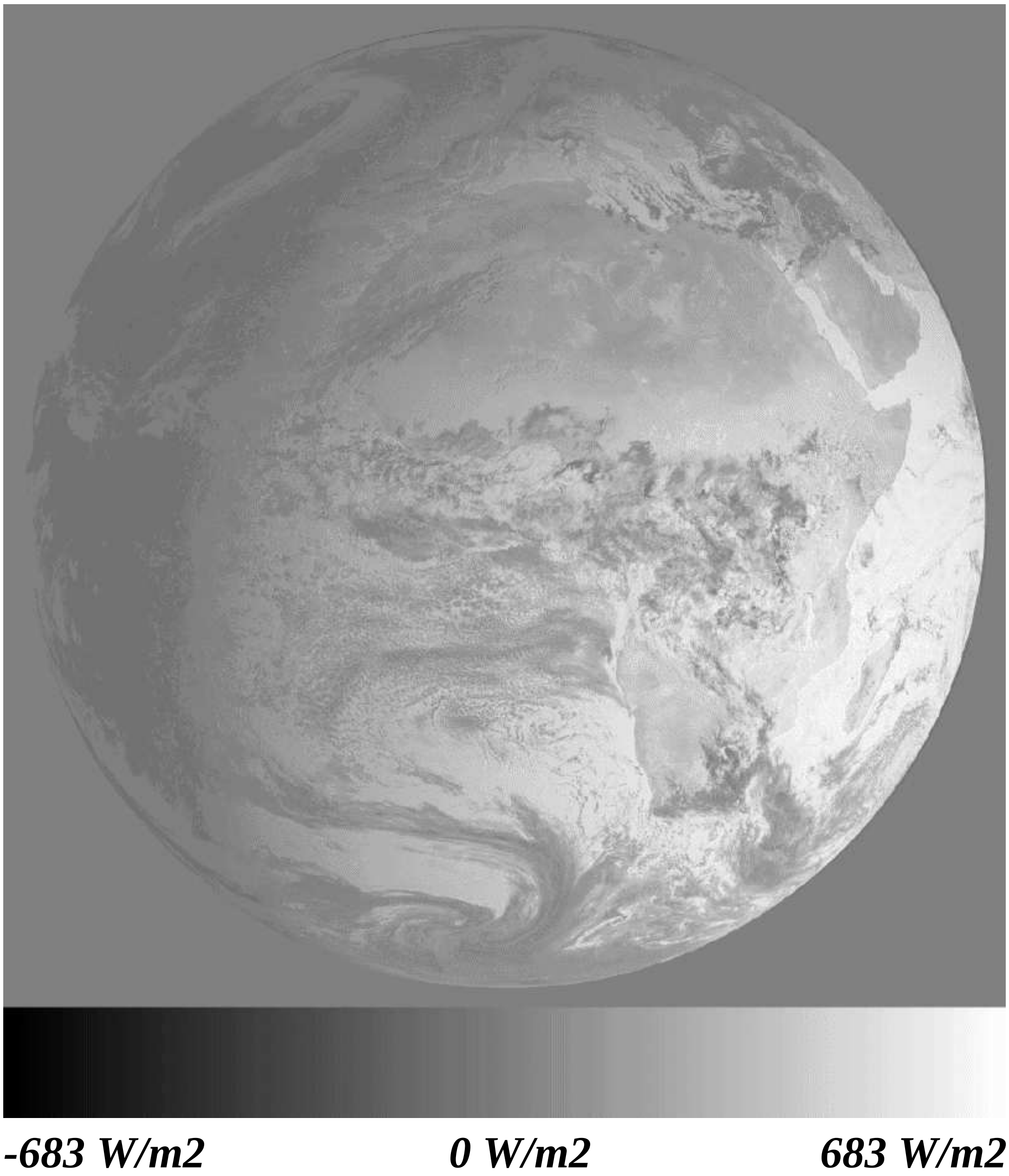

Figure 8.29: Radiation budget estimated from METEOSAT IR,WV and VIS data, for 08/11/1986 time slot 18 (nominally 08:30 UTC-08:55 UTC).

8.16.2 Description

The process of radiation budget term estimation from METEOSAT data, described in the previous sections, can be seen as a process that converts raw METEOSAT counts to radiation budget terms estimates. While the *physical* information content is strongly improved from the input to the output of this process, the information content in the sense of *information theory* has essentially remained the same.

In information theory, information content is governed by

- The relative quantification step of the data, i.e. the quantification step divided by the full range of the data.
- The spatial variability of the data, characterised by e.g. the fractal dimension [Bar88] of the data.

From this perspective of information theory, the radiation budget term estimation form METEOSAT data, described in the previous sections, can be decomposed in two types of processes:

- Global rescalings (calibration scaling, Lambertian white short wave flux surface density estimation for the short wave radiation budget term, linear terms for the IR contribution in the long wave flux surface density estimation). These global rescalings do not alter the relative quantification step and the spatial variability of the input data (METEOSAT VIS and IR counts).
- Modifications (calibration offsets, bidirectional reflection function application and spectral correction for the short wave flux surface density estimation, non linear terms and the WV contribution to the long wave flux estimation) relative to the global rescalings. These modifications change the local quantification step by "small"[23] amounts, so that the impact on the information content is also small. Moreover, the modification factors have a slow spatial variation for a fixed scene type, so the impact on the spatial variability is also small.

As a conclusion the METEOSAT-RB short wave flux surface density estimation can be quantised to an integer number using the same amount of bits[24] as used for the acquisition of the METEOSAT VIS input image, and the METEOSAT-RB long wave flux surface density estimation can be quantised to an integer number using the same amount of bits[25] as used for the acquisition of the METEOSAT IR input image, practically without losing measured information.

The lossless compression described in section 7.7.7 can be directly applied for the lossless archival of the integer quantised full resolution short wave and long wave flux surface density derived from METEOSAT data.

The compression performance for the long wave flux surface density image of figure 8.22 is illustrated in table 8.17, in function of the PRFB (Haar or lifted Haar) and the number of resolution levels used in the wavelet transform (see section 7.7).

	Haar	single lifted
1	3.32 bpp	3.21 bpp
2	2.89 bpp	2.75 bpp
3	2.80 bpp	2.65 bpp
4	2.78 bpp	2.62 bpp
5	2.77 bpp	2.62 bpp

Table 8.17: Mean entropy in bit per pixel (bpp) for different lossless wavelet transforms of the 8 bit quantified long wave flux surface density estimated from METEOSAT IR data, for 08/11/1986 time slot 18 (nominally 08:30 UTC-08:55 UTC). The PRFB type varies per column, the number of resolution levels varies per row.

It can be seen that

[23] e.g. values typically around 20 % or lower for the bidirectional reflection function correction (see e.g. table 10.3 in section 10.2.1), and typically 10 % or lower for the VIS spectral correction (see e.g. table 5.2 in section 5.2)

[24] 6 bits for METEOSAT 2, 8 bits for METEOSAT 5

[25] 8 bits

- Lifting improves the compression performances of the Haar PRFB.
- Increasing the number of resolution levels of the wavelet transform improves the compression performances of the compression algorithm.
- Three resolution levels gives a good compromise between compression performance and calculation complexity.
- A lossless compression factor of $8/2.62 = 3.05$ can be obtained for the METEOSAT-RB long wave flux surface density.

The compression performance for the short wave flux surface density image for 08/11/1986 slot 18, obtained in section 8.11, is illustrated in table 8.18 for the two PRFB's (Haar, lifted Haar) and for different numbers of resolution levels.

	Haar	single lifted
1	3.41 bpp	3.31 bpp
2	3.03 bpp	2.90 bpp
3	2.95 bpp	2.81 bpp
4	2.93 bpp	2.79 bpp
5	2.93 bpp	2.79 bpp

Table 8.18: Mean entropy in bit per pixel (bpp) for different lossless wavelet transforms of the 6 bit quantified short wave flux surface density estimated from METEOSAT VIS data, for 08/11/1986 time slot 18 (nominally 08:30 UTC-08:55 UTC). The PRFB type varies per column, the number of resolution levels varies per row.

It can be seen that

- Lifting improves the compression performances of the Haar PRFB.
- Increasing the number of resolution levels of the wavelet transform improves the compression performances of the compression algorithm.
- Three resolution levels gives a good compromise between compression performance and calculation complexity.
- A lossless compression factor of $6/2.79 = 2.15$ can be obtained for the METEOSAT-RB short wave flux surface density, to be compared with the compression factor of 3.05 for the METEOSAT-RB long wave flux surface density. The lower compression ratio for the METEOSAT-RB short wave flux surface density can be understood because the short wave data is spatially more variable than the long wave data (compare e.g. the figures 8.12 and 8.13).

8.17 Lossy distribution of METEOSAT-RB products

The METEOSAT projection format defines how METEOSAT pixels correspond with geographic regions on earth. This projection format is implicitly defined by the METEOSAT image acquisition method (see e.g. figure 4.17).

Until now, radiation budget term estimates have been derived from METEOSAT measurements *without changing the METEOSAT projection format.* This approach has the advantage of being very straightforward (one METEOSAT pixel yields one radiation budget term estimate pixel), but it has the disadvantage that different regions on earth are projected in very different ways (e.g. for the short wave radiation budget term, a resolution of approximately 2.5 km x 2.5 km is obtained over the Gulf of Guinea, while a resolution of approximately 2.5 km x 5 km is obtained over Western Europe).

By mapping the obtained METEOSAT-RB results on a spherical grid (described in section 7.8), and by applying the wavelet based compression method of section 7.8, the following advantages can be obtained:

- The data is represented in a form with quasi uniform resolution over the METEOSAT field of view. If the *final usage* of the data, e.g. in atmospheric models, requires a uniform resolution representation of the data, no *relevant* information has been lost in the spherical wavelet representation.
- The data is presented much more compactly than in the METEOSAT projection format. Moreover, further compression is obtained by wavelet based methods.
- The wavelet presentation is a time/frequency representation, which combines the advantages of e.g. a Fourier representation for fast model calculation and of the representation in the physical space for easy assimilation.

In this section, the procedures to map METEOSAT-RB data with quasi uniform resolution onto the sphere, and to compress this mapped data with spherical wavelet compression, are described.

8.17.1 Processing description card

name processing	lossy distribution of radiation budget results
technical novelty	high compression *and* metrological quality preserving multi resolution multi region uniform resolution
novel algorithms	spherical compression (section 7.8)
references	none

Table 8.19: Processing card for METEOSAT-RB distribution and application

8.17.2 Description

Spherical mapping of METEOSAT gridded data The METEOSAT narrow band data and the METEOSAT-RB flux surface density derived from it in the previous sections are projected in the default METEOSAT projection grid. In this section this data is mapped to a spherical grid.

Grid cell areas Only recursive pseudo-icosahedral grids as described in section 7.8 are used. The mean grid cell area obtained after n iterations is the earth surface area, equal to $4\pi r_{earth}^2$, divided by the number of grid cells, equal to $20 * 4^n$. The mean grid cell area, $S_n = (5050km/2^n)^2$, is shown in function of the number of recursions, n, in table 8.20.

n	2^n	S_n	n	2^n	S_n
5	32	$(158 \text{ km})^2$	9	512	$(9.86 \text{ km})^2$
6	64	$(78.9 \text{ km})^2$	10	1024	$(4.93 \text{ km})^2$
7	128	$(39.5 \text{ km})^2$	11	2048	$(2.47 \text{ km})^2$
8	256	$(19.7 \text{ km})^2$	12	4098	$(1.23 \text{ km})^2$

Table 8.20: Mean grid cell area in function of the number of recursions of the recursive icosahedron subdivision of the earth's surface. n = number of resolution levels, S_n = mean grid cell area.

Spherical sampling of remote sensing data Choosing a particular spherical sampling grid cell size S_{n_1}, remote sensing data in any arbitrary format, can be sampled *point wise* by the following procedure

- For every grid cell at resolution n_1, calculate the geolocation of the centre of the grid cell.
- Evaluate the remote sensing data value at this geolocation.

- Assign the remote sensing data value to the grid cell

Figure 8.30 shows the projection into a plane of the water fraction database described in section 4.3, sampled with $n = 9$, i.e. with mean grid cell size $S_9 = 9.86$ km^2.

Figure 8.30: The water fraction of the earth as described by the surface properties map (see section 4.3) at 10 arcminutes resolution, sampled with spherical triangles at $S_9 = 9.86$ km^2.

This kind of sampling assigns the value in the centre of the grid cell to the grid cell. If one wants to assign the mean value over the grid cell to the grid cell, one can use the following procedure:

- Choose a sampling resolution $n_2 >> n_1$.
- Sample the remote sensing data point wise at resolution n_2
- Calculate the mean values of a grid cell at resolution n_1 as the weighted mean of all the grid cell values of the grid cells at resolution n_2 which are part of the grid cell at resolution n_1.

The higher the value $n_2 - n_1$, the better the mean over the grid cell at resolution n_1 will be approximated.

Compression of spherically sampled data Once the remote sensing data is sampled spherically, lossless compression of the regridded data as described in section 7.8 can be applied. The regridding before the compression leads to a strong extra compression. Since the regridding is lossy, the whole scheme from original remote sensing data to compressed data is lossy too. However, this loss of information is not relevant to the target end user, if this user only works with uniform resolution data, as is e.g. the case for most of the atmospheric models.

Long wave flux surface density compression results Tables 8.21 and 8.22 show the compression results, using the Haar and the lifted Haar wavelet transform respectively (see section 7.8), for the long wave flux surface density data of 08/11/1986 slot 18 (nominally 08:30 UTC-08:55 UTC) (see figure 8.22), sampled point wise at (9.86 km)^2.

It can be seen that

- At all resolutions the lifted Haar wavelet gives better compression results than the simple Haar wavelet.
- Strong extra compression can be obtained by lowering the resolution of the data.

n	S	bit per $(9.86\text{ km})^2$ pixel	file size
5	$(158\text{ km})^2$	0.02	3.5 kB
6	$(78.9\text{ km})^2$	0.07	12 kB
7	$(39.5\text{ km})^2$	0.24	42 kB
8	$(19.7\text{ km})^2$	0.88	153 kB
9	$(9.86\text{ km})^2$	3.42	597 kB

Table 8.21: Long wave flux surface density data of 08/11/1986 slot 18 (nominally 08:30 UTC-08:55 UTC), sampled at $(9.86\text{ km})^2$: Mean entropy in bit per $(9.86\text{ km})^2$ pixel and mean file size in function of the resolution n for the spherical Haar wavelet transform with 4 resolution levels.

n	S	bit per $(9.86\text{ km})^2$ pixel	file size
5	$(158\text{ km})^2$	0.02	3.5 kB
6	$(78.9\text{ km})^2$	0.07	12 kB
7	$(39.5\text{ km})^2$	0.23	40 kB
8	$(19.7\text{ km})^2$	0.85	148 kB
9	$(9.86\text{ km})^2$	3.30	576 kB

Table 8.22: Long wave flux surface density data of 08/11/1986 slot 18 (nominally 08:30 UTC-08:55 UTC), sampled at $(9.86\text{ km})^2$: Mean entropy in bit per $(9.86\text{ km})^2$ pixel and mean file size in function of the resolution n for the spherical single lifted Haar wavelet transform with 4 resolution levels.

n	S	bit per $(9.86\text{ km})^2$ pixel	file size
5	$(158\text{ km})^2$	0.03	3.5 kB
6	$(78.9\text{ km})^2$	0.09	12 kB
7	$(39.5\text{ km})^2$	0.33	42 kB
8	$(19.7\text{ km})^2$	1.27	153 kB
9	$(9.86\text{ km})^2$	4.92	597 kB

Table 8.23: Short wave flux surface density data of 08/11/1986 slot 18 (nominally 08:30 UTC-08:55 UTC), sampled at $(9.86\text{ km})^2$: Mean entropy in bit per $(9.86\text{ km})^2$ pixel and mean file size in function of the resolution n for the spherical Haar wavelet transform with 4 resolution levels.

n	S	bit per $(9.86\text{ km})^2$ pixel	file size
5	$(158\text{ km})^2$	0.03	3.5 kB
6	$(78.9\text{ km})^2$	0.09	12 kB
7	$(39.5\text{ km})^2$	0.32	40 kB
8	$(19.7\text{ km})^2$	1.25	148 kB
9	$(9.86\text{ km})^2$	4.94	576 kB

Table 8.24: Short wave flux surface density data of 08/11/1986 slot 18 (nominally 08:30 UTC-08:55 UTC), sampled at $(9.86\text{ km})^2$: Mean entropy in bit per $(9.86\text{ km})^2$ pixel and mean file size in function of the resolution n for the spherical single lifted Haar wavelet transform with 4 resolution levels.

Short wave flux compression results Tables 8.23 and 8.24 show the compression results, using the Haar and the lifted Haar wavelet transform respectively, for the short wave flux surface density data of 08/11/1986 slot 18 (nominally 08:30 UTC-08:55 UTC), sampled point wise at $(9.86 \text{ km})^2$.

It can be seen that

- The short wave flux surface density compression ratio is lower than the long wave flux surface density compression ratio.
- At all resolutions, except at the last one, the lifted Haar wavelet gives better compression results than the simple Haar wavelet.
- Strong extra compression can be obtained by lowering the resolution of the data.

The lower compression ratio of the short wave flux surface density when compared to the long wave flux surface density, can be understood from the greater spatial variability of the short wave flux surface density.

Since lifting does not improve the compression results at the highest resolution, the smooth variation assumptions implicitly used in the prediction done by the lifting scheme, do not seem to be valid at the highest resolution. This can be understood because at the highest resolution, an additional spatial variability, due to the point wise sampling, is added to the natural variability of the short wave flux surface density.

Chapter 9

Validation of the improved processing techniques

9.1 METEOSAT geometry and time of acquisition

In order to validate the METEOSAT geolocation, solar zenith angle calculation and time of acquisition, the location of the day/night separation in the *measured* visible images is compared with the *calculated* day/night separation. Only the image of measured counts $C_{VIS}(i,j)$ for slot 12 (sunrise roughly in the centre of the image) and for slot 36 (sunset roughly in the centre of the image) are considered.

For those two slots and for every pixel, the expected acquisition time is defined as $t(slot,i,j)$.

To test whether the true acquisition time corresponds with the nominal acquisition time, different possible true acquisition times $t(slot,i,j)+t_{delay}$ were considered. t_{delay} gives the time delay from the expected acquisition time to the true acquisition time. Time delays t_{delay} of -5 minutes (the true acquisition time is 5 minutes earlier than the expected acquisition time), 0 minutes (the true acquisition time corresponds to the expected acquisition time) and +5 minutes (the true acquisition time is 5 minutes later than the nominal acquisition time) are considered.

For each of the two slots, for every pixel (i,j) and for every considered time delay t_{delay}, using the known position of the sun at time $t(slot,i,j)+t_{delay}$, the solar zenith angle $\theta_{sun}(i,j,slot,t_{delay})$ is calculated using the procedure of section 8.2.

If the calculated geolocation, solar zenith angles and timing is correct, the measured pixel grey values (counts) $C_{VIS}(i,j)$ should on average be roughly proportional to the cosine of the calculated solar zenith angles.

Therefore the measured counts are divided by the values $max(255*cos(\theta_{sun}(i,j,slot,t_{delay})),10)$. The resulting images give a visual impression of the correctness of the location of the calculated day/night separation. If the calculated location of the day/night separation is wrong, the grey values $C_{VIS}(i,j)$ are divided by too small values at some places of the image and they are divided by too high values at other places of the image. Division by too small values shows up as bright white zones in the divided images (see further on), division by too high values result in dark zones in the divided images.

Figures 9.1, 9.2, 9.3 give the resulting images for 08/11/1986 for time delays t_{delay} of -5 minutes, 0 minutes and +5 minutes respectively.

From the image obtained for a time delay of -5 minutes (figure 9.1), it can be seen that there is a small bright zone around the day/night separation in the left part of the image (at sunrise). This means[1] that the measured counts $C_{VIS}(i,j)$ are divided by calculated cosines of the solar zenith angles which are too small. Since this happens at sunrise, this means the applied time delay of -5 minutes is too small (at sunrise, the cosine of the solar zenith angle increases with time).

From the image obtained for a time delay of 0 minutes (figure 9.2), no obvious difference in appearance of the day/night separation in the left part of the image (at sunrise) compared to the right part of the image (at sunrise) can be seen. This means the applied time delay of 0 minutes is approximately correct.

[1] Too bright values are too high values.

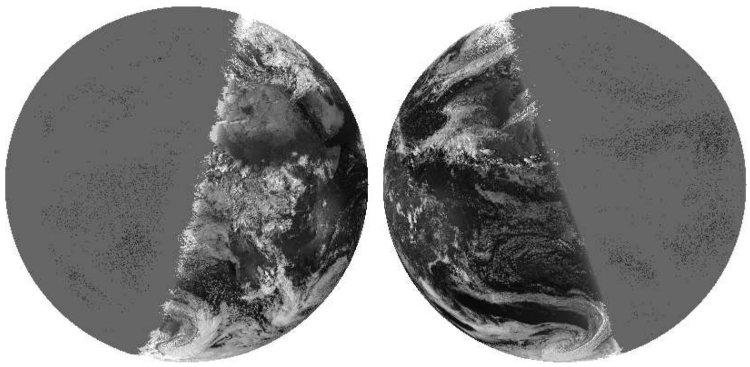

Figure 9.1: Divided images for the comparison of the measured and the calculated day/night border, 08/11/86, time delay -5 minutes. Left: slot 12 (sunrise). Right: slot 36 (sunset).

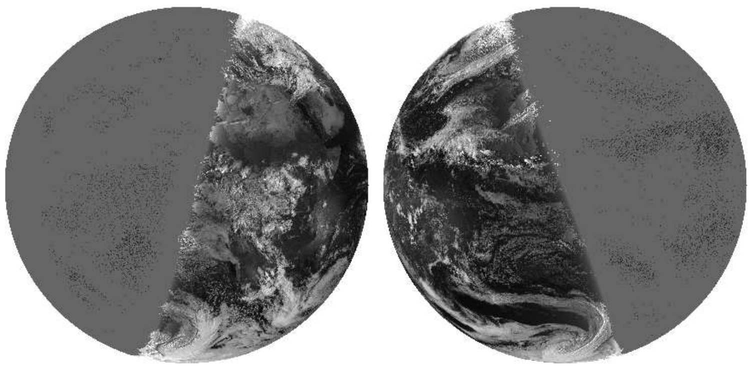

Figure 9.2: Divided images for the comparison of the measured and the calculated day/night border, 08/11/86, time delay 0 minutes. Left: slot 12 (sunrise). Right: slot 36 (sunset).

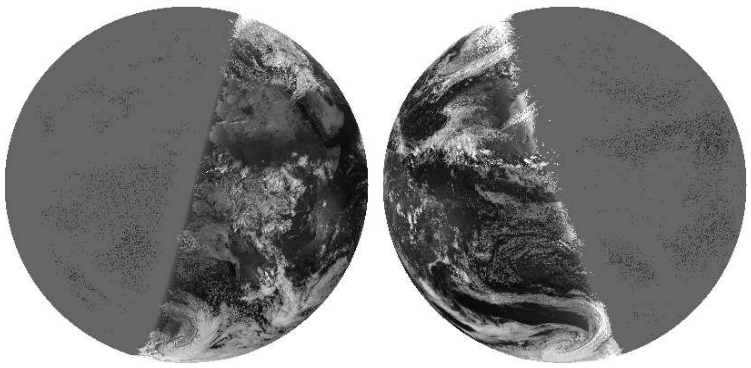

Figure 9.3: Divided images for the comparison of the measured and the calculated day/night border, 08/11/86, time delay +5 minutes. Left: slot 12 (sunrise). Right: slot 36 (sunset).

From the image obtained for a time delay of +5 minutes (figure 9.3), a small bright zone around the day/night separation in the right part of the image (at sunset) can be seen. This means that the measured counts $C_{VIS}(i,j)$ are divided by calculated cosines of the solar zenith angles which are too small. Since this happens at sunset, this means the applied time delay of +5 minutes is too high (at sunset, the cosine of the solar zenith angle decreases with time).

As a conclusion the day/night borders in the METEOSAT images occur at the expected places and at the expected times in the METEOSAT images. This gives a first validation the calculation of the time of acquisition and of the viewing angles (and hence implicitly also of the geolocation) for the METEOSAT images.

9.2 METEOSAT cloud motion winds

The distance matching technique used in section 7.5 for motion estimation, is validated by comparison with the cloud motion winds obtained operationally by ESOC/MIEC on 21/01/92.

Cloud Motion Wind Extraction (CMWE) from METEOSAT images have been performed operationally at ESOC/MIEC for many years [S+93]. The outline of the ESOC CMWE algorithm is as follows:

The speeds are derived from triplets of images, which are successive in time. The middle image contains the target zones, the outer ones contain the search zones. The middle image is divided in segments of 32x32 pixels. In every segment a multi spectral clustering [Tom81] is performed to determine how many cloud types are present in the segment and to estimate their height. If too many clusters are obtained, no further processing is done. Else the edges of the highest cloud are enhanced in a pre-processing step [Hof90]. Next, the cloud translation is estimated using the minimal Pattern Correlation Coefficient (PCC) matching technique. The translation vector is converted into a speed vector, taking into account the satellite viewing geometry. Finally, the quality of the obtained wind speeds is checked with an automatic quality check.

To automatically check the correctness of the obtained wind speeds, they are calculated twice for a given target zone at a given time: once by searching in the zone of the previous half hour, and once by searching in the zone of the next half hour. The obtained translations are both converted to speeds (the conversion of translation to speed vectors depends on the satellite viewing geometry) and the speeds are compared. If the speeds are large enough and close enough to each other, they are assumed to be correct, else they are rejected.

The following conditions must be fulfilled by the speeds to be accepted :

- The modulus of their mean vector must be greater than 5 m/s.
- The modulus of their vector difference must be smaller than half the modulus of their mean vector.
- The angle between them must be smaller than a, mean dependent, maximum direction difference, given in table 9.1.

mean speed (m/s)	maximum difference directions
$5-10$	$60°$
$10-30$	$40°$
>30	$20°$

Table 9.1: Maximum allowed wind speed vector difference angle in automatic wind speed quality check in function of the mean wind speed.

Table 9.2 shows the percentage of accepted wind vectors for the three METEOSAT channels for our distance matching technique and for the PCC matching technique used by ESOC. The automatic quality control is denoted as SC (Symmetry Check).

Distance matching clearly gives a much higher percentage of accepted vectors, compared to the ESOC PCC technique. This can be understood, as distance matching has been derived as a statistically optimal method in section 7.5.

	VIS	IR	WV
preprocessing+PCC+SC	25%	37%	28%
distance+SC	86%	93%	78%

Table 9.2: Percentage of accepted wind speeds for the three METEOSAT channels using the Symmetry Check (SC) as automatic quality control for the ESOC method and for the distance matching technique.

To verify whether the speeds derived by distance matching and accepted by the quality check are effectively correct, they are compared to the speeds derived and accepted by the full ESOC method [S+93]. In figures 9.4 and 9.5, the speeds modulus' and directions produced and accepted by distance matching and those produced and accepted by the full ESOC method are compared. The correspondence between the two methods is satisfactory.

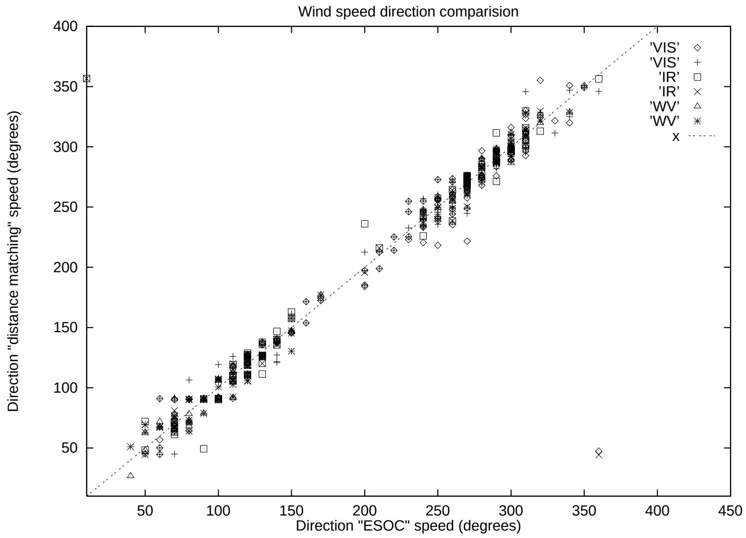

Figure 9.4: "ESOC/distance matching" speed direction comparison (0° = north to south, 90° = east to west, 180° = south to north, 270° = west to east), x-axis: "ESOC" accepted speed directions, y-axis: "distance matching" accepted speed directions.

9.3 METEOSAT time interpolation

In this section, the METEOSAT time interpolation (see section 8.8), which uses the motion estimation developed in section 7.5, is validated.

The METEOSAT IR images over Europe for the time slots 23, 24, and 25 of 04/04/95 are shown in figure 9.6, figure 9.7 and figure 9.8.

Figure 9.9 shows the approximation of figure 9.7 by simple linear time interpolation between the cloud fields of figure 9.6 and figure 9.8 obtained by equation 9.1 (application of equation 8.48)

$$C_{24}^{li}(i,j) = 0.5(C_{23}(i,j) + C_{25}(i,j)) \tag{9.1}$$

All the cloud borders which have moved from figure 9.6 to figure 9.8 are "doubled" (see arrows on figure 9.8) in the interpolated image, as no motion is taken into account.

Figure 9.10 shows the error image

$$C_{24}(i,j) - C_{24}^{li}(i,j) \tag{9.2}$$

The RMS value of image 9.10 is 10.9 counts, i.e. 4.27 % of the full range 255. Typically the highest errors occur at the edges which have moved most.

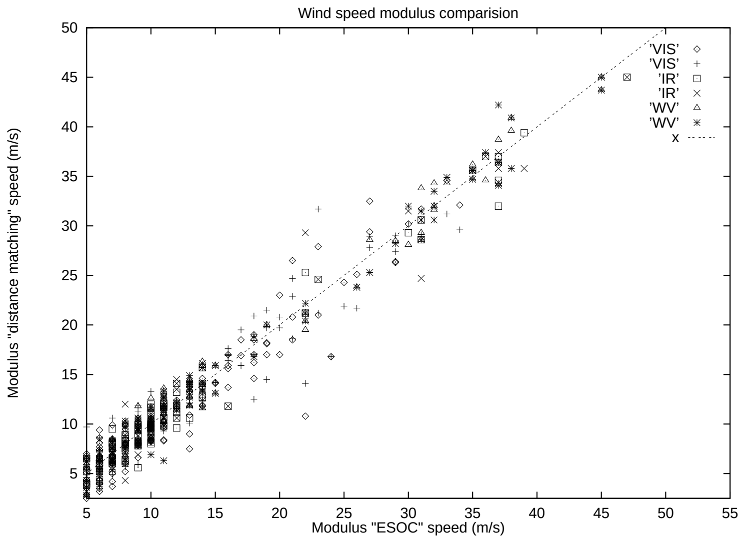

Figure 9.5: "ESOC/distance matching" speed modulus comparison, x-axis: "ESOC" accepted speed moduli, y-axis: "distance matching" accepted speed moduli.

Figure 9.11 shows the approximation of figure 9.7 by motion interpolation between figure 9.6 and figure 9.8 obtained by equation 9.3 (see equation 8.47)

$$\begin{aligned} C_{24}^{mi}(i,j) = 0.5(&C_{23}(i-0.5m_i(i,j), j-0.5m_j(i,j)) \\ &+C_{25}(i+0.5m_i(i,j), j+0.5m_j(i,j))) \end{aligned} \tag{9.3}$$

where m_i and m_j are the i and j direction motion components obtained by applying the top down Bayesian motion estimation of section 7.5 to figure 9.6 and figure 9.8 with f=0.5. The border doubling of figure 9.9 does not occur here.

Figure 9.12 shows the error image

$$C_{24}(i,j) - C_{24}^{mi}(i,j) \tag{9.4}$$

The RMS value of image 9.12 is 6.7 counts, i.e. 2.63 % of the full range 255. This means the motion estimation reduces the RMS interpolation error with 39 %. The largest errors remain where the clouds have been deformed too much to stay recognisable, i.e. where the rigid motion hypothesis of equations 7.47 and 7.48 is violated.

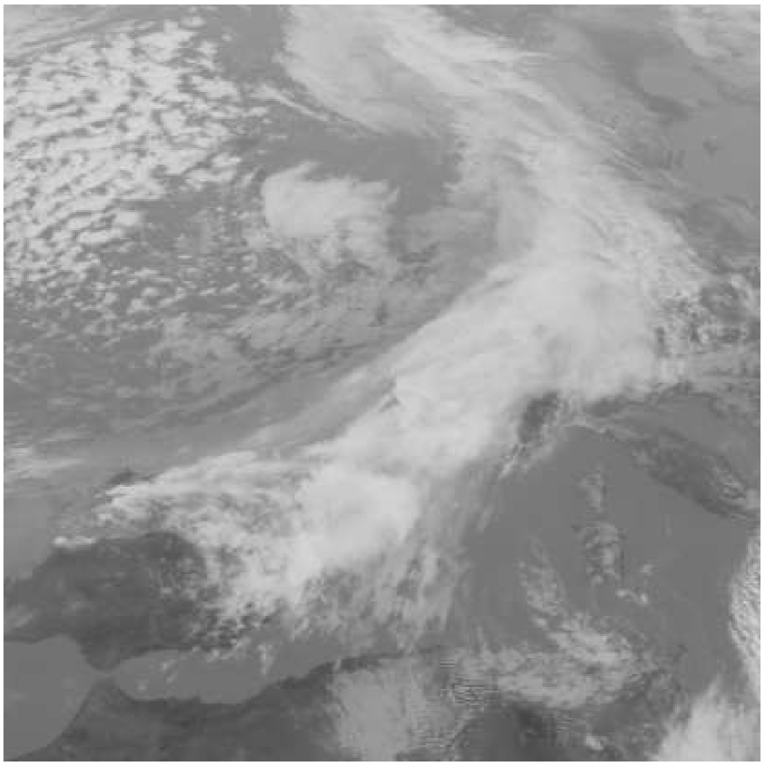

Figure 9.6: METEOSAT IR image 04/04/94 slot 23.

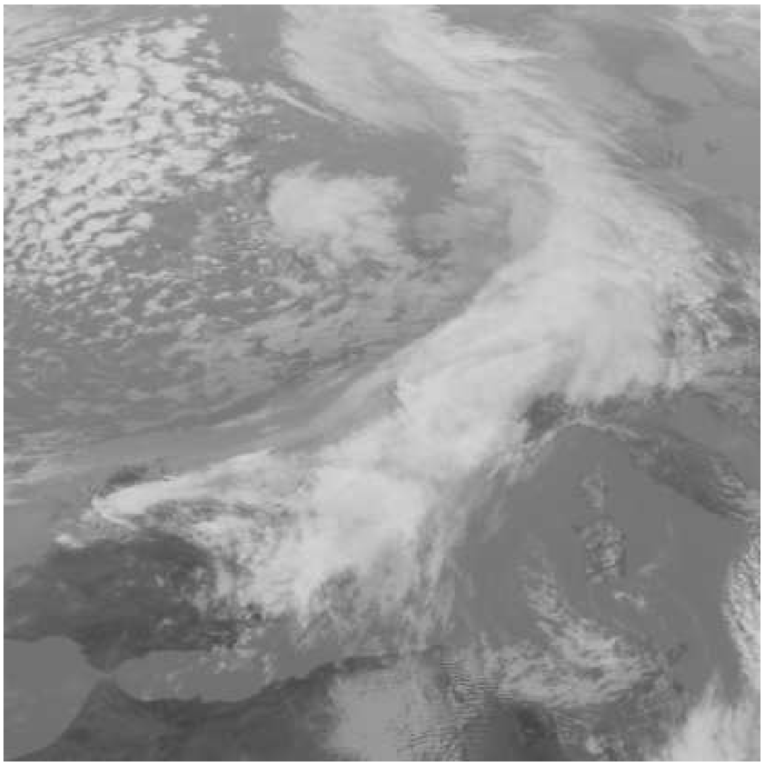

Figure 9.7: METEOSAT IR image 04/04/94 slot 24.

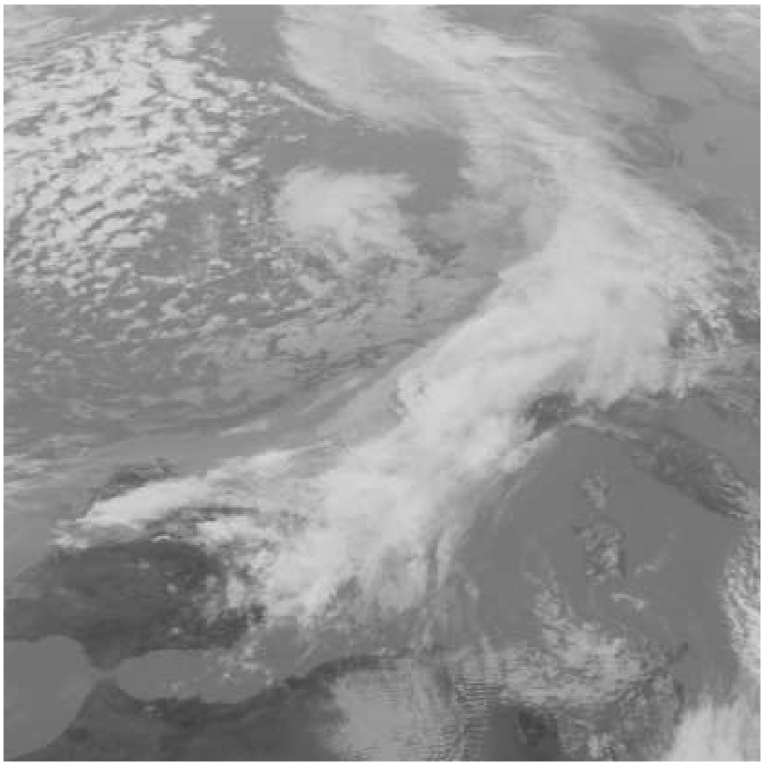

Figure 9.8: METEOSAT IR image 04/04/94 slot 25.

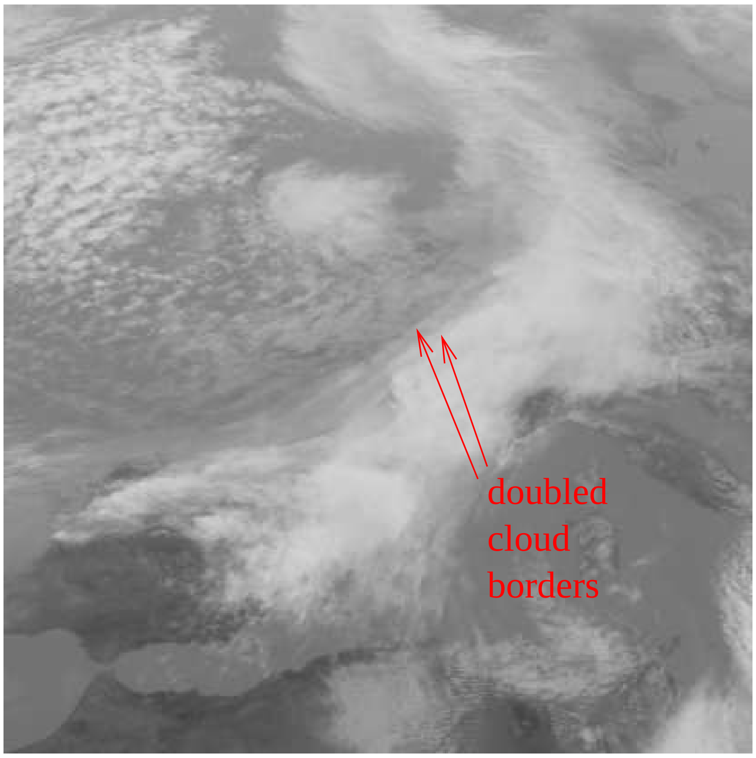

Figure 9.9: Approximation of figure 9.7 by simple linear interpolation between figure 9.6 and figure 9.8.

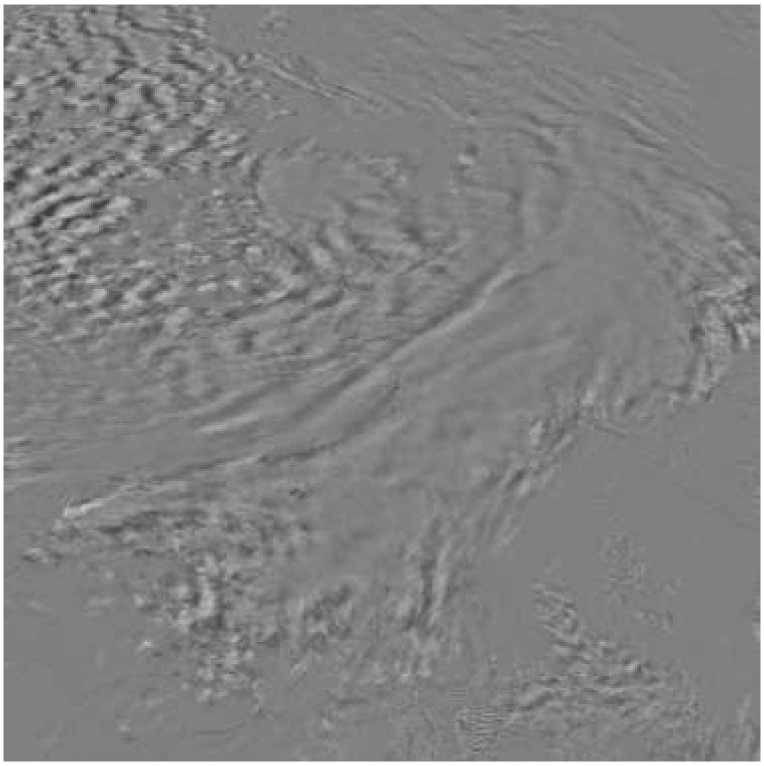

Figure 9.10: Difference between figure 9.7 and figure 9.9.

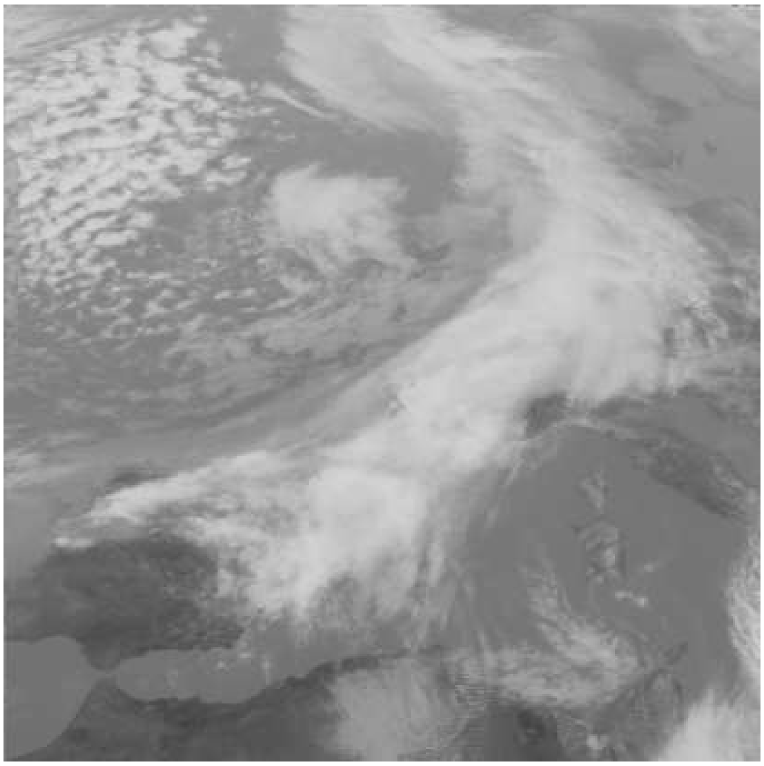

Figure 9.11: Approximation of figure 9.7 by motion interpolation between figure 9.6 and figure 9.8.

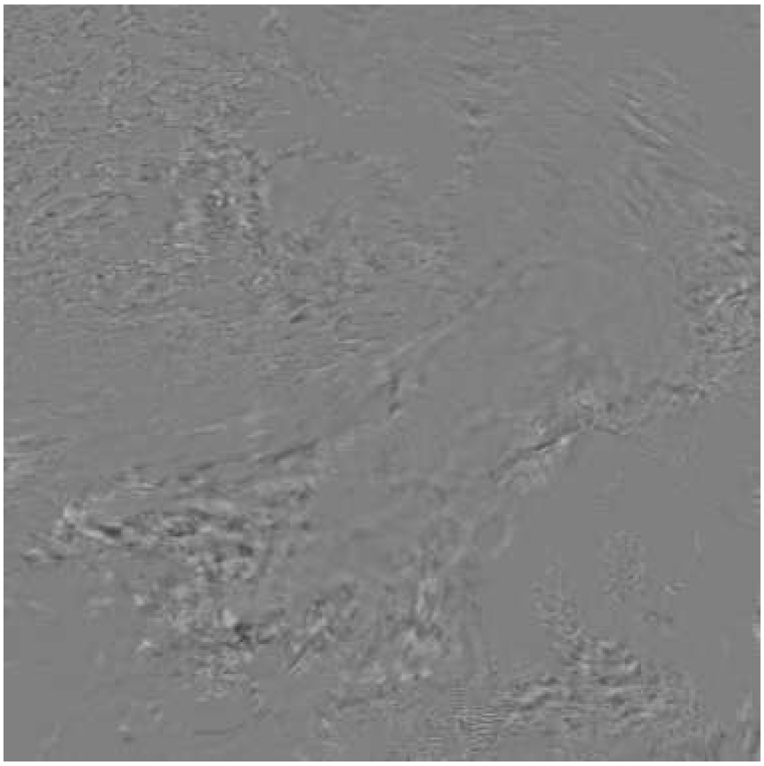

Figure 9.12: Difference between figure 9.7 and figure 9.11.

Chapter 10

High resolution radiation budget term validation

10.1 Limited validation possibility of radiation budget term estimates

Classically, "validation" of a method means : give the proof that the method results correspond with a well known "truth". However, since no well known "true" radiation budget measurement is available, this kind of "validation" is not possible for radiation budget term estimates. As an alternative, a more modest check of the quality of radaition budget term estimates, which consists in a check of the consistency of different independent radiation budget term estimates, can be used.

For the remainder of this chapter, "validation" should be understood as : check that no unexplained differences exist between different radiation budget term estimates.

10.2 Validation of the short wave flux surface density estimation

10.2.1 Comparison of clear sky desert short wave ADM's

The clear sky desert scene type is the brightest and the most stable of all clear sky surface scene types. Therefore it is the best suited scene type for the calibration of optical satellite sensors.

Clear sky desert scenes are used which are viewed simultaneously by the geostationary METEOSAT instrument and by a LEO (ERBE or ScaRaB) instrument.

Five different ADM's are used for the flux estimation from the geostationary radiances as well as from the LEO radiances. The geostationary and LEO flux surface density estimates are compared in function of the used ADM and in function of the used satellite instruments.

This comparison will yield a validation of the calibration of the geostationary sensors (the calibration of the LEO sensors is considered already validated by the on-board calibration of the LEO instruments), of the clear sky desert spectral conversion, and of the clear sky desert ADM's.

METEOSAT-2-RB and ERBE short wave comparison From all available full resolution METEOSAT 2 (described in section 4.2.2) and ERBE data (described in sections 4.2.1 and 6.1.1) which are collocated in space and time, the data was selected for which the ERBE scene identification (see section 6.1.1) is "clear sky desert".

Figure 10.1 shows an example of collocated METEOSAT 2 and ERBE ERBS for 09/07/1986 (dd/mm/yyyy) METEOSAT time slot 27 (13:00-13:25 UTC). ERBS record numbers from 2875 to 3025 are used. Only ERBS measurements with clear sky desert scene identification are shown.

All the selected data sets are identified in table 10.1. Along with a description of the METEOSAT data (date and slot) and the LEO data (date, LEO instrument and LEO instrument start and end record number) the mean solar zenith angle for the clear sky desert scenes is given.

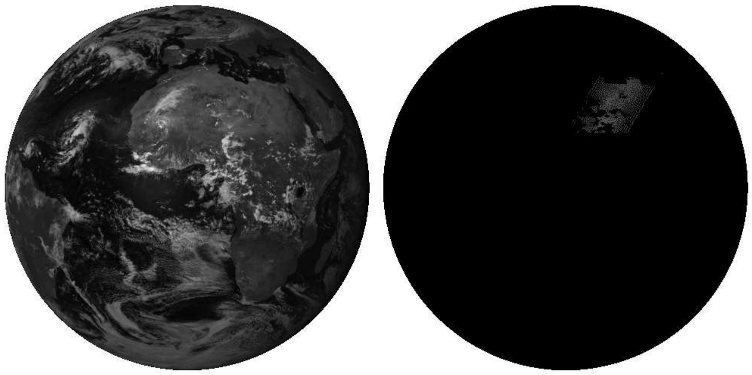

Figure 10.1: Space time collocated METEOSAT-2-RB (right) and ERBE ERBS (left) short wave data over ERBE footprints, for regions with ERBE scene identification "clear sky desert", for 09/07/1986 (dd/mm/yyyy) METEOSAT time slot 27 (13:00-13:25 UTC).

Date(yymmdd)	Slot	LEO instrument	LEO records	Mean θ_{sun}
860907	27	ERBS	2875 – 3025	38°
861109	27	NOAA-9	2950 – 3100	52°
861221	28	ERBS	2960 – 3110	52°
861221	29	NOAA-9	3037 – 3262	55°

Table 10.1: Selected data for comparison of collocated METEOSAT 2-RB and ERBE short wave flux surface density estimations for clear sky desert scenes.

For each of the four selected METEOSAT-2/ERBE combinations described in table 10.1, five available clear sky desert ADM's are applied to the METEOSAT 2 as well as to the ERBE radiances.

The five available clear sky desert ADM's are the ones for clear sky desert described in section 5.1.1 (denoted "ERBE"), in section 5.1.2 (denoted "ana"), in section 5.1.3 (denoted "rpm"), and the two ADM's described in section 5.1.4, namely the one derived from METEOSAT data (denoted "CapMet") and the one derived from ScaRaB data (denoted "CapSca").

Short wave flux surface density estimates F_{SW} are obtained from the METEOSAT 2 as well as from the ERBE estimates of the broad band short wave radiance L_{SW}, by the use of equation 5.6 for clear sky desert scenes.

$$F_{SW} = \frac{\pi L_{SW}}{R^{desert}(\theta_{sat}, \phi_{rel}, \theta_{sun})} \tag{10.1}$$

For the ERBE case, the radiance L_{SW} is the unfiltered radiance and the viewing angles $(\theta_{sat}, \phi_{rel}, \theta_{sun})$ are the viewing angles from the processed ERBE data (see section 6.1.1).

For the METEOSAT 2 case, the radiance L_{SW} is the radiance obtained with the spectral conversion of equation 8.62 and the viewing angles are the ones calculated in section 8.2.

For a good comparison between METEOSAT 2 and ERBE flux surface density estimates, the difference in resolution between the data to be compared should be taken into account. If this is not done, spatial variability effects might be the dominant reason of difference between the flux surface density estimates. To take this resolution difference into account in a simple way (the more elaborate convolution with the PSF, explained in section 8.15, will be validated in section 10.2.5), ERBE flux surface density estimates are compared with spatial means of METEOSAT-2-RB flux surface density estimates. Means over squares of 10 by 10 full resolution METEOSAT-2 pixels are taken. This removes most (although not all) of the spatial difference between an ERBE and a METEOSAT 2 pixel. As a secondary effect it also averages out the radiometric quantisation noise of the METEOSAT 2 pixels.

METEOSAT-2-RB short wave flux estimates are compared with ERBE flux estimates at ERBE pixel level. Figure 10.2 shows the METEOSAT-2-RB estimates versus the ERBE ERBS estimates of the reflected short wave flux surface density over the clear sky desert ERBE ERBS footprints shown in figure 10.1, with use of the “CapSca” ADM. In the case of perfect agreement between the estimated flux surface densities, this figure would show a perfect $y = x$ relation. In order to quantify the deviation from this perfect agreement case a linear fit $y = ax$ is performed. The best fitting line is shown in figure 10.2.

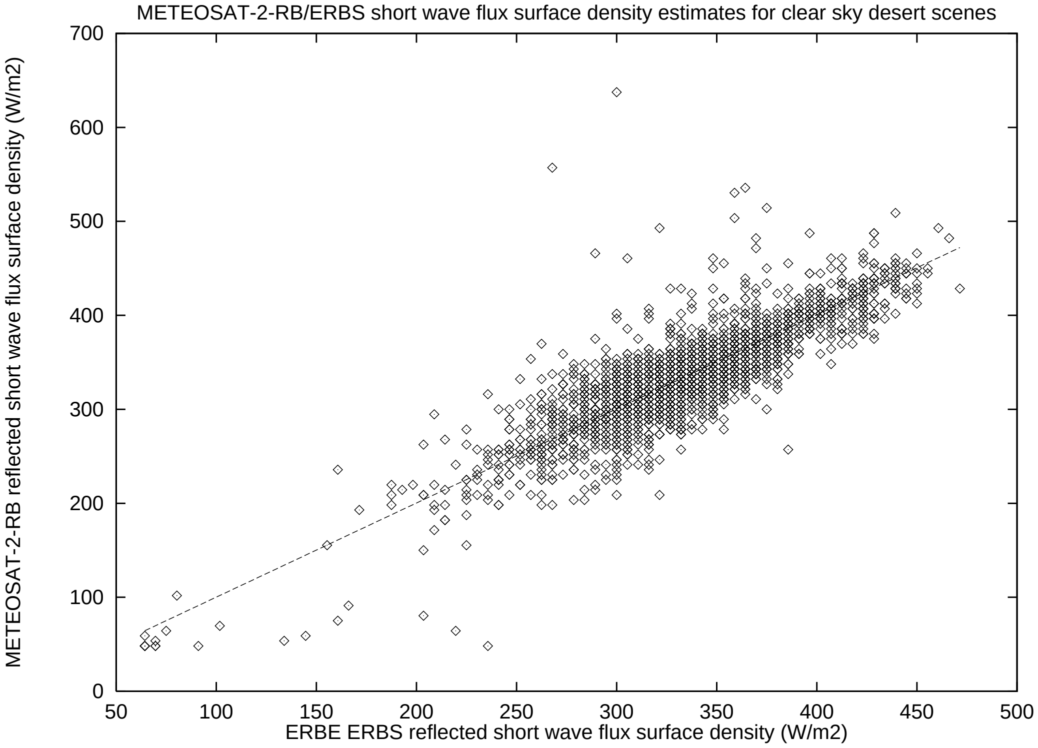

Figure 10.2: Comparison of ERBE ERBS and METEOSAT-2-RB estimations of short wave flux surface density (W/m^2) over ERBE footprints, for regions with ERBE scene identification “clear sky desert”, for 09/07/1986 (dd/mm/yyyy) METEOSAT time slot 27 (nominally 13:00-13:25 UTC). The “CapSca” ADM is used.

Table 10.2 shows the slopes a and the RMS differences $\sqrt{\overline{(y - ax)^2}}$ obtained for all the selected clear sky desert regions (see table 10.1), with the use of all five available clear sky desert ADM’s for the comparison of METEOSAT-2-RB and ERBE short flux surface density estimates. For comparison the slope and RMS difference for the case without angular dependency removal (denoted “Lambertian”) is also shown.

Table 10.3 shows the details of the performances of the five different ADM’s in the angular dependency removal for clear sky desert scenes. For every ADM, three statistical quantities are calculated over the four desert regions: the mean slope $\overline{\text{slope}}$, the standard deviation of the slope σ_{slope}, and the global RMS difference.

In the case of complete angular and spectral dependency removal σ_{slope} should be zero. If in addition the calibration and spectral conversion factor is correct, $\overline{\text{slope}}$ should be one. If in addition no instrumental noise (radiometric noise and statistical errors in the data processing) would exist and there would be a perfect match in space and time between the METEOSAT-2-RB and ERBE flux estimates, the RMS difference should be zero.

It can be seen that

- For the last three ADM’s (ERBE,rpm,ana), the values of $\overline{\text{slope}}$ are very close to each other. This can be expected since these three ADM’s are all derived from the NIMBUS 7 data set (see sections 5.1.1, 5.1.2 and 5.1.3). The slopes of the other two models (CapMet,CapSca), derived from METEOSAT and ScaRaB FM 1 data, are significantly different.
- The value σ_{slope} for the model “rpm” is the lowest, followed by the model “ana”.

Date(yymmdd)	Slot	ADM	Slope	RMS difference
860907	27	CapMet	1.03	33.7 W/m^2
860907	27	CapSca	1.00	29.6 W/m^2
860907	27	ERBE	0.96	29.1 W/m^2
860907	27	ana	0.93	27.3 W/m^2
860907	27	rpm	0.93	28.0 W/m^2
860907	27	Lambertian	1.06	33.6 W/m^2
861109	27	CapMet	1.17	33.3 W/m^2
861109	27	CapSca	1.09	25.5 W/m^2
861109	27	ERBE	0.94	33.1 W/m^2
861109	27	ana	0.92	24.2 W/m^2
861109	27	rpm	0.93	28.7 W/m^2
861109	27	Lambertian	1.20	24.1 W/m^2
861221	28	CapMet	0.98	32.8 W/m^2
861221	28	CapSca	0.92	21.9 W/m^2
861221	28	ERBE	0.85	26.0 W/m^2
861221	28	ana	0.83	23.5 W/m^2
861221	28	rpm	0.86	22.9 W/m^2
861221	28	Lambertian	0.92	34.3 W/m^2
861221	29	CapMet	1.10	27.9 W/m^2
861221	29	CapSca	1.00	21.0 W/m^2
861221	29	ERBE	0.88	30.2 W/m^2
861221	29	ana	0.88	20.8 W/m^2
861221	29	rpm	0.89	20.8 W/m^2
861221	28	Lambertian	1.02	26.0 W/m^2

Table 10.2: Results of the best linear fit between METEOSAT 2-RB and ERBE short wave flux surface density estimates for selected clear sky desert scenes. ERBE scene identification is used. METEOSAT 2 full resolution radiances are subsampled with a factor 10 (10 x 10 means are used) prior to flux surface density estimation.

	$\overline{\text{slope}}$	σ_{slope}	RMS difference
CapMet	1.07	0.085	32.0 W/m^2
CapSca	1.00	0.073	24.8 W/m^2
ERBE	0.91	0.052	29.7 W/m^2
ana	0.89	0.043	24.1 W/m^2
rpm	0.90	0.035	25.3 W/m^2
all	0.95	0.090	27.4 W/m^2
Lambertian	1.05	0.12	29.8 W/m^2

Table 10.3: Details of the performances of the different ADM's in the angular dependency removal for clear sky desert scenes, for the comparison METEOSAT-2-RB/ERBE.

- The RMS difference for the model "ana" is the lowest, followed closely by the models "CapSca" and "rpm". The RMS differences of the two other models, "CapMet" and "ERBE", are significantly higher.
- Overall the models "rpm" and "ana" are performing best (low σ_{slope}, fairly low RMS difference) in the removal of angular dependency for this comparison METEOSAT-2-RB/ERBE.

METEOSAT-5-RB and ScaRaB FM 1 short wave comparison A similar procedure as the one followed for the comparison METEOSAT-2-RB/ERBE has been followed for the comparison METEOSAT-5-RB/ScaRaB-FM-1.

As for the comparison METEOSAT-2-RB/ERBE, 4 regions of collocated METEOSAT-5-RB /ScaRaB-FM-1 data with ScaRaB FM 1 clear sky desert scene identification have been selected. The selected data sets are identified in table 10.4. Along with a description of the METEOSAT data (date and slot) and the LEO data (date, LEO instrument and LEO instrument start and end record number) the mean solar-zenith angle for the clear sky desert scenes is given.

Date(yymmdd)	Slot	LEO instrument	LEO records	Mean θ_{sun}
940316	18	ScaRaB FM 1	$1-60$	$50°$
940317	18	ScaRaB FM 1	$566-616$	$53°$
940318	17	ScaRaB FM 1	$546-655$	$54°$
940320	16	ScaRaB FM 1	$490-600$	$57°$

Table 10.4: Selected data for comparison of collocated METEOSAT-5-RB and ScaRaB FM 1 short wave flux estimations for clear sky desert scenes. ScaRaB FM 1 scene identification is used. METEOSAT 5 full resolution radiances are subsampled with a factor 10 (10 x 10 means are used) prior to flux surface density estimation.

For these selected regions, the same flux surface density estimation and comparison method has been used as for the METEOSAT-2-RB/ERBE case. Table 10.5 shows the slopes a and the RMS differences $\sqrt{\overline{(y-ax)^2}}$, obtained for all the selected clear sky desert regions (see table 10.4) and with the use of all five available clear sky desert ADM's, for the comparison of METEOSAT-5-RB and ScaRaB FM 1 short flux surface density estimates.

As for the METEOSAT-2-RB/ERBE comparison, for the last three ADM's (ERBE,rpm,ana), the values of $\overline{\mathrm{slope}}$ are very close to each other and the slopes of the other two models (CapMet,CapSca), derived from METEOSAT and ScaRaB FM 1 data, are significantly different. For all models the slopes obtained in this comparison METEOSAT-5-RB/ScaRaB-FM-1 are approximately 5 % lower than for the comparison METEOSAT-2-RB/ERBE.

Table 10.6 shows the details of the performances of the five different ADM's in the angular dependency removal for clear sky desert scenes. For every ADM, three statistical quantities are calculated over the four desert regions: the mean slope $\overline{\mathrm{slope}}$, the standard deviation of the slope σ_{slope}, and the global RMS difference.

It can be seen that

- The value σ_{slope} for the model "CapSca" is the lowest, closely followed by "ERBE" and "rpm".
- The values for the RMS differences are about the same for all models. They are always higher than for the METEOSAT-2-RB/ERBE comparison.
- Overall the models "CapSca", "ERBE" and "rpm" are performing best (low σ_{slope}) in the removal of angular dependency for this comparison METEOSAT-5-RB/ScaRaB-1.

Comparison of METEOSAT-2-RB/ERBE and METEOSAT-5-RB/ScaRaB-FM-1 short wave comparisons In figure 10.3, the scatter of the plot mean slope ($\overline{\mathrm{slope}}$), versus the RMS difference for the METEOSAT-2-RB/ERBE and for the METEOSAT-5-RB/ScaRaB-FM-1 comparison of the clear sky desert short wave flux surface density estimates, are put together for inter comparison.

Date(yymmdd)	Slot	ADM	Slope	RMS difference
940316	18	CapMet	0.98	45.3 W/m^2
940316	18	CapSca	0.92	46.4 W/m^2
940316	18	ERBE	0.82	47.9 W/m^2
940316	18	ana	0.81	46.7 W/m^2
940316	18	rpm	0.82	47.7 W/m^2
940316	18	Lambertian	0.91	45.0 W/m^2
940317	18	CapMet	1.03	41.3 W/m^2
940317	18	CapSca	0.96	40.9 W/m^2
940317	18	ERBE	0.85	41.0 W/m^2
940317	18	ana	0.85	40.7 W/m^2
940317	18	rpm	0.85	40.3 W/m^2
940317	18	Lambertian	0.97	42.2 W/m^2
940318	17	CapMet	1.01	37.0 W/m^2
940318	17	CapSca	0.94	37.3 W/m^2
940318	17	ERBE	0.86	39.7 W/m^2
940318	17	ana	0.87	38.2 W/m^2
940318	17	rpm	0.85	37.5 W/m^2
940318	17	Lambertian	0.95	38.8 W/m^2
940320	16	CapMet	1.00	44.5 W/m^2
940320	16	CapSca	0.94	44.7 W/m^2
940320	16	ERBE	0.86	48.4 W/m^2
940320	16	ana	0.91	46.2 W/m^2
940320	16	rpm	0.87	46.6 W/m^2
940320	16	Lambertian	0.93	45.0 W/m^2

Table 10.5: Results of best linear fit between METEOSAT-5-RB and ScaRaB FM 1 short wave flux surface density estimates for selected clear sky desert scenes. ERBE scene identification is used. METEOSAT 5 full resolution radiances are subsampled with a factor 10 (10x10 means are used) prior to flux surface density estimation.

	$\overline{\text{slope}}$	σ_{slope}	RMS difference
CapMet	1.01	0.023	42.2 W/m^2
CapSca	0.94	0.017	42.5 W/m^2
ERBE	0.85	0.019	44.4 W/m^2
ana	0.86	0.043	43.1 W/m^2
rpm	0.85	0.022	43.3 W/m^2
all	0.90	0.070	43.1 W/m^2
Lambertian	0.94	0.026	42.8 W/m^2

Table 10.6: Details of the performances of different ADM's in the angular dependency removal for clear sky desert scenes, for the comparison METEOSAT-5-RB/ScaRaB-1.

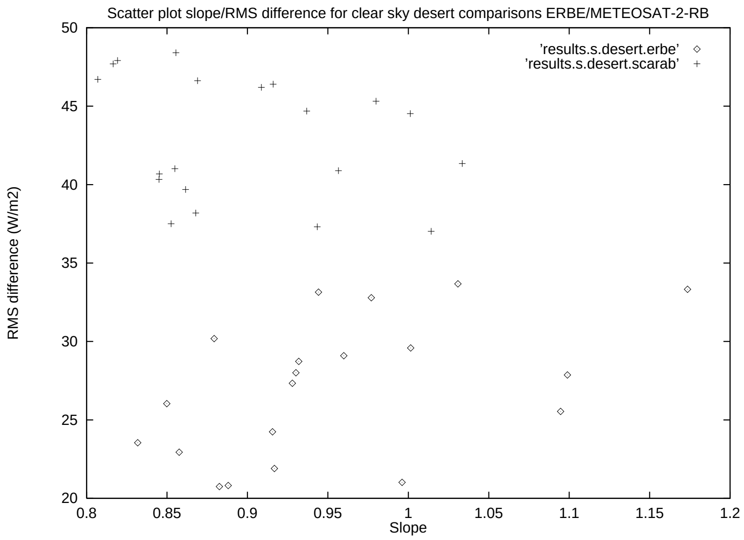

Figure 10.3: Combined scatter plot $\overline{\text{slope}}$/RMS difference for the ERBE/METEOSAT-2-RB and the ScaRaB-FM-1/METEOSAT-5-RB comparison of clear sky desert short wave flux surface density estimates.

It can be seen that for the METEOSAT-5-RB/ScaRaB-FM-1 case, the RMS difference is on average about 15 W/m2 higher compared to the METEOSAT-2-RB/ERBE case. This might be due to several reasons, among which a difference in noise characteristics of the concerned instruments or the difference in size of the PSF for both types of LEO (ERBE and ScaRaB) instruments, are the most probable.

It can also be seen that for the METEOSAT-5-RB/ScaRaB-FM-1 case, the slope is on average about 5 % lower compared to the METEOSAT-2-RB/ERBE case (the average slope for the METEOSAT-2-RB/ERBE case is 0.95, while for the METEOSAT-5-RB/ScaRaB-FM-1 case it is 0.90). This difference is probably due to remaining differences in calibration and spectral conversion between the METEOSAT-2-RB and the METEOSAT-5-RB flux surface density estimates.

For the METEOSAT clear sky desert flux surface density estimates, the sampling of the viewing angle space is very limited compared to the sampling of the viewing angle space for the LEO clear sky desert flux estimates. The METEOSAT viewing zenith angle and relative azimuth angle for Saharian desert pixels are very limited, while for LEO Saharian desert footprints all viewing zenith angles can occur and two distinct relative azimuth ranges (forward scattering and backward scattering) can occur. Therefore it is to be expected that the different ADM sets have their own typical mean[1] value of bidirectional reflection function for clear sky desert viewed by METEOSAT. This explains why, although the differences in average slopes of different ADM's listed in tables 10.3 and 10.6 are quite large, the differences between the slopes of corresponding ADM's in table 10.6 and table 10.3 are smaller.

Finally, it should be noted that the standard deviations of the slopes (values σ_{slope} in the tables 10.3 and 10.6) are for most of the ADM's significantly lower for the METEOSAT-5-RB/ScaRaB-FM-1 case compared to the METEOSAT-2-RB/ERBE when one compares single ADM's (e.g. 0.085 for the "CapMet" model for METEOSAT-2-RB/ERBE compared to 0.023 for the same model for METEOSAT-5-RB/ScaRaB-FM-1). This can be explained by the fact that there is a greater variability in the scenes used for the METEOSAT-2-RB/ERBE comparison compared to the variability in the scenes used for the METEOSAT-5-RB/ScaRaB-FM-1 comparison, for several reasons:

- In the ERBE case, ERBS and NOAA-9 measurements are mixed, while in the ScaRaB case, measurements from one single instrument and one single satellite are used.
- In the ERBE case, measurements at different times of the day are mixed, while in the ScaRaB case, the measurements are always taken at about the same time of the day.

[1]Mean over the limited region in the viewing angle space sampled by METEOSAT.

- In the ERBE case, measurements are taken over a relatively long period of 4 months, while in the ScaRaB case, measurements are taken over a relatively short period of only 5 days.

Conclusions The following overall conclusions about the METEOSAT VIS calibration, the clear sky desert spectral conversion and the clear sky desert ADM, can be made from this section

- The average slope a for all the ADM's, found in tables 10.3 and 10.6, which is a combined effect of the calibration and spectral conversion if angular dependencies are correctly removed, lies within the range of 0.9 to 1.0 . Moreover, the difference in slopes found for individual ADM's between the ERBE/METEOSAT-2-RB and the ScaRaB-FM-1/METEOSAT-5-RB case, is only 5 %. This suggests that the broad band reflected short wave radiances estimated from the METEOSAT data are accurate to within 10 %.
- Overall the "rpm" ADM seems to perform best in the removal of the angular dependency for clear sky desert scenes.
- For high variability clear sky desert data sets, the systematic uncertainty (σ_{slope}) for the "rpm" model is around 3.5 %. For low variability clear sky desert data sets the systematic uncertainty (σ_{slope}) for this model is reduced to around 2.2 %.
- The "rpm" ADM belongs to the family ("ana","CapSca","rpm") with the lowest RMS difference for the high variability clear sky desert data set.

The RMS difference will be reduced in sections 10.2.5, 10.2.6 and 10.2.7 by application of the PSF convolution of section 8.15, by application of the time interpolation of section 8.8, and by spatial integration.

10.2.2 Validation of clear sky short wave flux surface density estimation

The errors made in short wave flux surface density estimation from short wave radiances are in general a mixture of ADM errors and of scene identification errors. While in the previous section ADM errors were analysed apart from scene identification errors (since one single well defined, well detectable scene, clear sky desert, was used), this analysis will now be extended towards part of the scene identification errors, namely clear sky detection errors.

METEOSAT instantaneous clear sky count estimation (described in section 8.7) will be validated by comparing METEOSAT-2-RB short wave flux surface density estimates with ERBE flux surface density estimates over single ERBE footprints. On the ERBE side, only flux surface densities over footprints with clear sky scene identification will be used. On the METEOSAT-2-RB side flux surface density estimation with and without integration of instantaneous clear sky count estimation (described in section 8.11) will be used. The results will provide a validation of the clear sky count estimation (described in section 8.7) and of the production of clear sky count compatible ADM's (described in section 8.11).

The selected data sets for the validation of the clear sky flux surface density estimation are identified in table 10.7. A description of the METEOSAT 2 data (date and slot) and the LEO data (date, LEO instrument and LEO instrument start and end record number) is given.

For each of the ten selected METEOSAT-2-RB/ERBE combinations described in table 10.7, two ADM's are applied to the METEOSAT 2 as well as to the ERBE radiances to convert radiances to flux surface densities.

The two ADM sets used are the analytical one described in section 5.1.2 (denoted "ana"), and the one obtained with the Radiance Pair Method, described in section 5.1.3 (denoted "rpm").

On the ERBE side, only pixels with standard ERBE scene identification "clear sky" are used. The ERBE reflected short wave radiances are converted to reflected short wave flux surface densities by application of equation 5.6.

On the METEOSAT 2 side, the radiance to flux surface density conversion described in section 8.11 (illustrated in figure 8.27) is used, with and without instantaneous clear sky count compatible ADM production. In the case without instantaneous clear sky count compatible ADM production, $L^{cs,nd}$ (see equation 8.68) is used as L^{cs}_{VIS} for land and ocean scenes (identified from the surface

Date(yymmdd)	METEOSAT 2 slot	LEO instrument	LEO records
860907	27	ERBS	2875 – 3025
861108	34	ERBS	3570 – 3720
861108	34	NOAA-9	3740 – 3860
861109	26	ERBS	2870 – 3000
861109	33	ERBS	3600 – 3750
861109	27	NOAA-9	2950 – 3100
861109	34	NOAA-9	3712 – 3825
861213	33	NOAA-9	3480 – 3630
861221	28	ERBS	2960 – 3110
861221	29	NOAA-9	3037 – 3262

Table 10.7: Selected data for comparison of collocated METEOSAT-2-RB and ERBE short wave flux surface density estimations for clear sky scenes.

map of figure 4.19) while $L^{cs,desert}$ (see equation 8.69) is used as L^{cs}_{VIS} for desert scenes (also identified from the surface map of figure 4.19).

As a result, for every one of the ten METEOSAT-2-RB/ERBE data sets described in table 10.7, a comparison METEOSAT-2-RB/ERBE is made for four cases:

- Analytical ADM without instantaneous clear sky count compatible ADM production on METEOSAT 2 side
- RPM ADM without instantaneous clear sky count compatible ADM production on METEOSAT 2 side
- Analytical ADM with instantaneous clear sky count compatible ADM production on METEOSAT 2 side
- RPM ADM with instantaneous clear sky count compatible ADM production on METEOSAT 2 side

For every one of those (ten) data sets and for every one of those (four) cases, a comparison METEOSAT-2-RB/ERBE is made similar to the ones made for the clear sky desert ADM validation of section 10.2.1.

As in section 10.2.1, the difference in resolution between the data to be compared is taken into account in a simple way by comparing ERBE flux surface density estimates with spatial means of METEOSAT-2-RB flux surface density estimates. Means over squares of 10 by 10 full resolution METEOSAT 2 pixels are taken.

As in section 10.2.1, a linear fit $y = ax$ is performed for every one of the ten times four comparisons to be made. The difference of the slope a from the ideal value (one) and the RMS difference $\sqrt{\overline{(y-ax)^2}}$ (scatter around linear fit) quantify respectively the systematic and the stochastic errors.

Table 10.8 shows the slopes a and the RMS differences $\sqrt{\overline{(y-ax)^2}}$ obtained for all the selected clear sky data sets (see table 10.7) and for all the radiance to flux surface density conversion cases in the comparison of METEOSAT-2-RB and ERBE short flux surface density estimations. The column "ADM" contains the used ADM set (the analytical model is denoted by "ana", the RPM model is denoted by "rpm"). The column "clear sky" indicates whether clear sky count compatible ADM production is used on METEOSAT 2 side ("yes" means clear sky count compatible ADM production is used, "no" means clear sky count compatible ADM production is not used).

Table 10.9 shows the details of the performances of the four radiance to flux surface density conversion methods in the angular dependency removal of the radiances for clear sky scenes. For every angular conversion case, three statistical quantities are calculated over the ten clear sky data sets: the mean slope $\overline{\text{slope}}$, the standard deviation of the slope σ_{slope}, and the global RMS difference.

The main conclusions that can be drawn from these results are:

Date(yymmdd)	Slot(,LEO)	ADM	Clear sky	Slope	RMS difference
860907	27	ana	no	1.00	30.8 W/m^2
860907	27	rpm	no	1.00	31.4 W/m^2
860907	27	ana	yes	0.97	30.8 W/m^2
860907	27	rpm	yes	0.97	31.2 W/m^2
861108	34, ERBS	ana	no	0.79	26.7 W/m^2
861108	34, ERBS	rpm	no	0.72	28.4 W/m^2
861108	34, ERBS	ana	yes	0.82	29.6 W/m^2
861108	34, ERBS	rpm	yes	0.74	31.2 W/m^2
861108	34, NOAA-9	ana	no	0.83	24.9 W/m^2
861108	34, NOAA-9	rpm	no	0.88	40.9 W/m^2
861108	34, NOAA-9	ana	yes	0.86	26.9 W/m^2
861108	34, NOAA-9	rpm	yes	0.87	37.9 W/m^2
861109	26	ana	no	0.95	33.3 W/m^2
861109	26	rpm	no	0.98	34.7 W/m^2
861109	26	ana	yes	0.95	33.3 W/m^2
861109	26	rpm	yes	0.97	33.9 W/m^2
861109	33	ana	no	0.81	37.0 W/m^2
861109	33	rpm	no	0.76	35.6 W/m^2
861109	33	ana	yes	0.84	39.4 W/m^2
861109	33	rpm	yes	0.79	37.6 W/m^2
861109	27	ana	no	0.98	27.0 W/m^2
861109	27	rpm	no	0.99	29.8 W/m^2
861109	27	ana	yes	0.95	27.1 W/m^2
861109	27	rpm	yes	0.97	29.9 W/m^2
861109	34	ana	no	0.82	20.9 W/m^2
861109	34	rpm	no	0.84	35.4 W/m^2
861109	34	ana	yes	0.86	24.1 W/m^2
861109	34	rpm	yes	0.85	33.8 W/m^2
861213	33	ana	no	0.87	21.4 W/m^2
861213	33	ana	no	0.87	23.6 W/m^2
861213	33	ana	yes	0.91	25.8 W/m^2
861213	33	ana	yes	0.90	26.7 W/m^2
861221	28	ana	no	0.93	29.4 W/m^2
861221	28	rpm	no	0.92	28.0 W/m^2
861221	28	ana	yes	0.89	27.2 W/m^2
861221	28	rpm	yes	0.92	28.4 W/m^2
861221	29	ana	no	0.97	30.0 W/m^2
861221	29	rpm	no	0.93	32.2 W/m^2
861221	29	ana	yes	0.93	28.6 W/m^2
861221	29	rpm	yes	0.94	32.8 W/m^2

Table 10.8: Results of best linear fit between METEOSAT-2-RB and ERBE short wave flux surface density estimations for selected clear sky scenes. ERBE scene identification is used to convert ERBE radiances to flux surface densities. METEOSAT 2 full resolution radiances are subsampled with a factor 10 (10 x 10 means are used) prior to flux surface density estimation.

ADM	Clear sky	$\overline{\text{slope}}$	σ_{slope}	RMS difference
ana	no	0.90	0.080	28.5 W/m^2
rpm	no	0.89	0.095	32.3 W/m^2
ana	yes	0.90	0.052	29.6 W/m^2
rpm	yes	0.89	0.081	32.5 W/m^2

Table 10.9: Details of the performances of different ADM's and instantaneous clear sky count estimation in angular dependency removal for selected clear sky scenes, for the comparison METEOSAT-2-RB/ERBE.

- The slopes obtained for the four radiance to flux conversion cases are about the same. This is to be expected since this slope depends mainly on the calibration and spectral conversion, and on the angular conversion for the mean METEOSAT viewing angles. The angular conversion for the mean METEOSAT viewing angles seems to be comparable for both ADM sets used. This can be understood since both ADM sets are derived from the NIMBUS 7 data set.
- The standard deviation σ_{slope} of the fitted slopes and the RMS differences are smaller for the analytical ADM set compared to the RPM set. This might be due to different performances of these models in the removal of the angular dependency of the radiation for single scene types, but it might also be due to interferences of the different spectral behaviour of different clear sky scene types (e.g. blue clear sky ocean should have an other spectral coefficient than red desert) with the ADM's.
- The standard deviation σ_{slope} is systematically lower for the cases with clear sky count compatible ADM production compared to the cases with only the model ADM's. This validates the use of the instantaneous clear sky count estimation in the radiance to flux surface density conversion.
- The RMS difference remains essentially the same with and without instantaneous clear sky count estimation integration in the radiance to flux surface density conversion.

10.2.3 Comparison of short wave ADM's for all scenes

After the validation of the performance of the ADM's to remove the angular dependence of a single scene in section 10.2.1, the use of instantaneous clear sky count estimation for the correct selection of the clear sky ADM was validated in section 10.2.2. In this section the validation of the short wave radiance to flux surface density conversion is completed by an analysis of the radiance to flux surface density conversion for all scenes. This will give an overall validation of the performances of the ADM's for angular dependency removal of reflected short wave radiances *and* their usage for scene identification (both usages are described in section 8.11).

As in the previous sections, reflected short wave flux surface density estimates obtained from METEOSAT 2 will be compared with reflected short wave flux surface density estimates obtained from ERBE.

The selected data sets for validation of the short wave flux surface density estimation are the same as those identified in table 10.7.

For each of the ten selected METEOSAT-2-RB/ERBE combinations described in table 10.7, two ADM sets are applied to the METEOSAT 2 radiances as well as to the ERBE radiances to convert radiances to flux surface densities.

The two ADM sets used are the analytical ADM set described in section 5.1.2 (denoted "ana"), and the ADM set obtained with the Radiance Pair Method, described in section 5.1.3 (denoted "rpm").

On the ERBE side, the standard ERBE scene identification (i.e. the one based on the ERBE production ADM's, described in section 5.1.1) is used. The ERBE short wave radiances are converted to fluxes using the new ADM bidirectional reflection functions without modifying the previously derived scene identifications, by application of equation 5.6.

On the METEOSAT 2 side, the radiance to flux surface density conversion described in section 8.11 (illustrated in figure 8.27) is used, with instantaneous clear sky count compatible ADM production (which was validated in section 10.2.2).

As in sections 10.2.1 and 10.2.2, the difference in resolution between the data to be compared is taken into account in a simple way by comparing ERBE flux surface density estimates with spatial means of METEOSAT-2-RB flux surface density estimates. Means over squares of 10 by 10 full resolution METEOSAT 2 pixels are taken.

As in sections 10.2.1 and 10.2.2, a linear fit $y = ax$ is performed for every one of the ten times two (two ADM sets) comparisons to be made. The difference of the slope a from the ideal value (i.e. one), and the RMS difference $\sqrt{\overline{(y-ax)^2}}$ (scatter around linear fit) quantify respectively the systematic error and the stochastic error.

Table 10.10 shows the slopes a and the RMS differences $\sqrt{\overline{(y-ax)^2}}$ obtained for all the selected data sets (see table 10.7) and for both ADM sets. In the column "ADM" it is indicated which ADM set is used (the analytical model is denoted by "ana", the RPM model is denoted by "rpm").

Date(yymmdd)	Slot(,LEO)	ADM	Clear sky	Slope	RMS difference
860907	27	ana	yes	0.99	68.8 W/m^2
860907	27	rpm	yes	1.00	70.4 W/m^2
861108	34, ERBS	ana	yes	1.01	66.5 W/m^2
861108	34, ERBS	rpm	yes	0.95	61.5 W/m^2
861108	34, NOAA-9	ana	yes	1.14	67.3 W/m^2
861108	34, NOAA-9	rpm	yes	1.10	68.3 W/m^2
861109	26	ana	yes	1.04	75.6 W/m^2
861109	26	rpm	yes	1.04	77.3 W/m^2
861109	33	ana	yes	1.10	75.8 W/m^2
861109	33	rpm	yes	1.05	69.7 W/m^2
861109	27	ana	yes	1.05	75.7 W/m^2
861109	27	rpm	yes	1.04	75.1 W/m^2
861109	34	ana	yes	1.12	60.9 W/m^2
861109	34	rpm	yes	1.07	61.2 W/m^2
861213	33	ana	yes	0.99	62.9 W/m^2
861213	33	rpm	yes	0.93	61.7 W/m^2
861221	28	ana	yes	0.96	64.8 W/m^2
861221	28	rpm	yes	0.97	63.6 W/m^2
861221	29	ana	yes	1.06	75.6 W/m^2
861221	29	rpm	yes	1.02	72.1 W/m^2

Table 10.10: Results of best linear fit between METEOSAT-2-RB and ERBE short wave flux surface density estimations for all scenes. ERBE scene identification is used. Instantaneous clear sky count estimation is included in the METEOSAT radiance to flux surface density conversion. METEOSAT 2 full resolution radiances are subsampled with a factor 10 (10x10 means are used) prior to flux surface density estimation.

Table 10.11 shows the details of the performances of the two ADM sets in the angular dependency removal of the radiances for all scenes. For every ADM set, three statistical quantities are calculated over the ten clear sky data sets: the mean slope ($\overline{\text{slope}}$), the standard deviation of the slope σ_{slope}, and the global RMS difference.

The main conclusion that can be drawn from these results is:

- The mean slopes ($\overline{\text{slope}}$), the standard deviations, σ_{slope}, with which these slopes are measured and the RMS differences obtained for the two ADM sets, are not significantly different.

Overall conclusions that can be drawn from all the short wave radiance to flux surface density conversion validations obtained so far (clear sky desert, tables 10.3 and 10.6; clear sky, table 10.9;

	$\overline{\text{slope}}$	σ_{slope}	RMS difference
ana	1.05	0.059	69.6 W/m^2
rpm	1.02	0.054	68.3 W/m^2

Table 10.11: Details of the performances of the different ADM's in the angular dependency removal for all scenes, for the comparison METEOSAT-2-RB/ERBE.

all scenes, table 10.11), are

- The mean slopes ($\overline{\text{slope}}$), obtained in the comparison of METEOSAT and LEO short wave flux surface density estimates depend mainly on the scene type and the instruments for which the comparison is done.

- The standard deviation σ_{slope} (standard deviation, calculated over different regions, of slopes, calculated for groups of METEOSAT/LEO comparisons) depends mainly on the ADM set used to convert short wave radiances to flux surface densities. Comparable results for all scene types (using scene dependent spectral conversion on the METEOSAT side and standard scene identification on the ERBE side) are obtained for the analytical and the RPM ADM set. For these sets a standard deviation σ_{slope} of approximately 5% (0.05) is obtained. Using a solar constant value of 1366 W/m^2, this corresponds to a maximal stochastic difference METEOSAT-2-RB/ERBE (obtained for overhead sun and an albedo of 100 %) of 1366 W/m^2*0.05 $\approx$ 70 W/m^2. Using an average planetary albedo of 0.3, the maximal (obtained for overhead sun) average (average over all scenes) stochastic difference METEOSAT-2/ERBE is 0.3*1366 W/m^2*0.05 $\approx$ 20 W/m^2. Since the angular sampling of the LEO measurements is more complete than the METEOSAT angular sampling (for a given region the viewing angle of METEOSAT is limited, while for the LEO satellite all viewing zenith angles can occur; for a given region and a given time the relative azimuth angle of METEOSAT is limited and is almost always a backward scatter relative azimuth angle, while for the LEO satellite forward and backward scatter relative azimuth angles can occur), this value of 20 W/m^2 can be considered as the stochastic angular dependent METEOSAT flux surface density estimate error, that turns into a systematic error due to the limited METEOSAT angular sampling.

- The instantaneous RMS difference is of the order of 70 W/m^2 for comparisons over all scene types and is about 30 W/m^2 for comparisons over clear sky scene types only. A first reason for the higher RMS difference for the comparisons over all scene types might be the higher spatial and temporal variability of cloudy scenes compared to clear sky scenes. A second reason might be the higher scene identification errors (resulting in the selection of wrong bidirectional reflection functions for the conversion of radiances to flux surface densities) for cloudy scenes. The instantaneous RMS difference is not strongly dependent on the used ADM set.

- In the comparison of METEOSAT-2-RB/ERBE short wave flux surface density estimates over ERBE footprints, the instantaneous RMS difference of the order of 70 W/m^2, due to radiometric noise, spatial and temporal variability and scene identification errors, is dominant compared to the regional difference with standard deviation 20 W/m^2, due to angular and spectral conversion errors.

In sections 10.2.4, 10.2.5 and 10.2.6, it will be demonstrated how the RMS difference between METEOSAT-2-RB/ERBE short wave flux surface density estimates can be reduced by optimisation of the spatial and temporal correspondence of the METEOSAT-2-RB and ERBE short wave flux surface density estimates.

10.2.4 Importance of the temporal correspondence between geostationary and LEO measurements for short wave comparisons

In sections 10.2.1 to 10.2.3, the performance of different ADM sets in the short wave radiance to flux surface density conversion was validated by comparing METEOSAT and LEO short wave flux surface density estimates over LEO footprints. The emphasis was put on removal of the angular dependency of the radiance, while the spatial and temporal correspondence between the geostationary and LEO measurements was only assured in a simple way. The spatial correspondence between the geostationary and LEO measurements was assured by comparing LEO flux surface density estimates with 10 x 10 means of METEOSAT-x-RB flux surface density estimates. The temporal correspondence between the geostationary and LEO measurements was assured by comparing LEO flux estimates with the geostationary flux surface density estimates obtained during the METEOSAT time slot closest to the LEO time of acquisition.

In this section, a first quantification of the importance of the temporal correspondence between the geostationary and LEO measurements is obtained by comparing METEOSAT 2 to ERBE ERBS flux surface density estimates for three consecutive METEOSAT slots. The middle METEOSAT slot is the one with the best time correspondence with the ERBE measurements.

The selected data sets for quantification of the time correspondence importance are identified in table 10.12. A description of the METEOSAT 2 data (date and slot) and the LEO data (date, LEO instrument = ERBS and LEO instrument start and end record number) is given.

Date(yymmdd)	METEOSAT-2 slot	LEO instrument	LEO records
861221	27	ERBS	2960 – 3110
861221	28	ERBS	2960 – 3110
861221	29	ERBS	2960 – 3110

Table 10.12: Selected data for the investigation of the importance of the time correspondence between collocated METEOSAT-2-RB and ERBE short wave flux surface density estimates for all scenes.

The METEOSAT and ERBE ERBS data described in table 10.12 are processed and compared in exactly the same way as in section 10.2.3. The analytical ADM set is used for METEOSAT 2 and for ERBE ERBS. For METEOSAT 2, instantaneous clear sky count compatible ADM's are used. Means over 10 x 10 full resolution METEOSAT pixels are used. A fit $y = ax$ is performed for every one of the three combinations METEOSAT-2-RB/ERBE described in table 10.12.

Table 10.13 shows the slopes a and the RMS differences $\sqrt{\overline{(y-ax)^2}}$ obtained for the three selected data sets.

Date(yymmdd)	Slot	ADM	Clear sky	Slope	RMS difference
861221	27	ana	yes	1.05	73.2 W/m^2
861221	28	ana	yes	1.00	62.9 W/m^2
861221	29	ana	yes	0.95	66.5 W/m^2

Table 10.13: Results of the best linear fit between METEOSAT 2-RB and ERBE ERBS short wave flux surface density estimates, for time correspondence investigation. ERBE scene identification is used for the ERBS flux surface density estimation. METEOSAT 2 full resolution radiances are subsampled with a factor 10 (10 x 10 means are used) prior to flux surface density estimation.

It can be concluded that

- The middle slot 28 (the one with the best time correspondence METEOSAT-2-RB/ERBE) is also the one with the lowest RMS difference METEOSAT-2-RB/ERBE.
- For slot 29 (the slot with the second best time correspondence METEOSAT-2-RB/ERBE) the RMS difference is approximately 4 W/m^2 (approximately 6 % of the value for slot 28) higher than for slot 28.
- For slot 27, with a time difference METEOSAT-2/ERBE which is a little bit higher than 30 minutes, the RMS difference is approximately 10 W/m^2 (approximately 15 % of the value for slot 28) higher than for slot 28.

- The slope becomes approximately 5 % lower between two slots. This corresponds to the lowering of average solar zenith angle during the time interval (i.e. 30 minutes) between two slots.

These results suggest that improving the time difference between the geostationary and LEO measurements to a value lower than half a slot (15 minutes) can further improve the obtained METEOSAT-2-RB/ERBE RMS differences. This will be validated in section 10.2.6.

10.2.5 Validation of PSF convolution for short wave comparison

Until now, in the previous sections of this chapter, the spatial correspondence between the geostationary and LEO measurements was assured in a simple way by comparing flux surface density estimates obtained for 10 x 10 mean METEOSAT radiances with single footprint LEO radiances.

In this section, a better spatial correspondence is obtained between METEOSAT and LEO measurements by comparing ERBE ERBS flux surface density estimates with full resolution METEOSAT flux surface density estimates convoluted with the ERBE ERBS footprint PSF.

The selected data for quantification of the spatial correspondence importance are identified in table 10.14. The selected data set is a full resolution zoom of the data used in the previous section. A description of the METEOSAT 2 data (date and slot) and the LEO data (date, ERBS instrument start and end record number, full resolution METEOSAT window top left corner and bottom right corner coordinates) is given.

Date(yymmdd)	Slot	ERBS records	METEOSAT VIS window
861221	27	$2960-3110$	$2300,2800-3299,3799$
861221	28	$2960-3110$	$2300,2800-3299,3799$
861221	29	$2960-3110$	$2300,2800-3299,3799$

Table 10.14: Selected data for the validation of the convolution of the high resolution METEOSAT 2-RB short wave flux surface density with the PSF of collocated low resolution ERBE short wave flux surface density estimates, for all scenes.

Except for the spatial correspondence, the METEOSAT and ERBE ERBS data described in table 10.14 are processed and compared in exactly the same way as in section 10.2.3. The analytical ADM set is used for METEOSAT 2 and for ERBE ERBS. For METEOSAT 2, instantaneous clear sky count compatible ADM's are used.

Two approaches are considered to obtain METEOSAT-2-RB flux surface density estimates for low resolution ERBE ERBS footprints.

In a first approach (the central pixel approach), the spatial variability of the METEOSAT-2-RB flux surface density within the ERBS footprint field of view is neglected and the METEOSAT-2-RB flux surface density value of the central pixel of the ERBS field of view is compared to the estimated ERBS flux surface density.

In a second approach, the spatial variability of the METEOSAT-2-RB flux surface density within the ERBS field of view is taken into account, and the convolution value of the METEOSAT-2-RB flux surface density with the ERBS PSF is compared with the estimated ERBS flux surface density. The convolution value of the METEOSAT-2-RB flux surface density with the ERBS PSF is computed using equation 8.84.

A fit $y = ax$ is performed for every one of the three combinations METEOSAT-2-RB/ERBE described in table 10.12 and for the two approaches, to obtain METEOSAT-2 flux surface density estimates for low resolution ERBE ERBS footprints.

Table 10.15 shows the slopes a and the RMS differences $\sqrt{\overline{(y-ax)^2}}$ obtained for all six cases. In the column "PSF convolution" an indication is given of the approach used to obtain METEOSAT-2-RB flux estimates for low resolution ERBE ERBS footprints. PSF convolution is indicated by "yes", the central pixel approach is indicated by "no".

It can be concluded that

- The PSF convolution approach *drastically* reduces the RMS difference compared to the central pixel approach. This is mostly due to the removal of spatial variability within the ERBS

Date(yymmdd)	Slot	PSF convolution	Slope	RMS difference
861221	27	yes	1.08	73.6 W/m^2
861221	27	no	1.09	143 W/m^2
861221	28	yes	1.03	53.0 W/m^2
861221	28	no	1.05	117 W/m^2
861221	29	yes	0.97	70.0 W/m^2
861221	29	no	0.98	125 W/m^2

Table 10.15: Results of the best linear fit between high resolution METEOSAT-2-RB and single footprint ERBE ERBS short wave flux surface density estimates. ERBE scene identification is used for the ERBS flux surface density estimation. METEOSAT-2-RB full resolution flux surface density estimates are compared with single footprint ERBS flux surface density estimates. The analytical ADM's are used. Instantaneous clear sky count estimation is integrated in the METEOSAT flux surface density estimates.

footprint by the PSF convolution. The PSF convolution also lowers the radiometric noise on the METEOSAT 2 measurements, since the noise over several METEOSAT-2-RB pixels is averaged.

- For the same METEOSAT 2 slot, the slopes obtained with and without the PSF convolution are nearly the same. This indicates that the convolution of the METEOSAT 2 flux surface density with the ERBS PSF does not bias the results significantly.
- The lowest RMS differences are systematically obtained for the slot with the best time correspondence with the ERBS measurements, for both spatial correspondence approaches.

10.2.6 Validation of high resolution geostationary time interpolation for short wave radiation budget term estimation

In this section the good spatial correspondence between METEOSAT and ERBE flux estimates obtained in the previous section, is completed with a good *temporal* correspondence between those two flux estimates.

The good temporal correspondence is obtained using the time interpolation based on motion estimation developed in section 8.8. In a first step, time interpolation without motion estimation (also described in section 8.8) will be used, in order to *measure* the difference in time of acquisition of the used METEOSAT and ERBE data.

Detailed time correspondence analysis In this paragraph, the METEOSAT-2-RB flux surface density estimates over the ERBS footprints obtained in section 10.2.5 are linearly interpolated in time and compared with the ERBS flux surface density estimates, in order to optimise the correspondence in time of acquisition between the two datasets. The linear interpolation of the METEOSAT-2-RB flux surface densities convoluted with the ERBS PSF $F_{ERBS(METEOSAT-2-RB)}$ is done analogously as the linear time interpolation of METEOSAT counts in equation 8.48, as follows (* indicates multiplication)

$$
\begin{aligned}
& F_{ERBS(METEOSAT-2-RB),(1-f)*28+f*29} \\
& = (1-f) * F_{ERBS(METEOSAT-2-RB),28} \\
& \quad +f * F_{ERBS(METEOSAT-2-RB),29}
\end{aligned}
\tag{10.2}
$$

$F_{ERBS(METEOSAT-2-RB),28}$ is the ERBS footprint flux surface density estimate obtained from slot 28 of the METEOSAT-2 data, $F_{ERBS(METEOSAT-2-RB),29}$ is the ERBS footprint flux surface density estimate obtained from slot 29 of the METEOSAT-2 data. If, for a given ERBS footprint, the acquisition time of slot 28 is t_{28}, and the acquisition time of slot 29 is t_{29}, the METEOSAT-2-RB estimate of the flux surface density over the footprint at time $(1-f)*t_{28}+f*t_{29}$ is $F_{ERBS(METEOSAT-2-RB),(1-f)*28+f*29}$.

A fit $y = ax$ is performed for the eleven cases obtained when the time fraction varies from 0 to 0.5 (the range in which, from section 10.2.4 (table 10.13), the minimum RMS difference is expected to occur) with a step of 0.05. The time step with which the METEOSAT-2/ERBS acquisition time difference is measured is thus 0.05 slots or 1.5 minutes.

Table 10.16 shows the slopes a and the RMS differences $\sqrt{(y-ax)^2}$ obtained for all the eleven values of f.

Date(yymmdd)	Slot	PSF convolution	Slope	RMS difference	f
861221	28	yes	1.033	53.0 W/m^2	0
861221	28.05	yes	1.031	52.5 W/m^2	0.05
861221	28.1	yes	1.028	52.1 W/m^2	0.1
861221	28.15	yes	1.024	51.964 W/m^2	0.15
861221	28.2	yes	1.021	51.962 W/m^2	0.2
861221	28.25	yes	1.020	52.1 W/m^2	0.25
861221	28.3	yes	1.015	52.4 W/m^2	0.3
861221	28.35	yes	1.012	52.8 W/m^2	0.35
861221	28.4	yes	1.008	53.4 W/m^2	0.4
861221	28.45	yes	1.0056	54.1 W/m^2	0.45
861221	28.5	yes	1.0058	54.9 W/m^2	0.5

Table 10.16: Results of the best linear fit between high resolution METEOSAT-2-RB and single footprint ERBE ERBS short wave flux surface density estimates. ERBE scene identification is used for the ERBS flux surface density estimation. METEOSAT-2-RB full resolution flux surface density estimates are convoluted with the ERBS footprint PSF before comparison with the single footprint ERBS flux surface density estimates. The analytical ADM's are used. Instantaneous clear sky count estimation is integrated in the METEOSAT flux surface density estimation. Time interpolation without motion interpolation is used for a detailed time correspondence analysis between the METEOSAT-2-RB and ERBE ERBS measurements.

Figure 10.4 shows the RMS difference in function of the interpolated slot.

It can be seen from table 10.16 and figure 10.4 that the RMS difference in function of the interpolated slot is a convex function with minimum for interpolated slot 28.2, i.e. time fraction f=0.2 .

Motion estimation and interpolation In this section the time interpolation of the previous paragraph is refined using the motion interpolation developed in section 8.8, based on the motion estimation developed in section 7.5.

The same test data is used as in the first part of section 10.2.6, and the motion estimation and motion interpolation is done for the time fraction f=0.2 which yielded the best correspondence (minimal RMS difference) METEOSAT-2-RB/ERBS.

The motion estimation and motion interpolation is done at the level of unprocessed METEOSAT count images. From the image at time slot 28, with time of acquisition t_{28} and from the image at time slot 29, with time of acquisition t_{29}, the METEOSAT counts at time $t = 0.8t_{28} + 0.2t_{29}$ are estimated with the same technique as used in section 9.3.

From the motion interpolated METEOSAT counts the flux surface densities over the ERBS footprints are estimated in exactly the same way as in section 10.2.4.

A fit $y = ax$ is performed as in the previous section.

The resulting slope a is 1.01 and the resulting RMS difference $\sqrt{(y-ax)^2}$ is 51.8 W/m^2.

It can be concluded that

- The motion interpolation gives a lower RMS difference METEOSAT-2/ERBS than linear time interpolation, but the improvement is marginal.
- The improvement of motion interpolation compared to linear time interpolation for METEOSAT-2-RB/ERBS comparisons over ERBS footprints is much lower than the improvement for the single METEOSAT count estimation of section 9.3. This seems to indicate that comparisons of flux surface densities or radiances over larger areas (ERBS footprints are of the order of

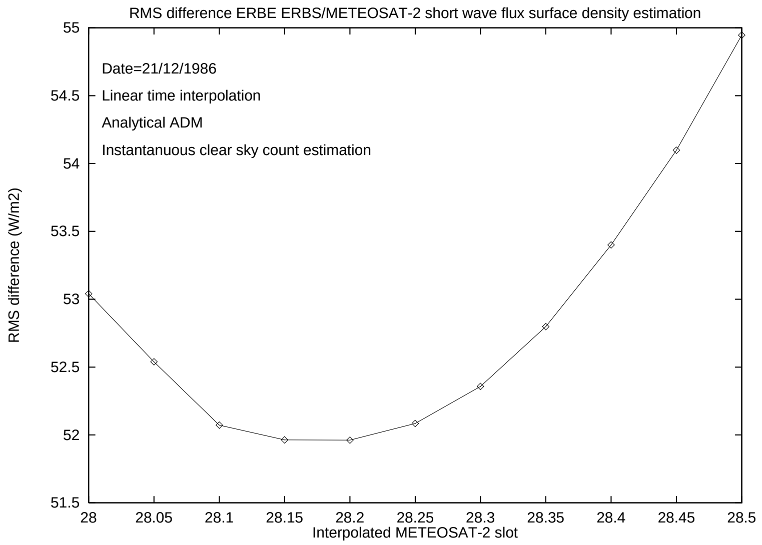

Figure 10.4: RMS difference METEOSAT-2-RB/ERBS short wave flux surface density estimates in function of linearly interpolated slot. Date=21/12/1986.

50 km x 50 km while the METEOSAT pixels of section 9.3 are of the order of 5 km x 10 km) are less sensitive to motion blurring than comparisons over smaller areas. This is reasonable, since for large regions the motion blurring is *relatively* smaller than for small regions.

10.2.7 Spatial integration of the short wave radiation budget term

In this section, the RMS difference between METEOSAT-2-RB and ERBS short wave flux surface density estimates obtained in section 10.2.6 is further reduced by performing the comparison METEOSAT-2-RB/ERBS not over single ERBS footprints, but over grid boxes which contain multiple ERBS footprints.

METEOSAT-2-RB and ERBS short wave flux surface density estimates over single ERBS footprints are obtained in exactly the same way as in section 10.2.6 (using motion interpolation on the METEOSAT-2-RB side).

Instead of comparing couples (y, x) where y and x are ERBS and METEOSAT-2-RB flux surface density estimates over single ERBS footprints, the comparison is done for couples where y and x are means over grid boxes of the individual footprint estimates. The grid boxes are defined as n times n METEOSAT VIS pixels. The width and height of those grid boxes is n times 2.5 km at the METEOSAT nadir.

A fit $y = ax$ is performed for the couples of mean grid box flux surface density estimates.

Grid boxes with size at METEOSAT nadir from 50 km to 225 km are considered.

Table 10.17 shows the fitted slope a and the RMS difference $\sqrt{(y - ax)^2}$ in function of the grid box size. Figure 10.5 shows the RMS difference in function of the grid box size.

It can be concluded that

- The slope is not affected by the grid box size. This indicates that the spatial integration does not bias the results.
- The RMS difference lowers with increasing grid box size. This indicates that with spatial integration, certain differences, e.g. due to radiometric noise and stochastic scene identification errors, are lowered by the spatial averaging process. This is only possible if there exists some stochastic independence between the values of these differences for different footprints.
- If the "LEO/geostationary" differences for different LEO footprints were completely stochastically independent, the standard deviation of the mean LEO/geostationary differences over

Date(yymmdd),slot	Grid box size (METEOSAT nadir)	Slope	RMS difference
861221, 28.2	50 km	1.00	49.8 W/m^2
861221, 28.2	75 km	1.00	43.8 W/m^2
861221, 28.2	100 km	1.00	42.0 W/m^2
861221, 28.2	125 km	1.00	41.0 W/m^2
861221, 28.2	150 km	1.00	39.6 W/m^2
861221, 28.2	175 km	1.00	37.4 W/m^2
861221, 28.2	200 km	1.00	36.6 W/m^2
861221, 28.2	225 km	1.00	34.7 W/m^2

Table 10.17: Evolution of the RMS difference between METEOSAT-2-RB and ERBS short wave flux surface density estimates in function of the grid box size over which the two flux surface densities are compared.

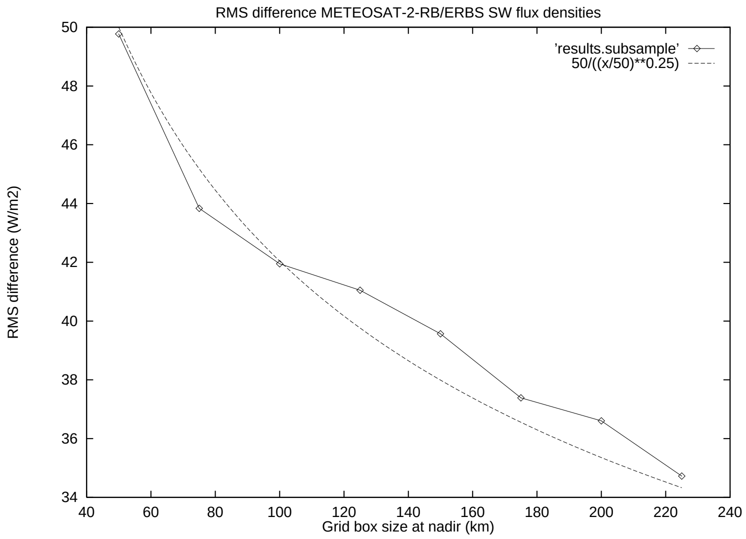

Figure 10.5: Evolution of the RMS difference between METEOSAT-2-RB and ERBS short wave flux surface density estimates in function of the grid box size over which the two flux surface densities are compared. X-axis: Grid box size (at METEOSAT nadir). Y-axis: RMS difference between METEOSAT-2-RB and ERBS short wave flux surface density estimates over the grid boxes.

the grid boxes would lower proportional to the square root of the number of footprints in a grid box. This means that the mean LEO/geostationary differences over the grid boxes would lower approximately as d^{-1}, with d the dimension of the grid box. The fit in figure 10.5 shows that in reality the mean LEO/geostationary differences over the grid boxes decrease much more slowly, as $d^{-0.25}$, with the dimension of the box.

10.3 Validation of the long wave flux surface density estimation

In this section the long wave flux surface density estimates obtained from METEOSAT data are compared with the LEO long wave flux surface density estimates, obtained by ERBE or ScaRaB. As for the short wave flux surface density comparisons in the sections 10.2.1 to 10.2.6, the comparison is done at LEO pixel level.

10.3.1 Comparison of METEOSAT-2-RB and ERBE long wave flux surface density estimates

METEOSAT-2-RB long wave flux surface density estimates are compared with ERBE NOAA 10 long wave flux surface density estimates for 08/11/1986 (dd/mm/yyyy) at time slot 18 (08:30-08:55 UTC).

Figure 10.6 shows the METEOSAT IR image, obtained on 08/11/1986 (dd/mm/yyyy) at time slot 18 (nominally 08:30-08:55 UTC) and the corresponding NOAA 10 long wave flux estimates.

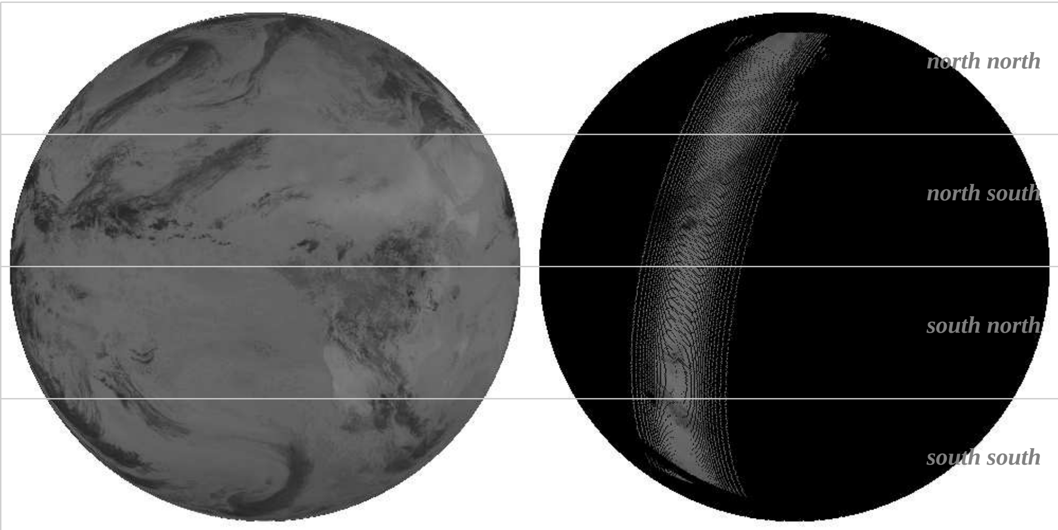

Figure 10.6: Left: METEOSAT IR image for time slot 18 (08:30-08:55 UTC) of 08/11/1986, right: Time space collocated long wave flux surface density estimates from the NOAA 10 ERBE instrument.

The METEOSAT-2 time slot 18 is the one with the best time correspondence with the NOAA 10 measurements respectively.

The METEOSAT-2-RB flux surface density estimates are convoluted with the estimated ERBE PSF before comparison with the ERBE flux surface density estimates over the ERBE footprints. The convolution value of the METEOSAT-2-RB flux surface density with the ERBS PSF is computed using equation 8.84.

For the four regions “north north”, “north south”, “south north” and “south south” (see figure 10.6), a linear fit $y = ax$ is performed where y and x are the ERBE (NOAA 10) and METEOSAT estimates of the emitted long wave flux surface density estimate over the ERBE (NOAA 10) footprints. Table 10.18 shows the slopes a and the RMS differences $\sqrt{\overline{(y-ax)^2}}$ obtained in the four regions for the comparison of METEOSAT 2 time slot 18 (08:30-08:55 UTC) compared to NOAA 10 measurements (see figure 10.6).

	North north	North south	South north	South south
Slope	0.98	0.98	0.95	0.95
RMS difference	$8.1W/m2$	$6.7W/m2$	$5.7W/m2$	$8.8W/m2$

Table 10.18: Slope of the best linear fit through the origin and the residual RMS difference between METEOSAT 2 derived and NOAA-10 ERBE emitted long wave flux surface density estimates. The fits are done over the four regions "north north", "north south", "south north" and "south south" (see figure 10.6) for the METEOSAT-2/NOAA-10 data of 08/11/1986 (dd/mm/yyyy), METEOSAT 2 slot 18 (08:30-08:55 UTC).

10.3.2 Comparison of METEOSAT-5-RB and ScaRaB FM 1 long wave flux surface density estimates

METEOSAT 5 derived long wave flux surface density estimates are compared with the long wave flux surface density estimates derived from the ScaRaB FM 1 instrument on board the METEOR 3/8 satellite. The comparison is done for the data obtained on 16/03/94 (dd/mm/yyyy) at time slot 18, over the METEOSAT north north region (defined as in figure 10.6).

The METEOSAT 5 time slot 18 is the one with the best time correspondence with the ScaRaB measurements.

Similarly as in section 10.2.5, two approaches are considered to obtain METEOSAT-5-RB flux surface density estimates for low resolution ScaRaB FM 1 footprints. In a first approach (the central pixel approach), the spatial variability of the METEOSAT-5-RB flux surface density within the ScaRaB FM 1 footprint is neglected and the METEOSAT-5-RB flux surface density value of the central pixel of the ScaRaB field of view is compared to the estimated ScaRaB FM 1 flux surface density. In a second approach, the spatial variability of the METEOSAT-5-RB flux surface density within the ScaRaB FM 1 footprint is taken into account, and the convolution value of the METEOSAT-5-RB flux surface density with the ScaRaB FM 1 PSF is compared with the estimated ScaRaB FM 1 flux surface density. The convolution value of the METEOSAT-5-RB flux surface density with the ScaRaB FM 1 PSF is computed using equation 8.84.

A fit $y = ax$ is performed for every one of the two approaches to obtain METEOSAT-5-RB flux surface density estimates over low resolution ScaRaB FM 1 footprints.

Table 10.19 shows the slopes a and the RMS differences $\sqrt{\overline{(y-ax)^2}}$ obtained with and without the PSF convolution.

	PSF convolution	Central pixel
Slope	0.91	0.91
RMS difference	14.6 W/m^2	17.4 W/m^2

Table 10.19: Slope of the best linear fit through the origin and the residual RMS difference between METEOSAT-5-RB and ScaRaB FM 1 emitted long wave flux surface density estimates. The fits are done with and without PSF convolution for the METEOSAT-5/ScaRaB-FM-1 data of 08/11/1986 (dd/mm/yyyy), METEOSAT 5 slot 18 (08:30-08:55 UTC).

10.3.3 Conclusions

From the METEOSAT/LEO long wave flux surface density estimation comparisons, it can be concluded that

- For the METEOSAT-2-RB/ERBE comparisons, slopes very close to one are obtained, for all regions and for all comparisons. This seems to indicate that the calibration is correct and that the angular dependency of the long wave radiation is correctly removed.

- For the METEOSAT-5-RB/ScaRaB comparison, a slope which is 10 % too low, is obtained. This seems to indicate a problem with calibration or spectral conversion, probably on the METEOSAT 5 side.
- For the METEOSAT-2-RB/NOAA-10 comparison (case with the best time correspondence METEOSAT-2-RB/NOAA-10) RMS differences around 8 W/m^2 are obtained.
- The convolution with the estimated ScaRaB FM 1 PSF reduces the RMS difference METEOSAT-5/ScaRaB-FM-1 with about 19 %. This seems to indicate that the spatial variability over a ScaRaB FM 1 footprint can not be neglected, and that the ScaRaB FM 1 PSF is reasonably well estimated.
- For the METEOSAT-5-RB/ScaRaB-FM-1 comparison the obtained RMS difference is almost twice the one obtained for the METEOSAT-2-RB/NOAA-10 comparison. This might be due to several reasons: the smaller size of the ScaRaB FM 1 PSF compared to the NOAA 10 PSF, possible higher radiometric noise of METEOSAT 5 compared to METEOSAT 2, possible higher radiometric noise of ScaRaB FM 1 compared to NOAA 10, possible worse knowledge of the ScaRaB FM 1 PSF compared to the NOAA 10 PSF.

10.4 Overall conclusions

In this chapter, the following differences between METEOSAT-RB and LEO radiation budget term estimates have been found :

- A systematic regional difference with RMS value (calculated over different regions) of approximately 5% between METEOSAT-RB and LEO reflected solar flux surface density estimates. This corresponds to a maximum (for overhead sun) mean (over all scenes) difference of approximately 20 W/m^2.
- A stochastic difference of the order of 50 W/m^2 at a resolution of 50 km, and of the order of 35 W/m^2 at a resolution of 250 km, between METEOSAT-RB and LEO reflected solar flux density estimates.
- A systematic difference less than 5 % between METEOSAT-2-RB and ERBE emitted thermal flux surface density estimates.
- A stochastic difference of the order of 8 W/m^2, at ERBE footprint resolution, between METEOSAT-2-RB and ERBE emitted thermal flux surface density estimates.

Chapter 11

Future applications

11.1 GERB/SEVIRI processing

11.1.1 Introduction

In this work, estimates of the terms of the local instantaneous radiation budget have been derived from geostationary data. The use of geostationary data is indispensable in order to obtain a good time and space sampling of the radiation budget terms, which in turn is indispensable for the study of physical atmospheric processes.

So far, the currently available METEOSAT data has been used. The use of this data is currently mandatory if one wants to study the terms of the local instantaneous radiation budget at high time and space resolution over Europe and Africa, but the METEOSAT instrument also has some important drawbacks for the study of the radiation budget terms:

- The number of bits to which METEOSAT radiances are quantified is relatively low. For the METEOSAT 2 and METEOSAT 5 data used in this work the number of bits for the IR and WV counts is 8, and the number of bits for the VIS counts is 6 in the case of METEOSAT 2 and 8 in the case of METEOSAT 5. This means that for the estimated reflected solar flux surface density, quantisation steps of approximately (1366 W/m^2)/63=22 W/m^2 are obtained in the METEOSAT 2 case, and of approximately (1366 W/m^2)/255=5.3 W/m^2 in the METEOSAT 5 case. These quantisation steps apply to single pixel flux surface density estimates.

- There is no on board VIS calibration source. Calibration of the VIS channel is only obtained indirectly through common observation of selected earth targets by the METEOSAT VIS channel and by other radiometers. This results in VIS calibration relative uncertainties of 5 to 10 %.

- METEOSAT has narrow spectral channels. Therefore METEOSAT does not measure spectrally integrated reflected solar radiance or emitted thermal radiance, but it measures only spectral samples of these radiances. The spectrally integrated radiances have to be approximated from the spectral narrow band measurements, with resulting spectral uncertainties.

- For a given time of the day, a geostationary satellite (e.g. METEOSAT) views a given region of the earth with a viewing geometry that is almost fixed. The viewing geometry changes only very slowly in time due to seasonal movements of the sun. As a result any error in bidirectional reflection function which is a systematic function of the viewing angles, results in a systematic regional error in the METEOSAT flux surface density estimates. This error can not be averaged out by time averaging.

In the future, the techniques developed in this work will be applied to the data measured by the instruments aboard the METEOSAT Second Generation (MSG) satellites. The first MSG satellite is planned to be launched by the year 2000.

Aboard the MSG satellite two instruments will be available, the low resolution broad band instrument GERB (Geostationary Earth Radiation Budget) and the high resolution multi spectral

Spinning Enhanced Visual and InfraRed Imager (SEVIRI). The synergy of those two instruments is expected to remove most of the drawbacks of the current METEOSAT instrument for the study of the top of the atmosphere radiation budget terms.

The drawback that is hardest to remove is the fixed viewing geometry problem, intrinsic to every geostationary satellite. The planned alleviation of this problem will be addressed partially in this section, partially in section 11.2.

11.1.2 GERB description

GERB is an instrument with two channels, a short wave channel (spectral range $\approx$ [0.32 to 4.0 μm]) and a total wave channel (spectral range $\approx$ [0.32 to 30 μm]). Similar channels can be found in ERBE, ScaRaB and CERES. The short wave channel uses the same optics and detectors as the total channel. The total channel is transformed to the short wave channel by insertion of a removable short wave filter (quartz filter). By subtraction (see figure 11.1 for the example of CERES Proto Flight Model (PFM) channels) of the short wave channel from the total channel, with the use of proper weights to account for the transmission of the short wave filter, a synthetic long wave channel (spectral range $\approx$ [4 to 30 μm]) can be obtained.

GERB has a linear detector array of 256 detector cells. During every MSG rotation period of 600 ms, these detector cells will measure, during 40 ms, one column of a 250x256 image of the earth. The total image for one spectral channel will be produced in 250x600 ms = 2.5 minutes. A couple of spectral images (one total wave image and one short wave image) will be produced every 5 minutes.

Thanks to the use of on board calibration sources (a black body for thermal calibration and an integrating sphere which acts as solar diffuser for solar calibration) absolute accuracies better than 0.5 % (corresponding approximately to an absolute long wave flux surface density estimation error of 1.7 W/m^2) are expected for the long wave radiances and absolute accuracies better than 1 % (corresponding approximately to an absolute short wave flux surface density estimation error of 13.7 W/m^2) are expected for the short wave radiances.

The high short wave absolute accuracy is expected to be obtained by the combined use of

- the pre flight characterisation of the integrating sphere
- the use of the total solar irradiance, measured with a systematic relative error estimated to be better than 0.1 %, as calibration reference (see section 4.1)
- use of the SOLSPEC derived solar spectrum (see section 4.1.6)
- the monitoring of the spectral aging of the integrating sphere by photodiodes

After averaging of the 5 minutes spectral images over a 15 minutes period, the RMS noise on the measurements is expected to be lower than 0.15 W/m^{2}sr (corresponding approximately to noise on the long wave flux surface density estimation with an RMS value of 0.47 W/m^2) for the long wave radiances, and lower than 0.8 W/m^{2}sr (corresponding approximately to noise on the short wave flux surface density estimation with an RMS value of 2.5 W/m^2) for the short wave radiances.

The sampling distance of GERB at nadir will be around 48 km. The effective resolution (PSF half width) will be around 100 km.

11.1.3 SEVIRI description

SEVIRI is an instrument with the following twelve spectral channels

- One channel in the reflected solar radiance spectral range, the High Resolution Visible (HRV) channel, which covers half of the earth disc with a sampling distance at nadir of 1 km x 1 km.
- Three channels in the reflected solar radiance spectral range, which cover the full earth disc with a sampling distance at nadir of 3 km x 3 km. These channels are named VIS 0.6, VIS 0.8 and IR 1.6 .

- One channel, the IR 3.8 channel, in the spectral range were both reflected solar and emitted thermal radiation are important, which covers the full earth disc with a sampling distance at nadir of 3 km x 3 km.
- Seven channels in the emitted thermal radiation spectral range, which cover the earth with a sampling distance at nadir of 3 km x 3 km. These channels are named IR 6.2, IR 7.3, IR 8.7, IR 9.7, IR 10.8, IR 12.0, IR 13.4 .

Table 11.1 shows the spectral intervals for which these different channels are sensitive.

Channel	Spectral range
HRV	0.6 – 0.9 μm
VIS 0.6	0.56 – 0.71 μm
VIS 0.8	0.74 – 0.88 μm
IR 1.6	1.50 – 1.78 μm
IR 3.8	3.40 – 4.20 μm
IR 6.2	5.35 – 7.15 μm
IR 7.3	6.85 – 7.85 μm
IR 8.7	8.30 – 9.10 μm
IR 9.7	9.38 – 9.94 μm
IR 10.8	9.80 – 11.80 μm
IR 12.0	11.00 – 13.00 μm
IR 13.4	12.40 – 14.40 μm

Table 11.1: Spectral ranges in which the SEVIRI channels measure radiation.

The functioning of the SEVIRI instrument will be more or less analogous to the current METEOSAT imager. SEVIRI images are build up of line units, which are scanned automatically by the rotation of the satellite. One line unit consists of 3 lines (measured by an array of 3 detector cells) for the channels with 3 km sampling distance. One line unit consists of 9 lines (measured by an array of 9 detector cells) for the HRV channel with 1 km sampling distance. A complete image is build up in 10 minutes. The time interval between two images is 15 minutes.

A small internal black body will be used for in flight calibration of the thermal emission channels. No on board solar calibration channel is foreseen.

The relative RMS noise on the measurements is expected to be lower than 1 % for the reflected solar radiation channels, and the RMS noise is expected to be lower than 1 K equivalent blackbody temperature change for a blackbody at 3OO K for the emitted thermal radiation channels.

The radiances of all channels will be quantised to 10 bits.

11.1.4 Synergy of GERB and SEVIRI

Applying the algorithms developed in this work, GERB radiances will be converted to flux surface densities in the future Royal Meteorological Institute of Belgium (RMIB) GERB Ground Segment Processing System (GGSPS) branch. SEVIRI data and SEVIRI derived products will be used as auxiliary data in this process.

The combined use of GERB and SEVIRI data for the determination of the local instantaneous radiation budget terms at the top of the atmosphere will remove a lot of the drawbacks of the current METEOSAT imager mentioned before:

- GERB and SEVIRI will have a high number of bits and a low radiometric noise compared to the current METEOSAT.
- Thanks to the on board calibration sources (black bodies on GERB and SEVIRI, integrating sphere on GERB) the calibration accuracy of the radiances will be improved compared to the current METEOSAT, especially in the short wave spectral region.
- GERB has spectral broad band channels. Therefore the spectral uncertainty will be strongly reduced compared to the current METEOSAT.

- SEVIRI has a higher spatial resolution and more spectral channels than the current METEOSAT. This will allow a good scene identification at GERB pixel level, and should result in the selection of accurate bidirectional reflection functions to convert GERB radiances to fluxes. Improved ADM's, coming from POLarization and Directionality of Earth Reflectances (POLDER) data (see section 11.2.1), and/or from the combination Clouds and the Earth's Radiant Energy System (CERES)/MODerate resolution Imaging Spectroradiometer (MODIS) (see section 11.2.1), will be applied to the combination GERB/SEVIRI.

11.2 Reduction of angular dependent errors.

As mentioned before, the fixed viewing geometry of a geostationary satellite for a given region on earth and for a given time of day, makes the estimation of radiation budget terms from geostationary satellite instrument measurements vulnerable for ADM errors. ADM errors that are a function of the viewing angles, become regional systematic errors in the geostationary flux surface density estimates.

Two precautions can be taken to minimise the angular dependent errors made in geostationary flux estimation:

- The best a priori ADM sets should be used.
- Regular comparisons should be made with data from LEO instrument(s) having more variable viewing geometry than the geostationary instrument(s). This allows quantification of the inevitable angular dependent errors. The angular dependent errors can be minimised by the choice of the best a posteriori ADM set.

Both precautions will be taken in the future RMIB GGSPS branch. The best available ADM sets will be used. They are expected to come either from POLDER or from the combination CERES/MODIS.

11.2.1 Use of improved ADM sets

Description of POLDER The POLDER instrument is a 244 x 274 camera measuring in nine solar reflection solar reflection spectral channels. Six of these nine spectral channels are useful for measurements of the reflected solar radiation for all scene types (the remaining three spectral channels have low dynamic range and are dedicated to ocean colour measurements). For three of those six channels, the polarisation is measured for three different polarisation angles. POLDER has been mounted on the LEO ADvanced Earth Observing Satellite (ADEOS). 10 months of data have been collected prior to 30 June 1997, when the instrument stopped functioning. Thanks to the movement of the LEO platform, and the multi angle viewing geometry of the POLDER camera, POLDER can observe a given point on earth quasi simultaneously from 13 directions during a single satellite pass. This makes the instrument ideally suited for the derivation of Bidirectional Reflection Distribution Functions (BRDF's) and of Bidirectional Polarisation Distribution Functions (BPDF's).

The *derivation* of new ADM sets is not within the scope of future applications (in the future RMIB GGSPS branch) of the algorithms developed in this work. However, if good quality ADM sets become available from POLDER, they will be used in the future RMIB GGSPS branch.

Description of CERES/MODIS It is planned [WBH+96] to obtain a strongly improved version of the ERBE project in the CERES project. CERES instruments are broad band instruments analogous to ERBE, ScaRaB and GERB, with a total wave channel and a short wave channel. A synthetic long wave channel can be obtained by weighted subtraction of the short wave from the total wave channel. As for ScaRaB, an atmospheric window channel around 11 μm (corresponding approximately to the METEOSAT IR channel) is added. Figure 11.1 shows the measured spectral responses for the CERES Proto Flight Model (PFM), to be launched (at the time of this writing) with the Tropical Rainfall Measurement Mission (TRMM) satellite in November 1997.

TRMM will contain one CERES instrument. The next two satellites carrying CERES instruments, Earth Observing System - AM I (EOS-AM I), to be launched in 1998, and Earth Observing

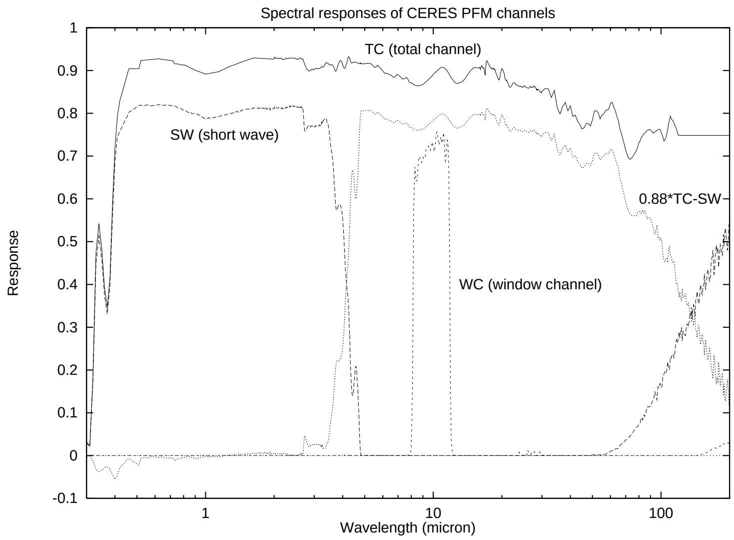

Figure 11.1: CERES PFM spectral responses: TC (Total Channel), SW (Short Wave), WC (Window Channel) and synthetic long wave channel calculated as 0.88*TC-SW.

System - PM I (EOS-PM I), to be launched in 2000, will contain two CERES instruments each, together with the high resolution multi spectral MODIS instrument. One of the CERES instruments on each satellite will be operated in order to obtain a maximum number of quasi simultaneous multi angle views of particular scenes on earth. A strongly improved scene identification for the CERES pixels will be obtained thanks to the use of high resolution (the highest resolution channel will have 250 m resolution at nadir), multi spectral MODIS (MODerate resolution Imaging Spectroradiometer) data. New ADM sets will be derived based on the multi-angle views and the improved scene identification. This should lead to ADM errors which are a factor 2 to 4 times smaller than the errors of the current available, NIMBUS 7 derived, ADM sets [WBH+96].

This *derivation* of new ADM sets is not within the scope of future applications (in the future RMIB GGSPS branch) of the algorithms developed in this work. However, if good quality ADM sets become available from the CERES/MODIS synergy, they will be used in the future RMIB GGSPS branch.

11.2.2 Comparison with CERES and ScaRaB radiation budget term estimates

GERB/SEVIRI derived flux surface densities will be compared with LEO flux surface densities in the future RMIB GGSPS branch, using the algorithms developed in this work to compare flux surface densities derived from METEOSAT with LEO (ERBE or ScaRaB) flux surface densities. This will assure that not only *a priori* good ADM sets are used, but it will also provide an *a posteriori* measurement of the angular dependent errors made. Different ADM sets will be compared, as has been done in this work, and the one with the best performance in the removal of the angular dependency of the radiation will be selected.

The LEO data sets that are expected to be available for comparison with GERB/SEVIRI fluxes are:

- ScaRaB, with next launch foreseen on the Russian satellite RESURS by the end of 1997, and with possible other flights on future LEO satellites.
- CERES, with first launch on TRMM foreseen in November 1997. CERES on EOS-AM and EOS-PM is planned to be first launched in 1998 and 2000 respectively. The total EOS-AM and EOS-PM flight period is foreseen to cover 18 years, with a refreshment period of 6 years.

Chapter 12

Conclusions

In the presented work the TOA radiation budget terms at high space and time resolution have been estimated from geostationary and LEO satellite measurements.

It has been shown that, for a correct integration of the primitive atmospheric budget equations, the knowledge of the radiative source term of the energy equation is necessary. Spatial integration of this radiative source term reveals that the radiation budget at the top of the earth's atmosphere and at the earth's surface give the *border conditions* for this radiative source term. Hence satellite observation of the radiation budget terms at the top of the earth's atmosphere is potentially useful for atmospheric model monitoring and/or correction[1].

An ensemble of new techniques to estimate the TOA radiation budget terms from radiances measured by satellite instruments has been developed, as an essential extension and improvement of existing classical techniques.

The classical techniques, which have been used by the authors of the ERBE and ScaRaB data and which have also been applied to *subsampled* geostationary data, yielded TOA radiation budget term estimates at *individual measurement points* (footprints), with large possible variation of the error on the TOA radiation budget term estimates between two neighbouring measurement points. This approach maximises the number of *stochastically independent samples* of the earth radiation field, which is useful for *statistical climate studies.*

The new techniques, which have been developed and validated in this work, yield TOA radiation budget term estimate samples, which are *complete* in space, i.e. no gaps exist between two neighbouring samples (in space), at the METEOSAT resolution. The new techniques have been designed for optimal *spatial and temporal coherence*, i.e. for minimal variation of the error on the TOA radiation budget term estimates between neighbouring (in space or in time) measurement points. This approach yields a maximally correct sampling of the *spatial and temporal variation* of the earth radiation field, which is potentially useful for *physical atmospheric process studies.*

In order to obtain maximally spatially coherent TOA radiation budget estimates, a new short wave scene identification and radiance to flux surface density conversion scheme has been developed, which is characterised by a *continuous* radiance to flux surface density conversion curve (see figure 8.27), while the classical radiance to flux surface density conversion curve (see figure 6.1) is discontinuous. A continuous radiance to flux surface density conversion curve assures that for radiances which are varying continuously in space and time, the flux surface density estimates will also be varying continuously in space and time. *Image processing* has been used as a tool to obtain results which are varying, to a maximum extent, continuously in space and time.

The TOA radiation budget terms are related to the radiances measured by satellite instruments by scene dependent spectral and angular dependency functions. In order to select good spectral and angular dependency models, the scene type of a given sample should be recognised. Since the spectral and angular dependency functions are different for clear sky and for cloudy scenes, those two scenes have to be well separated by the scene type recognition.

For this purpose the new technique of instantaneous clear sky count determination has been developed. The instantaneous clear sky count determination is based on the combined image processing techniques of morphological filtering and non smoothing interpolation. Morphological

[1] Through the assimilation mechanism.

filtering is used for the recognition of cloudy scenes based on the temporal variation of pixel radiances. Non smoothing interpolation is used in order to obtain spatially coherent results.

Besides a good separation between clear sky and cloudy scenes, the integration of the instantaneous clear sky count determination in the scene identification allows the monitoring of changing surface states, e.g. due to seasonal evolution of non permanent desert areas.

The radiation budget term estimates which are directly derived from METEOSAT satellite measurements, are not complete in time, i.e. a time gap exists between the measurements of the radiation of a given location on earth (a given METEOSAT pixel) during the acquisition of two consecutive METEOSAT images. In order to estimate the radiation for a given location on earth *for any arbitrary moment in time* in an optimal way, a time interpolation based on motion interpolation has been developed.

Top down Bayesian image analysis has been developed as a novel image processing framework. This framework has the advantage, that for any kind of image processing task, results can be obtained which have high resolution *and* good spatial coherence. This combination of high resolution and spatial coherence is difficult to obtain with classical bottom-up image processing techniques. The top down Bayesian image analysis framework, has been applied for the development of a novel method of non smoothing interpolation (which has been used itself for the instantaneous clear sky count determination) and for the development of a novel motion estimation method (which has been applied for the METEOSAT time interpolation).

The validation of the final METEOSAT derived TOA radiation budget term estimates has been obtained by comparison with LEO instrument TOA radiation budget term estimates. This comparison has been done at the highest available spatial resolution for the LEO estimates, i.e. for individual LEO footprints. For an optimal spatial correspondence between the METEOSAT derived and the LEO TOA radiation budget term estimates, the METEOSAT derived estimates have been convolved by the LEO footprint PSF. To make this possible, the ERBE and ScaRaB PSF's have been calculated.

In the comparison of METEOSAT derived and LEO TOA radiation budget term estimates, the radiation budget term with the highest uncertainty appeared to be the short wave term. This corresponds well with the findings of other authors.

The measured METEOSAT-RB/LEO differences of the short wave term have been investigated as a superposition of systematic and of stochastic differences.

Systematic regional difference with a standard deviation of the order of 5 % were measured. This corresponds to a maximum (obtained for overhead sun) mean (over all scenes) difference of the order of 20 W/m^2. These differences can not be lowered by spatial integration.

Stochastic differences for individual footprints (with a resolution around 50 km) with an RMS value around 50 W/m^2 were obtained. It was demonstrated that by spatial integration over grid boxes with a size of approximately 225 km, this stochastic difference can be reduced to a value around 35 W/m^2.

For the long wave radiation budget term, METEOSAT-RB/LEO comparisons with systematic differences less than 5 % and stochastic differences of the order of 8 W/m^2 were obtained. This indicates that the long wave term differences are small compared to the short wave differences.

For usage in atmospheric models, radiation budget term data need to be derived and distributed in (near) real time. To minimise the required bandwidth for (near) real time distribution of the data, novel image compression algorithms, which are lossless *and* have a relatively high compression ratio, have been developed. A compression algorithm for classically sampled (sampled on a cartesian grid) and for spherically sampled data have been developed. A spherical sampling algorithm, which allows presentation of data on the earth's sphere with uniform resolution, has been developed. Both compression algorithms are based on the wavelet transform. The wavelet transform has the advantages of being a multi resolution data representation, and of being a combined space frequency presentation. The multi resolution data presentation is interesting in the context of atmospheric modelling, since it allows comparison/assimilation of one single data set in different atmospheric models, with their own individual resolution. The combined space frequency representation provided by the wavelet transform, is also interesting in the context of atmospheric modelling, since it could be used to avoid the time consuming swapping between the space representation and the frequency representation which is often used in atmospheric models.

The results we have obtained in this work, will be applied in the near future for the near real time processing/distribution of data from GERB/SEVIRI. From the presented results, we think that the improved calibration, spectral conditions, and resolution of future GERB/SEVIRI data compared to the current METEOSAT satellite data, will, in conjunction with our processing, lead to TOA radiation budget terms with improved accuracy compared to the results currently presented in this work.

List of acronyms

1D	One dimensional
A.U.	Astronomical Unit
ACRIM	Active Cavity Radiometer Irradiance Monitor
ADEOS	ADvanced Earth Observing Satellite
ADM	Angular Dependency Model
AM	Ante Meridian
ATLAS	Atmospheric Laboratory for Applications and Science
BPDF	Bidirectional Polarisation Distribution Function
BRDF	Bidirectional Reflection Distribution Function
CDS	Climate Data Set
CERES	Clouds and the Earth's Radiant Energy System
CMWE	Cloud Motion Wind Extraction
DIARAD	DIfferential Absolute RADiometer
EOS-AM	Earth Observing System - AM
EOS-PM	Earth Observing System - PM
ERBE	Earth Radiation Budget Experiment
ESOC	European Space Operation Control
EUMETSAT	EUropean organization for the exploitation of METeteorological SATellites
EURECA	EUropean REtrievable CArrier
FM	Flight Model
GCM	Global Circulation Model
GERB	Geostationary Earth Radiation Budget
GGSPS	GERB Ground Segment Processing System
GOES	Geostationary Operational Environmental Satellite
HRV	High Resolution Visible
IRW	InfraRed Window (ScaRaB terminology)
IR	InfraRed (METEOSAT terminology)
ISCCP	International Satellite Cloud Climatology Project
LEO	Low Earth Orbit
LMT	Local Mean Time
LOS	Line Of Sight
LW	Long Wave
METEOSAT	METEOrological SATellite
MIEC	Meteorological Information Extraction Chain
MLE	Maximum Likelihood Estimation
MODIS	MODerate resolution Imaging Spectroradiometer
MPEF	Meteorological Product Extraction Facility
MSG	METEOSAT Second Generation
NWP	Numerical Weather Prediction
PCC	Pattern Correlation Coefficient
PFM	Proto Flight Model

PM	Post Meridian
POLDER	POLarisation and Directionality of Earth Reflectances
PRFB	Perfect Reconstruction Filter Bank
PSF	Point Spread Function
RESURS	Acronym for Russian research satellite
RMIB	Royal Meteorological Institute of Belgium
RMS	Root Mean Square
RPM	Radiance Pair Method
SARR	Space Absolute Radiometric Reference
SC	Symmetry Check
SEVIRI	Spinning Enhanced Visible and InfraRed Imager
SMM	Solar Maximum Mission
SOHO	SOlar and Heliospheric Observatory
SOLCON	SOLar CONstant
SOLSPEC	SOLar SPECtrum
SOVA	SOlar VAriability
SW	Short Wave
ScaRaB	Scanning radiometer for Radiation Budget measurements
TC	Total Channel
TOA	Top Of Atmosphere
TOTAL	Total wave
TRMM	Tropical Rainfall Measurement Mission
TST	True Solar Time
UARS	Upper Atmospheric Research Satellite
UTC	Universal Time Code
UT	Universal Time
VE	Vernal Equinox
VIRGO	Variability of solar IRradiance and Gravity Oscillations
VIS	VISible
WC	Window Channel (CERES terminology)
WV	Water Vapour

List of symbols

$\cdot$	Scalar product of two vectors.
$\times$	Vector product of two vectors.
$*$	Multiplication of two scalars.
$\circledast$	Convolution of two functions.
$\ominus$	Morphological filtering of the minimum type. See equation 7.8.
$\oplus$	Morphological filtering of the maximum type. See equation 7.9.
$\vec{1'}_A$	Unit vector in the earth scaled space (see section 8.1.3) in the direction of vector $\vec{A}$.
$\vec{1}_A$	Unit vector in the physical space in the direction of vector $\vec{A}$.
$\vec{1}_{perp}$	Local geometrical vertical in point P of the earth ellipsoid = unit vector perpendicular to the earth ellipsoid in P.
$\vec{1}_{sun}$	Unit vector pointing from the earth to the sun.
$\vec{A}$	Vector from the origin O to point A.
$\vec{AB}$	Vector from point A to point B.
A	Linear transformation matrix. See e.g. equation 7.76.
B	Inverse linear transformation matrix. See e.g. equation 7.80.
$\vec{C}[F_e]$	Vector with as i'th component (i = 1,2,3) the amount of F_e flowing per unit time and per unit surface through a surface with normal along the i'th axis (first axis = x axis, second axis = y axis, third axis = z axis).
$C(g)$	Cumulative histogram. See equation 7.5.
$C(i,j)$	Class of pixel (i,j) of a grey value image. See equation 7.27.
$CM_{IR}^{mono}(pixel, slot, day, month)$	Mono spectral METEOSAT IR cloud mask. See equation 8.41.
$CM_{VIS}(pixel, slot, day, month)$	Multi spectral METEOSAT VIS cloud mask. See equation 8.42.
$CM_{VIS}^{mono}(pixel, slot, day, month)$	Mono spectral METEOSAT VIS cloud mask. See equation 8.37.
$C_{24}(i,j)$	Grey value count for pixel (i,j) of METEOSAT image at slot 24.
$C_{24}^{li}(i,j)$	Approximation for $C_{24}(i,j)$ by linear interpolation between slot 23 and 25.
$C_{24}^{mi}(i,j)$	Approximation for $C_{24}(i,j)$ by motion interpolation between slot 23 and 25. See equation 9.3.
$C_{IR,0}$	METEOSAT IR offset count. See equation 8.49.
C_{IR}	METEOSAT IR count.
$C_{IR}(pixel, slot, day)$	METEOSAT IR count for a given *pixel*, for a given *slot* of the day, and for a given *day*.
$C_{IR}^{cs,fit}(t)$	Fitted function that describes the variation of the monthly METEOSAT IR clear sky counts for given slots of the day in function of the slot of the day. See equation 8.27.
$C_{IR}^{cs,hs}$	Fitted half sine amplitude of the monthly METEOSAT IR clear sky count. See equation 8.27 and figure 8.18.

$C_{IR}^{cs,sr}$	Fitted sunrise value of the monthly METEOSAT IR clear sky count. See equation 8.27 and figure 8.18.
$C_{IR}^{cs,ss}$	Fitted sunset value of the monthly METEOSAT IR clear sky count. See equation 8.27 and figure 8.18.
$C_{IR}^{cs}(pixel, slot, month)$	Monthly METEOSAT IR clear sky value for a given $pixel$, for a given $slot$ of the day, and for a given $month$. See equation 8.21.
$C_{IR}^{eq,cd}(pixel, slot, day, month)$	Mono spectral equalised METEOSAT IR cloud difference count. See equation 8.40.
$C_{IR}^{eq}(pixel, slot, day, month)$	Equalised METEOSAT IR count. See equation 8.38.
$C_{I^{eq}}(g')$	Cumulative histogram of the equalised image I^{eq}.
$C_{VIS,0}$	METEOSAT VIS offset count. See equation 8.58.
C_{VIS}	METEOSAT VIS count.
$C_{VIS}^{cs,diff-ip}(pixel, slot, day, month)$	Interpolated value of $C_{VIS}^{cs,diff}(pixel, slot, day, month)$, defined for all pixels. See equation 8.44.
$C_{VIS}^{cs,diff}(pixel, slot, day, month)$	Instantaneous difference between METEOSAT VIS clear sky count and monthly METEOSAT VIS clear sky count. Only defined for instantaneous clear sky pixels. See equation 8.43.
$C_{VIS}^{cs}(pixel, slot, day, month)$	Instantaneous METEOSAT VIS clear sky count. See equation 8.45.
$C_{VIS}^{cs}(pixel, slot, month)$	Monthly METEOSAT VIS clear sky value for a given $pixel$, for a given $slot$ of the day, and for a given $month$. See equation 8.24.
$C_{VIS}^{eq,cd}(pixel, slot, day, month)$	Mono spectral equalised METEOSAT VIS cloud difference count. See equation 8.36.
$C_{VIS}^{eq,cs}(pixel, slot, day, month)$	Mono spectral equalised METEOSAT VIS clear sky count. See equation 8.35.
$C_{VIS}^{eq}(pixel, slot, day, month)$	Equalised METEOSAT VIS count. See equation 8.34.
$C_{WV,0}$	METEOSAT WV offset count. See equation 8.50.
C_{WV}	METEOSAT WV count.
$D_S(o_1, o_2)$	Euclidean distance between image i_1 and image i_2 for displacement (o_1, o_2) in (row,column) direction of segment S at time t. See equation 7.51.
E	Internal energy in volume V.
F	Radiative energy flux surface density = amount of radiative energy flowing out of a surface per unit time and per unit surface.
$F(o_1, o_2)$	Regularised Euclidean distance between image i_1 and image i_2 for displacement (o_1, o_2) in (row,column) direction of segment S at time t. See equation 7.54.

$F^{SOL}_{METx,VIS}$	Incoming solar flux surface density, filtered with the METEOSAT x (2 and 5 are considered) VIS channel spectral sensitivity $\Phi_{METx,VIS}$.
F^{cs}_{SW}	Model reflected solar flux surface density F_{SW} for a clear sky scene. See equation 8.73.
$F^{scene-lower}_{SW}$	Reflected short wave flux surface density for scene with METEOSAT VIS radiance $L^{scene-lower}_{VIS}$. See equation 8.83 and figure 8.27.
$F^{scene-upper}_{SW}$	Reflected short wave flux surface density for scene with METEOSAT VIS radiance $L^{scene-upper}_{VIS}$. See equation 8.83 and figure 8.27.
$F^{scene}_{METx,VIS}$	Model reflected short wave flux surface density for a given scene type, filtered with the METEOSAT x (2 and 5 are considered) VIS channel spectral sensitivity $\Phi_{METx,VIS}$.
$F^{scene}_{SW,\lambda}$	Spectral distribution of the model reflected short wave flux surface density for a given scene type.
$F^{scene}_{SW}(\theta_{sun})$	Model reflected short wave flux surface density for a given scene type.
F_e	Extensive quantity defined over volume V.
$F_{ERBS(METEOSAT-2-RB),28}$	$F_{ERBS(METEOSAT-2-RB)}$ with time t_{28}.
$F_{ERBS(METEOSAT-2-RB)}$	$F_{LEO(METEOSAT-RB)}$ with LEO = ERBS
F_{IR}	METEOSAT IR narrow band flux surface density = filtered flux surface density, $F_{channel}$, for the METEOSAT IR channel.
$F_{LEO(METEOSAT-RB)}$	Flux surface density (reflected short wave flux surface density, F_{SW}, or emitted long wave surface density, F_{LW}) over Low Earth Orbit (LEO) footprint, estimated by convolution of METEOSAT-RB flux surface density with LEO footprint PSF.
$F_{LW,ERBE}$	ERBE estimate of emitted long wave flux surface density, F_{LW}.
$F_{LW,ScaRaB}$	ScaRaB estimate of the emitted long wave flux surface density, F_{LW}.
F_{LW}	Emitted long wave flux surface density at a point at the top of the atmosphere = amount of emitted thermal energy flowing per unit time and per unit surface trough a surface with normal along the local vertical (i.e. flowing upward) due to thermal emission of the underlying atmosphere-earth system.
$F_{SOL,\lambda}$	Spectral distribution of the incoming solar flux surface density.
F_{SOL}	Total (spectrally integrated) solar flux surface density at a point at the top of the atmosphere = amount of radiative solar energy flowing per unit time and per unit surface trough a surface with normal opposite to the local vertical (i.e. flowing downward), if the underlying atmosphere-earth system is non reflective.
$F_{SW,ERBE}$	ERBE estimate of the reflected short wave flux surface density, F_{SW}.
$F_{SW,IN}$	Net short wave flux surface density entering the top of the atmosphere = amount of radiative solar energy flowing per unit time and per unit surface trough a surface with normal opposite to the local vertical (i.e. flowing downward).

$F_{SW,ScaRaB}$	ScaRaB estimate of the reflected short wave flux surface density, F_{SW}.
F_{SW}	Reflected short wave flux surface density at a point at the top of the atmosphere = amount of radiative solar energy flowing per unit time and per unit surface trough a surface with normal along the local vertical (i.e. flowing upward) due to atmospheric-earth reflection.
F_{WV}	METEOSAT WV narrow band flux surface density = filtered flux surface density, $F_{channel}$, for the METEOSAT WV channel.
$F_{\ldots,(1-f)*28+f*29}$	Linear time interpolated value of $F_{\ldots}$ at time $t=(1-f)*t_{28}+f*t_{29}$. Linear time interpolation is done between $F_{\ldots,28}$ and $F_{\ldots,29}$.
$F_{channel}$	Filtered flux surface density = integral of the upward component of the filtered radiance, $L_{sat,channel}(\theta,\phi)$, over all directions (θ,ϕ) of the upper hemisphere.
$G^c_{s_{ri}}$	Centred grid for ri'th iteration of topdown Bayesian image analysis, with grid height $N_{g,ri}$ and grid width $M_{g,ri}$. See equation 7.17 and right part of figure 7.8.
$G_s(i_g,j_g,N_g,M_g)$	Grid with segment size s, top left corner (i_g,j_g), height N_g and width M_g. See equation 7.14 and middle part of figure 7.8.
G^c_s	Centred grid with segment size s. See equation 7.15 and right part of figure 7.8.
H	Observation matrix for weighted least squares fit. See equations 8.29 and 8.30.
$H(g)$	Histogram count for the grey value g = number of times the grey level occurs in a given image or time series of images.
$H(s)$	Global transfer function = Laplace transform of the global impulse response $h(t)$.
H_{mean}	Weighted mean entropy of the wavelet transform of an image. See equation 7.88.
$H_{subimage}$	Entropy of a subimage of the wavelet transform of an image. See equation 7.89.
$\vec{I}$	Vector (multiband) image with height n, width m and p bands, which is the input of a top down Bayesian image analysis. See left part of figure 7.7.
$\vec{I}(i,j)$	Vector pixel of vector image $\vec{I}$ with row coordinate i and column coordinate j.
I	Grey level image with height n and width m.
$I(i,j)$	Pixel value of image I with row coordinate i and column coordinate j.
I^{eq}	New image obtained after mapping of the grey values of a given image with the equalising grey value mapping function. See equation 7.3.

I_1	Unity matrix in equation 7.82.
I_t	Time series of K grey level images with height n and width m.
I_t^{eq}	New image time series obtained after mapping of the grey values of a given image time series with the equalising grey value mapping function. See equation 7.3
$K(t)$	Morphological kernel.
$L(\theta, \phi)$	Radiance flowing out of a surface in the direction (θ, ϕ) = amount of radiative energy flowing out of the surface in the direction (θ, ϕ) per unit time and per unit apparent surface. The apparent surface is defined as the surface measured in the plane perpendicular to the direction (θ, ϕ).
$L_{VIS}^{cs,desert}$	Model clear sky desert VIS (narrow band) radiance for an individual METEOSAT pixel. See equation 8.69.
$L_{VIS}^{cs,nd}$	Model clear sky non desert VIS (narrow band) radiance for an individual METEOSAT pixel. See equation 8.68.
L_{VIS}^{cs}	Clear sky VIS (narrow band) radiance for an individual METEOSAT pixel. See equation 8.70.
L_{VIS}^{mc}	Model mostly cloudy VIS (narrow band) radiance for an individual METEOSAT pixel. See equation 8.81.
L_{VIS}^{ov}	Model overcast cloudy VIS (narrow band) radiance for an individual METEOSAT pixel. See equation 8.74.
L_{VIS}^{pc}	Model partly cloudy VIS (narrow band) radiance for an individual METEOSAT pixel. See equation 8.81.
$L_{VIS}^{scene-lower}$	METEOSAT VIS radiance for scene with radiance just lower than given METEOSAT VIS radiance L_{VIS}. See equation 8.82 and figure 8.27.
$L_{SW,VIS}^{scene-upper}$	METEOSAT VIS radiance for scene with radiance just higher than given METEOSAT VIS radiance L_{VIS}. See equation 8.82 and figure 8.27.
$L_{SW,METx}^{white}$	White broad band short wave radiance = broad band short wave radiance obtained from METEOSAT x (2 and 5 are considered) VIS narrow band radiance under assumption of white reflection. See equation 8.61.
L_{IR}	METEOSAT IR narrow band radiance = filtered satellite radiance, $L_{sat,channel}$, for METEOSAT IR channel.
$L_{LW}(\theta, \phi)$	Emitted long wave radiance at a point P at the top of the atmosphere = amount of radiative energy flowing per unit time, per unit surface and per unit solid angle trough a surface centred in P, flowing in the direction with zenith angle θ and azimuth angle ϕ, due to emission of the underlying earth-atmosphere system.

$L_{SW}(\theta,\phi)$	Reflected short wave radiance at a point P at the top of the atmosphere = amount of radiative solar energy flowing per unit time, per unit apparent surface and per unit solid angle trough a surface centred in P, flowing in the direction with zenith angle θ and azimuth angle ϕ, due to reflection by the underlying earth-atmosphere system.
$L_{SW}^{scene}(\theta_{sat},\phi_{sat},\theta_{sun})$	Model reflected short wave radiance, $L_{SW}(\theta=\theta_{sat},\phi=\phi_{sat})$, for a given scene type and for a given solar zenith angle, θ_{sun}.
L_{VIS}	METEOSAT VIS narrow band radiance = filtered satellite radiance, $L_{sat,channel}$, for METEOSAT VIS channel.
L_{WV}	METEOSAT WV narrow band radiance = filtered satellite radiance, $L_{sat,channel}$, for METEOSAT WV channel.
$L_{\lambda}^{earth}(\theta,\phi)$	Spectral radiance from earth origin emitted at the top of the earth's atmosphere = amount of radiative energy flowing per unit time, per unit surface, per unit solid angle and per unit wavelength interval trough a given surface, flowing in the direction with zenith angle θ and azimuth angle ϕ, due to emission of the underlying earth-atmosphere system, for an infinitesimal wavelength interval centred at a given wavelength λ.
$L_{\lambda}^{solar}(\theta,\phi)$	Spectral radiance from solar origin reflected at the top of the earth's atmosphere = amount of radiative solar energy flowing per unit time, per unit apparent surface, per unit solid angle and per unit wavelength interval trough a given surface, flowing in the direction with zenith angle θ and azimuth angle ϕ, due to reflection of solar radiation by the underlying earth-atmosphere system, for an infinitesimal wavelength interval centred at a given wavelength λ.
$L_{sat,channel}$	Filtered satellite radiance = radiance observed by a given satellite channel with spectral response $\Phi_{channel}(\lambda)$ from a given point P at the top of atmosphere.
L_{sat}^{type}	Unfiltered radiance = spectrally integrated radiance of a given type (solar or earth type) flowing in a given satellite direction.
M	Mass within volume V.
$M(i,j)$	Mask value for pixel (i,j), which indicates whether the pixel value is known (mask value=1) or unknown (mask value=0). See equation 7.28.
$N(m,\sigma^2)$	Gaussian distribution with mean n and standard deviation σ.
$\vec{O}$	Vector (multiband) image with height n, width m and q bands, which is the output of a top down Bayesian image analysis. See right part of figure 7.7.
$\vec{O}(i,j)$	Vector pixel of vector image $\vec{O}$.
$\vec{O}_{ri}(i,j)$	Intermediate output image with height $N_{g,ri}$, width $M_{g,ri}$ and q bands for ri'th iteration of top down Bayesian image analysis. See equation 7.19 and figure 7.9.

O	Origin of the XYZ coordinate system = centre of the earth.
$OF'_{channel}(\alpha,\beta)$	Optical angular sensitivity function, $OF_{channel}(\delta_a,\delta_c)$, of a ScaRaB channel expressed as a function of the detector angles α,β.
$OF'_{ideal}(\alpha,\beta)$	Idealised ScaRaB broad band angular sensitivity function. See equation 4.25.
$OF_{channel}(\delta_a,\delta_c)$	Optical angular sensitivity function = Static PSF of a radiometer channel = angular sensitivity function by which the contribution of the radiance viewed in the direction (δ_a,δ_c) is weighted in the measurement of the radiometer channel, if the radiometer is not scanning.
$\vec{P}$	Vector from origin to arbitrary point P in the earth's atmosphere. In the particular case of figure 8.6, P is the intersection of the METEOSAT pixel Line Of Sight (LOS) and the earth ellipsoid.
$P(a\|\|b)$	Probability of realisation of the event "a", given "b".
$P(a)$	Probability of realisation of the event "a"
$PSF_{channel}(\delta_a,\delta_c)$	Total Point Spread Function (PSF) of a radiometer channel = angular sensitivity function by which the contribution of the radiance viewed in the direction (δ_a,δ_c) is weighted in the measurement of the radiometer channel.
$PSF_{ideal}(\delta_a,\delta_c)$	Idealised ScaRaB broad band Point Spread Function (PSF). See equation 4.28.
P_i	Amount of momentum in the i direction in the xyz coordinate system, contained within the volume V.
P_n	Gaussian noise distribution = Gaussian distribution with mean 0 and standard deviation σ_n.
R	R coordinate of the spherical coordinates, (R,Θ,Φ), in the XYZ reference system. See equation 8.1.
R'	R' of the spherical coordinates, (R',Θ',Φ'), in the earth scaled space, related to (X',Y',Z') as (R,Θ,Φ) to (X,Y,Z).
RB	Local instantaneous radiation budget at a point at the top of the atmosphere. See equation 2.16.
RI	Number of iterations of top down Bayesian image analysis minus one.
$R^{cs,desert}(\theta_{sat},\phi_{rel},\theta_{sun})$	Model clear sky desert bidirectional reflection function for given viewing angles $(\theta_{sat},\phi_{rel},\theta_{sun})$.
$R^{cs,land}(\theta_{sat},\phi_{rel},\theta_{sun})$	Model clear sky land bidirectional reflection function for given viewing angles $(\theta_{sat},\phi_{rel},\theta_{sun})$.
$R^{cs,ocean}(\theta_{sat},\phi_{rel},\theta_{sun})$	Model clear sky ocean bidirectional reflection function for given viewing angles $(\theta_{sat},\phi_{rel},\theta_{sun})$.
$R^{mc,land-desert}(\theta_{sat},\phi_{rel},\theta_{sun})$	Model mostly cloudy land or desert bidirectional reflection function for given viewing angles $(\theta_{sat},\phi_{rel},\theta_{sun})$.

$R^{mc,ocean}(\theta_{sat},\phi_{rel},\theta_{sun})$	Model mostly cloudy ocean bidirectional reflection function for given viewing angles $(\theta_{sat},\phi_{rel},\theta_{sun})$.
$R^{mc}(\theta_{sat},\phi_{rel},\theta_{sun})$	Mostly cloudy bidirectional reflection function for an individual METEOSAT pixel for given viewing angles $(\theta_{sat},\phi_{rel},\theta_{sun})$. See equation 8.78.
$R^{ov}(\theta_{sat},\phi_{rel},\theta_{sun})$	Model overcast cloudy bidirectional reflection function for given viewing angles $(\theta_{sat},\phi_{rel},\theta_{sun})$.
$R^{pc,land-desert}(\theta_{sat},\phi_{rel},\theta_{sun})$	Model partly cloudy land or desert bidirectional reflection function for given viewing angles $(\theta_{sat},\phi_{rel},\theta_{sun})$.
$R^{pc,ocean}(\theta_{sat},\phi_{rel},\theta_{sun})$	Model partly cloudy ocean bidirectional reflection function for given viewing angles $(\theta_{sat},\phi_{rel},\theta_{sun})$.
$R^{pc}(\theta_{sat},\phi_{rel},\theta_{sun})$	Model partly cloudy bidirectional reflection function for an individual METEOSAT pixel for given viewing angles $(\theta_{sat},\phi_{rel},\theta_{sun})$. See equation 8.77.
R_E	Equatorial earth radius.
R_P	Polar earth radius.
$R_{geostat}$	Geostationary radius = radius R of a geostationary satellite.
$R^{scene}(\theta_{sat},\phi_{rel},\theta_{sun})$	Bidirectional reflection function = ratio of the "Lambertian estimate" over the true value of the reflected short wave flux surface density." See equation 5.6.
$\hat{\overline{S}}$	Statistical estimator of $\overline{S}$.
$\overline{S_i}$	Mean "solar constant" measured by instrument i during the ATLAS 2 space shuttle flight period.
$\overline{S}$	Mean value of the "solar constant" during the ATLAS 2 space shuttle flight period.
$\vec{S}$	METEOSAT satellite position vector = vector of origin O (earth centre) to METEOSAT position.
$S(t)$	"Solar constant" time series.
$S^{SARR}(t)$	Space Absolute Radiometric Reference (SARR) referenced measurements of the "solar constant" obtained as a mean of all available daily mean SARR referenced instrument measurements.
$S^{SARR}_{acrimii}(t)$	Space Absolute Radiometric Reference (SARR) referenced measurements of the "solar constant", obtained from the ACRIM II instrument.
$S^{SARR}_i(t)$	Space Absolute Radiometric Reference (SARR) referenced measurements of the "solar constant", obtained from instrument i.
$S^{SOL}_{METx,VIS}$	METEOSAT instrument solar constant = solar constant spectral components convolved with METEOSAT x VIS spectral sensitivity, $\Phi_{METx,VIS}$.
S_n	Mean grid cell size of recursive pseudo-icosahedral division of the sphere, if the number of recursive divisions is n.
$S_{SOL,\lambda}$	Spectral solar irradiance = amount of solar radiative energy flowing per unit time, per unit surface and per unit wavelength interval for an infinitesimal wavelength interval centred at a given wavelength λ through a surface perpendicular to the earth-sun direction at the mean distance earth-sun (= 1 astronomical unit).

S_{SOL}	Total solar irradiance = amount of solar radiative energy flowing per unit time and per unit surface through a surface perpendicular to the earth-sun direction at the mean distance earth-sun (= 1 astronomical unit).
S_λ^{SG}	Spectral solar irradiance $S_{SOL,\lambda}$ from [SG74] for the wavelength range 876 to 20025 nm.
$S_\lambda^{SOLSPEC}$	Spectral solar irradiance $S_{SOL,\lambda}$ measured by the SOLSPEC instrument during the ATLAS 1 space shuttle flight, in the wavelength range 199 to 876 nm.
$S_\lambda^{composite}$	Spectral solar irradiance, $S_{SOL,\lambda}$, composed of $S_\lambda^{SOLSPEC}$ and S_λ^{SG}. See equation 4.11.
S_c	Known pixel values of class c of segment S.
$S_i(t)$	"Solar constant" time series measured by instrument i.
$S_{s_{ri}}(i_c(i), j_c(j))$	Segment with segment row coordinate i and segment column coordinate j in centred grid $G^c_{s_{ri}}$ for ri'th iteration of top down Bayesian image analysis. See equation 7.20.
$S_s(i_c, j_c)$	Segment with linear size s and top left corner (i_c,j_c). See equation 7.13 and left part of figure 7.8.
$\vec{T_i}$	(T_i^1, T_i^2, T_i^3)
$\vec{T}$	Vector which is tangent in the point P to the earth ellipsoid, which lies in the plane formed by P and the Z axis, and which points towards the Z axis. See figure 8.7.
T_i^j	The internal force in the xyz coordinate system (pressure force plus viscosity force) in the i-direction per unit surface with normal in the j-direction.
$T^{eq}(g)$	Equalising grey value mapping function = function that maps the grey values of an image or time series of images to new grey values with an histogram that is close to uniform.
V	General volume in the atmosphere of the earth which does not change in time in the XYZ coordinate system.
$V_{-sl}(t)$	Downward V shaped morphological kernel with slope parameter sl. See equation 7.11.
V_{atm}	Volume which covers the entire atmosphere of the earth.
$V_{sl}(t)$	Upward V shaped morphological kernel with slope parameter sl. See equation 7.10.
W	Weight matrix for weighted least squares fit. See equations 8.29 and 8.31.
$\vec{X} = (X_1, X_2, X_3)$	Vector of the external force in the xyz coordinate system (apparent gravity force plus Coriolis force) per unit mass.

X X coordinate of the XYZ coordinate system rotating together with the earth, with origin in the earth's centre.
The Z axis lies on the rotation axis and points to the north pole.
The X axis lies in the Greenwich meridian half plane.
The Y axis completes the right hand set.

X' First cartesian coordinate in the Earth scaled space.
See equation 8.3.

X'_t Cartesian coordinate X' of $\vec{T}$ in the earth scaled space.

X_t Cartesian coordinate X of $\vec{T}$ in the physical space.

X_{eq} First equatorial cartesian coordinate of $\vec{1}_{sun}$.
See figure 8.10.

X_{ls} Parameter vector for weighted least squares fit.
See equations 8.29 and 8.32.

X_{tr} Input vector of a forward linear transformation.
See e.g. equation 7.76.

Y Y coordinate of the XYZ coordinate system rotating together with the earth, with origin in the earth's centre.
The Z axis lies on the rotation axis and points to the north pole.
The X axis lies in the Greenwich meridian half plane.
The Y axis completes the right hand set.

Y' Second cartesian coordinate in the Earth scaled space.
See equation 8.3.

Y'_t Cartesian coordinate Y' of $\vec{T}$ in the earth scaled space.

Y_t Cartesian coordinate Y of $\vec{T}$ in the physical space.

Y_{eq} Second equatorial cartesian coordinate of $\vec{1}_{sun}$.
See figure 8.10.

Y_{ls} Vector of observations for weighted least squares fit.
See equations 8.29 and 8.33.

Y_{tr} Output vector of a forward linear transformation.
See e.g. equation 7.76.

Z Z coordinate of the XYZ coordinate system rotating together with the earth, with origin in the earth's centre
The Z axis lies on the rotation axis and points to the north pole.
The X axis lies in the Greenwich meridian half plane.
The Y axis completes the right hand set.

Z' Third cartesian coordinate in the Earth scaled space.
See equation 8.3.

Z'_t Cartesian coordinate Z' of $\vec{T}$ in the earth scaled space.

Z^2 Set of couples of integer numbers.

Z_t Cartesian coordinate Z of $\vec{T}$ in the physical space.

Z_{eq} Third equatorial cartesian coordinate of $\vec{1}_{sun}$.
See figure 8.10.

Δ	Mechanical energy dissipated by the viscosity forces per unit mass.
Δt^{corr}	Equation of time = difference between the True Solar Time (TST) and the Local Mean Time (LMT).
Δ_i	Absolute error of instrument i which measures the "solar constant" time series.
Γ	Day angle = angle of rotation of the earth around the sun. Γ is zero for the first day of the year. See equation 8.12.
$\vec{\Omega}$	Earth rotation vector, pointing in the positive Z direction.
Φ	Φ coordinate of the spherical coordinates, (R, Θ, Φ), in the XYZ reference system.
Φ'	Φ' coordinate of the spherical coordinates, (R', Θ', Φ'), in the earth scaled space, related to (X', Y', Z') as (R, Θ, Φ) to (X, Y, Z).
$\Phi_{IRW}(\lambda)$	Spectral response function of the infrared window channel of the ScaRaB radiometer. Spectral range $\approx$ 10.5 to 12.5 μm.
$\Phi_{IR}(\lambda)$	Spectral response function of the infrared channel of the METEOSAT radiometer. Spectral range $\approx$ 10.5 to 12.5 μm.
$\Phi_{LW}(\lambda)$	Spectral response function of the long wave channel of an ERBE like broad band scanning radiometer. Long wave spectral range $\approx$ 4 to 60 μm.
$\Phi_{METx,VIS}$	Spectral response function of the visible channel of a specific METEOSAT radiometer.
$\Phi_{SW}(\lambda)$	Spectral response function of the short wave channel of an ERBE or ScaRaB like broad band scanning radiometer. Short wave spectral range $\approx$ 0.2 to 4 μm.
$\Phi_{TOTAL}(\lambda)$	Spectral response function of the total wave channel of an ERBE or ScaRaB like broad band scanning radiometer. Total wave spectral range $\approx$ 0.2 to 60 μm.
$\Phi_{VIS}(\lambda)$	Spectral response function of the visible channel of the ScaRaB or METEOSAT radiometer. Spectral range ScaRaB $\approx$ 0.55 to 0.65 μm. Spectral range METEOSAT $\approx$ 0.4 to 1.1 μm.
$\Phi_{WV}(\lambda)$	Spectral response function of the water vapour channel of the METEOSAT radiometer. Spectral range $\approx$ 5.7 to 7.1 μm.
$\Phi_{channel}(\lambda)$	Spectral response function of a given channel of a given satellite instrument.
Φ_j	Second angular spherical coordinate of the viewing direction for a given METEOSAT pixel (i, j). See figure 8.5 and equation 8.5.
$\Phi_{sun}(t)$	Spherical coordinate Φ of the sun in the XYZ coordinate system at a given time t.
Σ	Surface limiting the volume V.
Θ	Θ coordinate of spherical coordinates, (R, Θ, Φ), in the XYZ reference system. See equation 8.1.

Θ'	Θ' coordinate of the spherical coordinates, (R', Θ', Φ'), in the earth scaled space, related to (X', Y', Z') as (R, Θ, Φ) to (X, Y, Z).
Θ_i	First angular spherical coordinates of the viewing direction for a given METEOSAT pixel (i, j). See figure 8.4 and equation 8.4.
$\Theta_{sun}(t)$	Spherical coordinate Θ of the sun in the XYZ coordinate system at a given time t.
α	First of the two detector angles, (α, β), defined in the edge directions of the ScaRaB angular sensitivity function.
β	Second of the two detector angles, (α, β), defined in the edge directions of the ScaRaB angular sensitivity function.
δ	The angle between $\vec{1}_{sun}$ and the positive equatorial X_{eq} axis. See figure 8.8.
δV	Elementary volume.
δ_{ap}	The angle between $\vec{1}_{sun}$ at a given time t and $\vec{1}_{sun}$ at the apohelium.
δ_a	Along scan angle of a scanning radiometer = angle with which the radiometer views a given scene, measured in the direction of the scanning of the radiometer.
δ_c	Cross scan angle of a scanning radiometer = angle with which the radiometer views a given scene, measured perpendicular to the direction of the scanning of the radiometer.
$\delta_l(\delta_c)$	Left border of a given function of (δ_a, δ_c) = Along scan angle, δ_a, in function of the cross scan angle, δ_c, for the left border of the function.
$\delta_r(\delta_c)$	Right border of a given function of (δ_a, δ_c) = Along scan angle, δ_a, in function of the cross scan angle, δ_c, for the right border of the function.
γ	Angle between the METEOSAT pixel LOS and the METEOSAT satellite nadir direction. See figure 8.6.
λ	Regularisation parameter in top down Bayesian image analysis. See equations 7.40, 7.54 and 7.55.
ϕ	Azimuth angle of a direction in the local xyz reference system = angle between the xz-plane and the plane formed by the given direction and the z axis.
ϕ_{MET}	Azimuth angle, ϕ, under which METEOSAT views a given scene on earth.
ϕ_{step}	METEOSAT step angle = angle which defines the latitude position of the METEOSAT (longitudinal) scanner.
ϕ_{rel}	Relative azimuth angle = absolute difference between the satellite azimuth angle, ϕ_{sat}, and the sun azimuth angle, ϕ_{sun} = angle between the plane formed by the local vertical and the sun and the plane formed by the local vertical and the satellite.

ϕ_{sat}	Satellite azimuth angle = azimuth angle, ϕ, of the radiance which reaches a given satellite from a given point on earth.
ϕ_{sun}	Solar azimuth angle = azimuth angle, ϕ, of the direction of the sun seen from a given point in the earth's atmosphere.
ρ	Mass density = amount of mass per unit volume.
$\rho_{\mathrm{h_2o}}$	Total water mass density = mass of water per unit volume.
$\sigma_{c,k}$	Observed standard deviation for the k known values of S_c. See equation 7.41.
$\sigma_{c,p}$	Standard deviation of the prior probability distribution 7.37 for mean grey value estimation.
σ_p	Standard deviation of the prior probability distribution 7.52 for displacement estimation.
$\sigma[F_e]$	Amount of F_e produced per unit time and per unit volume.
$\widehat{\sigma_\Delta}$	Statistical estimator of σ_Δ.
σ_Δ	Standard deviation of the absolute error of a stochastic instrument that is built and operated to measure the "solar constant" time series.
θ	Zenith angle of a direction in the local spherical coordinate system = angle between the given direction and the z axis.
θ_{MET}	Zenith angle, θ, under which METEOSAT views a given scene on earth.
θ_{sat}	Satellite viewing zenith angle = zenith angle, θ, of the radiance which reaches a given satellite from a given point on earth.
θ_{sun}	Solar zenith angle = angle between the direction of the sun and the local vertical in a given point of the earth's atmosphere.
a	Albedo = ratio of the reflected short wave flux surface density, F_{SW}, to the incoming solar flux surface density, F_{SOL}.
$a^{SARR}_{\mathrm{acrimi,new}}$	Updated Space Absolute Radiometric Reference (SARR) adjustment coefficient of the ACRIM I instrument.
$a^{SARR}_{\mathrm{diarad}}$	Space Absolute Radiometric Reference (SARR) adjustment for the DIARAD instrument.
$a^{SARR}_{\mathrm{nimbus7,new}}$	Updated Space Absolute Radiometric Reference (SARR) adjustment coefficient of the NIMBUS 7 instrument, applicable to measurements made before 1989.
$a^{SARR}_{\mathrm{nimbus7,old}}$	Space Absolute Radiometric Reference (SARR) adjustment coefficient of the NIMBUS 7 instrument derived in [CFLR95].
a^{SARR}_i	Space Absolute Radiometric Reference (SARR) adjustment coefficient for instrument i = factor by which the measurements of instrument i have to be multiplied to obtain SARR referenced measurements.
$a^{cs,desert}(\theta_{sun})$	Model clear sky desert albedo for a given solar zenith angle, θ_{sun}.
$a^{cs,land}(\theta_{sun})$	Model clear sky land albedo for a given solar zenith angle, θ_{sun}.
$a^{cs,ocean}(\theta_{sun})$	Model clear sky ocean albedo for a given solar zenith angle, θ_{sun}.
$a^{cs}(\theta_{sun})$	Model clear sky albedo for an individual METEOSAT pixel for a given solar zenith angle, θ_{sun}. See equation 8.72.

$a^{mc,land-desert}(\theta_{sun})$	Model mostly cloudy land or desert albedo for a given solar zenith angle, θ_{sun}.
$a^{mc,nd}(\theta_{sun})$	Model mostly cloudy non desert albedo for a given solar zenith angle, θ_{sun}. See equation 8.76.
$a^{mc,ocean}(\theta_{sun})$	Model mostly cloudy ocean albedo for a given solar zenith angle, θ_{sun}.
$a^{mc}(\theta_{sun})$	Model mostly cloudy albedo for an individual METEOSAT pixel for a given solar zenith angle, θ_{sun}. See equation 8.79.
$a^{ov}(\theta_{sun})$	Model overcast cloudy albedo for a given solar zenith angle, θ_{sun}.
$a^{pc,land-desert}(\theta_{sun})$	Model partly cloudy land or desert albedo for a given solar zenith angle, θ_{sun}.
$a^{pc,nd}(\theta_{sun})$	Model partly cloudy non desert albedo for a given solar zenith angle, θ_{sun}. See equation 8.75.
$a^{pc,ocean}(\theta_{sun})$	Model partly cloudy ocean albedo for a given solar zenith angle, θ_{sun}.
$a^{pc}(\theta_{sun})$	Model partly cloudy albedo for an individual METEOSAT pixel for a given solar zenith angle, θ_{sun}. See equation 8.79.
$a^{scene}(\theta_{sun})$	Model albedo, a, for a given scene type.
a^{scene}_{METx}	Model METEOSAT x VIS model narrow band albedo for a given scene type. See equation 5.12.
b	Predictor parameter. See e.g. equation 7.86.
cf^{mc}	Cloud fraction of a model mostly cloudy METEOSAT pixel. See equation 8.79.
cf'^{mc}	Radiance cloud fraction of a model mostly cloudy METEOSAT pixel. See equation 8.81.
cf^{pc}	Cloud fraction of a model partly cloudy METEOSAT pixel. See equation 8.79.
cf'^{pc}	Radiance cloud fraction of a model partly cloudy METEOSAT pixel. See equation 8.81.
ct	Centre triangle value for the definition of the spherical Haar Perfect Reconstruction Filter Bank (PRFB). See figure 7.25.
$d(n)$	Time series of difference coefficients in the Haar Perfect Reconstruction Filter Bank (PRFB). See equation 7.83.
dA	Elementary surface.
$d\Omega$	Elementary solid angle.
$d^*(n)$	Time series of lifted unquantified difference coefficients in the lifted Haar Perfect Reconstruction Filter Bank (PRFB). See equation 7.87.
$d^*_q(n)$	Time series of lifted quantified difference coefficients in the lifted Haar Perfect Reconstruction Filter Bank (PRFB). See equation 7.86.
$d_q(n)$	Time series of quantified difference coefficients in Haar PRFB. See equation 7.84.
$day_{max}(pixel, slot, month)$	The day of the month for which the maximum in equation 8.21 is reached.

$day_{min}(pixel, slot, month)$	The day of the month for which the minimum in equation 8.24 is reached.
dc	Low pass coefficient of the spherical Haar Perfect Reconstruction Filter Bank (PRFB). See equation 7.90 and figure 7.25.
dc_s	Scaled version of dc. See equation 7.92.
dc_l	Haar low pass coefficient of the left neighbour triangle of a given central triangle for the definition of the spherical Haar lifting operation. See figure 7.26.
dc_q	Quantified version of dc_s. See equation 7.93.
dc_r	Haar low pass coefficient of the right neighbour triangle of a given central triangle for the definition of the spherical Haar lifting operation. See figure 7.26.
dc_t	Haar low pass coefficient of the top neighbourtriangle of given central triangle for the definition of the spherical Haar lifting operation. See figure 7.26.
$\mathrm{div}(\vec{x})$	Divergence of the vector $\vec{x}$.
df	Desert fraction of a METEOSAT pixel = fraction of the pixel covered by the scene type "desert".
dl	Centre left high pass coefficient of the spherical Haar Perfect Reconstruction Filter Bank (PRFB). See equation 7.90 and figure 7.25.
dl^*	Lifted spherical centre left Haar high pass coefficient. See equation 7.104.
dl_s	Scaled versions of dl. See equation 7.92.
dl_q	Quantified version of dl_s. See equation 7.93.
dr	Centre right high pass coefficient of the spherical Haar Perfect Reconstruction Filter Bank (PRFB). See equation 7.90 and figure 7.25.
dr^*	Lifted spherical centre right Haar high pass coefficient. See equation 7.104.
dr_s	Scaled version of dr. See equation 7.92.
dr_q	Quantified version of dr_s. See equation 7.93.
dt	Centre top high pass coefficient of the spherical Haar Perfect Reconstruction Filter Bank (PRFB). See equation 7.90 and figure 7.25.
dt^*	Lifted spherical centre top Haar high pass coefficient. See equation 7.104.

dt_s	Scaled version of dt. See equation 7.92.
dt_q	Quantified versions of dt_s. See equation 7.93.
e	Atmospheric fluid internal energy per unit mass.
ecc	Eccentricity of the elliptical orbit of the earth around the sun.
f	Time fraction between t_1 and t_2 for which the motion has to be estimated between images i_1 and i_2. See equation 7.44.
$f(t)$	Time series of function values for discrete times t.
$f(\|x\|)$	Measured, trapezium-like, cross section of a ScaRaB angular sensitivity function. See equation 4.24.
f_{METx}^{scene}	Model spectral conversion factor for a given scene type = ratio of the broad band reflected short wave flux surface density to the METEOSAT x VIS filtered reflected short wave flux surface density. See equation 5.13.
f_{METx}^{white}	Spectral conversion factor, f_{METx}^{scene}, for spectrally white (uniform reflective) scenes.
f_i	The intensive quantity associated with the extensive quantity F_e.
$f_{hs}(t)$	Half sine regression function. See equation 8.27, figure 8.17 and equation 8.28.
$f_{ideal}(\|x\|)$	Idealised, rectangular, cross section of a ScaRaB angular sensitivity function. See equation 4.26.
$f_{sr}(t)$	Sun rise regression function. See equation 8.27, figure 8.17 and equation 8.28.
$f_{ss}(t)$	Sun set regression function. See equation 8.27, figure 8.17 and equation 8.28.
$fc_{METx}^{cs,desert}$	Model spectral correction factor, fc_{METx}^{scene}, for clear sky desert scenes.
$fc_{METx}^{cs,land}$	Model spectral correction factor, fc_{METx}^{scene}, for clear sky land scenes.
$fc_{METx}^{cs,ocean}$	Model spectral correction factor, fc_{METx}^{scene}, for clear sky ocean scenes.
fc_{METx}^{ov}	Model spectral correction factor, fc_{METx}^{scene}, for overcast cloudy scenes.
fc_{METx}^{scene}	Model spectral correction factor for a given scene type. See equation 5.16.
fs	Scene fraction. See equation 8.82.
$\vec{g_0}$	Local gravity acceleration.
$\vec{g}$	Apparent gravity acceleration = resultant from local gravity acceleration $\vec{g_0}$ and centrifugal acceleration. See equation 2.1.
$\tilde{g}(n)$	Impulse response of a Perfect Reconstruction Filter Bank (PRFB) high pass synthesis filter. See figure 7.12.
g	Image grey value.
g'	Mapped grey value.

$g(n)$	Impulse response of a Perfect Reconstruction Filter Bank (PRFB) high pass analysis filter. See figure 7.12.
$g_1(\|\delta_a\|, \|\delta_c\|)$	Shape function in the decomposition of $PSF_{ideal}(\delta_a, \delta_c)$. See equation 4.29.
$g_2(\|\delta_c\|)$	Amplitude function in the decomposition of $PSF_{ideal}(\delta_a, \delta_c)$. See equation 4.29.
g_{max}	Maximum grey value occurring in a given image or time series of images.
g_{min}	Minimum grey value occurring in a given image or time series of images.
$\tilde{h}(n)$	Impulse response of a Perfect Reconstruction Filter Bank (PRFB) low pass synthesis filter. See figure 7.12.
$h(n)$	Impulse response of a Perfect Reconstruction Filter Bank (PRFB) low pass analysis filter. See figure 7.12.
$h(t)$	Global time impulse response of a detector = impulse response of the detector plus the pre-sampling electronics.
$h_{ang,ideal}(\delta_a)$	Idealised ScaRaB detector global angular impulse response. See equation 4.27.
$h_{ang}(\delta_a)$	Equivalent global angular impulse response of a scanning radiometer. See equation 3.5.
inc	Inclination = angle between the equatorial plane of the earth and the ecliptic plane in which the earth translates around the sun.
$i_{(1-f)*1+f*2}(i,j)$	Interpolated image at slot $s = (1-f) * slot_1 + f * slot_2$ from images i_1 at slot $slot_1$ and i_2 at slot $slot_2$. See equation 8.47 or 8.48.
k_{IR}	METEOSAT IR calibration factor. See equation 8.49.
$k_{VIS,ISCCP}(date)$	METEOSAT VIS calibration factor, k_{VIS}, given by the International Satellite Cloud Climatology Project (ISCCP) for a particular date.
$k_{VIS,ISCCP}^{nominal \rightarrow absolute}(date)$	Correction relative to the nominal METEOSAT VIS calibration factor, $k_{VIS}^{nominal}$, given by the International Satellite Cloud Climatology Project (ISCCP) for a particular date. See equation 8.59.
k_{VIS}	METEOSAT VIS calibration factor. See equation 8.58.
$k_{VIS}^{nominal}$	Nominal METEOSAT VIS calibration factor k_{VIS}.
k_{WV}	METEOSAT WV calibration factor. See equation 8.50.
lt	Top triangle value for the definition of the spherical Haar Perfect Reconstruction Filter Bank (PRFB). See figure 7.25.
$last2bits(d)$	Last 2 bits of the integer value d.
$lastbit(d)$	Last bit of the integer value d.
m	Height of a given image = number of rows in the image.
$m(n)$	Time series of mean coefficients in the Haar Perfect Reconstruction Filter Bank (PRFB). See equation 7.83.
m_Δ	Mean instrument absolute error of a stochastic instrument that is built and operated for measuring the "solar constant" time series.

$m_q(n)$	Time series of quantified mean coefficients in Haar Perfect Reconstruction Filter Bank (PRFB). See equation 7.84.
$maxcount$	Maximum count that can occur in a grey value image (= 255 for 8 bit images).
$\vec{n}$	The outward pointing normal on the elementary surface $\delta\Sigma$.
n	Width of a given image = number of columns in the image.
$n_i(t)$	Noise of instrument i which measures the "solar constant" time series.
$o_{1,p}$	A priori estimation of the component o_1 of the displacement (o_1, o_2).
$o_{2,p}$	A priori estimation of the component o_2 of the displacement (o_1, o_2).
$o_{c,m}$	Observed mean value of the pixels of S_c. See equation 7.35.
$o_{c,p}$	Prior estimation of the mean value of the pixels of S_c.
o_c	Estimated mean value of the pixels of S_c.
p	Fluid pressure.
$p(n)$	Predictor for lifting operation. See figure 7.16.
$q_{\vec{cond}}$	Conductive energy flux surface density vector = the vector with as i'th component the energy flux density (amount of energy flowing through a unit surface per unit time) due to thermal conductivity trough a surface with normal in the i'th direction (first direction = x axis, second direction = y axis, third direction = z axis).
$q_{\vec{rad}}$	Radiative energy flux surface density vector = the vector with as i'th component the energy flux density (amount of energy flowing through a unit surface per unit time) due to radiation trough a surface with normal in the i'th direction (first direction = x axis, second direction = y axis, third direction = z axis).
rt	Top triangle value for the definition of the spherical Haar Perfect Reconstruction Filter Bank (PRFB). See figure 7.25.
r	Radius of a point in the local spherical coordinate system = distance between the point and the origin P.
$r^{scene}(\theta_{sat}, \phi_{rel}, \theta_{sun})$	Model angular reflection function of a given scene type = ratio of the reflected short wave radiance to the incoming solar flux surface density.
r_{P-sun}	Distance between the sun and a given point P on the earth.
θ_{sun}	Solar zenith angle = angle between the direction of the sun and the local vertical in a given point in the earth's atmosphere.
$r_{earth-sun}$	Distance between the sun and the centre of the earth.
ri	Iteration counter for topdown Bayesian image analysis.
sl	Slope parameter of morphological kernel(s). See equations 7.8 and 7.9.

s_{RI}	Start segment size for topdown Bayesian image analysis
$s_{ang}(\delta_a)$	Equivalent global angular step response of a scanning radiometer. See equation 4.15.
s_{ri}	Segment size for ri'th iteration of topdown Bayesian image analysis. See equation 7.18.
tt	Top triangle value for the definition of the spherical Haar Perfect Reconstruction Filter Bank (PRFB). See figure 7.25.
$t(l, slot)$	METEOSAT time of acquisition of line unit l of slot $slot$.
$t(slot, i, j)$	Expected acquisition time for pixel (i, j) of METEOSAT image at given $slot$.
t_{delay}	True acquisition time minus expected acquisition time.
t_1	Time of acquisition of first image i_1 for motion estimation.
t_{28}	Time of acquisition of given METEOSAT pixel for slot 28.
t_{29}	Time of acquisition of given METEOSAT pixel for slot 29.
t_2	Time of acquisition of second image i_2 for motion estimation.
t_{VE}	Time at which the sun passes the vernal equinox.
$t_{\text{end}}(\text{slot})$	End time of the acquisition of the METEOSAT image for a given time slot.
$t_{\text{start}}(\text{slot})$	Start time of the acquisition of the METEOSAT image for a given time slot.
$u^{cs}_{IR}(pixel, slot, month)$	Uncertainty on $C^{cs}_{IR}(pixel, slot, month)$. See equation 8.23.
$u^{cs}_{VIS}(pixel, slot, month)$	Uncertainty on $C^{cs}_{VIS}(pixel, slot, month)$. See equation 8.26.
$\vec{v}$	Instantaneous speed in the xyz coordinate system of the fluid parcel contained within δV.
v_{scan}	Angular scan speed of a scanning radiometer.
wf	Water fraction of a METEOSAT pixel = fraction of the pixel covered by water.
x	x coordinate of the local xyz coordinate system with origin in point P, with z axis oriented opposite to the apparent gravity acceleration $\vec{g}$ and with the yz plane containing $\vec{\Omega}$. See figure 2.2.
$x(n)$	Input of a Perfect Reconstruction Filter Bank (PRFB). See figure 7.12.
$x_g(n)$	High pass coefficients at the output of the forward part of a Perfect Reconstruction Filter Bank (PRFB). See figure 7.12.
$x_h(n)$	Low pass coefficients at the output of the forward part of a Perfect Reconstruction Filter Bank (PRFB). See figure 7.12.
y	y coordinate of the local xyz coordinate system with origin in point P, with z axis oriented opposite to the apparent gravity acceleration $\vec{g}$ and with the yz plane containing $\vec{\Omega}$. See figure 2.2.
z	z coordinate of the local xyz coordinate system with origin in point P, with z axis oriented opposite to the apparent gravity acceleration $\vec{g}$ and with the yz plane containing $\vec{\Omega}$. See figure 2.2.

Bibliography

[ABMD92] M. Antonini, M. Barlaud, P. Matthieu, and I. Daubechies. Image coding using wavelet transform. *IEEE Transactions on Image Processing*, 1(2):205–220, April 1992.

[B+89] B.R. Barkstrom et al. Earth radiation budget experiment (erbe) archival and april 1985 results. *Bulletin of the American Meteorological Society*, 70:1254–1262, 1989.

[Bar88] M. Barnsley. *Fractals everywhere*. Academic Press, 1988.

[BCL+95] B. Blancke, J.L. Carr, E. Lairy, F. Pomport, and B. Pourcelot. The aerospatiale meteosat image processing system (amips). In *Proceedings of the First International Symposium on Scientific Imagery and Image Processing*. Association Aeronautique et Astronautique de France, 1995.

[Ben85] L. Bengston. Medium-range forecasting–the experience of ecmwf. *Bulletin of the American Meteorological Society*, 66(9):1133–1146, September 1985.

[Cam79] J. S. Campbell. A climatological archive of radiance data recorded by meteosat. MDMD/MET 20, European Space Operation Control, 1979.

[Cap96] M. Capderou. Determination of the shortwave anisotropic function for clear-sky desert scenes from scarab - comparison with results from sun-synchronuous and geosynchronuous satellite data. In *Proceedings of the international radiation symposium*, August 1996.

[CD97] D. Crommelynck and S. Dewitte. Solar constant temporal and frequency characteristics. *Solar Physics*, 173:171–191, June 1997.

[CDFL94] D. Crommelynck, V. Domingo, A. Fichot, and R.B. Lee. *Total Solar Irradiance Observations from the EURECA and ATLAS Experiments*, pages 63–69. Cambridge University Press, 1994.

[CFLR95] D. Crommelynck, A. Fichot, R.B. Lee, and J. Romero. First realisation of the space absolute radiometric reference (sarr) during the atlas 2 flight period. *Advances in Space Research*, 16(8):17–23, 1995.

[CJ92] D. Crommelynck and A. Joukoff. Estimation of the spectral distribution using a simple algorithm. In *IRS' 92: Current Problems in Atmospheric Radiation*, Tallinn, Estonia, August 1992. Deepak Publishing ISBN0-937194-28-X (1993).

[CK95] M. Capderou and R. Kandel. Determination of the shortwave anisotropic function for clear-sky desert scenes from meteosat data. *Journal of Applied Meteorology*, June 1995.

[CR94] B. Cushman-Roisin. *Introduction to geophysical fluid dynamics*. Prentice Hall, 1994. 320 p.

[CTV+96] R.P. Cebula, G. Thuillier, M.E. VanHoosier, et al. Observation of the solar irradiance in the 200-360 nm interval during the atlas-1 mission: A comparison among three sets of measurements - ssbuv, solspec, and susim. *Geophysical Research Letters*, 23:2289–2292, August 1996.

[D+90] D. Doelling et al. On the role of satellite-measured narrowband radiances for computing the earths's radiation balance. In *Seventh Conference on Atmospheric Radiation*, San Francisco, July 23-27 1990. American Meteorological Society.

[DB94] W. III Donat and A. Boksenberg. *The astronomical almanac*. US Government Printing Office/Her Majesty's Stationary Office, 1994.

[DC97] S. Dewitte and J. Cornelis. Lossless integer wavelet transform. *IEEE Letters on Signal Processing*, 4(6):158–160, June 1997.

[DCC96] S. Dewitte, J. Cornelis, and D. Crommelynck. A generic image processing tool : topdown bayesian image analysis. In *Proceedings of NATO AGARD conference* Remote Sensing: A valuable source of information, April 1996.

[DMSCC] S. Dewitte, N. Manalo-Smith, D. Crommelynck, and J. Cornelis. Determination of tropical radiation budget at high time and space resolution by combination of geostationary and polar satellite measurements. presented at 'International Conference on *Tropical Climatology, Meteorology and Hydrology* in memoriam F. Bultot (1924-1995), Brussels, Belgium, May 22-24, 1996.

[DNCC95] S. Dewitte, E. Nyssen, D. Crommelynck, and J. Cornelis. Multi stage analysis of meteosat images. In *Proceedings of European Symposium on Satellite Remote Sensing II*, volume 2579, pages 170–181. SPIE, November 1995.

[DS89] F. J. Diekmann and G. L. Smith. Investigation of scene identification algorithms for radiation budget measurements. *Journal of Geophysical Research*, 94(D3):3395 – 3412, March 1989.

[DVAC95] S. Dewitte, M. Vemis, M. Acheroy, and J. Cornelis. Comparison of matching techniques for cloud motion wind extraction. In *Proceedings of the First International Symposium on Scientific Imagery and Image Processing*, volume S, pages 40–60. L'Association Aeronautique et Astronautique de France, 1995.

[EF91] R.G. Ellingson and Y. Fouquart. The intercomparison of radiation codes for climate models: an overview. *Journal of Geophysical Research*, 96:8925–8927, 1991.

[Ehr92] M. Ehrendorfer. Four-dimensional data assimilation: comparison of variational and sequential algorithms. *Quarterly Journal of Royal Meteorological Society*, pages 673–713, 1992.

[FCW+97] C. Fröhlich, D. Crommelynck, C. Wherli, M. Anklin, S. Dewitte, A. Fichot, W. Finsterli, A. Jimenez, A. Chevalier, and H. Roth. In-flight performance of the virgo solar irradiance instruments on soho. accepted for publication by Solar Physics, 1997.

[Frö97] C. Fröhlich. Solar irradiance monitoring programs. In *Proceedings of the SOLERS22 Workshop*. Kluwer Academic Publishers, 1997.

[GOH96] R.N. Green and P. O'Rawe-Hinton. Estimation of angular distribution models from radiance pairs. *Journal of Geophysical Research*, pages 16591–16959, 1996.

[GOH97] R.N. Green and P. O'Rawe-Hinton. Validation of new set of angular distribution models for broadband radiance to flux convrsion. In *Proceedings of the ninth conference on atmospheric radiation*, pages 221–224. American Meteorological Society, 1997.

[Gre87] R. N. Green. Processed archival tape s-8 pat users' guide. Users' Guide ERBE 3-3-12-6-85-1-1, NASA, December 1987.

[HKHM92] D. V. Hoyt, H. L. Kyle, J. R. Hickey, and R. H. Maschhoff. The nimbus-7 solar total irradiance: a new algorithm for its derivation. *Journal of Geophysical Research*, 97:51–63, 1992.

[Hof90] J. Hoffman. Use of spatial coherence method for cloud motion wind retrieval. In *Proceedings of the 8th METEOSAT Scientific Users' meeting*, volume EUM P 05, pages 97–100, 1990.

[Hum86] A. G. Hume. Exact descriptions of regular and semi-regular polyhedra and their duals. *Computing Science Technical Report 130*, November 1986.

[Iqb83] M. Iqbal. *An introduction to solar radiation.* Academic Press, 1983. 390 pp.

[K+95] E. Kalnay et al. The nmc/ncar 40-year reanalysis project. accepted for publication by Bulletin of the American Meteorological Society, April 1995.

[Kon69] K.YA. Kondratyev. *Radiation in the atmosphere.* International Geophysics Series. Academic Press, 1969. 912 pp.

[KVP+97] R. Kandel, M. Viollier, L.A. Pakhomov, V.A. Golovko, E. Raschke, and R. Stuhlmann. The scarab earth radiation budget dataset. submitted for publication to the Bulletin of the American Meteorological Society, 1997.

[LBC87] III Lee, R.B., B.R. Barkstrom, and R.D. Cess. Chararteristics of the earth radiation budget experiment solar monitors. *Applied Optics*, 26:3090–3096, 1987.

[Lea91] J. Lean. Variations in the sun's radiative output. *Reviews of Geophysics*, 29:505–535, 1991.

[LGWT95] III Lee, R.B., M.A. Gibson, R.S. Wilson, and S. Thomas. Long term total solar irradiance variability during sunspot cycle 22. *Journal of Geophysical Research*, 100:1667–1675, 1995.

[Mal89] S.G. Mallat. A theory for multiresolution signal decomposition: The wavelet representation. *IEEE Transactions on Pattern Analysis and Machine Intelligence*, 11:674–693, July 1989.

[Mar89] P. Maragos. Pattern spectrum and multiscale shape representation. *IEEE Transactions on Pattern Analysis and Machine Intelligence*, 11:701–716, July 1989.

[MH84a] P. Minnis and E.F. Harrison. Diurnal variability of regional cloud and clear-sky radiative parameters derived from goes data. parti: Analysis method. *Journal of Climate and Applied Meteorology*, 23(7):993–1011, July 1984.

[MH84b] P. Minnis and E.F. Harrison. Diurnal variability of regional cloud and clear-sky radiative parameters derived from goes data. partiii: November 1978 radiative parameters. *Journal of Climate and Applied Meteorology*, 23(7):1032–1051, July 1984.

[MKPA91] J.L. Monge, R.S. Kandel, L.A. Pakhomov, and V.I. Adasko. Scarab earth radiation budget scanning radiometer. In *Proc. New Developments and Applications in Optical Radiometry III.*, number 28 in Metrologia, pages 261–264, Davos, 1991.

[MSSS94] N. Manalo-Smith, W.F. Staylor, and G.L. Smith. Analytic forms of bi-directional reflectance functions. In *Proceedings of Seventh Conference on Satellite Meteorology and Oceanography*, Monterey, California, June 6-10 1994.

[MYH91] P. Minnis, D.F. Young, and E.F. Harrison. Examination of the relationship between outgoing infrared window and total longwave fluxes using satellite data. *Journal of Climate*, 4(11):1114–1133, November 1991.

[Pro92] Meteosat Exploitation Project. Meteosat - description of magnetic files and tapes. Technical report, European Space Operation Control, 1992.

[R+85] W.B Rossow et al. Isccp cloud algorithm intercomparison. *Journal of Climate and Applied Meteorology*, 24(9):877–903, 1985.

[R+90] P. K. Rao et al. *Weather Satellites: Systems, Data and Environmental Applications.* American Meteorological Society, 1990. 503 pp.

[Rai96] F. Raison. *Modélisation et étude du bilan radiométrique de l'instrument ScaRaB embarqué sur le satellite Météor-3/7*. PhD thesis, Universite de Paris VII (Denis Diderot), November 1996. 197 pp.

[RB86] C. K. Roberts and A. Boksenberg. *The astronomical almanac*. US Government Printing Office/Her Majesty's Stationary Office, 1986.

[RDBW92] W.B. Rossow, Y. Desormeaux, C.L. Brest, and A. Walker. International satellite cloud climatology project (isccp). WMO/TD 520, World Meteorological Organisation, October 1992. WCRP-77.

[RWF94] J. Romero, C. Wherli, and C. Fröhlich. Solar total irradiance variability from sova2 on board eureca. *Solar Physics*, 152:23–29, 1994.

[RYG96] P. Ricchiazzi, S. Yang, and C. Gautier. Sbdart: A practical tool for plane-parallel radiative transfer in the earth's atmosphere. available at http://arm.mrcsb.com/sbdart, 1996.

[S+93] J. Schmetz et al. Operational cloud-motion winds from meteosat infrared images. *Journal of Applied Meteorology*, 32(7):1206–1225, 1993.

[Sch86] J. Schmetz. An atmospheric-correction scheme for operational application to meteosat infrared measurements. *ESA Journal*, 10:145–159, 1986.

[SD87] G. Seze and M. Desbois. Cloud cover from satellite imagery using spatial and temporal characteristics of the data. *Journal of Climate and Applied Meteorology*, 26(2):287–303, 1987.

[SG74] E.V.P. Smith and D.M. Gottlieb. Solar flux and its variation. *Space Science Reviews*, 16:771, May 1974.

[SG+88] J. T. Suttles, R. N. Green, et al. Angular radiation models for earth-atmosphere system: Volume 1 - shortwave radiation. Reference Paper 1184-1, NASA, July 1988.

[SK96] F. Sirou and R.S. Kandel. Scarab fm1 characterization/documentation. Minutes of ISSWG-2, Hamburg, March 1996.

[SL88] J. Schmetz and Q. Liu. Outgoing longwave radiation and its diurnal variation at regional scales derived from meteosat. *Journal of Geophysical Research*, 93(D9):11192–11204, September 1988.

[Smi94] G.L. Smith. Effects of time response on point spread function of a scanning radiometer. *Applied Optics*, 33:7031–7037, October 1994.

[SMvdB90] J. Schmetz, M. Mhita, and L. van de Berg. Meteosat observations of longwave cloud-radiative forcing for april 1985. *Journal of Climate*, 3:784–791, July 1990.

[SS88] R. Stuhlmann and G. L. Smith. A study of cloud generated radiative heating and its generation of available potential energy, part i: Theoretical background. *Journal of Atmospheric Sciences*, 45:3911–3927, December 1988.

[SS95] P. Schroeder and W. Sweldens. Spherical wavelets: efficiently representing functions on a sphere. *Computer Graphics*, 29, 1995.

[SU97] S. K. Solanki and Y.C Unruh. A model of the wavelength dependence of solar irradiance variations. accepted for publication by Astronomy and Astrophysics, 1997.

[Swe94] W. Sweldens. The lifting scheme: A custom-design construction of biorthogonal wavelets. Technical Report 7, University of South Carolina, Department of Mathematics, 1994.

[T+81] G. Thuillier et al. An instrument to measure the solar spectrum from 170 to 3200 nm on board spacelab. *Solar Physics*, 74:531–, 1981.

[Tom81] C. Tomassini. Objective analysis of cloud fields. Technical Report SP-159, ESA, 1981.

[VF94] M. Vesperini and Y. Fouquart. Determination of broad-band shortwave fluxes from the meteosat visible channel by comparison to erbe. *Beitr. Phys. Atmosph.*, 67(2):121–132, 1994.

[VM49] J. Van Mieghem. *Les equations generales de la mecanique et de l'energetique des milieux turbulents en vue des applications a la meteorologie.* Number 14 in Memoires. Royal Meteorological Institute of Belgium, 1949.

[VM58] J. Van Mieghem. Radiation data needed in dynamical meteorology. *Archiv für Meteorologie, Geophysik und Bioklimatologie*, 10(4), 1958.

[VM62] J. Van Mieghem. Pour une exploration synoptique du champ du rayonnement dans l'atmosphère. *Archiv für Meteorologie, Geophysik und Bioklimatologie*, 13(2), 1962.

[WBH+96] B. Wielicki, B.R. Barkstrom, E.F. Harrison, R.B. Lee, G.L. Smith, and J.E. Cooper. Clouds and the earth's radiant energy system (ceres): An earth observing system experiment. *Bulletin of the American Meteorological Society*, 77:853–868, May 1996.

[WCK+95] B. Wielicki, R.D. Cess, M.D. King, D.A. Randall, and E.F. Harrison. Mission to planet earth: Role of clouds and radiation in climate. *Bulletin of the American Meteorological Society*, 76:2125–2153, 1995.

[WG89] B. Wielicki and R. Green. Cloud identification for erbe radiative flux retrieval. *Journal of Applied Meteorology*, 28:1138–1146, 1989.

[Wil94] R.C. Willson. *Irradiance observations of SMM, Spacelab 1, UARS, and Atlas experiment*, pages 54–62. Cambridge University Press, 1994.